2016

Study On Anisotropic Plasticity And Fracture Of Lightweight Metal Sheets

Yueqian Jia
University of Central Florida

STUDY ON ANISOTROPIC PLASTICITY AND FRACTURE OF LIGHTWEIGHT METAL SHEETS

by

YUEQIAN JIA
M.S. University of Central Florida, 2013
B.S. Northwestern Polytechnical University, China, 2011

A dissertation submitted in partial fulfillment of the requirements
for the degree of Doctor of Philosophy
in the Department of Mechanical and Aerospace Engineering
in the College of Engineering and Computer Science
at the University of Central Florida
Orlando, Florida

Spring Term
2016

Major Professor: Yuanli Bai

ABSTRACT

How to reduce weight and increase fuel efficiency is a critical challenge in transportation industries. One way to resolve the problem is to adopting lightweight alloys (i.e. advanced high strength steel, aluminum alloys, or magnesium alloy) in structure designs and manufacturing. Fully understanding the mechanical properties of these materials is a key step.

In order to fully characterize the plasticity and fracture of magnesium AZ31B-H24 sheets, a set of mechanical experiments (170 in total) were performed under both monotonic and non-proportional loading conditions, including monotonic uniaxial tension, notch tension, in-plane uniaxial compression, wide compression (or called biaxial compression), plane strain compression, through-thickness compression, in-plane shear, punch test, uniaxial compression-tension reverse loading, and two-step uniaxial tension (cross-loading).

Both the plastic strain histories and stress responses were obtained under the above loading conditions, which give a comprehensive picture of mechanical behaviors of this material. No apparent cross-hardening effect was observed for this material.

An extended orthotropic yield criterion involving two linear anisotropic transformation tensors, CPB06ex2, in conjunction with its associated flow rule was fully calibrated to describe both the anisotropy in plastic flow and tension-compression asymmetry in stress-strain behaviors.

A fully modularized framework to combine isotropic, kinematic, and cross hardening behaviors was established under non-monotonic loading conditions. Three sets of state variables were

defined and applied to consider the effects of, a) loading history, b) twinning and de-twinning and c) different pre-strain.

In order to predict ductile fracture of metal sheets, the "mixed" stress/strain invariants based Modified-Mohr-Coulomb (MMC) fracture model was transferred into an all-strain based MMC (eMMC) model under plane stress condition, predicting the fracture strain dependent on strain ratio or Φ angle, instead of stress triaxiality and Lode angle parameter. The strain ratio or Φ angle could be directly measured by digital image correlation (DIC), while the latter required finite element analysis to be determined. This method makes it possible to study material fracture behavior while bypassing plasticity. The eMMC fracture locus can be fully calibrated by fracture strains directly measured from DIC. The fracture strain was also extended by a linear transformation operating to the plastic strain tensor to incorporate the fracture anisotropy. All models were implemented into Abaqus/Explicit as a user material subroutine (VUMAT). Good prediction capability has been demonstrated for magnesium AZ31B-H24 sheets by FE simulation using shell elements.

The current framework was also applied for TRIP780, BH240, DP600, and EDDQ steel sheets with adjustment, under different loading conditions. The FE simulation results for TRIP780 correlated well with experimental data under different monotonic loading conditions. The analytical results for BH240, DP600, and EDDQ demonstrated good prediction capability for cross-hardening behavior, and validated by the non-proportional experimental data under two-stage uniaxial tension.

KEYWORDS: Magnesium AZ31B Sheet, Anisotropic plasticity, Isotropic Hardening, Kinematic Hardening, Cross Hardening, Non-linear Strain Path, Finite Element Analysis, All-strain Based Modified-Mohr-Coulomb Fracture Model, Anisotropic Fracture

ACKNOWLEDGMENTS

First and foremost, I would like to express my sincere gratitude to my academic advisor, Professor **Yuanli Bai**, for his guidance, encouragement, and patience through four years of study at University of Central Florida (UCF). I'm extremely grateful for his suggestions and daily discussions throughout my doctoral research. This dissertation would not have been possible without his persistent help. Partial financial supports from Volkswagen (Germany), Auto Steel Partnership (A/SP), State Key Laboratory of Automotive Safety and Energy, Tsinghua University (Beijing, China), and UCF are greatly appreciated.

Profound gratitude goes to my PhD committee members, Professor **Jihua Gou**, Professor **Alain Kassab**, Professor **Seetha Raghavan** from Department of Mechanical and Aerospace Engineering, and Professor **Thomas Wu** from Department of Electrical Engineering and Computer Science, for providing indispensable advice, information, and support on different aspects of my thesis and for their cooperation in a different field assignment. Sheet metal forming related theories and practical experiences from Dr. **Edmund Chu** of Alcoa are also gratefully acknowledged.

I would like to extend my thanks to those who offered collegiate guidance and support over the years, Professor **Tuhin Das**, Professor **Ali Gordon**, Professor **Suhada Jayasuriya**, Professor **Jayanta Kapat**, Professor **An Linan**, Professor **Faissal Moslehy**, and Professor **Chengying Xu**.

I am also indebted to the members of Lab of Solid and Structure Mechanics, with whom I have interacted during my graduate studies. Particularly I would like to acknowledge **Mohammed Algarni**, **Sami Ghazali**, **Xiang Long**, **Hao Pan**, and **Yangyang Qiao**, for the assistance of all

related experiments and modeling. I appreciate the efforts of many undergraduate students, **John Bermudez**, **Alec Jacobs**, **Aung Maung**, **Erin Shoemaker**, and **Jonathan Sosa**, for their contributions to various projects.

I would like to give my sincere thanks to Dr. **Meng Luo** and Dr. **Kai Wang** of MIT for their assistance of conducting the reversal loading tests for magnesium sheets. I am also grateful to Dr. **Gregory Freihofer** of UCF in coordinating experiment schedules. I would like to acknowledge the ***Auto Steel Partnership*** for providing numerous experimental data to validate the cross-hardening model under two-step uniaxial tension. I would also like to give my special thanks to **Timothy Linder** of UCF machine shop for manufacturing numerous magnesium sheet specimens. I would be remiss if I did not thank **Jeanine Clements**, who deserves credit for providing needed assistance with administrative tasks.

For the ancestors who paved the path before me upon whose shoulders I stand. This is dedicated to my family and many friends who supported me on this memorable journey. Thank you.

TABLE OF CONTENTS

LIST OF FIGURES

LIST OF TABLES

CHAPTER 1 INTRODUCTION

1.1 Magnesium Alloy and Experiments

The magnesium alloys have been very competitive in the automotive industry to enable lightweight design and reduce energy consumption and greenhouse gas emission. With their very high ratio of strength/stiffness versus density, the magnesium alloys have also been applied in new products by major leading car manufactures to replace steels and aluminum. For instance, Volkswagen, Audi, Mercedes Benz, BMW, Ford, and Jaguar are all using magnesium transmission casings in recent models. General Motor is using 57 pounds of magnesium in the full-sized Savana and Express vans, offering a $20\% - 25\%$ weight saving over aluminum alloys (Elektron, 2014).

The magnesium alloy sheets (AZ31B) exhibit different mechanical responses as compared to steels and aluminum sheets and highly anisotropic characteristic because of their hexagonal close packed (HCP) crystal structure and strong basal crystallographic texture from rolling process (S.R. Agnew, 2002; Roberts, 1960). This also results in strong tension/compression asymmetry based on the test data from Kelley and Hosford (1968). More experiments under different loading conditions are required for magnesium alloy sheets to fully understand their comprehensive mechanical behaviors. A comprehensive set of experiments on plasticity and fracture of magnesium AZ31B-H24 was conducted by Jia and Bai (2015c) under various multi-axial loading conditions.

For uniaxial loading, the cumulative and instantaneous Lankford ratios under uniaxial tension were reported by Khan, Pandey, Gnäupel-Herold, and Mishra (2011); X. Y. Lou, Li, Boger,

Agnew, and Wagoner (2007). The in-plane uniaxial compression has been performed using reduced-size dogbone specimens with anti-buckling device by X. Y. Lou et al. (2007), using stacked cubic specimens by Ghaffari Tari, Worswick, Ali, and Gharghouri (2014); D. Steglich, Tian, Bohlen, and Kuwabara (2014), using single cylindrical specimens by Barnett, Keshavarz, and Ma (2006). The in-plane compressive hardening behavior differs significantly from tension because of the activation of twinning-dominated deformation (Ball & Prangnell, 1994; Barnett, 2007; Barnett, Keshavarz, Beer, & Atwell, 2004). The strain-stress relationship exhibits a concave shape under uniaxial compression, while it is typically a convex curve under tension. Under compression-tension reverse loading, the de-twinning phenomenon occurs when the subsequent tensile load is performed along the c-axis of the twinned areas (Brown et al., 2005; X. Y. Lou et al., 2007; Nguyen, Lee, Kim, & Kim, 2013; H. Wang, Wu, Wang, & Tomé, 2013).

For biaxial tension loading, cruciform specimens have been applied using biaxial testing machine, with different ratios between the forces along horizontal and vertical conditions, by Abu-Farha, Hector, and Khraisheh (2009); Andar, Kuwabara, and Steglich (2012); D. Steglich et al. (2014). For certain materials, an alternative approach is to add a pair of notches for the sheet specimen, which is equivalent to the biaxial tension condition at approximately the center (Bai, 2008). The analytical solution of the stress triaxiality at the center of the specimen can be determined by its geometry. It is reported that the equi-biaxial tension has also been performed by bulge test (Kaya, Altan, Groche, & Klöpsch, 2008; D. Steglich, Jeong, Andar, & Kuwabara, 2012), punch test (Ambrogio et al., 2008; H. J. Kim, Choi, Lee, & Kim, 2008), and through-thickness compression (Kurukuri, Worswick, Ghaffari Tari, Mishra, & Carter, 2014; D. Steglich et al., 2014) . Note that the cruciform test for equi-biaxial tension was stopped at a strain level of

0.015 because shear fracture occurred prior to the equi-biaxial tension failure (Andar et al., 2012). The bulge test could achieve a higher strain level up to 0.05 in room temperature (Kaya et al., 2008; D. Steglich et al., 2012). The punch test is capable to measure the plastic flow under equi-biaxial tension at the center point, however, the corresponding strain-stress curve could not be directly obtained due to the non-uniform out-plane loading. The through-thickness compression is equivalent to the equi-biaxial tension superimposed with a hydrostatic pressure. The similar strain-stress response with bulge test or cruciform specimen test has been obtained by through-thickness compression with a strain level of 0.12, based on the comparison from D. Steglich et al. (2014).

The report of in-plane biaxial compression loading is currently not adequate. At present, a few channel die compression tests for magnesium alloy sheets were reported, achieving plane strain compression in the transversal direction (Barnett et al., 2006; Staroselsky & Anand, 2003). Data that allow comparing the difference in response between uniaxial compression and plane strain compression for magnesium AZ31B is currently missing. Cyclic simple shear tests have been conducted for magnesium alloy sheets with a maximum strain level of 0.1 in equivalent plastic strain by X. Y. Lou et al. (2007).

1.2 Sheet Metal Forming

Sheet metal forming is an essential part of automobile industry because it allows manufacturing high quality products with complex geometry and low costs. It is also possible to produce a wide range of drawn-parts, from the metal components of car-body elements to the structural elements of aircrafts. Recently, more and more lightweight materials like advanced high strength steels or nonferrous metallic alloys (aluminum or magnesium) are adopted due to the urgent need to

reduce vehicle weight and increase both fuel efficiency and performance. However, these materials are relatively brittle and vulnerable to fracture during forming or subsequent procedures. It is necessary to have an adequate plasticity and fracture model to precisely predict the final shape without producing strains that exceeds the forming limit or fracture limit during metal forming.

Numerous experiments have been conducted for investigating the dependency of ductile fracture on stress states. The relationship between ductile fracture strain and stress triaxiality for steels has been investigated by Johnson and Cook (1985); Mackenzie, Hancock, and Brown (1977), using notched axisymmetric tensile specimens. It was concluded that the ductility is negatively related to the stress triaxiality. A comprehensive set of experiments was conducted on aluminum 2024-T351 by Bao (2003); Khan and Liu (2012a), including compression, pure shear, uniaxial and bi-axial tensions under axisymmetric and plane stress loading conditions. The results exhibited a non-monotonic trend of fracture strain dependency on stress triaxiality. A comparison was made between the notched axisymmetric and flat grooved specimens by Bai, Teng, and Wierzbicki (2009), yielded that ductility is affected by not only stress triaxiality but also Lode angle parameter. A butterfly-shaped flat specimen was applied to study the fracture initiation under a wide range of loading conditions by D. Mohr and Henn (2007); Wierzbicki, Bao, and Bai (2005). Another series of multi-axial fracture tests on tubular specimens was performed by Barsoum and Faleskog (2007). These tests have also proven that the ductility depends on both stress triaxiality and the Lode angle parameter.

During a sheet metal forming process, the mechanical behavior can be dramatically influenced by non-proportional strain histories, based on the reports from Bai and Wierzbicki (2008a);

Barlat, Ferreira Duarte, Gracio, Lopes, and Rauch (2003); Min, Jeon, Kim, and Kim (1995); Schmitt, Shen, and Raphanel (1994). For example, the loading condition in a deep drawing could alter into biaxial tension from pure shear when the material flows into the die from the flange area, resulting in a non-proportional deformation (Thuillier, Manach, Menezes, & Oliveira, 2002).

For magnesium alloys, the de-twinning phenomenon occurs under compression-tension reversal loading when the subsequent tensile load is performed along the c-axis of the twinned areas, generating an unusual concave shape in the tensile stress-strain curve (Brown et al., 2005; X. Y. Lou et al., 2007; Piao, Chung, Lee, & Wagoner, 2012). This phenomenon has a different tendency from the monotonic compression/tension loading. A much lower yield stress occurs at the second-stage tension loading, resulting in another low stress plateau followed by a rapidly increasing hardening rate.

1.3 Constitutive Modeling

1.3.1 Anisotropic Yield Criterion

With the complicated mechanical behavior under different loading conditions, the accurate prediction of both plastic behavior and ductile fracture property is still a big challenge. Several typical anisotropic yield criterion with symmetric yield surface, including Hill 1948, Barlat 1989, and Yld2000-2D, have been evaluated using uniaxial and biaxial tension data, and claimed to be inadequate for compression status by Andar et al. (2012); Jia, Long, Wang, and Bai (2013); J. Park, Lee, You, Choi, and Kim (2007). An anisotropic yield criterion with asymmetrical tension/compression surface is therefore required because twinning is operational in HCP metals and induces tension/compression asymmetry and texture evolution. To account for both

anisotropy and tension/compression asymmetry induced by twinning, several anisotropic criteria expressed in terms of the stress deviator were developed by Cazacu and Barlat (2004); Cazacu, Plunkett, and Barlat (2006); Nixon, Cazacu, and Lebensohn (2010); Plunkett, Cazacu, and Barlat (2008).

For AZ31B magnesium alloys, primarily based on monotonic uniaxial tension and compression data sets for this material, a modified Drucker-Prager yield criterion with asymmetrical yield surface (J. H. Kim et al., 2008) has been calibrated by M.-G. Lee, Wagoner, Lee, Chung, and Kim (2008), the Cazacu-2004 yield criterion (Cazacu & Barlat, 2004) has been evaluated by Mekonen, Steglich, Bohlen, Letzig, and Mosler (2012); Dirk Steglich, Brocks, Bohlen, and Barlat (2011). The CPB06 yield criterion (Cazacu et al., 2006) has been calibrated and applied in three-point bending finite element (FE) analysis by J. Kim et al. (2008). The CPB06 yield criterion was applied to describe the anisotropy in the stress-strain response among uniaxial tension, uniaxial compression and torsional loading by Chandola et al. (2015); Revil-Baudard, Chandola, Cazacu, and Barlat (2014). The CPB06 yield criterion with two stress linear transformations (CPB06ex2) (Plunkett et al., 2008), which improved the yield surface correlation with the area of biaxial tension, has been evaluated by Andar et al. (2012); Plunkett et al. (2008). The CPB06 yield criterion with different linear transformations (one as CPB06, two as CPB06ex2, three as CPB06ex3, and four as CPB06ex4) have been compared and implemented in the bending simulation by Ghaffari Tari et al. (2014), showing that the CPB06ex3 could provide improved bending stress distribution. Additionally, it is also important to develop a hardening rule which is capable to consider the effects of twinning under complex loading conditions. Using the monotonic uniaxial tension and compression data, a viscoplastic self-

consistent polycrystal model has been developed and applied by Jain and Agnew (2007). A semi-analytical Sachs model has been developed, combining the Schmid law, power law hardening and a sigmoidal function based on the twinning fraction, together with an isotropic hardening rule by Barnett (2007); Barnett et al. (2004). Correlating with the experimental data under compression-tension reverse loading, a nonlinear mixture isotropic hardening rule (J. H. Kim et al., 2008) together with the Chaboche kinematic hardening model (Chaboche, 1977) has been calibrated by M. G. Lee, Kim, Wagoner, Chung, and Kim (2009); M.-G. Lee et al. (2008). A set of deformation evolution rules (named as "TWINLAW"), incorporating slip and twinning/de-twinning effects, has been developed and calibrated by M. Li, Lou, Kim, and Wagoner (2010). Some crystal-plasticity based models have been applied by Hama and Takuda (2011); H. Wang et al. (2013). Another phenomenological model, identifying the slip and twinning modes for isotropic hardening behavior, has been proposed by Nguyen et al. (2013).

1.3.2 Hardening Model

Two types of constitutive model are capable to incorporate the twinning/de-twinning effect under reversal loading conditions: crystal plasticity model and phenomenological-based hardening model. A visco-plastic self-consistent polycrystalline model was proposed and applied by Jain and Agnew (2007), using the monotonic uniaxial tension and compression data. This model was further incorporated within the Marciniak–Kuczynski (M–K) approach for forming limit curve prediction by John Neil and Agnew (2009). A set of deformation evolution rules, "TWINLAW", was developed by M. Li et al. (2010), incorporating slip and twinning/de-twinning effects in the constitutive model. Crystal-plasticity based models have been implemented into finite element (FE) analysis by Hama and Takuda (2011); H. Wang et al. (2013). Alternatively, a nonlinear

mixed isotropic and Chaboche (1977) kinematic hardening rule has been calibrated by M. G. Lee et al. (2009), directly using experimental data under compression-tension reverse loading. An Armstrong and Frederick (1966) (AF) type back stress was applied and coupled with crystallographic slip and twinning/de-twinning through the plastic flow rule by Dirk Mohr, Chevin, and Greve (2013). Another phenomenological model has been proposed by Nguyen et al. (2013), identifying a sigmoidal shape equation for isotropic hardening under three deformation modes: slip, twinning and de-twinning. A semi-analytical Sachs model has been developed, combining the Schmid law, power law hardening and a sigmoidal increase based on the twinning fraction, and applied in monotonic loading cases as an isotropic hardening rule by Barnett (2007); Barnett et al. (2004). The semi-analytical Sachs model was modified to correlate with different monotonic and multi-axial loading conditions by Jia and Bai (2015b, 2015c), where the twinning fraction parameter was generalized as a function of the stress triaxiality and Lode angle (Bai & Wierzbicki, 2008b) for the isotropic hardening. This model offers a good framework in handling the twinning-activation effect under different scenarios, exhibiting its potential in being generalized to predict the non-linear hardening behavior.

In addition to reverse loading, the strain path in real applications can be very complicated. One type of test commonly used in the lab is the uniaxial tension test with pre-strain along different orientations with regard to the rolling direction. The pre-strain could be uniaxial tension, equi-biaxial tension or shear. It is reported that the flow stress for the second step may exceed the monotonic strain-stress curve with a few stagnation, dependent on the angle change of orientation (Barlat et al., 2013; Ha, Lee, & Barlat, 2013; S. Li, Hoferlin, Bael, Houtte, & Teodosiu, 2003; Schmitt, Fernandes, Gracio, Vieira, & Vieira, 1991; Teodosiu & Hu, 1995).

This phenomenon is called cross-loading where inactive slip systems in the first loading step were activated in the second step. Microscopic-based hardening rules and crystal plasticity models were developed for the cross-loading phenomenon. Dislocation structure based state variables, expressed as a fourth order tensor, were applied in a continuum plasticity theory by Teodosiu and Hu (1998). This model can also provide good results for reversal loading as well as any possible strain path changes. A special case of the Teodosiu model has been evaluated by Levkovitch and Svendsen (2007), neglecting distortional hardening. Another similar modification of Teodosiu model was done by H. Feigenbaum and Dafalias (2008); H. P. Feigenbaum and Dafalias (2007), capturing higher curvature of the yield surface in loading direction and the respective flattening in the orthogonal direction. The three models above have been compared and extended for magnesium alloy sheets by Shi and Mosler (2013). A single strain history change with dislocation microstructure was investigated by Rauch, Gracio, and Barlat (2007), using three variables associated with dislocation densities to model the cross-loading stress-strain behavior. A homogeneous yield function based anisotropic hardening (HAH) model Barlat, Gracio, Lee, Rauch, and Vincze (2011), was extended to the cross-loading case with latent hardening effect for steel sheets proposed by Barlat et al. (2013); Ha et al. (2013). This approach could also capture the Bauschinger effect without using the kinematic hardening concept.

1.4 Fracture Property and Modeling

Many ductile fracture models have been developed and applied in the past decades. The foundation of the micromechanics associated with the void growth was set by McClintock (1968); Rice and Tracey (1969). A micromechanical based porous plasticity model was proposed

by Gurson (1977). The ductile fracture could be carried out subsequently based on void growth and void nucleation. This theory has been validated using axisymmetric notched tensile tests by Hancock and Brown (1983). Tvergaard and Needleman (1984) introduced shear and coalescence effects of micro-voids in representative volume elements. The micro-void shear effect was also considered by Xue (2008) and Nahshon and Hutchinson (2008) with applying an additional shear damage term. Gurson-Tvergaard-Needleman (GTN) model has been modified to predict ductile fracture in incremental sheet forming simulation byGatea, Lu, Ou, and McCartney (2015); Malcher, Andrade Pires, and César de Sá (2014). Another modified GTN model was proposed by Malcher, Andrade Pires et al. (2014) focusing on low stress triaxiality, and applied for both 2024-T351 aluminum alloy and 1045 steel through FE simulation. A different type of micromechanical void growth model was proposed by Ravi Kiran and Khandelwal (2013), choosing cylindrical domain with an embedded spheroidal void, verified by R. Kiran and Khandelwal (2014), using ASTM A992 steels under uniaxial and notch tensions.

As an alternative to void growth type models, non-associated fracture model has been developed and applied with a separate plasticity model, which can bypass the effect of the plastic material behavior on the damage. An empirical model based on the experimental results under different strain rates and temperatures was proposed by Johnson and Cook (1985). It is also typically expressed that the fracture initiates when a weighted function of equivalent plastic strain approaches a critical value by Fischer, Kolednik, Shan, and Rammerstorfer (1995). A fracture model using a weighting function dependent individually on both pressure and stress ratio was proposed by Wilkins, Streit, and Reaugh (1980). The stress triaxiality effect on fracture was applied in the continuum damage mechanics (CDM) by Lemaitre (1996) within a consistent

thermodynamics framework. Lemaitre's ductile damage model has been generalized to anisotropic damage by describing the damage variable into a fourth-order tensor (Armero & Oller, 2000; Hammi, Bammann, & Horstemeyer, 2004). The CDM-based Lemaitre's model and GTN model have been evaluated and implemented into FE simulation by H. Li, Fu, Lu, and Yang (2011), for aluminum 6061-T6 under a wide range of stress triaxialities. Another CDM-based model was applied by Shojaei, Dahi Taleghani, and Li (2014) to predict hydraulic fractures growth in porous rock.

To generalize the non-associated fracture criterion, the third invariant of the stress tensor was introduced by Wierzbicki and Xue (2005). The effect of Lode angle (related to the third deviatoric stress invariant) was then incorporated into the ductile fracture model by Bai and Wierzbicki (2008b). A general form of an asymmetric fracture model was postulated by Bai and Wierzbicki (2010), with a transformation of the classical Mohr-Coulomb fracture model into the space of the equivalent plastic strain, stress triaxiality, and Lode angle. The Modified-Mohr-Coulumb (MMC) fracture model was validated by Y. Li, Luo, Gerlach, and Wierzbicki (2010); Luo and Wierzbicki (2010), using experimental results on advanced high strength steels and aluminum alloys. MMC model was evaluated and implemented by Lian, Wu, and Münstermann (2015) for high-strength low-alloy steel plates with modified fracture locus. It was also applied in edge fracture and plane strain blanking simulation for AHSS sheet by K. Wang, Luo, and Wierzbicki (2014); K. Wang and Wierzbicki (2015), together with an anisotropic yield criterion. A criterion using the magnitude of stress vector (MSV) was proposed by Khan and Liu (2012a, 2012b). A Lou–Huh ductile fracture model for sheet metal fracture prediction was proposed by Lou, Huh et al. (2012), incorporating the existence of cut-off value of stress triaxiality. The Lou-

Huh model was modified to consider both anisotropic and loading path effect in sheet metal fracture by N. Park, Huh, Nam, and Jung (2015). A review of different groups of fracture model was presented by Bai and Wierzbicki (2015).

The fracture properties for this material have been investigated under monotonic loading conditions. The fracture toughness of this material has been investigated using cohesive FE approach by Guo, Chang, Chen, and Zhou (2012). The Johnson-Cook fracture model (Johnson & Cook, 1985) has been evaluated using the high strain-rate tensile tests by Feng et al. (2014). Based on uniaxial and biaxial tension results, the fracture forming limit diagram has been plotted by Jia, Long, and Bai (2012), and a modified Mohr-Coulumb (MMC) fracture model by Bai and Wierzbicki (2007) has been applied to obtain the fracture locus by Jia et al. (2012); Jia et al. (2013). An all-strain based Modified Mohr-Coulumb (eMMC) model, transferred from the MMC model (Bai & Wierzbicki, 2010), was developed, calibrated to obtain the fracture locus for magnesium alloy sheets, and implemented into FE analysis to predict fracture behaviors under a wide range of monotonic stress states by Jia and Bai (2015b).

1.5 Outline of the Thesis

In the presented thesis, chapter 2 is devoted to design and conduct a comprehensive set of experiments for magnesium AZ31B-H24, including monotonic uniaxial tension, notch tension (for biaxial tension loading condition), uniaxial compression, wide compression (for biaxial compression loading), plane strain compression, through-thickness compression, pure shear, punch test. Also a set of non-proportional experiments was conducted, including uniaxial compression-tension reversal loading, and two-step uniaxial tension with orientation changes.

Chapter 3 analyzes and summarizes the experimental results for magnesium sheets, in material strength, plastic flow, and fracture behavior, under monotonic loading conditions. A new parameter, Φ, is defined and depicted under each loading condition to describe the anisotropic material plastic flow.

Chapter 4 describes the constitutive model framework, including CPB06ex2 anisotropic yield criterion, and a new developed modified Sach hardening model to incorporate isotropic, kinematic, and cross hardening behaviors. Three sets of state variables are defined in this model, to respectively describe a) loading history, b) twinning and de-twinning behaviors, and c) pre-strain effects. A calibration procedure with non-aftereffect is introduced.

Chapter 5 introduces an all-strain based MMC (eMMC) fracture model with Hill 1948 type anisotropic equivalent plastic strain. This fracture model is calibrated individually for tension and compression dominated regions to obtain a comprehensive fracture locus. The fracture model is partially associated with one of the twinning-related state variables to incorporate the non-linear fracture behavior.

Chapter 6 demonstrates the finite element models for all cases of loading condition to reproduce the experimental results using shell elements. All constitutive models and fracture model is written into a user-subroutine (VUMAT) in FE software Abaqus/Explicit. All numerical results are exhibited and compared to the experimental ones in this chapter for magnesium alloy sheet, under monotonic, reversal, and cross loading conditions.

Chapter 7 studies the model performance for steel sheets, including TRIP780, BH240, DP600, and EDDQ. FE simulation is conducted and compared to the experimental results for TRIP780

under monotonic loading conditions. The analytically modeled results are correlated with the experimental results under cross loading conditions for the rest of materials.

Chapter 8 summaries the contributions of the present thesis and describes the recommended research in the future.

1.6 List of Related Papers Published, Submitted or in Preparation

- Jia, Y., and Bai, Y., "Experimental Study of the Mechanical Properties in AZ31B-H24 Magnesium Alloy Sheets under Various Loading Conditions", *International Journal of Fracture*, pp 1-24, 2015.

- Jia, Y., and Bai, Y., "Ductile Fracture Prediction for Metal Sheets using All-strain-based Modified Mohr-Coulomb model", *Journal of the Mechanics and Physics of Solids*, submitted for publication, 2015.

- Jia, Y., and Bai, Y., "A Combined Isotropic, Kinematic and Cross Hardening Model for Magnesium AZ31B-H24 under Non-linear Strain Loading Path", ready to submit, 2016.

- Jia, Y., Long, X., and Bai, Y., "Experimental study on mechanical properties of AZ31B-H24 magnesium alloy sheets under multi-axial loading conditions", *Journal of Automotive Safety and Energy*, December, 2012, 3(4).

- Jia, Y., Bai, Y., "Application of eMMC model to fracture of Metal Sheets", *2016 SEM 13th International Congress & Exposition on Experimental and Applied Mechanics*, June 6-9, 2016, Orlando, FL.

•Jia, Y., Bai, Y., "A Combined Isotropic, Kinematic and Cross Hardening Model for BH240 and DP600 Steel Sheets", *International Deep-Drawing Research Group (IDDRG 2015)*, May 31 – June 3, 2015, Shanghai, China.

•Jia, Y., Bai, Y., Ma. C., Zhang, J., "Ductile fracture prediction for metal sheets using all-strain-based modified Mohr-Coulomb model", *International Deep-Drawing Research Group (IDDRG 2015)*, May 31 – June 3, 2015, Shanghai, China.

•Jia, Y., Long, X., Wang, K., and Bai, Y., "Calibration of Plasticity and Fracture of Magnesium Alloy Sheets Under Multi-Axial Loading Conditions", *Plasticity 2013*, Nassau, Bahamas, Jan. 3-8, 2013.

CHAPTER 2 EXPERIMENT METHODS

The material investigated in this paper is AZ31B-H24 magnesium sheet, which was mechanically tested at room temperature. Aiming to comprehensively describe the mechanical properties of this material, tests were conducted under different loading conditions. All deformations were recorded and measured by the Digital Image Correlation (DIC) technique.

2.1 Material and Equipment

In the discussion that follows, AZ31B-H24 magnesium alloy sheet refers to a cold rolled sheet with partially annealed (H24 temper) AZ31B magnesium alloy, which ordered from Magnesium Elektron (Elektron, 2014). All specimens were machined parallel to the following degrees with respect to the rolling direction (RD), 0°, 22.5°, 45°, 67.5° and 90° respectively, for monotonic loading. Three orientations were machined, 0°, 45°, and 90° respectively for non-proportional loading. Three identical specimens were manufactured for each orientation to assess experimental repeatability. The sheet thickness was $2mm$ and all the specimens were cut from two sheets belonging to the same production batch, according to the manufacturer. Only the two-step uniaxial tension tests were using sheets with $1mm$ thickness. Semi-gloss black and white paint was sprayed in small dots randomly on the surface of all the specimens one day before the test.

All tests were conducted quasi-statically using MTS universal testing machine. A quasi-static strain rate of about $10^{-3}/s$ was applied for all tests reported. It was found that there is no apparent effect of strain rate at room temperature with quasi-static loading condition for AZ31B magnesium (Khan et al., 2011; Maksoud, Ahmed, & Rödel, 2009). Optical measurements with

the DIC system were utilized to obtain the precise strain fields. The system is consisted of a Tokina AT-X Pro macro $100mm - f/2.8 - d$ lens with a resolution of 2448×2048 and VIC-2D 2009 software by Correlated Solutions, Inc.. The capture frequency was $1Hz$.

2.2 Uniaxial Tension

Uniaxial tension test was performed under standard of ASTM-E8-00 (2000). Figure 1 illustrates the slant fracture surfaces of the rolling direction (0°) and transverse direction (90°) in both front and side views, which shows shear dominated fracture mechanism in this magnesium sheet.

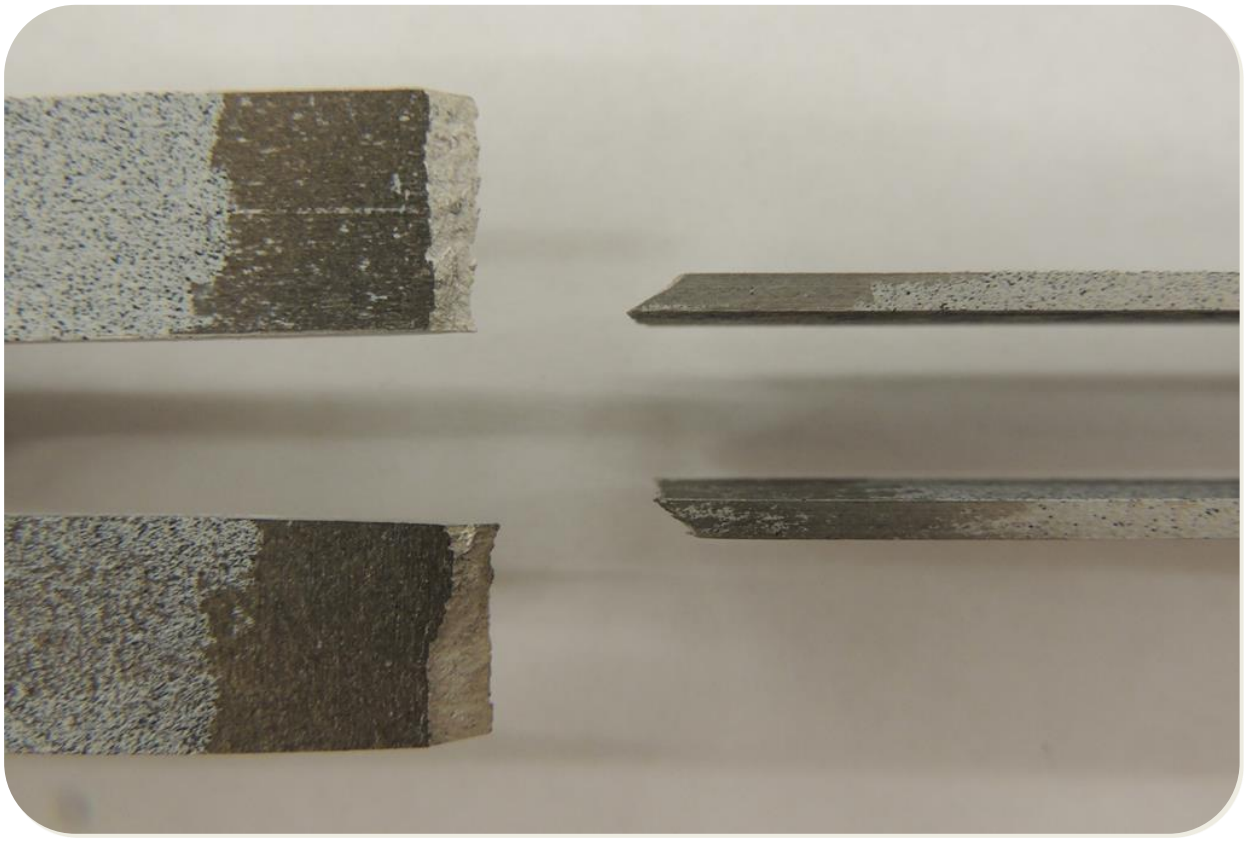

Figure 1 The 0° (top side) and 90° (bottom) dogbone specimens after test show shear dominated fracture mode.

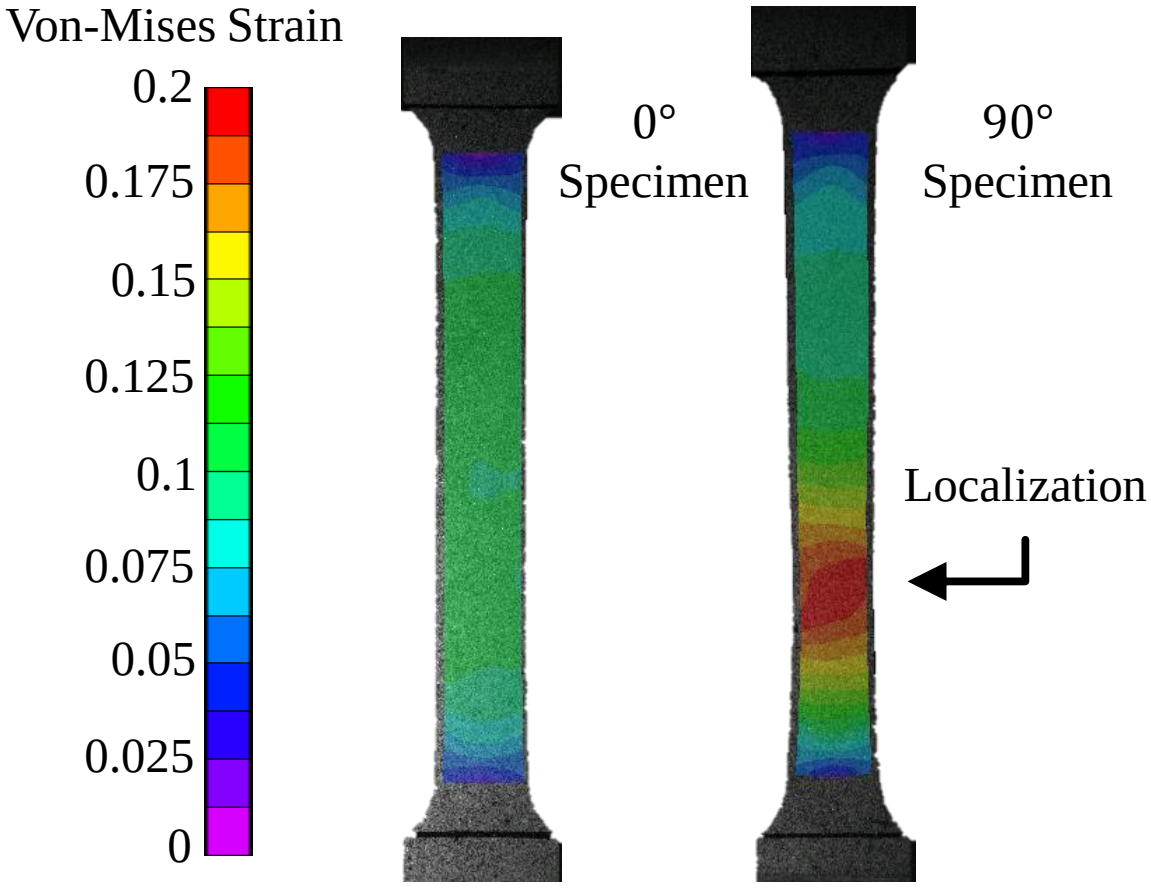

Figure 2 The contour of equivalent strain post-processed by DIC for both 0° (left) and 90° dogbone specimen at the moment just before fracture initiation.

It is also possible to see the brittle nature of fracture because no apparent localized necking was observed. The diffuse dominated localization is indicated by less shrinkage of thickness than width. Figure 2 compares between the strain fields of both 0° and 90° specimens, which were obtained from DIC measurement at the moment just before fracture initiation. One can see that the 90° specimen exhibits more strain localization.

The plastic behaviors along different orientations are assessed by Lankford ratio (r-value, the ratio between the plastic strain rate in width and thickness direction) under uniaxial loading condition, with the volume constancy in plastic deformation, as follows:

$$r = \frac{\dot{\varepsilon}^p_{width}}{\dot{\varepsilon}^p_{thickness}} = -\frac{\dot{\varepsilon}^p_{width}}{\dot{\varepsilon}^p_{width} + \dot{\varepsilon}^p_{axial}}. \quad (1)$$

The r valuewas usually computed as a ratio by using a) cumulative plastic strains after the test (Rousselier, Barlat, & Yoon, 2009) under the assumption of proportional loading, b) cumulative plastic strains chronologically measured at different test pauses (Beese, 2011; X. Y. Lou et al., 2007), and c) incremental plastic strain obtained by pausing the test at different known strains (X. Y. Lou et al., 2007). It can be improved by measuring the effective strain through DIC technique during a test, for the reasons of a) obtaining precise strain value after specimen necking, b) the consistency between the ratio of incremental plastic strains and cumulative plastic strains under proportional loading, and c) maintaining the continuity of an experiment. The plastic strain components were obtained from the DIC's logarithmic strain while subtracting the elastic parts.

2.3 Notch Tension

Notch sheet specimen was designed to achieve the biaxial tension condition (between uniaxial tension and plane strain tension) at approximately the center (Bai, 2008). Figure 3 shows the geometry shape with key dimensions of the notch tension specimen and its fracture surface. Different biaxial stress ratios at the center point are capable to be obtained by adjusting the radius of the notch, using a uniaxial tensile loading frame. The stress triaxiality under plane stress condition can be computed by

$$\eta = \frac{\sigma_m}{\bar{\sigma}} = \frac{(\sigma_1 + \sigma_2)}{3\sqrt{\sigma_1^2 + \sigma_2^2 - \sigma_1\sigma_2}}, \quad (2)$$

where σ_m and $\bar{\sigma}$ are the mean stress and equivalent stress, respectively. The analytical solution for the stress triaxiality at the center point can be obtained by Bai (2008), as follows

$$\eta = \frac{1 + 2\Lambda}{3\sqrt{\Lambda^2 + \Lambda + 1}} = 0.4486, \tag{3}$$

where $\Lambda = ln(1 + a/2R)$. a is the distance between the center point and the edge point at the neck of the notch, while R is the radius of the notch.

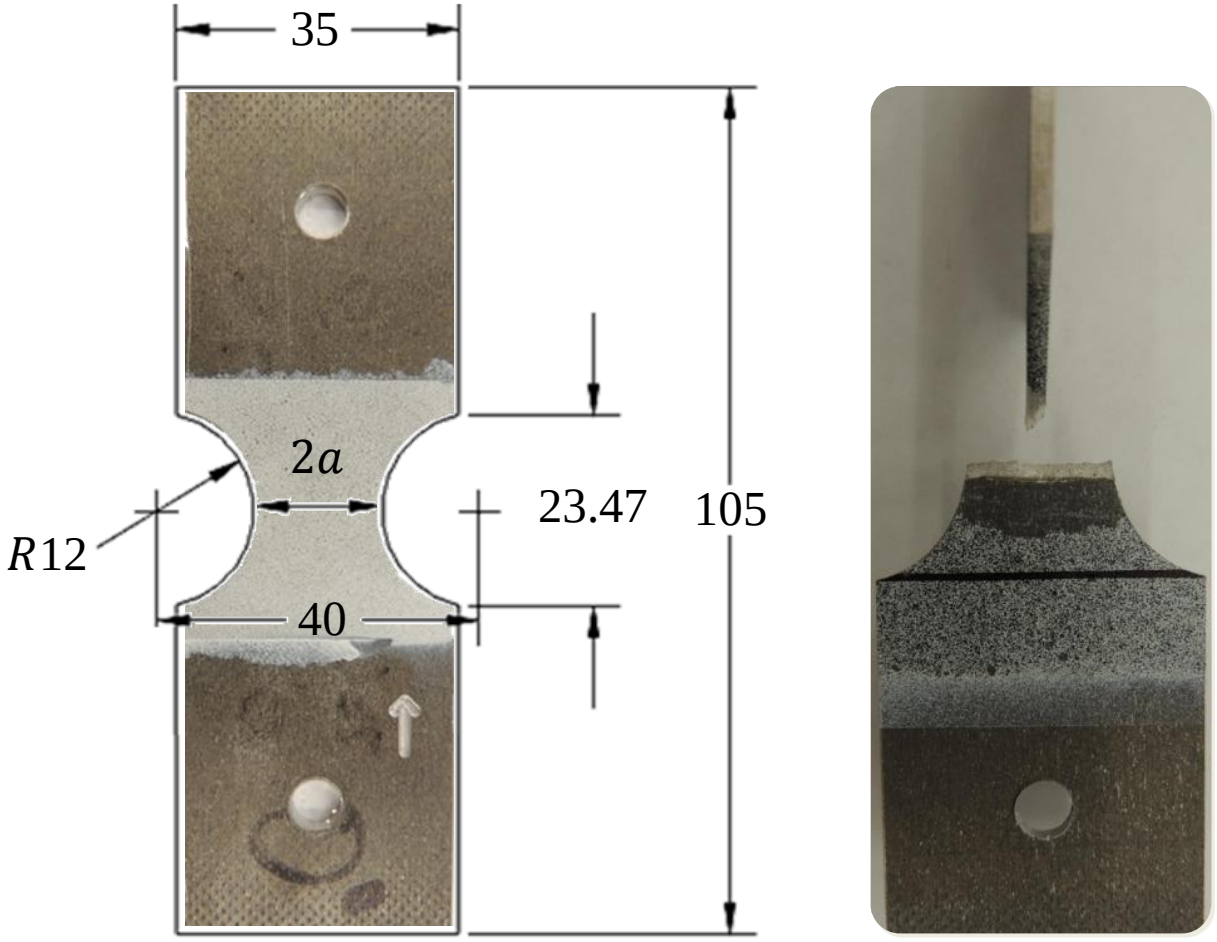

Figure 3 The notch specimen with sizes for biaxial tension. The arrow on the bottom shoulder of specimen on the left figure indicates the rolling direction. All the units are mm. The fracture surface is similar with uniaxial tension.

The true strain-stress curve and Lankford ratio under notch tension, however, cannot be directly measured in this test due to non-uniform cross-section and uneven distribution in thickness deformation. In this manner, it is necessary to define another plastic strain based parameter to

represent the effect of in-plane anisotropic flow under all the possible loading conditions. Therefore, a new parameter Φ is used hereafter, defined as

$$\Phi = atan2\left(-\dot{\varepsilon}_2^p, \dot{\varepsilon}_1^p\right) + 90^\circ, \tag{4}$$

where $atan2$ is two arguments arctangent function with sign information included. The analogical equation in stress field can be used to calculate the Lode angle (Bai & Atkins, 2011).

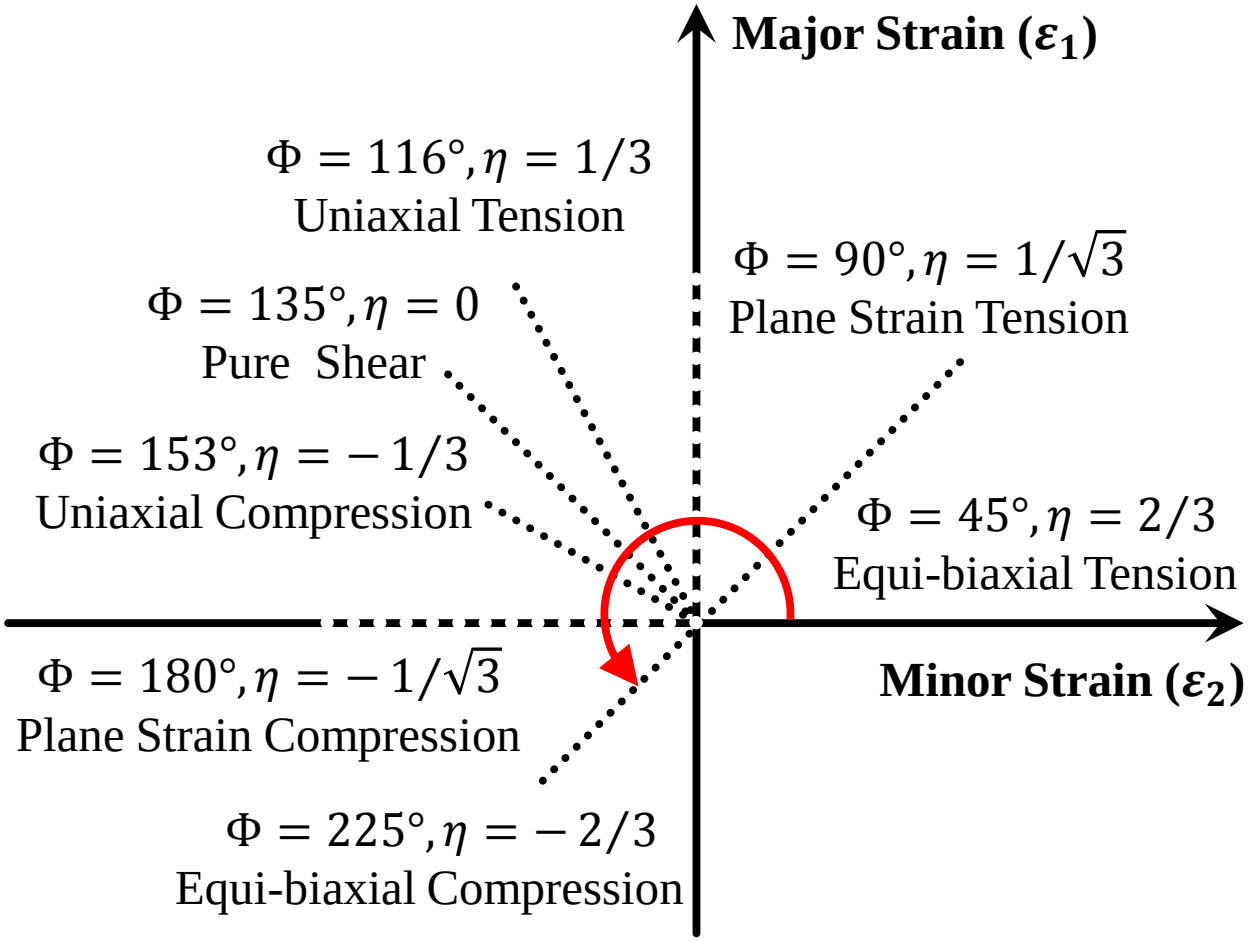

Figure 4 The schematic FFLD describes the definition of Φ under proportional loading. The symbol η means the stress triaxiality.

As a matter of fact, Φ denotes the angle to the positive minor strain direction in the forming fracture limit diagram (FFLD), which is illustrated in Figure 4. Under proportional loading

conditions, the value of Φ keeps constant, therefore the cumulative plastic strains can be used to calculate the value of Φ instead of using the plastic strain rates. The anisotropic effect is thus measured quantitatively by the angle offset to the specified loadings. Under the assumption of isotropic J2 plasticity, the Φ value equals to 45° corresponding to equi-biaxial tension; $\Phi = 90°$ corresponds to plain strain tension; 116° is for uniaxial tension; 135° is for pure shear, and 153° is for uniaxial compression etc.. In this way, this new parameter is utilized to comprehensively describe the plastic flow and calibrate the constitutive model under all possible loading conditions. It is more general than the Lankford ratio whose definition is based on uniaxial loading.

2.4 Punch

The Hasek (1978) punch test without cutout was conducted to effectuate the loading condition of equi-biaxial tension at the point of the disk center. The geometry of the disk specimen is shown in Figure 5. The disk specimen was clamped onto the top surface of the die by 16 fastening bolts. A mirror was placed below the die at 45° to assist the camera to capture the deformation of the disk. The punch was controlled to move vertically downwards onto the disk until it failed. More details about the testing procedure can be found in Walters (2009). The specimen after testing is displayed to the right of Figure 5, where the fracture initiation was not precisely at the absolute center point because a) the material fracture limit of the equi-biaxial point was expected to be higher than the peripheral region, and b) the anisotropic effect at the area around the center point. Therefore the limit of equi-biaxial fracture strain cannot be directly measured by DIC. However, the plastic flow under equi-biaxial tension can be well obtained.

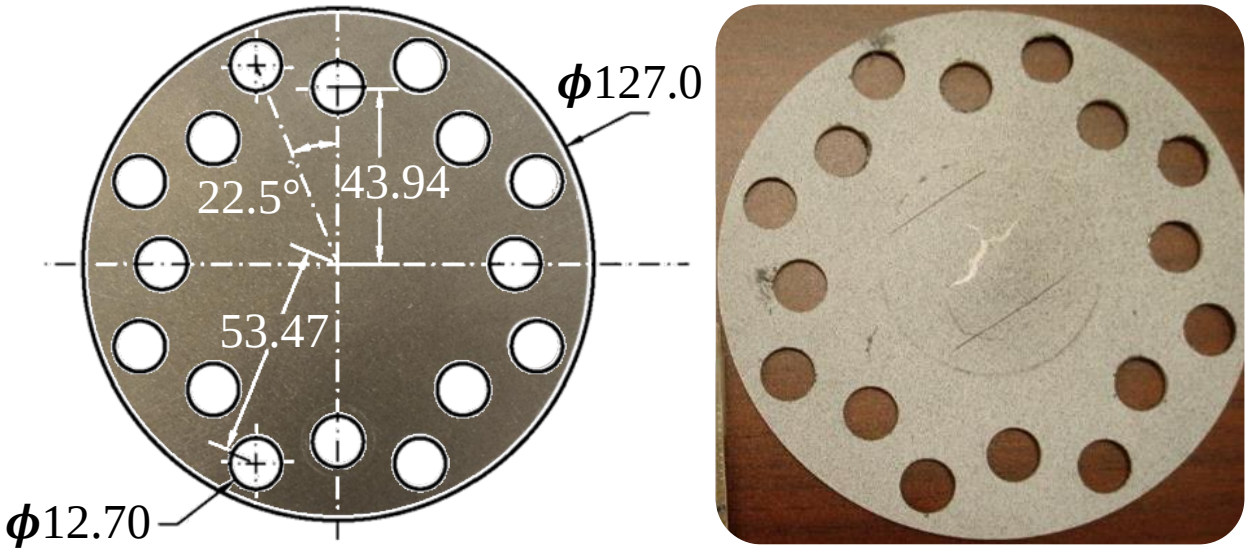

Figure 5 The disk specimen with sizes for punch test. All the units are mm. The crack initiation site is a little bit offset from the absolute center of the disk after forming.

2.5 Uniaxial Compression

A set of small cuboid specimens were designed instead of the dogbone-like shape for in-plane sheet compression due to the aforementioned reason, in order to obtain more hardening information stably (Hammer, 2012). These cuboid specimens were cut into $3mm$ in width and $4mm$ in length, with the original thickness of $2mm$, and compressed along the length direction. The length-to-width (L/W) ratio was therefore 1.33. The two surfaces on which the compressive force was applied had been lubricated by Vaseline to decrease the friction effect. Figure 6 shows the difference between a) uniaxial compression test of small cuboid specimen, and b) compressive stage in reverse loading of the reduced-size dogbone specimen, with anti-buckling device described in next section. The fracture initiated at compressive strain of 11% for small cuboid specimens with no buckling, and a shear-dominated fracture surface is shown in Figure 7. It is found that the fracture initiated at the edge rather than center due to the stress concentration with the edge effect, therefore, accurate measurement of uniaxial compressive fracture strain was

unavailable in this test. However, its entire loading history can be precisely observed by DIC to reveal its plastic behavior.

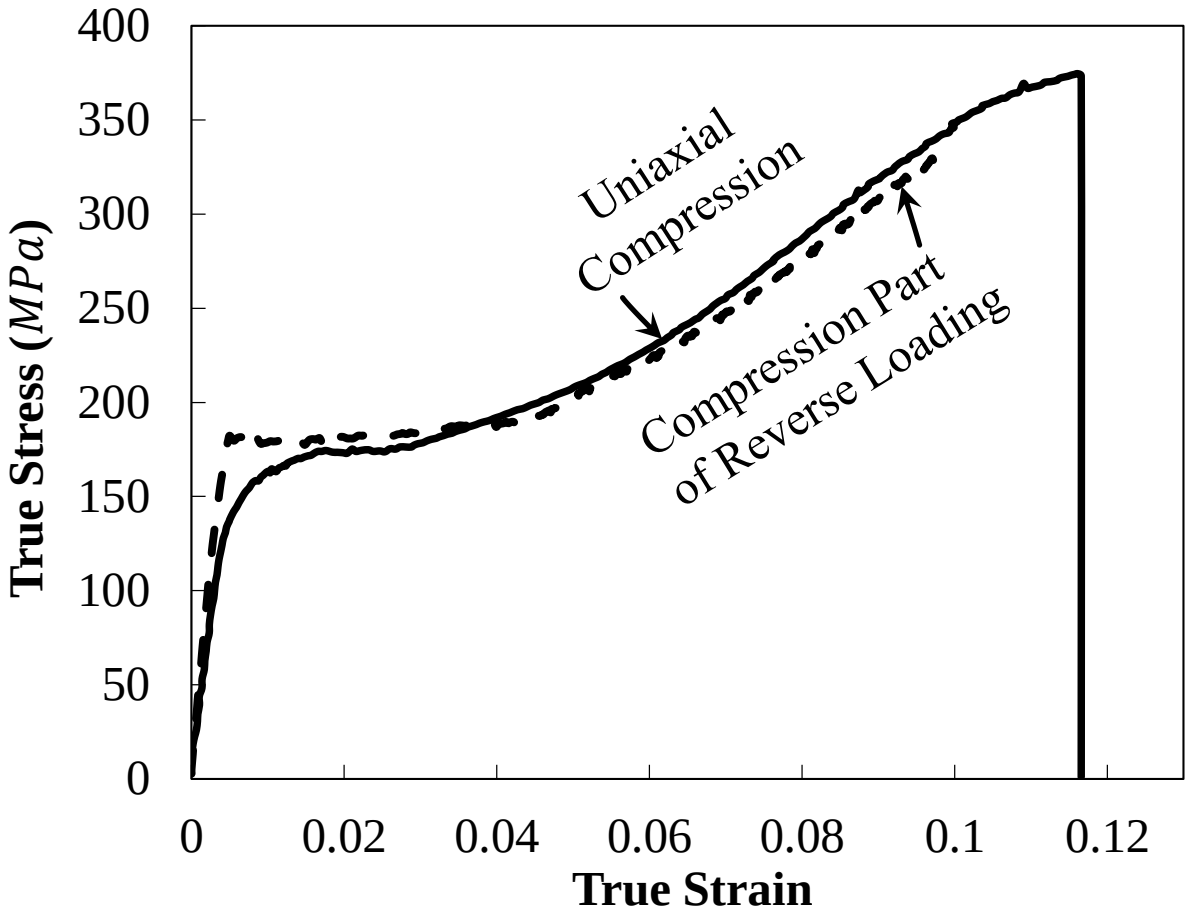

Figure 6 True strain-stress curves for uniaxial compression, comparing between small cuboid specimen (solid line) and reduced-size dogbone specimen with anti-buckling device (dash line).

2.6 Biaxial and Plane Strain Compression

Similarly, another small cuboid sample was carried for biaxial compression with a larger width of $16mm$, which was four times more than the length of $4mm$ to exert horizontal stress occurred at the center during a test. Plane strain compression was achieved by further increasing the width to $40mm$, which restricts the horizontal strain.

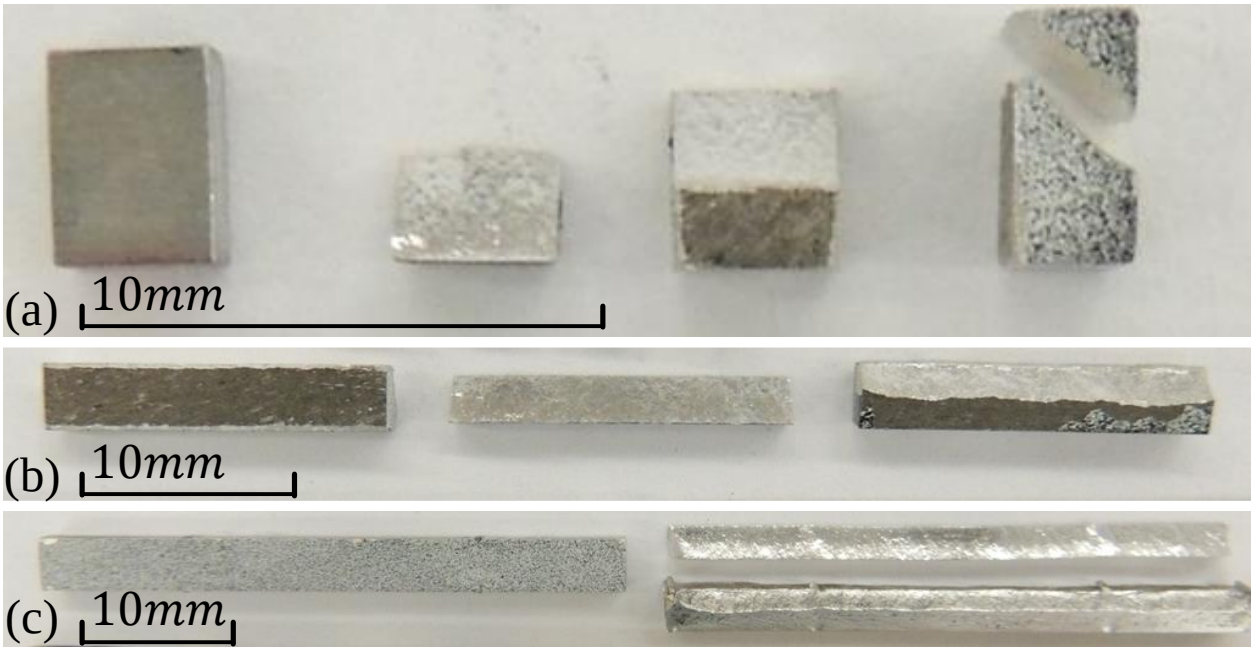

Figure 7 The compression specimens after test shows shear dominated fracture mechanism. The specimens before test are shown side by side to compare with. (a) Uniaxial compression, (b) Biaxial compression and (c) Plane strain compression.

The L/W ratios for biaxial and plane strain compression were 0.25 and 0.10, respectively. An identical procedure of the cuboid uniaxial compression test was applied for biaxial and plane strain compression tests. Using this method, biaxial compression loading conditions between uniaxial compression and plane strain compression can be achieved under a uniaxial testing machine. The fracture surfaces of biaxial and plane strain compression specimens after test, similar with uniaxial compression, are shown in Figure 7b and Figure 7c. The usual definitions of the von Mises equivalent stress and strain for the plane strain test ($L/W = 0.1$) can be approximated as follows

$$\begin{aligned} \overline{\sigma} &= \frac{\sqrt{3}}{2} Y \\ \overline{\varepsilon} &= \frac{2}{\sqrt{3}} \varepsilon \end{aligned}, \tag{5}$$

where Y and ε are the true stress and strain computed by the experimental data, along the compressive direction. However, for the biaxial compression test, the stress triaxiality cannot be obtained directly from the test and hence the result will be presented in the form of true strain-stress (strain/stress component at loading axis) instead of equivalent strain-stress, comparing to the uniaxial and plane strain compression tests.

2.7 Through-Thickness Compression

The uniaxial compression in a through-thickness direction is equivalent to a stress state involving both in-plane equi-biaxial tension and a hydrostatic pressure. Therefore, the same stress-strain response with equi-biaxial tension (e.g. bulge test or cruciform specimen test) will be obtained by through-thickness compression, under the assumption of pressure insensitivity to plasticity. A technique was designed for through-thickness compression concerning with eliminating the frictional effects at the loading surfaces (Vial, Hosford, & Caddell, 1983). A series of two $10mm$ diameter discs were stacked together (without glue or bonding agent) to produce a "cylindrical" specimen. The L/W ratio was therefore 0.40. Teflon tapes of $0.075mm$ thickness were cut into the disc shape and placed between the specimens and the platens for lubrication. Different from the punch test, the information of the plastic flow is unobtainable due to the limitation of DIC (the images can be only captured on side view). However, the equivalent strain-stress response can be directly obtained.

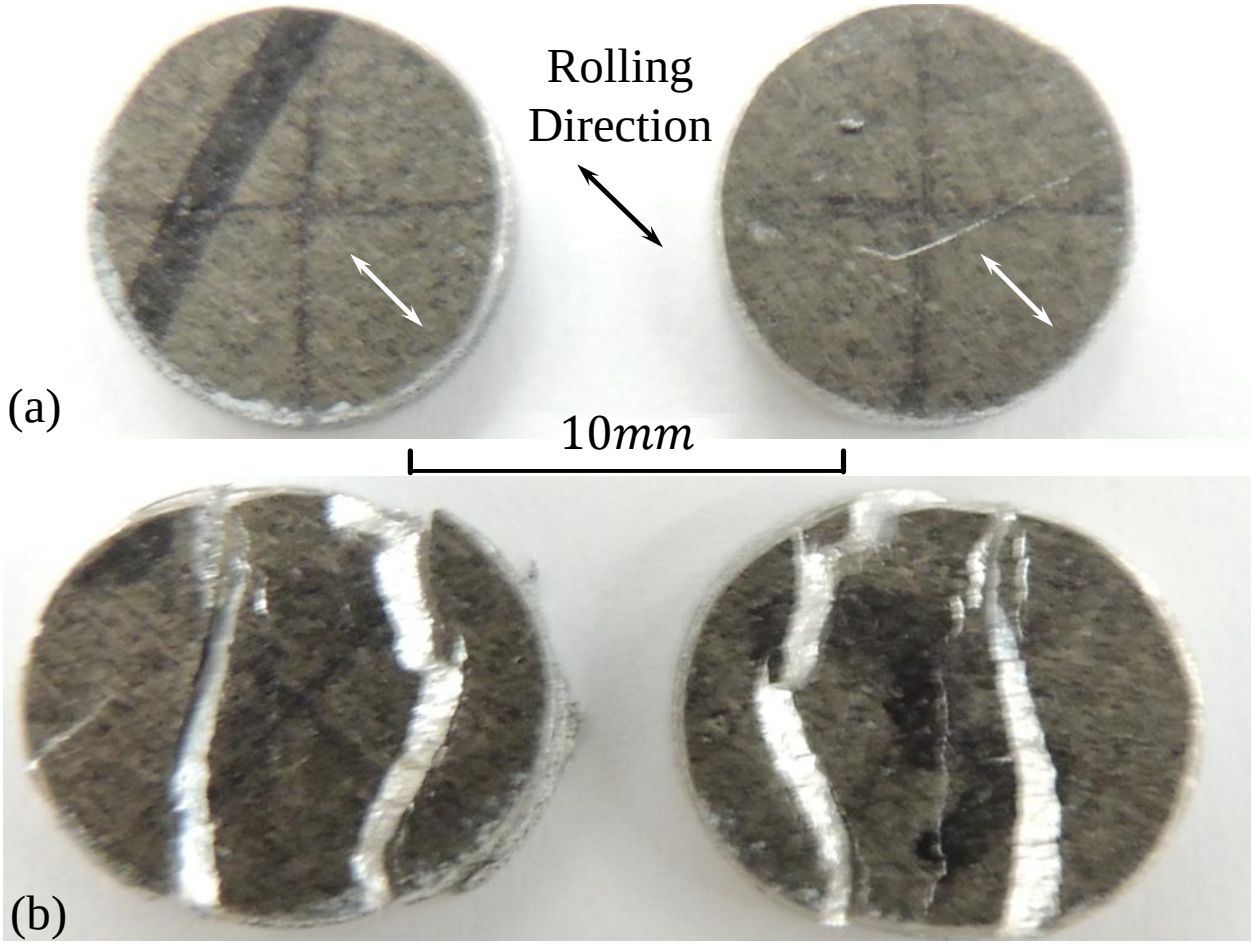

Figure 8 The through-thickness compression specimens before and after test. Both of the specimens were stacked together as a "cylinder" specimen. (a) The specimens before the test, (b) The specimens after the test.

The fracture surfaces of the through-thickness compression specimens are shown in Figure 8b. Specimen failure was initiated by small cracks on the edge, and the subsequent loadings cannot represent the equi-biaxial loading condition. The diameters vary with different radial orientations after the test (forming an oval shape), which indicates the anisotropic effect.

2.8 Pure Shear

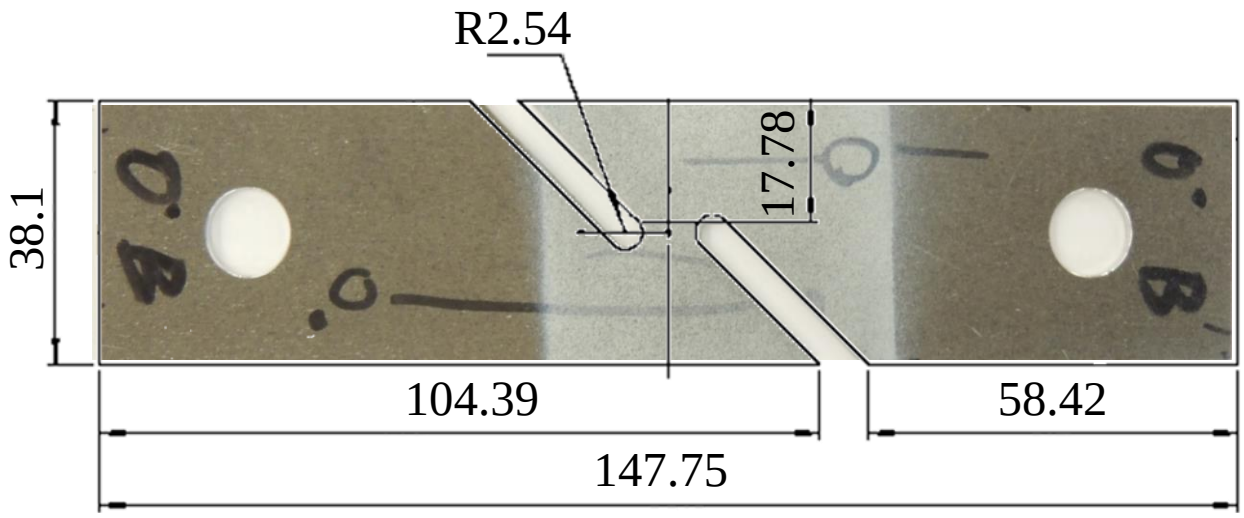

Figure 9 The shear specimen with sizes. All the units are mm.

Figure 9 illustrates the geometry of the in-plane shear test specimen, which was used by Khan et al. (2011); Y. Lou and Huh (2013) with no thickness reduced in the shear zone based on an original design proposed by Bao and Wierzbicki (2004). It is worth mentioning that the thickness reduction may introduce surface effects such as residual stresses and micro-cracks, and the material properties of rolling AZ31B magnesium sheet along the thickness direction can also be different (D.-G. Kim, Son, Kim, Kim, & Lee, 2011; Yan, Zhang, Chen, Zhong, & Weng, 2007). The constraint of the shear specimen was achieved by using one pin at each end to guarantee that no rotational loadings were introduced. No instability was observed prior to fracture. Figure 10 shows fractured shear specimens.

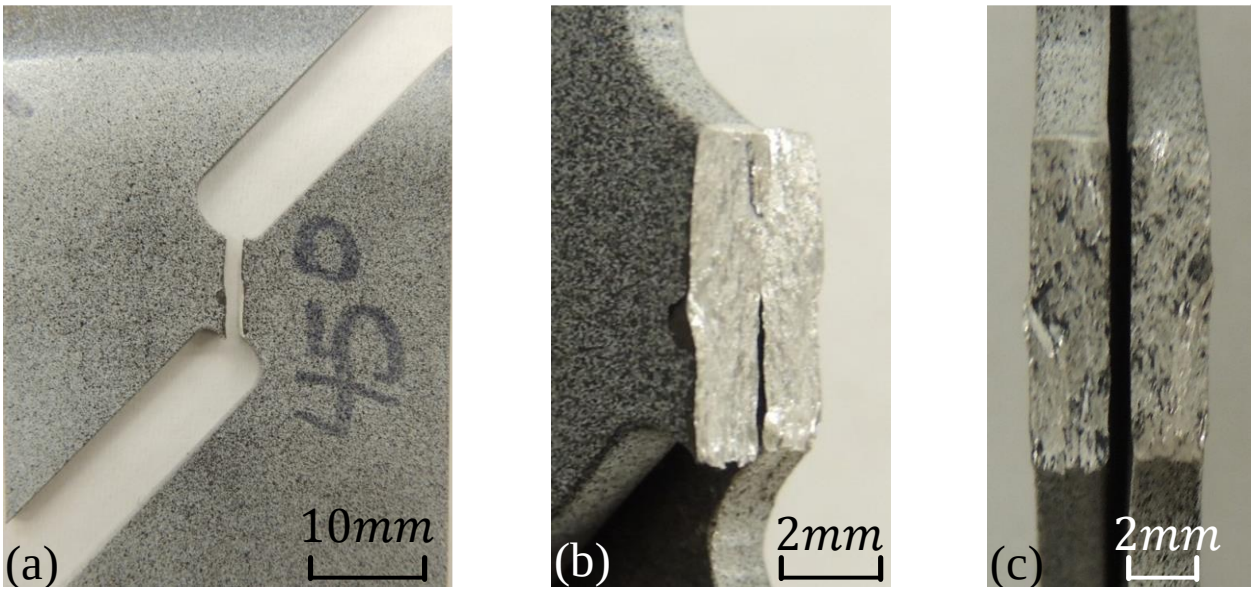

Figure 10 The fracture surface for shear specimen in the view of (a) front, (b) side and (c) thickness, respectively.

Under this loading condition, the shear stress σ_{12} is calculated as follows

$$\sigma_{12} = \frac{F}{bt}, \tag{6}$$

where t is the specimen thickness. Due to notable large deformation, the logarithmic engineering shear strain in incremental form is evaluated using the following method suggested by D. Mohr and Oswald (2007)

$$\gamma_{12}^{i} = \gamma_{12}^{i-1} + \frac{1}{2}\left(\frac{1}{\Delta Y + v_A^{i-1} - v_B^{i-1}} + \frac{1}{\Delta Y + v_A^{i} - v_B^{i}}\right)\left(u_A^{i} - u_B^{i} - u_A^{i-1} + u_B^{i-1}\right), \tag{7}$$

where u and v denote the horizontal and vertical displacements measured by DIC respectively, i and $i-1$ indicate the time steps. The remaining symbols are expressed in Figure 11. By Equation (7) the shear strain is obtained by $\varepsilon_{12} = \gamma_{12}/2$, hence the equivalent stress and strain for the shear test read

$$\begin{aligned} \bar{\sigma} &= \sqrt{3}\sigma_{12} \\ \bar{\varepsilon} &= \frac{2}{\sqrt{3}}\varepsilon_{12} \end{aligned} \tag{8}$$

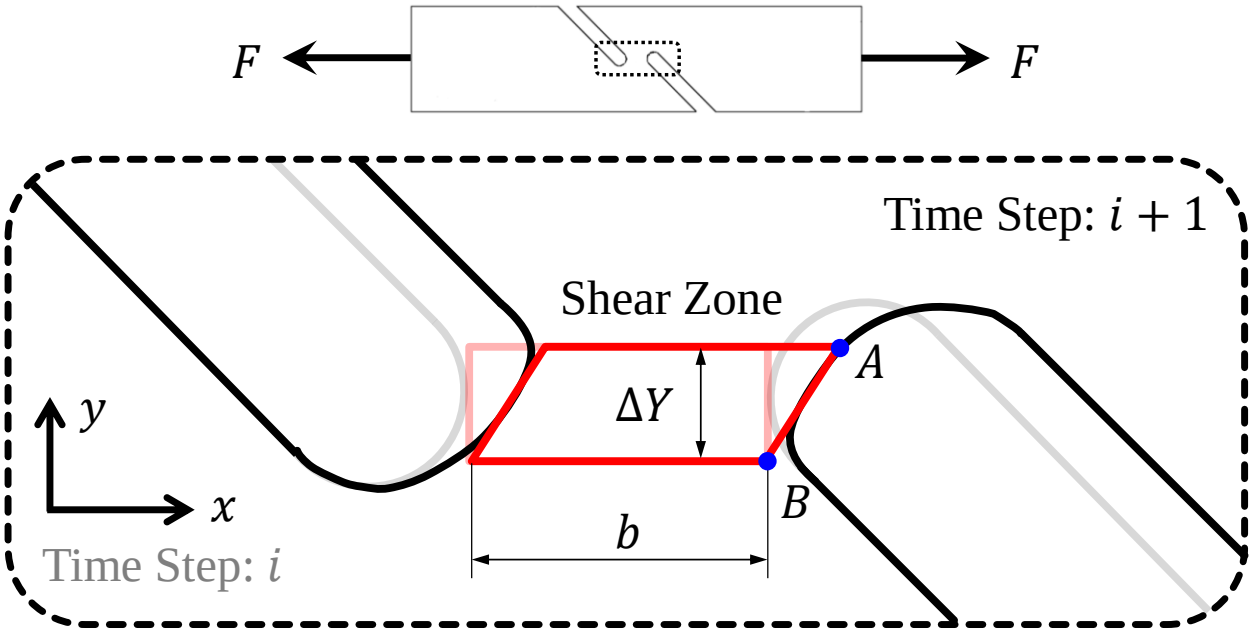

Figure 11 Geometry of the shear test and the description of the deformation at the specimen center.

2.9 Compression-Tension Reverse Loading

Reversal loading test can reveal the kinematic hardening behavior for this material. Different types of anti-buckling device have been designed in order to prevent the sheet specimen from buckling during the compression phase. The compression strain can be achieved as 8% (Boger, Wagoner, Barlat, Lee, & Chung, 2005), 10% (Yoshida, Uemori, & Fujiwara, 2002), 13% (Beese, 2011) and 20% (Khan et al., 2011) reported, using the anti-buckling device. The reduced-size dogbone specimen for reverse loading test is illustrated in Figure 12 and Figure 13, using the same approach and device reported by Beese (2011). The sheet specimen was clamped by two steel plates with 14 bolts and springs. The springs were loaded to provide enough pressure,

preventing the buckling effect. A window was opened in the anti-buckling device for optical strain measurement. Teflon tapes were applied between the plate and the specimen for both sides in order to eliminate the frictional effect. The montage of the specimen assembled with the anti-buckling device is shown in Figure 13. Three different amounts of compressive strain, 3%, 6%, and 10% were conducted respectively, followed by uniaxial tension until fracture occurred.

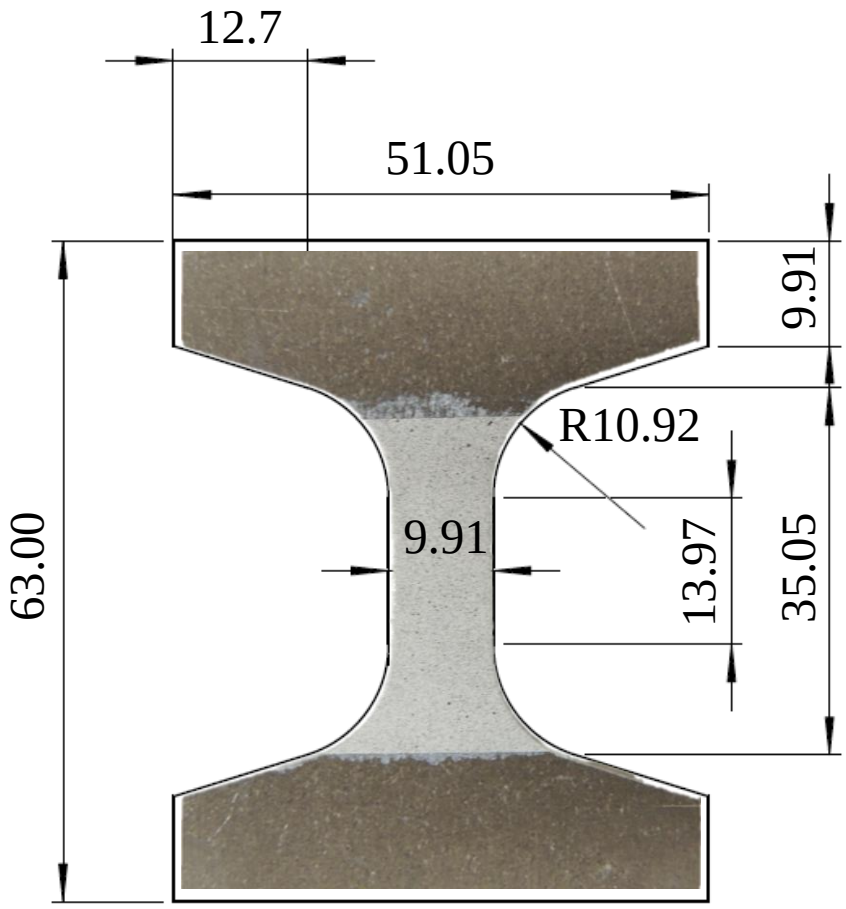

Figure 12 The reduced-size dogbone specimen for reverse loading. All the units are mm.

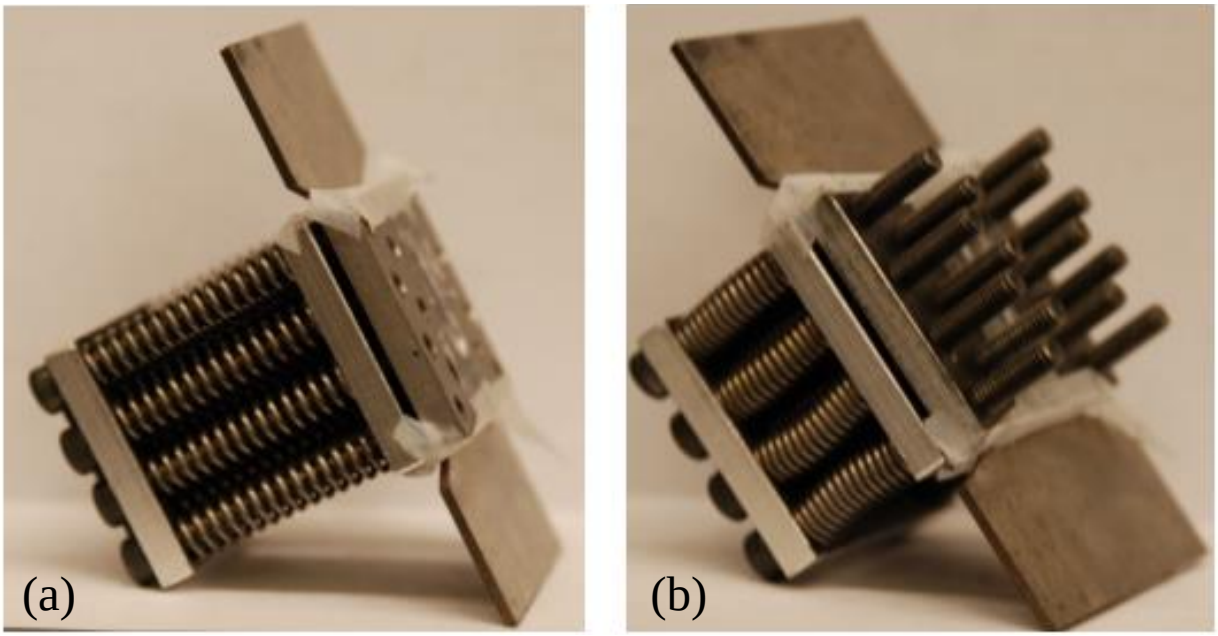

Figure 13 The assembled anti-buckling device and the reduced-size dogbone specimen designed by Beese (2011), with (a) unloaded springs and (b) loaded springs.

2.10 Two-Step Uniaxial Loading

The conduction of a two-step uniaxial tension test is capable to achieve the cross-loading condition. A large-scaled dogbone specimen was used for the first step uniaxial tension.

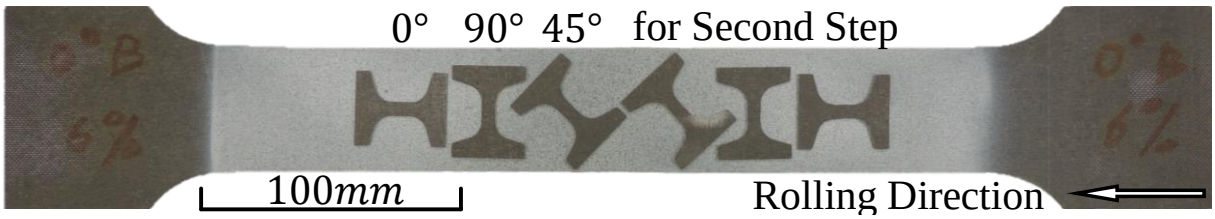

Figure 14 The large-scaled and small-scaled dogbone specimens for two-step uniaxial tension. The small ones were cut from the large specimen based on the assembly. The central area was painted for the purpose of DIC measurement.

The amount of true strains in the first step were 2%, 5.5%, and 8% for both 0° and 90° orientation, and 2% and 5.5% for 45° orientation. The large dogbone specimens were unloaded after approaching the specified pre-strain, and then they were cut into small-scaled dogbone

specimens along the orientations of 0°, 45°, and 90° to conduct the second step uniaxial tension. Two identical specimens were cut along each orientation, to assess experimental repeatability. The geometries and assembly of both large and small scaled dogbone specimens are illustrated in Figure 14, with the rolling direction marked. All the orientations mentioned were according to the rolling direction of the original metal sheets.

CHAPTER 3 RESULTS AND ANALYSIS

This section aims to characterize the yielding, hardening, and fracture properties of magnesium AZ31B alloy sheet under different loading conditions. The experimental results for different loading conditions are exhibited including material strength, plastic flow, and strain histories to fracture. It should be noted that the stress dropping on the stress-strain curves presented in this section are not due to unloading but the fracture initiation.

3.1 Uniaxial and Notch Tension

The true strain-stress curves under uniaxial tension are given below in Figure 15a. The data points of normalized stress (with respect to 0° orientation) extracted at the true strain of 0.08 in Figure 15b. One can see that the specimen has both higher strength and larger fracture strain when the orientation approaches 90° (transversal direction), where there are about 10% difference in stress observed between 0° and 90° specimens. A similar anisotropic characteristic is also observed in notch tension, whose force-displacement curves are shown Figure 15c. Therefore, this material exhibits strong anisotropic plastic behavior in strength under uniaxial and biaxial tension.

Figure 16a illustrates the strain histories under uniaxial tension in the space of Lankford ratio versus equivalent plastic strain, which were extracted at the fracture initiation points using DIC.

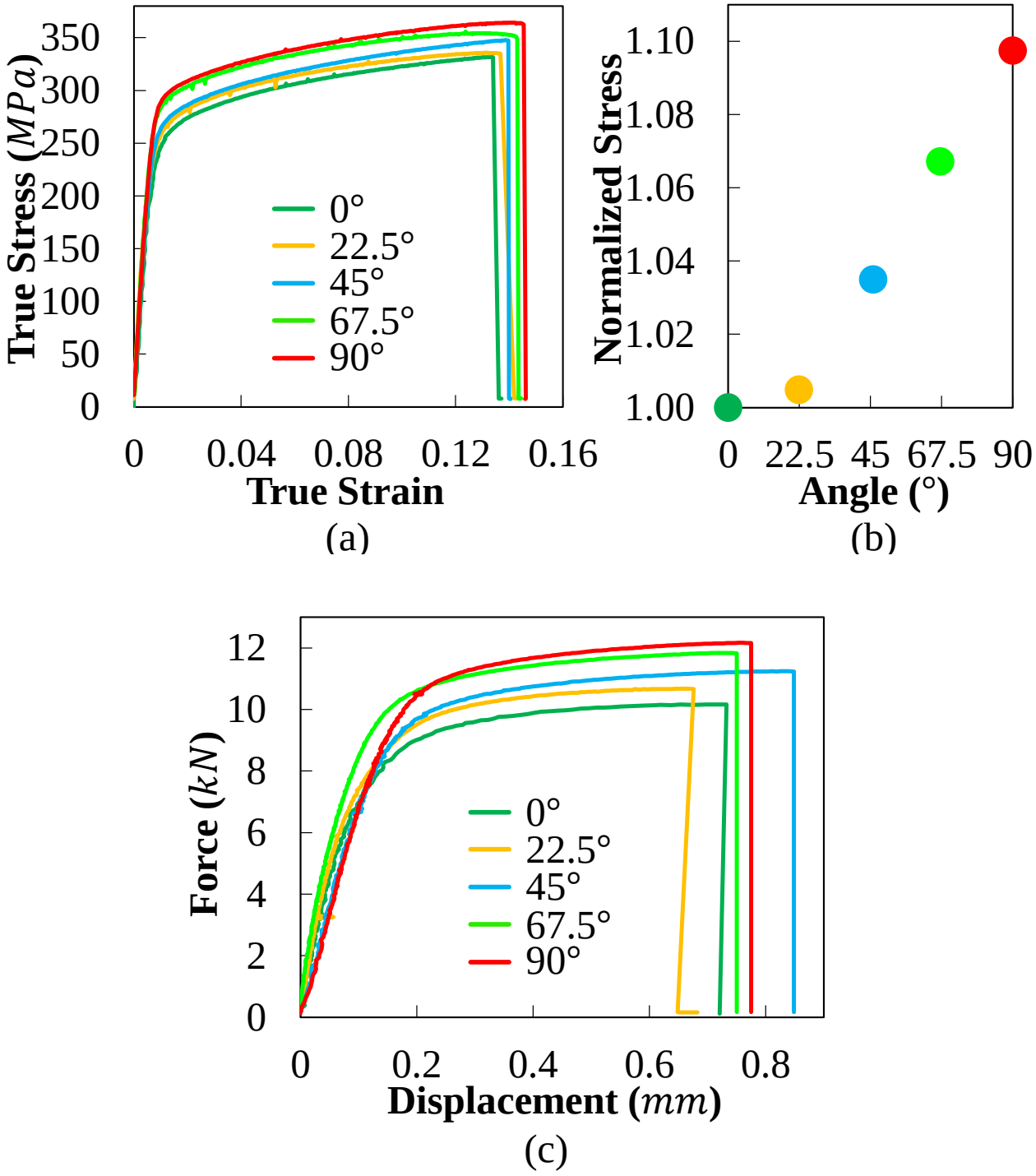

Figure 15 The anisotropic plastic behaviors for both uniaxial and notch tension specimens. (a) True strain-stress curves for uniaxial tension specimens along five different loading orientations with respect to the rolling directions (0°), (b) Normalized yield stress for uniaxial tension at the true strain of 0.08 with different loading orientations, where the baseline is $323MPa$, and (c) Force-displacement curves for notch tension specimens.

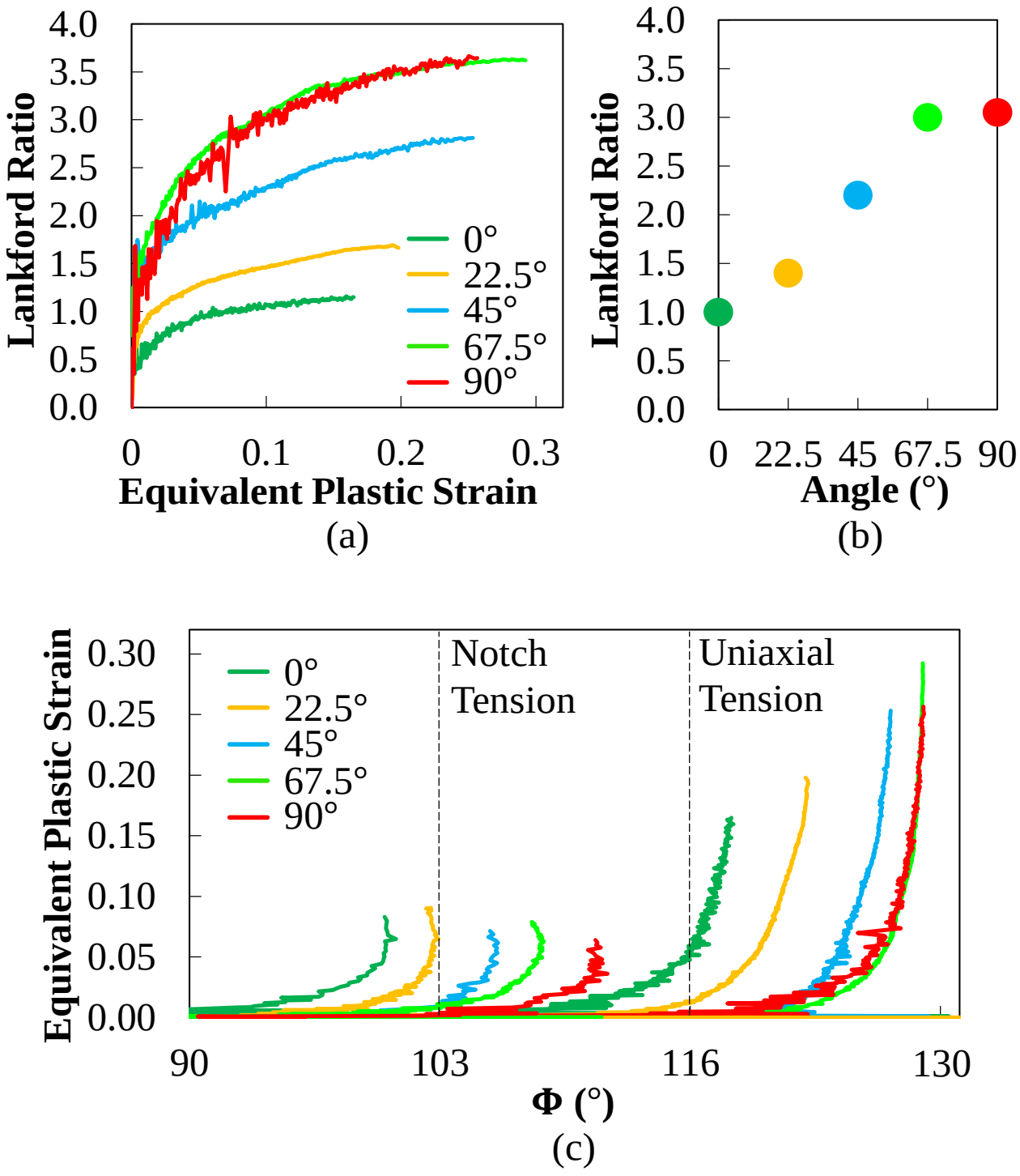

Figure 16 Plastic flow for both uniaxial and notch tension specimens. (a) Lankford ratio versus equivalent plastic strain for uniaxial tension, (b) Lankford ratio versus different orientations for uniaxial tension, extracted at strain level of 0.08, and (c) Equivalent plastic strain versus Φ for both uniaxial and notch tension.

One can see that the increment of r-value is diminishing after the growth of the equivalent plastic strain for a certain period of time in the presented Lankford ratio curves. The maximum and minimum in-plane principal strains were approximately proportional with a confidence level of 0.99 for all orientations, based on the DIC measurement. Therefore, it can be deduced that a) the loading histories were proportional, and b) the Lankford ratio tended to stabilize at some value (for this material) under a given loading condition for a specific orientation. The comparison of r-values among different orientations is exhibited in Figure 16b, which were extracted at 0.08 true strain. It can be observed that the r-value approaches unity for 0° specimen, while $r = 3.5$ for 90° specimen, indicating strong anisotropy in plastic flow. The Lankford ratio was unobtainable for notch tension because it was defined for uniaxial condition only. The general plastic flow parameter Φ defined in previous section was therefore applied to quantitatively describe the anisotropic plastic flow under different loading conditions. There is a one-to-one correspondence between Lankford ratio and Φ under uniaxial loading condition. The definition of r-value from Equation (1) reads

$$r = \frac{\dot{\varepsilon}^p_{width}}{\dot{\varepsilon}^p_{thickness}} = -\frac{\dot{\varepsilon}^p_{width}}{\dot{\varepsilon}^p_{width} + \dot{\varepsilon}^p_{axial}}.$$

Equation (1) can be rewritten into

$$\frac{r}{r+1} = \frac{\dot{\varepsilon}^p_{width}}{\dot{\varepsilon}^p_{axial}} = -\frac{\dot{\varepsilon}^p_2}{\dot{\varepsilon}^p_1}. \tag{9}$$

Under uniaxial condition, the principle values of in-plane plastic strain rate are: $\dot{\varepsilon}^p_1 = \dot{\varepsilon}^p_{axial} > 0$, $\dot{\varepsilon}^p_2 = \dot{\varepsilon}^p_{width} < 0$. The new plastic flow parameter Φ from Equation (4) reads,

$$\Phi = atan2\left(-\dot{\varepsilon}_2^p, \dot{\varepsilon}_1^p\right) + 90^\circ = arctan\left(-\frac{\dot{\varepsilon}_2^p}{\dot{\varepsilon}_1^p}\right) + 90^\circ = arctan\left(\frac{r}{r+1}\right) + 90^\circ. \quad (10)$$

Therefore, a similar curve shape as Lankford ratio is obtained for Φ under uniaxial condition in Figure 16c according to Equation (10). Moreover the plastic flow for notch tension described by Φ is can be obtained concurrently in Figure 16c. By this approach, the calibration of material constitutive model will be based on the general plastic flow parameter Φ. The stabilized value of Φ was extracted for the model calibration, which was obtained at the time when the change of its value along the growth of equivalent strain was less than 5%, or from the final value of Φ along the strain history if the change was still larger than 5%. The stress triaxiality in the center of the notch specimen is $\eta = 0.4486$ according to Equation (3), hence the theoretical value of Φ is 103° assuming J2 plasticity. This is approximately the same with the experimental value of 22.5° notch tension. And for the other notch tension specimens, they all deviate from 103° to considerable varying degrees, demonstrating anisotropic behavior in plastic flow under biaxial tension. The similarly overall tendency in plastic flow is observed under uniaxial tension.

In addition, the fracture strains can be obtained in Figure 16c from the loading histories of both uniaxial and notch tension. It is worthwhile distinguishing between edge and center fracture initiation for notch tension tests, because the loading conditions were actually different in one single notch specimen: bi-axial tension was achieved at the center while uniaxial tension was found at the both of the notch edges. It was observed that the equivalent strain at the edge (0.087, under uniaxial tension) was fairly smaller than the fracture strain under the dogbone uniaxial tension (0.16) based on the DIC measurement. Therefore, the equivalent strain at the center point at that frame could represent the fracture strain under notch tension.

3.2 Punch

The force-displacement curve and the plastic flow are shown in Figure 17 for the punch tests. The Φ angle approaches $45°$ due to the enforcement of deformation at the center of the disk specimen, indicating that the equi-biaxial tension loading condition can be achieved approximately at the punch center. However, the material under equi-biaxial tension was theoretically limited to a single point. Said differently, the stress triaxiality η equaled to $2/3$ at the absolute center point. It decreased rapidly when straying around, where the anisotropic effect took place. Hence, the loading history shown in Figure 17b deviated $\Phi = 45°$ slightly, and according to Figure 17c, fracture initiates off the center when the punch displacement approaches $3mm$ with equivalent plastic strain turning at approximately 0.13. This is indicated by the transition points between two colors in both Figure 17a and Figure 17b. Subsequently, the punch load could still be supported until completely fracture due to strain hardening, but the loading condition diverged. Figure 17b also shows the comparison of the plastic flow between uniaxial tension and two punch tests. One can see that the turning strain 0.13 for punch test is slightly less than the fracture strain of $0°$ uniaxial tension.

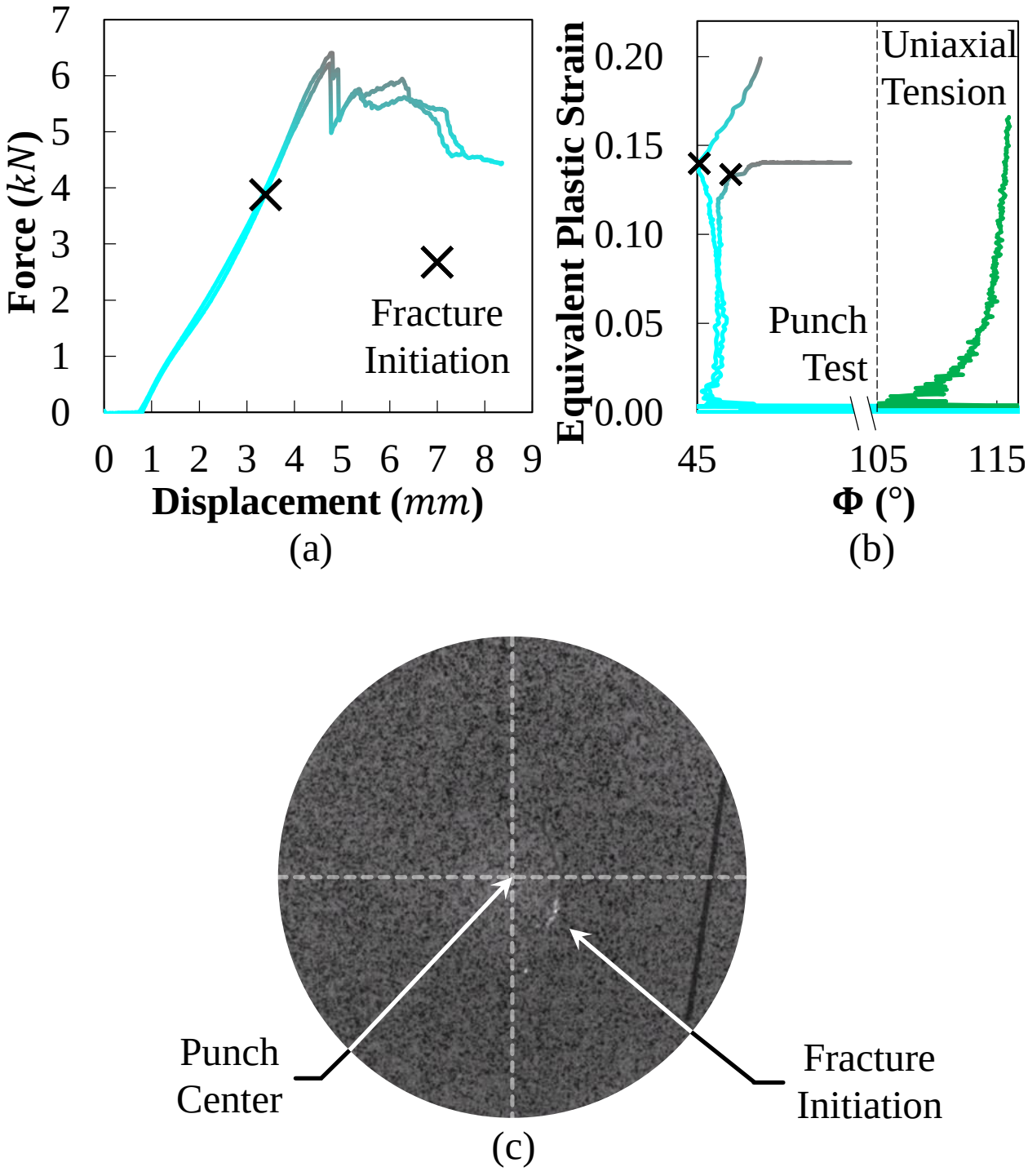

Figure 17 Punch test results, indicating the fracture initiation points. (a) Force-displacement curve, (b) Equivalent plastic strain with Φ angle, comparing with the 0° uniaxial tension result. The loading condition change for punch test is distinguished by two colors. (c) The DIC image at the time when fracture initiated.

3.3 Uniaxial, Biaxial and Plane Strain Compression

The true strain-stress curves (strain/stress component at loading axis) for uniaxial, biaxial and plane strain compression are shown in Figure 18a and Figure 18b. Significant characteristics of asymmetric yield and unusual hardening behavior were observed under compression loading. Figure 18c and Figure 18d show the equivalent plastic strains with Φ parameters for those loading conditions. The noise in plastic flow was observed during the plateau period of flow stress after initial yield. After that, he Φ angle gradually grows towards 153° for uniaxial compression, and 180° for plane strain compression. It can be also seen from Figure 18d that the Φ angles under plane strain compression tests slightly changed after the initial yield plateau, though, approximately only 3% of the compressive strain was measured in the horizontal direction in that period, which assured the plane strain loading condition.

Similar to the uniaxial tensile loading condition, the flow stresses from 0° to 90° are in an increasing order. For the plastic flow however, the J2 plasticity are consistent with the results of 90° specimen instead of 0° in tension test. In particular for plane strain compression, the anisotropic effect is not as apparent as uniaxial compression based on less difference in Φ value. The fracture strain for all the compressive tests with small cuboid cannot be reflected from the result due to contact friction effect, which usually leads to initiate tensile crack. For the same reason, the uniaxial compression test failed before their Φ values approached 153°.

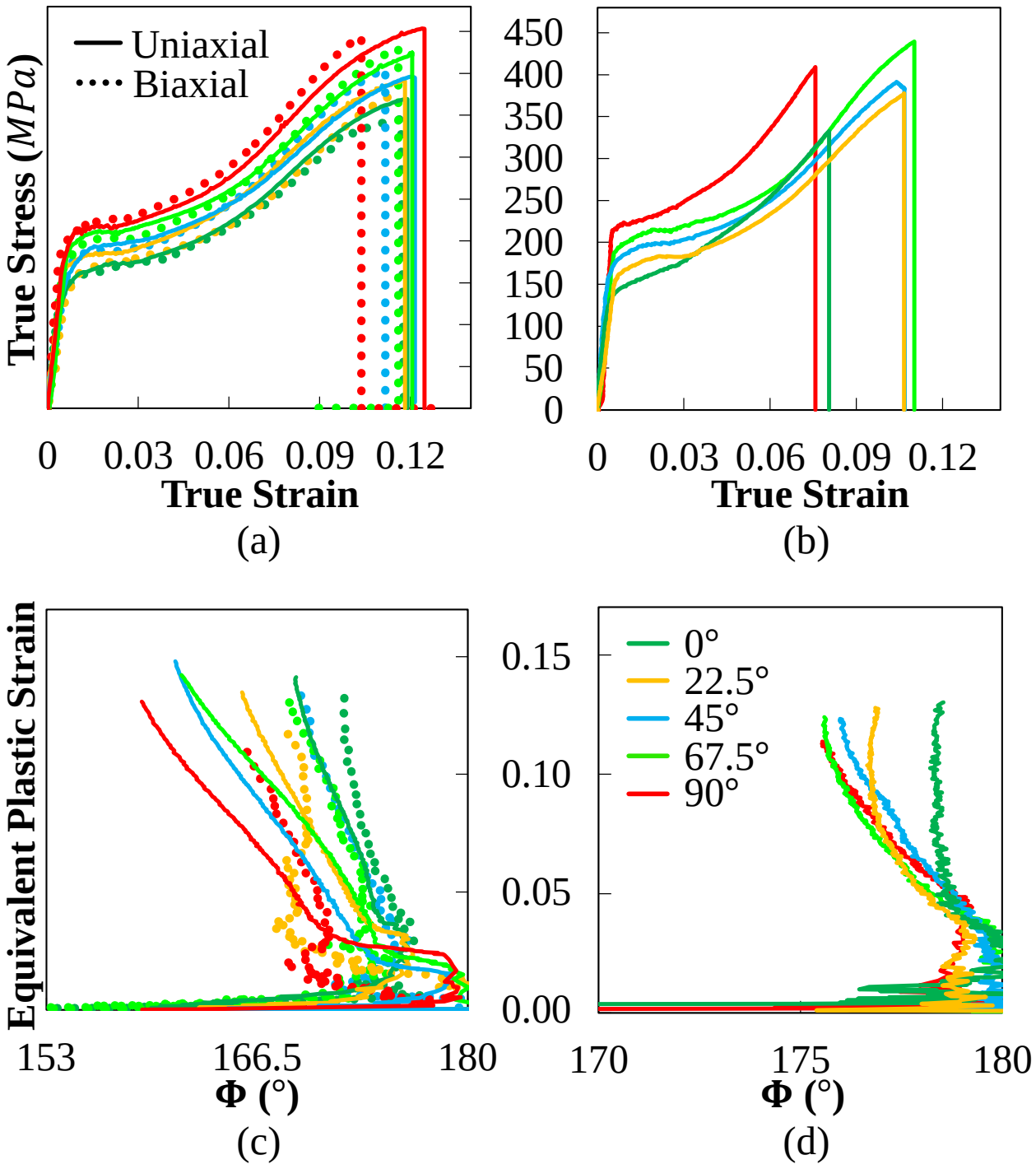

Figure 18 The results for uniaxial, biaxial and plane strain compression. The dot line indicates the biaxial loading condition. (a) True strain-stress curves for both uniaxial and biaxial compression, (b) True strain-stress curves for plane strain compression, (c) Equivalent plastic strain versus Φ angle for both uniaxial and biaxial compression, and (d) Equivalent plastic strain versus Φ angle for plane strain compression.

3.4 Through-Thickness Compression

The true stress-strain curve of the through-thickness compression test is shown in Figure 19, comparing to the result of 0° uniaxial tension.

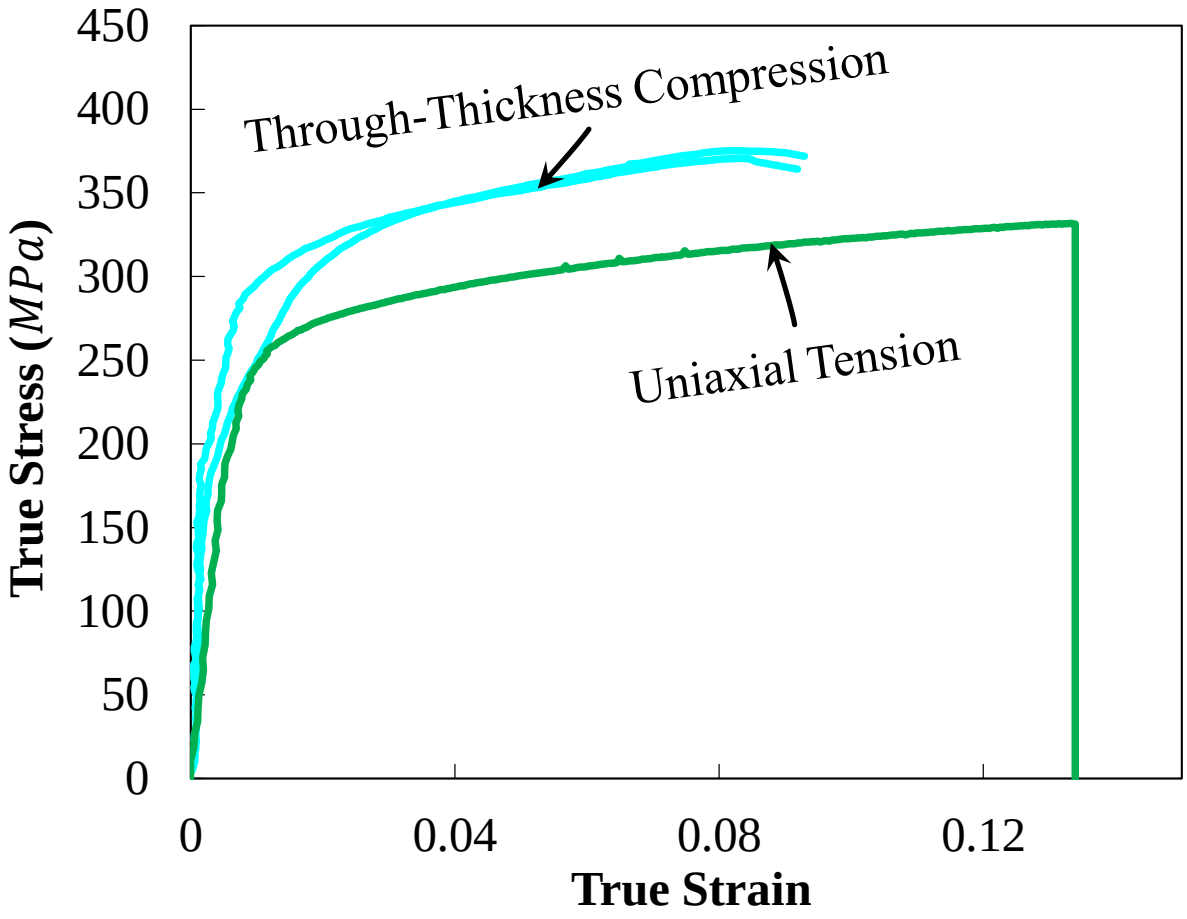

Figure 19 The true stress-strain curves (two tests) of through-thickness compression, comparing with the 0° uniaxial tension result.

Different from in-plane compression tests, the hardening behavior was similar to the one under uniaxial tension test. The fracture initiation strain is unknown in this test, because the fracture was initiated by edge crack at the strain of 0.08. The in-plane plastic strains were unable to be obtained due to the compressive loading direction. The equivalent stress-strain under through-

thickness compression can be unified with the plastic flow from punch tests, exhibiting the loading condition of equi-biaxial tension.

3.5 Pure Shear

Figure 20 exhibits both the equivalent strain-stress curves and plastic flow under shear loading. The curves are more compliant among all the orientations in shear than those under tension and compression, which indicates less anisotropic effect. Both the highest strength and the largest offset from $\Phi = 135°$ (isotropic) was observed in $45°$ shear specimen. The normalized equivalent stresses for shear tests were extracted when the equivalent strain equals to 0.05 and 0.15 in Figure 20c, respectively. A larger difference in shear strength at 0.15 strain was observed than at 0.05 strain, among all the orientations. This indicates a special phenomenon that the hardening curves are not consistent but dependent on orientations, in particular for shear loading.

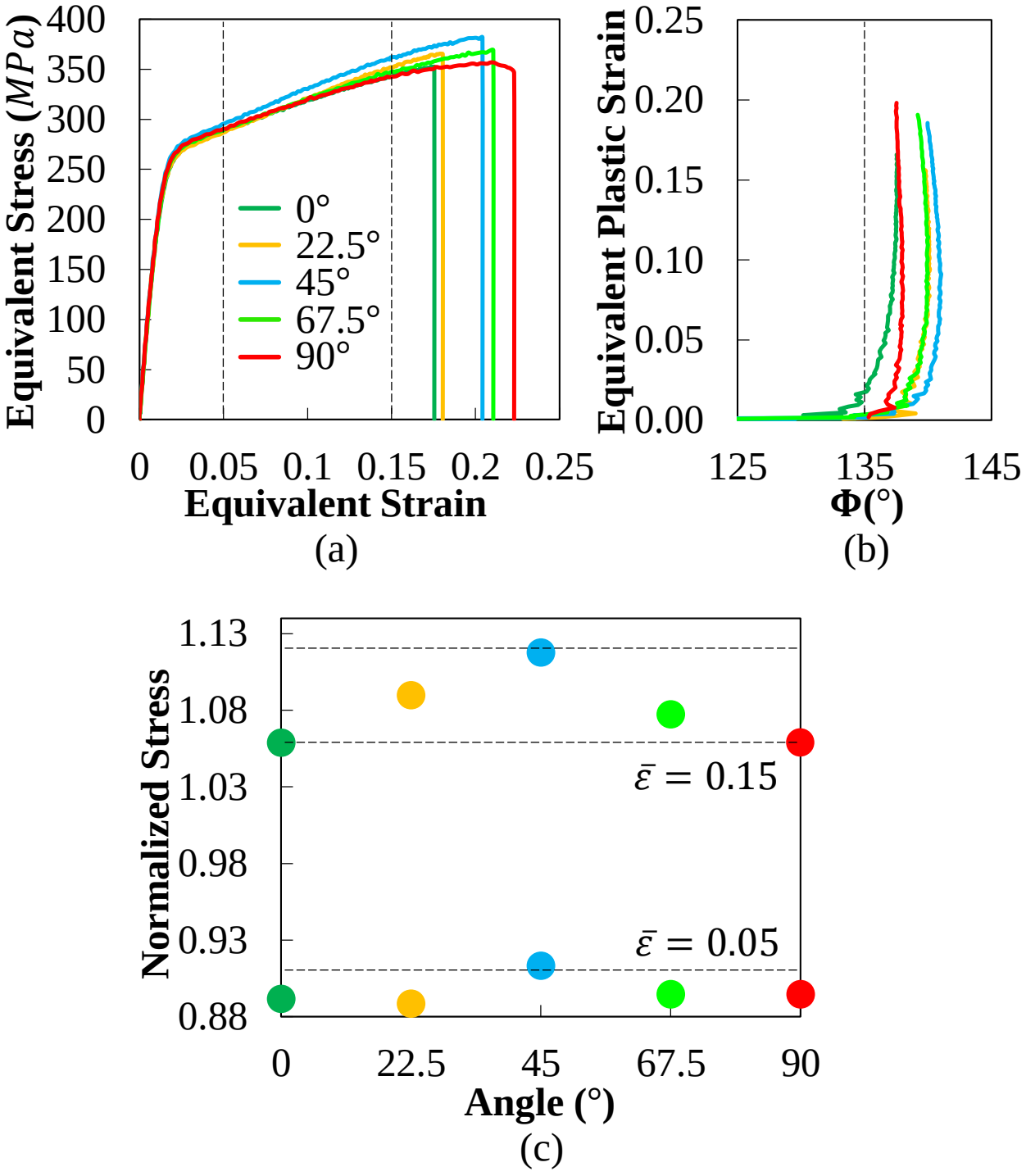

Figure 20 The results for shear tests. (a) Equivalent strain-stress curves, (b) Equivalent plastic strain versus Φ angle, the dash line marks pure shear loading condition based on von-Mises plasticity, and (c) Normalized stress at specific equivalent plastic strains. The baseline is $323MPa$.

3.6 Summary for Plasticity and Fracture

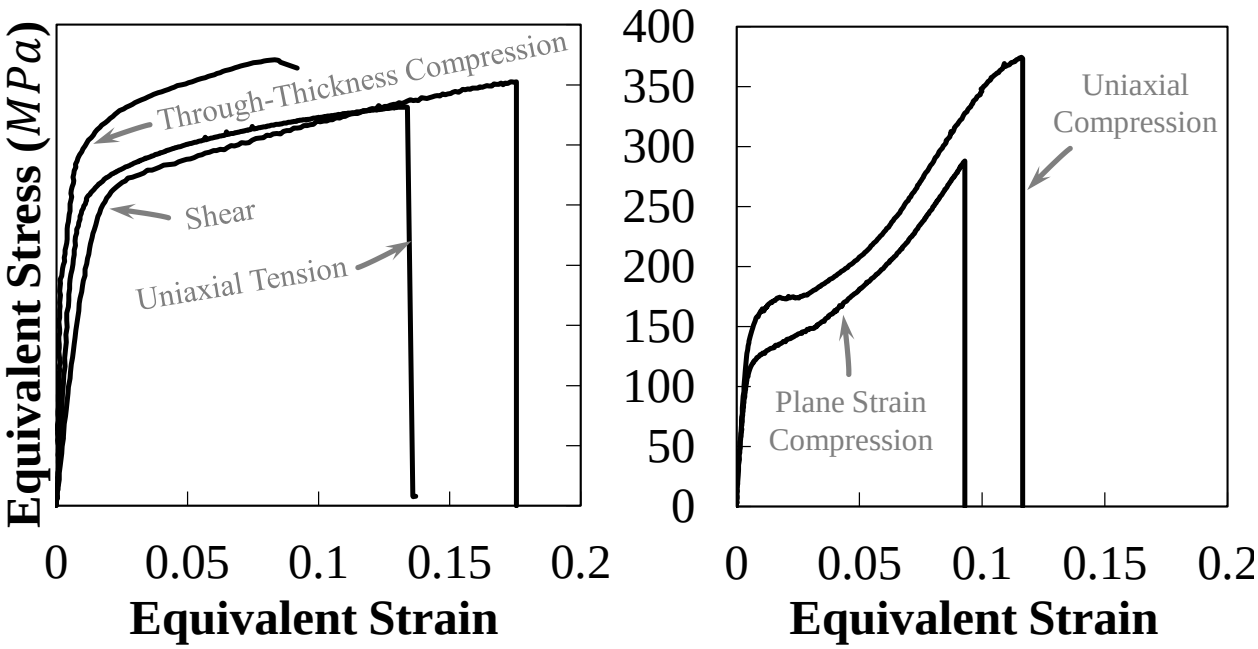

Figure 21 The hardening curves for 0° specimens, comparing with uniaxial tension, shear, through-thickness compression, uniaxial and plane strain compression.

Nine different loading conditions (uniaxial tension, notch tension, punch, uniaxial reversal compression-tension, uniaxial compression, biaxial compression, plane strain compression, through-thickness compression, and shear) were applied, five orientations were tested for each loading condition except for punch (one), uniaxial reversal compression-tension (three) and through-thickness compression (one). Three tests were repeated for each case, therefore 105 mechanical test were conducted for magnesium AZ31B-H24 in total. An overall picture of the magnesium AZ31B-H24 plasticity and fracture properties is exhibited. Good repeatability was observed when the strength data were summarized.

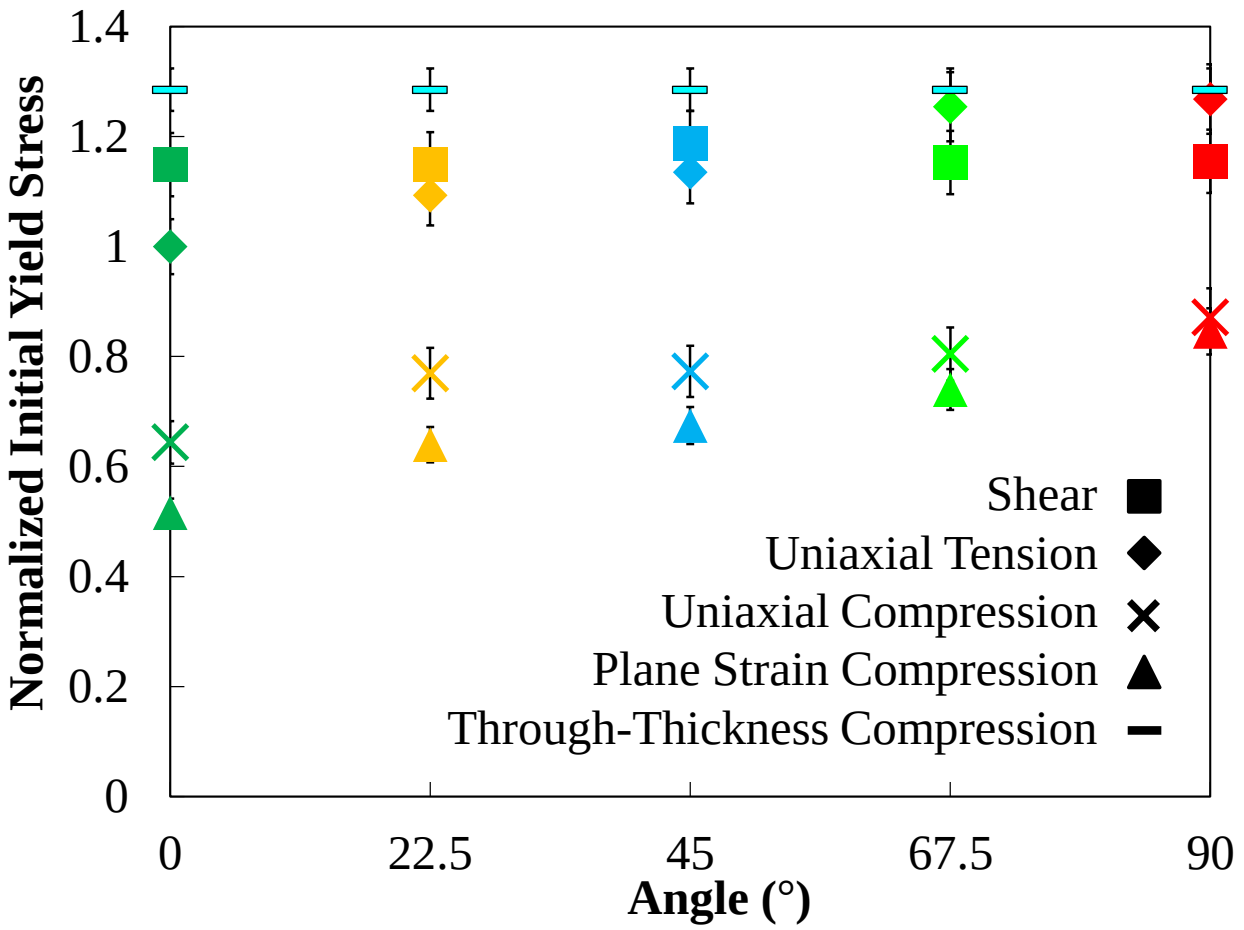

Figure 22 Normalized equivalent stresses versus orientations at initial yield among different loading conditions and orientations. The baseline values are all $220MPa$. Error bars of test data are provided.

The equivalent strain-stress curves obtained by 0° specimens under different monotonic loading conditions are shown in Figure 21 and Figure 22. The results of notch tension, biaxial compression, and punch test are not included due to non-uniform deformation. The hardening curves can be then classified into two groups, a) classical "convex" curves, for uniaxial, shear, punch, and through-thickness compression (equi-biaxial tension) tests, and b) "concave" curves, for uniaxial and plane strain compression tests. Large asymmetrical initial yield stress between tension and compression can be observed for this material.

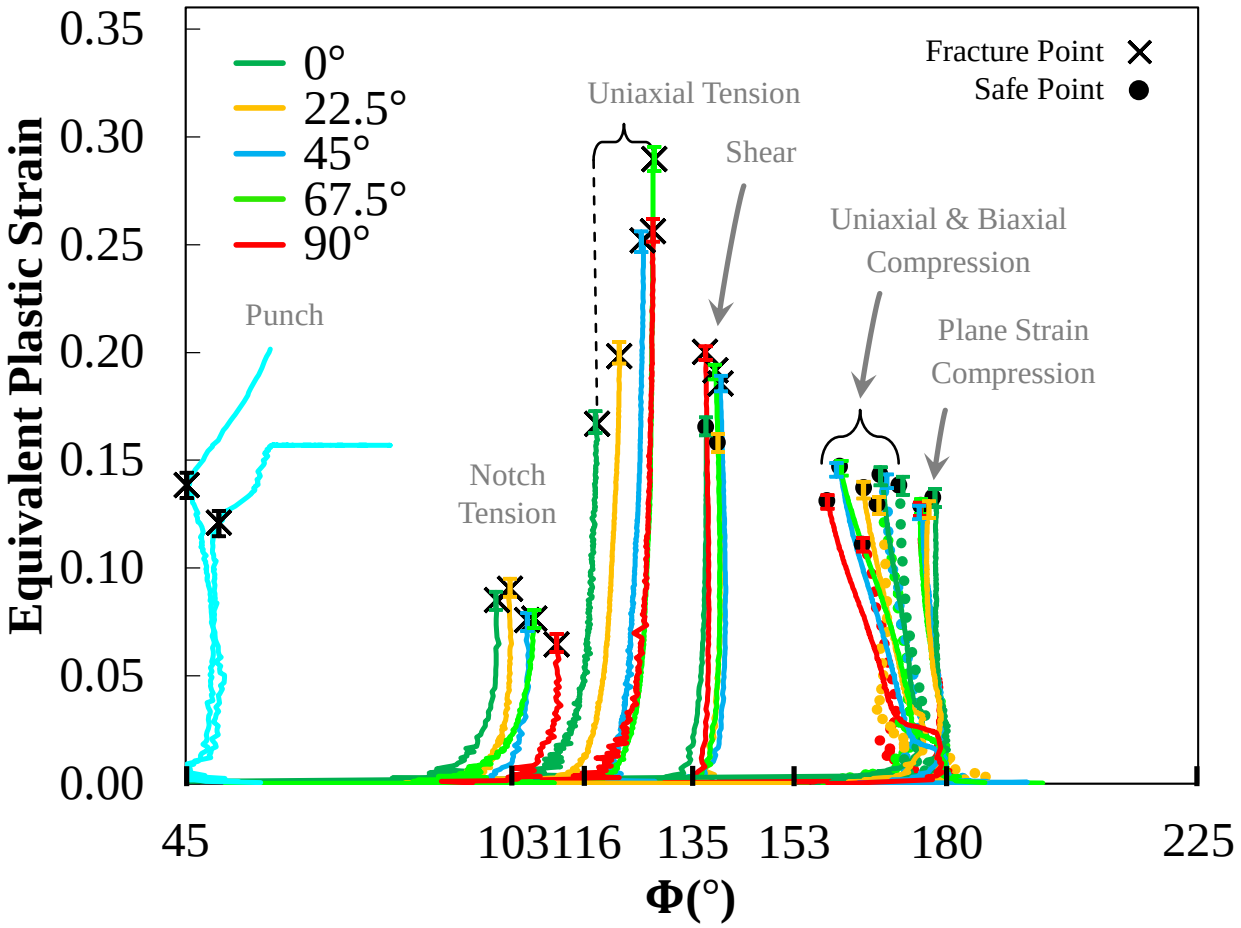

Figure 23 The entire loading histories with plastic flow and fracture strains, for all the loading conditions and orientations. Error bars of test data are provided.

Figure 23 illustrates all the monotonic loading histories, which are distinguished by different loading conditions. The error bars were individually determined by comparing the difference between two continuous frames, when fracture initiated in a single test. The corresponding Φ values under J2 plasticity are indicated from left to right in Figure 23 as following: 45° for punch test (equi-biaxial tension), 103° for notch (biaxial) tension, 116° for uniaxial tension, 135° for pure shear, 153° for uniaxial compression and 180° for plane strain compression, respectively. Concurrently the fracture strains and safe points (no fracture initiation) are included in Figure 23 as well, hence a fracture locus can be determined.

CHAPTER 4 CONSTITUTIVE MODELING

This material, magnesium AZ31B-H24, exhibits strong anisotropy according to the experimental results in the previous chapter. In order to describe the plastic behaviors in a general stress state, an accurate yield criterion and a hardening rule are required.

4.1 CPB06ex2 Anisotropic Yield Criterion

To account for both anisotropy in material strength and plastic flows for magnesium AZ31B alloys, an extension of Cazacu et al. (2006) orthotropic yield criterion was proposed by Plunkett et al. (2008). This criterion, denoted CPB06ex2, reads

$$F(\boldsymbol{\Sigma}, \boldsymbol{\Sigma}') = (\Sigma_1 - k|\Sigma_1|)^a + (\Sigma_2 - k|\Sigma_2|)^a + (\Sigma_3 - k|\Sigma_3|)^a + (\Sigma_1' - k'|\Sigma_1'|)^a + (\Sigma_2' - k'|\Sigma_2'|)^a + (\Sigma_3' - k'|\Sigma_3'|)^a, \quad (11)$$

where k and k' are material parameters describing the asymmetrical strength between tension and compression, a is the degree of homogeneity, while $\boldsymbol{\Sigma}$ and $\boldsymbol{\Sigma}'$ are transformed stress tensors obtained through application of two linear 4th order orthotropic tensors, denoted $\boldsymbol{C}$ and $\boldsymbol{C}'$, on the Cauchy stress deviator $\boldsymbol{S}$. In the axes of orthotropy, $\boldsymbol{C}$ and $\boldsymbol{C}'$ are represented as

$$\boldsymbol{\Sigma} = \boldsymbol{C} \cdot \boldsymbol{S}, \qquad \boldsymbol{\Sigma}' = \boldsymbol{C}' \cdot \boldsymbol{S}, \quad (12)$$

where $\boldsymbol{C}$ and $\boldsymbol{C}'$ are fourth-order tensors operating on the stress deviator, represented as

$$\boldsymbol{C} = \begin{bmatrix} C_{11} & C_{12} & C_{13} & 0 & 0 & 0 \\ C_{12} & C_{22} & C_{23} & 0 & 0 & 0 \\ C_{13} & C_{23} & C_{33} & 0 & 0 & 0 \\ 0 & 0 & 0 & C_{44} & 0 & 0 \\ 0 & 0 & 0 & 0 & C_{55} & 0 \\ 0 & 0 & 0 & 0 & 0 & C_{66} \end{bmatrix}, \boldsymbol{C}' = \begin{bmatrix} C_{11}' & C_{12}' & C_{13}' & 0 & 0 & 0 \\ C_{12}' & C_{22}' & C_{23}' & 0 & 0 & 0 \\ C_{13}' & C_{23}' & C_{33}' & 0 & 0 & 0 \\ 0 & 0 & 0 & C_{44}' & 0 & 0 \\ 0 & 0 & 0 & 0 & C_{55}' & 0 \\ 0 & 0 & 0 & 0 & 0 & C_{66}' \end{bmatrix}. \quad (13)$$

In this study C_{44}, C_{55}, C'_{44} and C'_{55} are zeros due to the plane stress condition, and a was set as another material coefficient for calibration. Therefore 15 anisotropic parameters are involved in total, based on the orthotropic configuration with respect to the given Cartesian coordinate system. This yield surface was proven to be convex when $k, k' \in [-1,1]$ and $a \geq 1$ (Cazacu et al., 2006). The calibrated parameters are given in Table 1.

Table 1 CPB06ex2 yield criterion parameters for magnesium AZ31B-H24 alloy

a	k	C_{11}	C_{12}	C_{13}	C_{22}	C_{23}	C_{33}	C_{66}
1.65	0.67	1.63	−0.21	−0.21	0.94	−0.48	−1.72	1.69
	k'	$C_{11}{}'$	$C_{12}{}'$	$C_{13}{}'$	$C_{22}{}'$	$C_{23}{}'$	$C_{33}{}'$	$C_{66}{}'$
	−0.98	0.66	0.28	0.14	0.41	−0.82	−0.34	0.50

4.2 Modified Semi-analytical Sachs Model

Based on the activation of deformation twinning under compressive load, a semi-analytical Sachs model (Barnett, 2007; Barnett et al., 2006) has been evaluated for multi-axial hardening of AZ31B-H24 by Jia and Bai (2015c). It was then modified and extended to include the dependency on stress triaxiality and Lode angle parameter. Let X_T be the fraction of grains undergoing twinning and χ is the fraction of these grains that have twinned, thus the following volumes can be defined: volume I, $(1-\chi)X_T$, material undergoing deformation by twinning; volume II, χX_T, twinned material undergoing deformation by glide; and volume III, $1-X_T$, material that deforms only by glide. In volume I, the constant stress σ_I is assumed, partially due to the "easy" lateral advance of the $\{10\bar{1}2\}$ twinning front once the twin has formed. Therefore

$$\sigma_I = (1-\chi)X_T \frac{\tau_{0t}}{m_I}, \tag{14}$$

where τ_{0t} is the critical resolved shear stress (CRSS) and m_I is the effective Schmid factor for twinning in this volume. In volume II, additional hardening is controlled by an *ad-hoc* hardening factor ξ due to twin boundaries and dislocation-twin interactions, and thus the stress

$$\sigma_{II} = \chi X_T \xi \frac{k}{m_{II}^{n+1}} (\varepsilon^p + \varepsilon_0)^n, \tag{15}$$

where m_{II} is the effective Schmid factor for basal slip in this volume and k reflects the magnitude of CRSS for basal slip. Note that the original power-hardening item was $(\varepsilon^p - 0.13 m_I \chi)^n$ in Barnett (2007); Barnett et al. (2006), where the item $0.13 m_I \chi$ indicates the strain accommodated by the twinning reaction. This was modified into a single constant ε_0 with its sign reversed because it would cause model instability when $\varepsilon^p - 0.13 m_I \chi$ was smaller than zero. Also, the value of $0.13 m_I \chi$ is actually small enough to be neglected. For volume III which does not undergo twinning, the stress is given as

$$\sigma_{III} = (1 - X_T) \frac{k}{m_{III}^{n+1}} (\varepsilon^p + \varepsilon_0)^n, \tag{16}$$

where m_{III} is the effective Schmid factor for basal slip in this volume. Therefore, to approximate the combined effect of these stresses, with the Sachs assumption, a convenient approximation is provided for the equivalent stress, as follows

$$\begin{aligned} \overline{\sigma}_{Sachs} &= \sigma_I + \sigma_{II} + \sigma_{III} \\ &= (1 - \chi) X_T \frac{\tau_{0t}}{m_I} + \chi X_T \xi \frac{k}{m_{II}^{n+1}} (\varepsilon^p + \varepsilon_0)^n + (1 - X_T) \frac{k}{m_{III}^{n+1}} (\varepsilon^p + \varepsilon_0)^n. \end{aligned} \tag{17}$$

An additional parameter ε_0 was added in the third item for controlling the initial yield stress. The value of χ is assumed to be a sigmoidal function,

$$\chi = 1 - exp\left[-4(\frac{\varepsilon^p}{\varepsilon_1})^a\right], \tag{18}$$

where a is a rate exponent and ε_1 is the macroscopic strain at which the twinning reaction is 98% complete. Two extensions were made to incorporate the stress triaxiality and Lode angle dependencies, in order to capture the complicated hardening behavior of this material. First, the parameter X_T is generalized into a function of stress triaxiality, which reads

$$X_T = X_{TT} + \frac{X_{TC} - X_{TT}}{1 + \exp[C(\eta - \eta_C)]}, \tag{19}$$

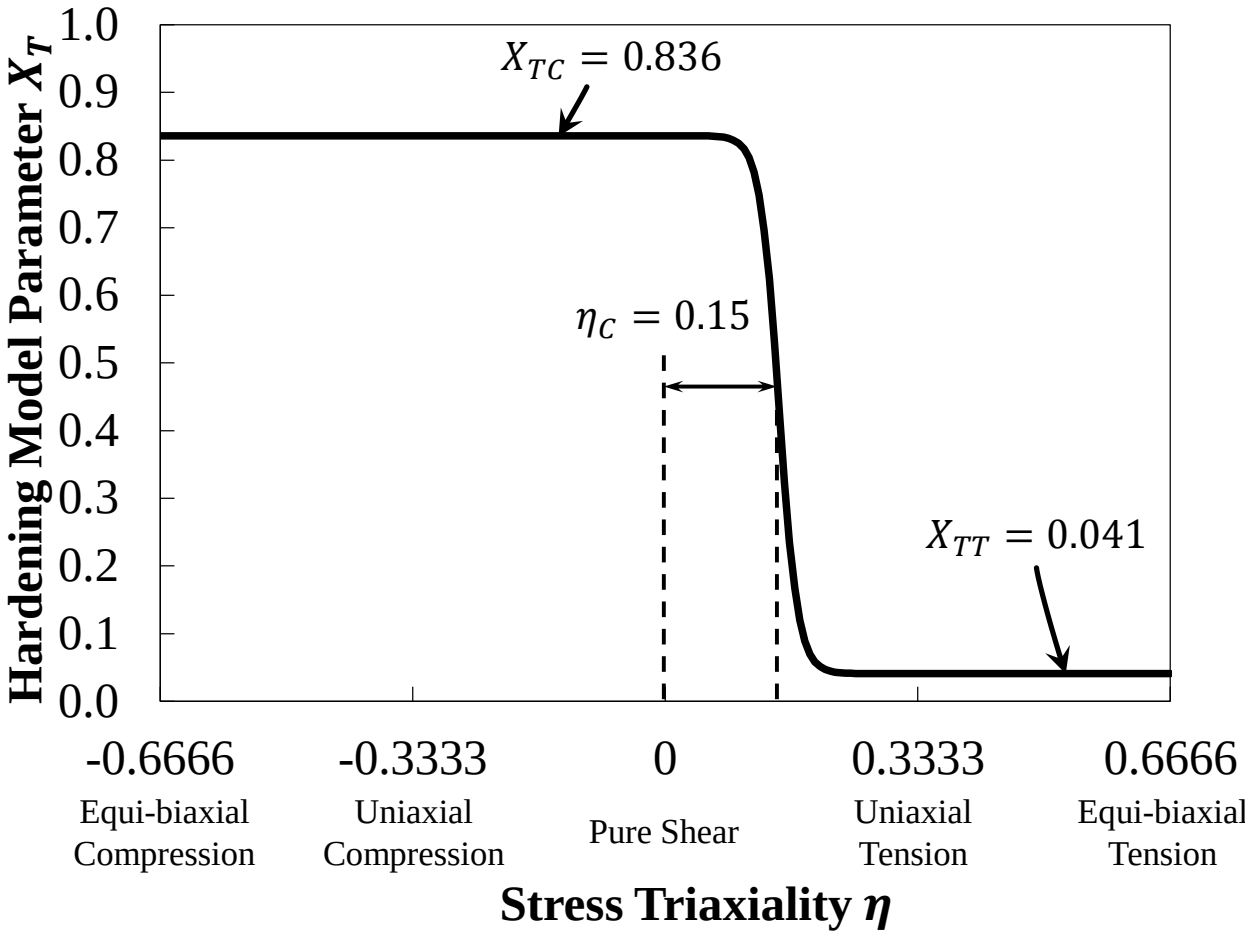

Figure 24 The parameter X_T as a function of stress triaxiality η, with interpretation of used coefficients.

Here, X_{TT} and X_{TC} are the individual X_T values based on the measurement of twinning volume fraction under uniaxial tension and compression loading conditions, respectively. C and η_C are two more material coefficients, added to control the X_{TT}-to-X_{TC} transition rate and position, respectively. η is the stress triaxiality according to Equation (2),

$$\eta = \frac{\sigma_m}{\overline{\sigma}} = \frac{(\sigma_1 + \sigma_2)}{3\sqrt{\sigma_1^2 + \sigma_2^2 - \sigma_1\sigma_2}}$$The function of X_T versus stress

The second extension was made to adjust the magnitude of $\overline{\sigma}_{Sachs}$ by adding a correction term based on Algarni, Bai, and Choi (2015); Bai and Wierzbicki (2008b). The final equivalent stress now reads

$$\overline{\sigma} = \overline{\sigma}_{Sachs}\left[1 - c_\eta(\eta - \eta_0)^2\right]\left[c_\theta^s - \frac{m+1}{m}(c_\theta^{ax} - c_\theta^s)\left(\gamma - \frac{\gamma^{m+1}}{m+1}\right)\right], \tag{20}$$

where

$$c_\theta^{ax} = \begin{cases} c_\theta^t & \overline{\theta} \geq 0 \\ c_\theta^c & \overline{\theta} < 0 \end{cases}$$ γ is related to the normalized Lode

$$\gamma = \frac{\sqrt{3}}{2 - \sqrt{3}}\left[\sec\left(\frac{\bar{\theta}\pi}{6}\right) - 1\right], \tag{21}$$

where c_η, η_0, c_θ^s, c_θ^t, c_θ^c, and m are material coefficients. $\bar{\theta}$ is the normalized Lode angle parameter. It is expressed, under plane stress condition, as follows,

$$\overline{\theta} = 1 - \frac{2}{\pi} arccos\left[-\frac{27}{2}\eta\left(\eta^2 - \frac{1}{3}\right)\right]. \tag{22}$$

Note that two items were modified compared to the original equation from Bai and Wierzbicki (2008b), a) the original item $(\eta - \eta_0)$ was modified into a quadratic item $(\eta - \eta_0)^2$ to increase its flexibility, and b) the coefficient $(m+1)/m$ was newly added for user friendly consideration.

This modification could increase the robustness of the hardening model when a loading condition abruptly changes. The calibration of this model could be partially guided by rudimentary crystal plasticity type calculations to determine the values of the material coefficients m_I, m_{II}, m_{III}, X_{TT} and X_{TC}, based on the measurement from Barnett et al. (2006); X. Y. Lou et al. (2007) with adjustment. The rest of them, τ_0, ε_1, ε_0, n, a, ξ, k, C, η_C, c_η, η_0, c_θ^s, c_θ^t, c_θ^c, and m were optimized to simultaneously correlate with the tested equivalent stress-strain curves under different loading conditions. The set of calibrated plasticity parameters is listed in Table 2.

Table 2 Modified Sachs hardening model coefficients for magnesium AZ31B-H24

X_{TT}	X_{TC}	m_I	m_{II}	m_{III}	a	ε_1	ε_0	n	$\tau_0\ (MPa)$
0.041	0.836	0.450	0.450	0.250	2.920	0.124	0.005	0.091	84.20
ξ	C	η_C	c_η	η_0	c_θ^s	c_θ^t	c_θ^c	m	$k\ (MPa)$
1.443	80.00	0.150	-0.150	0.000	0.969	0.971	1.155	0.050	87.40

4.3 Kinematic and Cross Hardening Rules Described by New State Variables

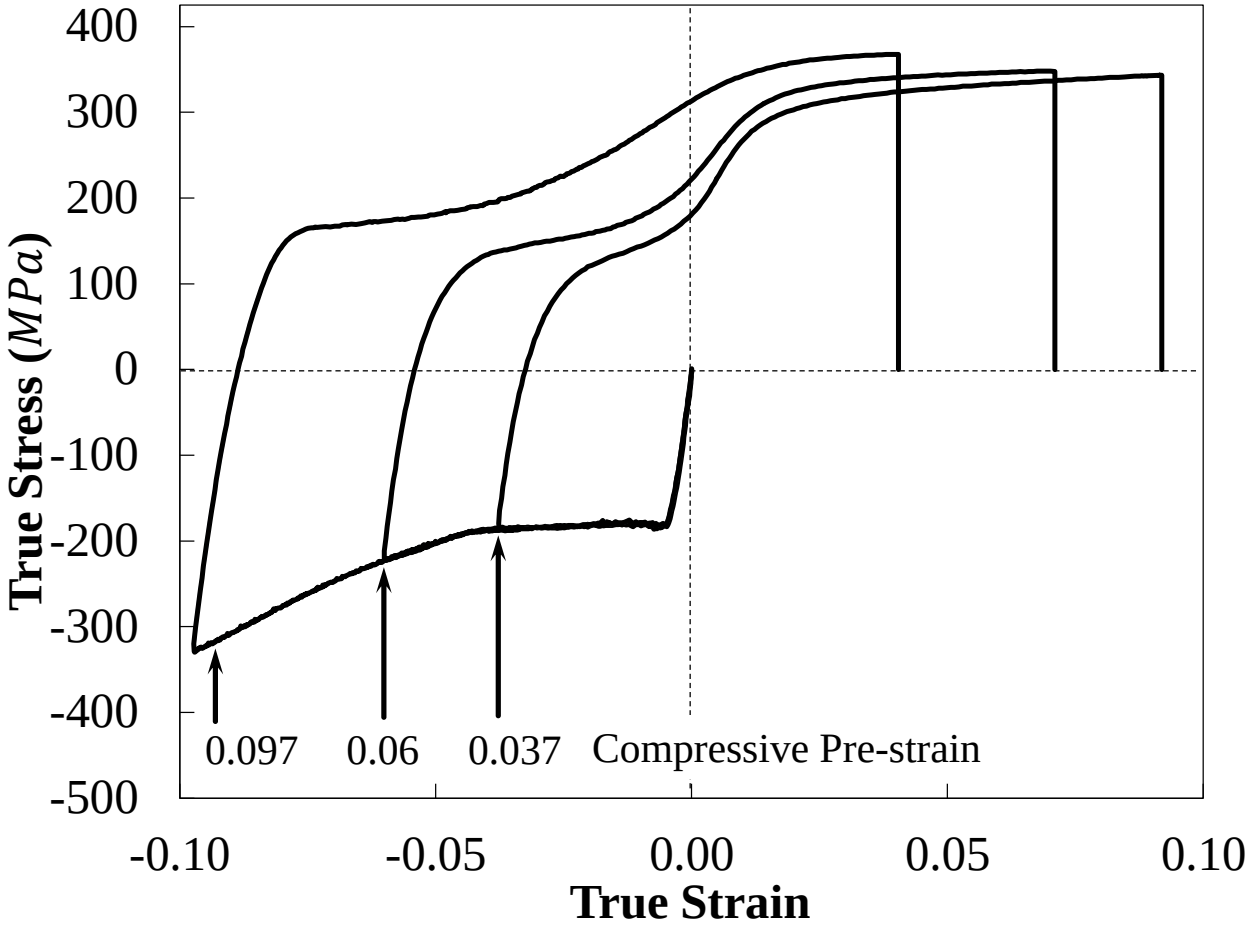

Figure 25 Experimental true stress-strain curves under uniaxial compression-tension reversal loading with different compressive pre-strains. Note that the drops of last data points are due to fracture.

Examples of true stress-strain curves under a uniaxial compression-tension reversal loading condition are illustrated in Figure 25, with three different compressive pre-strains, 0.037, 0.060, and 0.097. The orientations are all along rolling direction (RD). The details of experimental method and results are provided in the later sections. The first stage of compressive part is compliant with the monotonic experimental result (Jia & Bai, 2015c). However, three characteristics different from the monotonic loading in the sequential tensile stress-strain curves

can be observed, a) Another sigmoidal shape is exhibited, similar with the compressive part. b) This shape is dependent on the amount of compressive pre-strain. c) The stress-strain curve under reversal tension is consistent with the one under monotonic uniaxial tension, when the sequential sigmoidal shape approaches an ultimate plateau. Therefore, three different sets of state variables are defined to incorporate these effects into the hardening model.

4.3.1 Loading History Effect

An AF-type "dummy" back stress $\boldsymbol{\alpha}$ is defined as follows, in an increment form

$$\dot{\alpha_{ij}} = C_0 \left(\rho \frac{\sigma_{ij} - \alpha_{ij}}{\bar{\sigma}} - \alpha_{ij} \right) \dot{\bar{\varepsilon}}^p, \tag{23}$$

where C_0 and ρ are material coefficients, and $\dot{\bar{\varepsilon}}^p$ is the increment of equivalent plastic strain. It is nominated as "dummy" because the Cauchy stress σ_{ij} will not be directly influenced by this back stress, and the plastic flow potential function still remains, as follows

$$f(\sigma_{ij}) - \bar{\sigma} = 0, \tag{24}$$

where $f(\sigma_{ij})$ is the CPB06ex2 anisotropic yield criterion. Therefore, α is only a state tensor to record the loading history. In order to characterize the strain path effect, a parameter was introduced by Schmitt et al. (1994), which reads

$$\Theta = \frac{\dot{\boldsymbol{\varepsilon}}^p_{(1)} : \dot{\boldsymbol{\varepsilon}}^p_{(2)}}{\left\| \dot{\boldsymbol{\varepsilon}}^p_{(1)} \right\| \left\| \dot{\boldsymbol{\varepsilon}}^p_{(2)} \right\|}, \tag{25}$$

where $\dot{\varepsilon}^p_{(1)}$ and $\dot{\varepsilon}^p_{(2)}$ indicate plastic strain tensors under the pre-strain and the subsequent deformation, respectively. Similarly, a stress-based definition was proposed by Barlat et al.

(2013), where the strain tensors were replaced by Cauchy stress tensor and microstructure deviators in Equation (25). Analogously, a state variable ψ is defined in this paper, as follows

$$\cos\psi = \frac{\boldsymbol{\sigma}:\boldsymbol{\alpha}}{\|\boldsymbol{\sigma}\|\|\boldsymbol{\alpha}\|}. \tag{26}$$

The phenomenological meaning of this variable is the angle between Cauchy stress and "dummy" back stress, which is exhibited in Figure 26 under different loading conditions.

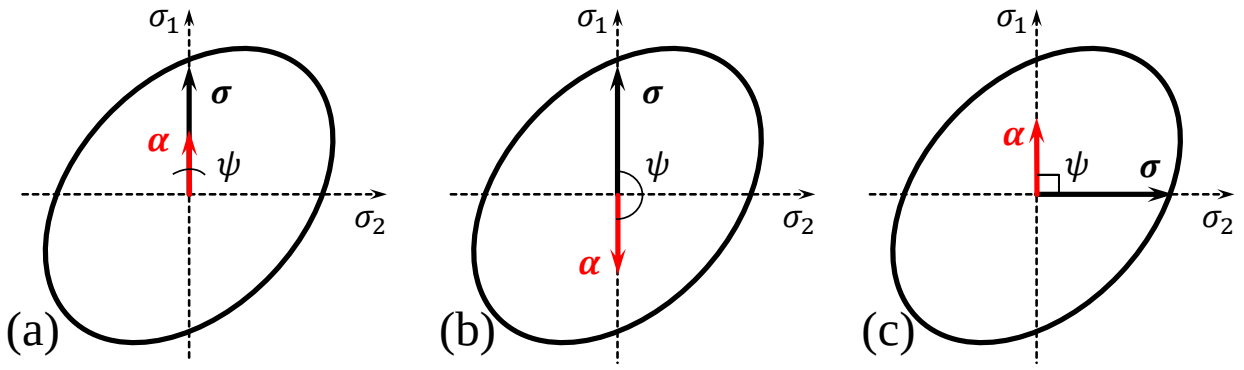

Figure 26 A schematic graph of the angle ψ in the stress space under (a) monotonic uniaxial tension, (b) reversal uniaxial compression-tension, and (c) two-step uniaxial tension (cross loading).

This variable can then be further normalized into two different forms,

$$X_K = \frac{1-\cos\psi}{2}, \tag{27}$$

$$X_C = 1 - |\cos\psi|. \tag{28}$$

These two state variables are capable for distinguishing different types of loading histories, as follows:

1. Monotonic loading (Figure 26a): $\cos\psi = 1$, $X_K = 0$, $X_C = 0$, when $\boldsymbol{\sigma}$ is co-directional with $\boldsymbol{\alpha}$.

2. Reversal loading (Figure 26b): $\cos\psi = -1$, $X_K = 1$, $X_C = 0$, when $\boldsymbol{\sigma}$ is completely

opposite to $\boldsymbol{\alpha}$.

3. Cross loading (Figure 26c): $\cos\psi \in (-1,1)$, $X_K \in (0,1)$, $X_C \in (0,1]$, when it is under the rest types of loading transitions, for example a transition in uniaxial tension from along 0° to 90° orientation, or a transition from uniaxial tension to pure shear.

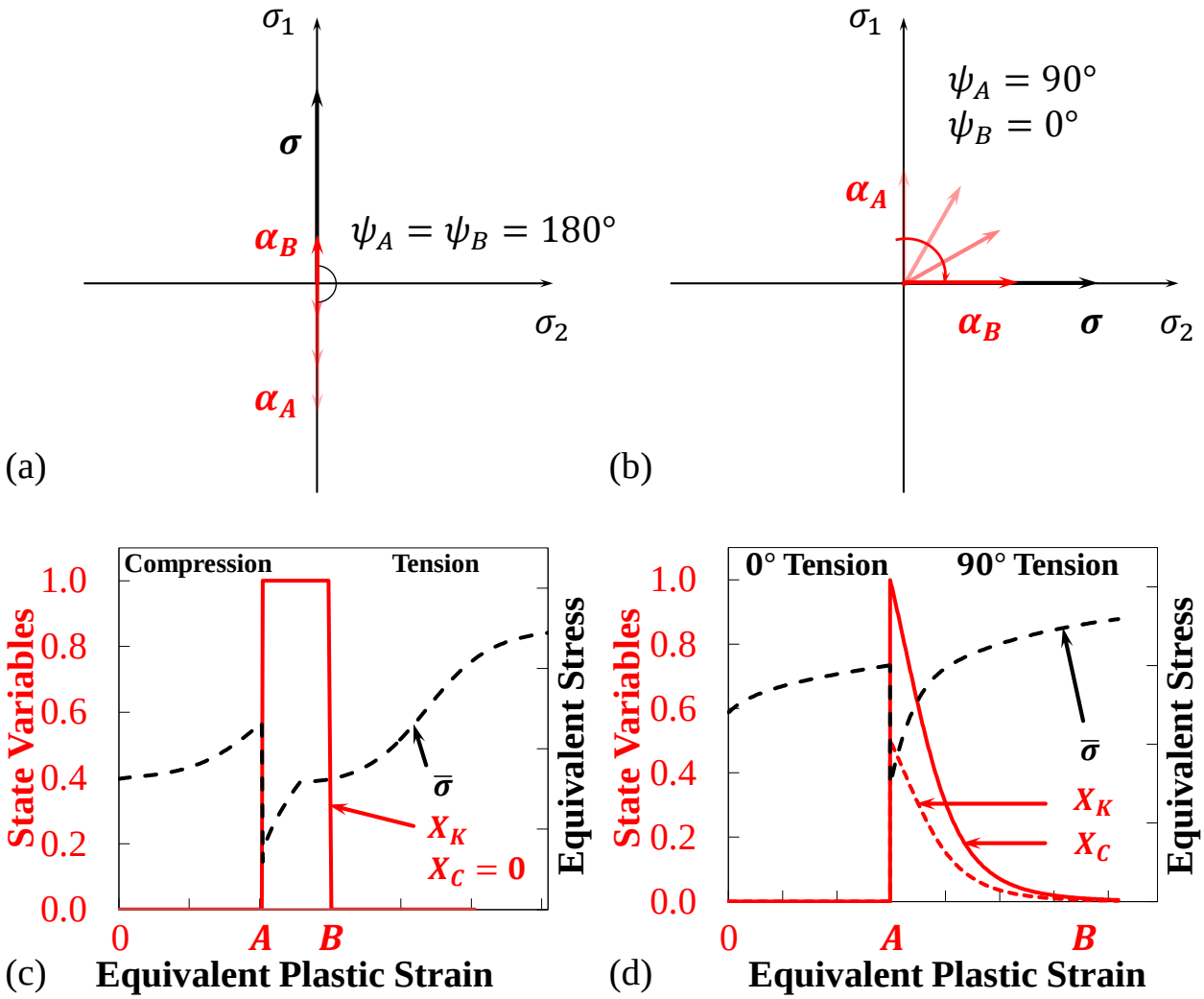

Figure 27 Schematic evolutions of new state variables X_K and X_C under (a), (c) reversal compression-tension, and (b), (d) two-step uniaxial tension (cross loading), in the space of (a), (b) stress, and (c), (d) equivalent plastic strain, comparing to their hardening curves.

X_K and X_C, whose evolutions are schematically illustrated in Figure 27, can then be utilized to identify the transitional strain history. Figure 27a and Figure 27c depict the loading condition

change from uniaxial compression to uniaxial tension. X_K increases from zero to one and remains, while X_C is constantly zero during the transition. It is because the "dummy" back stress $\boldsymbol{\alpha}$ is uniaxially driven by the Cauchy stress $\boldsymbol{\sigma}$. When $\boldsymbol{\alpha}$ evolves into the same direction of the Cauchy stress, X_K returns into zero, generating a square shape with unity magnitude along the growth of equivalent plastic strain. The evolution scenarios of both X_K and X_C are different during cross loading from reversal loading. Figure 27b and Figure 27d depict a two-step uniaxial tension, from along 0° to 90° orientation. X_K and X_C increase from both 0 to 0.5 and 1, respectively. Since $\boldsymbol{\alpha}$ is non-uniaxially evolving from along 0° to 90° orientation to follow the direction of $\boldsymbol{\sigma}$, the angle between $\boldsymbol{\alpha}$ and $\boldsymbol{\sigma}$ changes all the time, resulting in a decay instead of uniform shape in both of them along the growth of the equivalent plastic strain. A peak value is obtained at the beginning of the transition. The peak value and decaying rate are dependent on the angle between $\boldsymbol{\sigma}$ and $\boldsymbol{\alpha}$ when transition initiates, and the material coefficients in the "dummy" back stress, respectively. Therefore, X_K is the state variable for recording loading histories under both reversal and cross conditions, while X_C is for the cross loading histories only. In this way, reversal and cross loading histories can be fully decoupled to simplify the modeling and calibration processes.

4.3.2 Twinning/De-twinning Effects

A new state variable κ, indicating the real-time absolute twinning ratio in a grain, is defined in form of differential equation,

$$\dot{\kappa} = \omega(\kappa + \kappa_0)[X_T(\eta) - \kappa]\dot{\bar{\varepsilon}}^p, \quad \kappa(0) = 0, \tag{29}$$

where κ_0 and ω are material coefficients to adjust the twinning/de-twinning rate. This function has a sigmoidal shape along twinning ratio growth, which is similar with the empirical rule of twinning evolution χ in Equation (18).

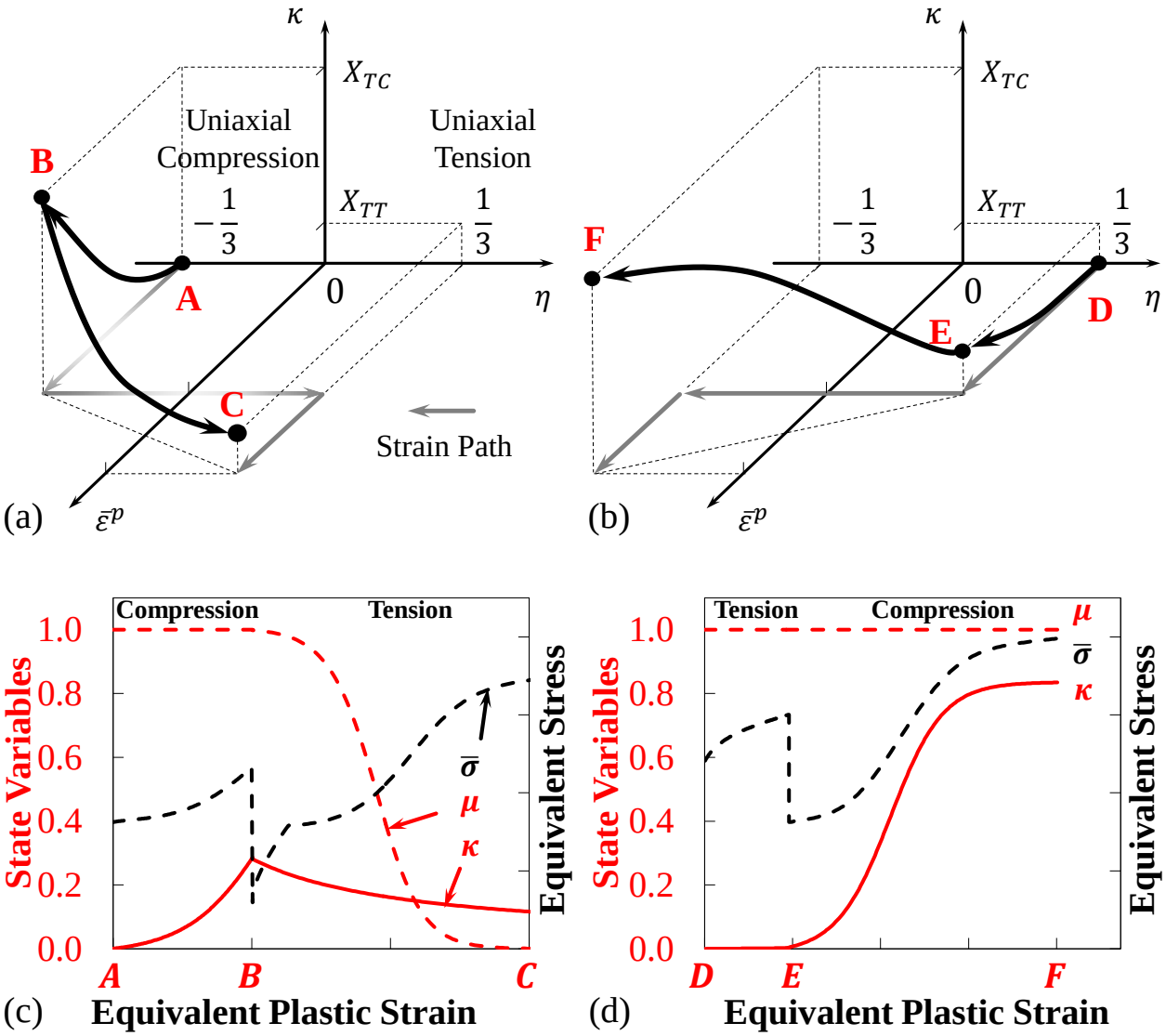

Figure 28 Schematic evolutions of new state variables κ and μ under reversal a), c) compression-tension, and b), d) tension-compression, in the space of a), b) equivalent plastic strain with stress triaxiality, and c), d) equivalent plastic strain, comparing to their hardening curves.

On the contrary, χ is an ever-increasing function that approaches an ultimate value of one and then stagnates, while κ can be increased/decreased towards X_T, indicating the expected twinning

ratio under a specific loading condition (represented by stress triaxiality). The schematic evolution of this state variable is depicted in Figure 28. Therefore, the twinning/de-twinning effect can be expressed by κ, under the following scenarios:

1. Monotonic tension (D to E), κ grows from zero towards X_{TT}.

2. Monotonic compression (A to B), κ grows from zero towards X_{TC},

3. Tension followed by compression (D to E to F), κ grows from zero towards X_{TT}, and the n continues to grow towards X_{TC},

4. Compression followed by tension (A to B to C), κ firstly grows from zero to κ_1 towards X_{TC}. If κ_1 is larger than X_{TT}, κ decreases towards X_{TT}, otherwise κ continues to grow towards X_{TT}. The position of κ_1 can be controlled by the twinning/de-twinning rate, represented by the m aterial coefficients ω and κ_0.

An *ad-hoc* de-twinning state variable μ is defined in form of differential equation, to represent the fraction of these twinned regions that expected to be de-twinned, as follows

$$\dot{\mu} = \begin{cases} -\Omega\mu(1.005-\mu)\dot{\bar{\varepsilon}}^p & \dot{\kappa} < 0 \\ 0 & \dot{\kappa} \geq 0 \end{cases}, \qquad \mu(0) = \mu(\dot{\kappa} > 0) = 1, \tag{30}$$

where Ω is a material coefficient representing the *ad-hoc* de-twinning rate. It is noted that the evolution of μ is governed by $\dot{\kappa}$, the rate of the absolute twinning ratio in a grain. μ is set as unity when there is no de-twinning in progress ($\dot{\kappa} > 0$). Once a de-twinning initiates ($\dot{\kappa} < 0$), μ is activated to evolve until all the twinned area is de-twinned ($\mu = 0$), which can be expressed as an inverse sigmoidal shape function. The schematic evolution of this state variable is also depicted in Figure 28. When the compressive pre-strain is larger, the sequential tensile part exhibits the following dependency: a) the magnitudes of both initial and ultimate plateau are

larger; and b) the transition from the initial to the ultimate plateau is slower, indicating a slower de-twinning rate. These two phenomena are recalled in Figure 25. Therefore, the ad-hoc de-twinning rate coefficient Ω should be generalized into a function of compressive pre-strain ε_C, which will be determined in the next section. Using a sigmoidal function again, Ω can be expressed as follows

$$\Omega = \frac{\Omega_1}{1 + \exp(\Omega_2 \varepsilon_c)} + \Omega_3, \tag{31}$$

where Ω_1, Ω_2 and Ω_3 are three additional material coefficients.

4.3.3 Pre-strain Effect

Let ε_C be the compressive strain in a loading history. It can be defined, with another state variable ε_{C0} at time step $i+1$, as follows

$$(\varepsilon_C)_{i+1} = \begin{cases} \bar{\varepsilon}^p - (\varepsilon_{C0})_{i+1} & \dot{\kappa} \geq 0 \\ (\varepsilon_C)_i & \dot{\kappa} < 0, \quad \mu < 0.95 \end{cases}$$

$$(\varepsilon_{C0})_{i+1} = \begin{cases} \bar{\varepsilon}^p & X_K = 1 \\ (\varepsilon_{C0})_i & X_K \neq 1 \end{cases}, \qquad \varepsilon_C(0) = \varepsilon_{C0}(0) = 0, \tag{32}$$

The determination of ε_C is dictated by both twinning/de-twinning rate $\dot{\kappa}$ and the reversal loading historical state variable X_K, to exclusively record the compressive strain during reversal loading. This can be explained as follows,

1. Monotonic and cross loading ($\dot{\kappa} \geq 0$, $X_K \neq 1$): ε_{C0} are always equal to zero and then ε_C is always following the total equivalent plastic strain $\bar{\varepsilon}^p$ because $\varepsilon_C = \bar{\varepsilon}^p - 0 = \bar{\varepsilon}^p$.
2. Tension-compression reversal loading ($\dot{\kappa} \geq 0$, $X_K = 1$): Let $\bar{\varepsilon}^p_{C0}$ be the equivalent plastic strain at the beginning of sequential compressive loading, where satisfies $\dot{\kappa} \geq 0$ and $X_K = 1$.

Therefore, it can be obtained that $\varepsilon_{C0} = \bar{\varepsilon}^p_{C0}$ and $\varepsilon_C = \bar{\varepsilon}^p_{C0} - \varepsilon_{C0} = \bar{\varepsilon}^p_{C0} - \bar{\varepsilon}^p_{C0} = 0$, indicating the initiation of the compressive loading. After the transition, it can be obtained $X_K = 0$ during the sequential compression. Therefore, ε_{C0} remains as $\bar{\varepsilon}^p_{C0}$, and ε_C equals to $\bar{\varepsilon}^p - \varepsilon_{C0} = \bar{\varepsilon}^p - \bar{\varepsilon}^p_{C0}$ since $\dot{\kappa} \geq 0$ still remains, recording the extracted amount of equivalent plastic strain under compressive loading only. This is because the accumulated strain in all previous loadings $\bar{\varepsilon}^p_{C0}$ has been removed from $\bar{\varepsilon}^p$. The twinning ratio is always either growing or remaining ($\dot{\kappa} \geq 0$) till the end of the sequential compression loading.

3. Compression-tension reversal loading ($\dot{\kappa} < 0, X_K = 1$): The pre-compressive part can be either monotonic (scenario 1) or reversal (scenario 2). As described above, the compressive strain can be recorded by ε_C under both cases. In the sequential tension part where $\dot{\kappa} < 0$, ε_C remains as a constant value from the previous step, which can then be applied in Equation (31) with de-twinning effect activated. An additional identification $\mu < 0.95$ is added to eliminate noises in FE simulation, ensuring the pre-strain starts to be recorded after the expected tension part.

On the other hand, a general pre-strain ε_B can be similarly defined as follows, utilizing both X_K and the twinning rate $\dot{\kappa}$,

$$(\varepsilon_B)_{i+1} = \begin{cases} X_K \bar{\varepsilon}^p & \dot{\kappa} \geq 0, \dot{X_K} > 0 \\ (\varepsilon_B)_i & Other \end{cases}, \qquad \varepsilon_B(0) = 0. \tag{33}$$

Different from ε_C, ε_B indicates a pre-strain under all rest loading conditions, including cross loading. This can be explained as follows,

1. Monotonic loading ($\dot{\kappa} \geq 0, X_K = 0$): ε_B are always equal to zero.

2. Cross loading ($\dot{\kappa} \geq 0, X_K \in (0,1), \dot{X_K} > 0$): Cross loading includes all possible stress

states transitions within the range of $(-180°, 180°)$ on the yield surface. For example, a transition from 0° uniaxial tension to 90° uniaxial tension can be expressed as a 90° transition on the yield surface. It could result in $\dot{X_K} > 0$, an impulse peak value for X_K ranges in $(0,1)$, followed by an exponential decay shape as discussed in section 4.3.1The twinning behavior remains in this range ($\dot{\kappa} \geq 0$) because X_T, governing the target value of the evolution of κ, remains the same. For example, the 0° uniaxial tension shares the same stress triaxiality $1/3$ with the 90° uniaxial tension. Therefore, $\varepsilon_B = X_K \bar{\varepsilon}^p$, indicating the current equivalent plastic strain with distinguishing the effects among different types of cross-loading by X_K. ε_B remains once the state variable X_K decays because $\dot{X_K}$ is now smaller than zero.

3. Tension-compression reversal loading ($\dot{\kappa} \geq 0, X_K = 1, \dot{X_K} > 0$): Let $\bar{\varepsilon}^p_{C0}$ be the current equivalent plastic strain at the beginning of sequential compressive loading. An impulse is generated for X_K at the beginning of the transition, where $\dot{X_K} > 0$ and $X_K = 1$. The twinning ratio is always either growing or remaining ($\dot{\kappa} \geq 0$) during compression loading. Therefore, ε_B is set as $X_K \bar{\varepsilon}^p_{C0} = \bar{\varepsilon}^p_{C0}$, and remained after the impulse since X_K will either stagnate (during the transition) or return into 0 (after the transition). This can be considered as a specific case under scenario 2 above.

4. Compression-tension reversal loading ($\dot{\kappa} < 0, X_K = 1, \dot{X_K} > 0$): ε_B are always equal to zero or the previous recorded value since $\dot{\kappa} \geq 0$ doesn't satisfy.

Therefore, ε_B records the equivalent plastic strain under all loading conditions except compression, compensating to the other strain state variable ε_C. It is noted that ε_C and ε_B can then be applied for modeling all types of kinematic hardening behavior.

4.4 Derivation of a New Hardening Model

The modified semi-analytical Sachs model (Jia & Bai, 2015b) can be extended to incorporate the kinematic hardening behavior, using the state variables. Therefore, an additional item is defined, as follows

$$\bar{\sigma}_K = sign(\dot{\mu})\left[(A_{K1}\mu - A_{K2}\varepsilon_C)(\bar{\varepsilon}^p + \varepsilon_0 - \varepsilon_C)^n + X_K\sqrt{\boldsymbol{\alpha}^{dev}:\boldsymbol{\alpha}^{dev}}\right], \tag{34}$$

where

μ is the *ad-hoc* de-twinning state variable, evolves from 1 (no de-twinning) to 0 (de-twinning finished) evaluated by Equation (30). This is the key state variable to generate the sigmoidal shape in the sequential tensile stress-strain curve.

$sign(\dot{\mu})$ is the de-twinning activation factor, which can be either -1 (activated) or 0 (deactivated) based on Equation (30). The entire item vanishes when it is deactivated.

ε_C is the compressive strain in previous loading history, computed by Equation (32). An amount of ε_C is subtracted from the total equivalent plastic strain in the power hardening item. This is to consider the dependency on compressive pre-strain.

A_{K1} and A_{K2} are material coefficients, controlling the magnitudes of the initial and ultimate plateau in the sequential tensile part.

X_K is the loading history state variable identifying the transition area.

$\boldsymbol{\alpha}^{dev}$ is the deviatoric part of the "dummy" back stress, whose von-Mises type equivalent value is expressed by $\sqrt{\boldsymbol{\alpha}^{dev}:\boldsymbol{\alpha}^{dev}}$. A smoother transition can be generated by adding this item.

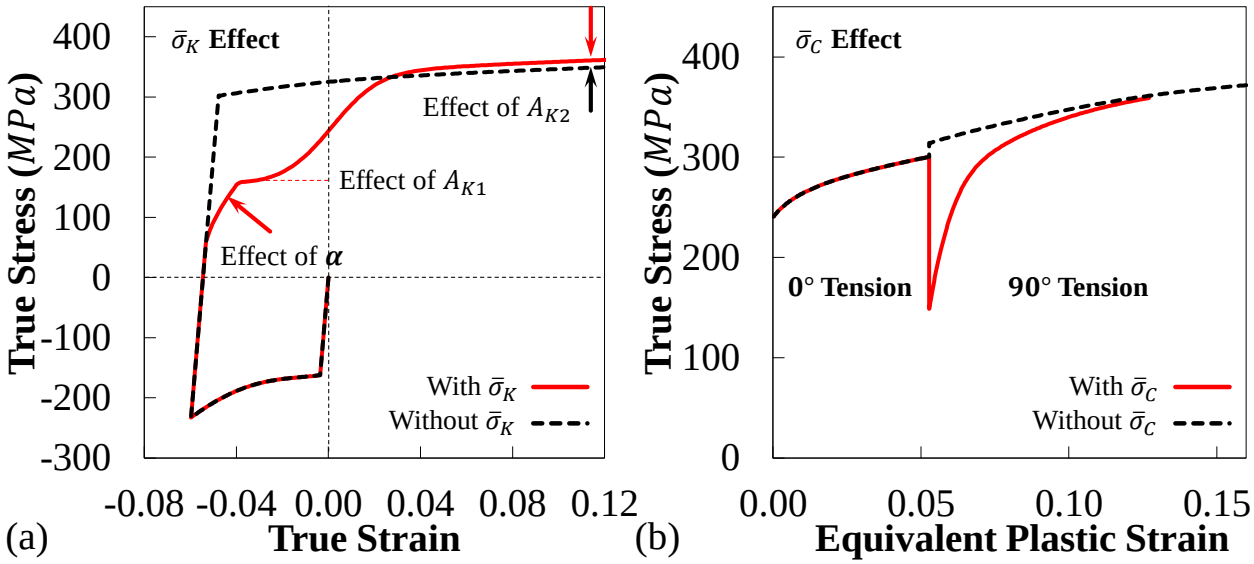

Figure 29 Schematic effects for new added items, (a) $\bar{\sigma}_K$ under a compression-tension reversal loading, and (b) $\bar{\sigma}_C$ under a two-step uniaxial tension (cross loading).

The effect of $\bar{\sigma}_K$ on the stress-strain curve under compression-tension reversal loading is illustrated in Figure 29a. This item $\bar{\sigma}_K$ governs the compression-tension part in kinematic hardening exclusively, utilizing the special de-twinning effect. The kinematic hardening behavior under the rest conditions, including tension-compression and cross loadings, can be incorporated by subtracting ε_B from the accumulated equivalent plastic strain $\bar{\varepsilon}^p$. The micro-structure related coefficients can be also combined and simplified to improve user friendliness, especially when those parameters are not readily available from micro-structural investigation. Therefore, the modified Sachs hardening model based on Equation (17) becomes,

$$\overline{\sigma}_{NewSachs} = A_1(1-\chi)X_T + [A_2\chi X_T + A_3(1-X_T)](\bar{\varepsilon}^p + \varepsilon_0 - h\varepsilon_B)^n, \qquad (35)$$

where

χ indicates the fraction of the to-be-twinned grains that have already twinned, ranges from 0 to 1. It is defined as follows,

$$\chi = 1 - exp\left[-4(\frac{\bar{\varepsilon}^p - h\varepsilon_B}{\varepsilon_1})^a\right]. \tag{36}$$

X_T is the fraction of grains expected to be twinned based on Equation (19). ε_B is the historical accumulated plastic strain from the previous loading transitions, excluding the de-twinning process. By subtracting it from the total equivalent plastic strain $\bar{\varepsilon}^p$, the kinematic hardening behavior can be achieved under tension-compression loading and cross loadings.

h is an additional material coefficient attached to ε_B to control the isotropic hardening. h ranges from 0 (no kinematic hardening) to 1 (no isotropic hardening). For example, if $h = 1$, the stress-strain curve in sequential compression part would be exactly the same with the one under monotonic compression.

A_1, A_2, and A_3 are simplified material coefficients, which can be directly calibrated. If the micro-structural parameters are available they can be expressed as follows

$$A_1 = \frac{\tau_{0t}}{m_I}, \qquad A_2 = \xi\frac{k}{m_{II}^{n+1}}, \qquad A_3 = \frac{k}{m_{III}^{n+1}}, \tag{37}$$

The rest of material coefficients are identical in previous section. It is noted that ε_B always equals to zero under monotonic loading conditions. Therefore, it is ensured that the material coefficients calibrated by monotonic loading results (Jia & Bai, 2015b) are consistent. The kinematic hardening behavior during cross loading can be further compensated by an additional item $\bar{\sigma}_C$, defined as

$$\bar{\sigma}_C = -X_C^{\lambda}\sqrt{\boldsymbol{\alpha}^{dev}:\boldsymbol{\alpha}^{dev}}, \tag{38}$$

Here, X_C is the key state variable governing the smoothness in transition during cross loading, as discussed in section 4.3.1. It equals to zero under both monotonic loading and reversal loading.

This parameter also exclusively represents a decay function under cross loading, see Figure 27d. This provides an advantage to isolate the cross hardening from the rest kinematic hardening behavior. λ is an exponential material coefficient adjusting the decaying rate of X_C. The term of $\sqrt{\boldsymbol{\alpha}^{dev}:\boldsymbol{\alpha}^{dev}}$ dictates the magnitude during the cross hardening.

The effect of this item is illustrated in Figure 29b, comparing to a case without ε_B and $\bar{\sigma}_C$ in the example of 0° to 90° two-step uniaxial tension. Conclusively, the final constitutive model for magnesium AZ31B-H24 becomes

$$\bar{\sigma} = (\bar{\sigma}_{NewSachs} + \bar{\sigma}_K + \bar{\sigma}_C) f_{ext}(\eta, \bar{\theta}), \tag{39}$$

Together with the yield criterion, the governing equation is

$$\frac{f(\sigma_{ij})}{f(\boldsymbol{\sigma}_{UT})} - \bar{\sigma} = 0, \tag{40}$$

where $f(\sigma_{ij})$ is CPB06ex2 anisotropic yield criterion and $\boldsymbol{\sigma}_{UT}$ is a constant stress tensor defined as

$$\boldsymbol{\sigma}_{UT} = \begin{bmatrix} 1 & & \\ & 0 & \\ & & 0 \end{bmatrix}. \tag{41}$$

This is used to normalize the plane stress anisotropic yield criterion to the uniaxial tension condition, in order to assure the equivalent stress $\bar{\sigma}$ always equals to the first component of the stress tensor under uniaxial tension. Through this section, a fully decoupled plasticity model is established.

4.5 Alternative Interpretation to Twinning/De-twinning State Variables

Reminding of Equation (29),

$$\dot{\kappa} = \omega(\kappa + \kappa_0)[X_T(\eta) - \kappa]\dot{\bar{\varepsilon}}^p, \quad \kappa(0) = 0$$

The twinning/de-twinning effect can be well incorporated by applying the new added state variables κ and μ. However, the characteristic of this key state variable κ partially overlaps with the one of an existed function χ, from Equation (36),

$$\chi = 1 - exp\left[-4(\frac{\bar{\varepsilon}^p - h\varepsilon_B}{\varepsilon_1})^a\right]$$The differences between those two

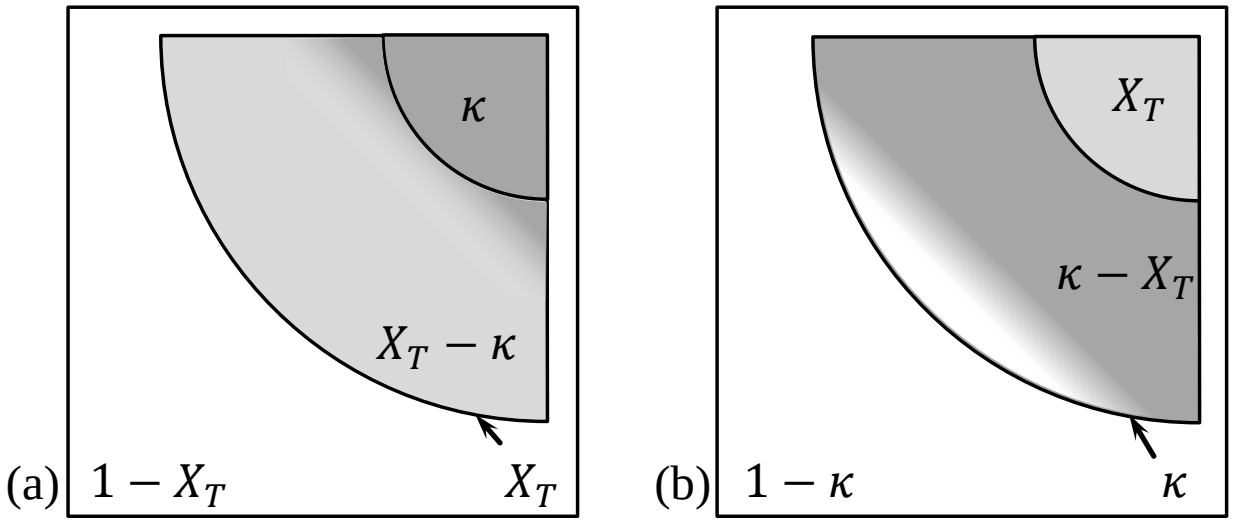

Figure 30 Schematic graph of a grain with the alternative interpretation under (a) twinning and (b) de-twinning. The gradient region indicates the growth/shrinkage of twinned area.

After the replacement, these three areas can then be expressed by: a) $X_T - \kappa$, b) κ, and c) $1 - \kappa$ under a twinning scenario. $X_T - \kappa$ is always larger or equal than zero because X_T is the saturated value of κ along twinning growth. On the other hand, the de-twinning effect can be incorporated into the main framework. Assume the evolution of twinning is completed ($\kappa = X_T$, $X_{TC} = X_T = \kappa > X_{TT}$), and the loading condition changes from compression to tension. The de-twinning effect takes place when X_T, the area that supposed to be twinned, shrinks into X_{TT}, which is much smaller than the current κ. Alternatively, a grain can now be divided into three other

different areas: a) $\kappa - X_T$, going to be de-twinned, in the area undergone twinning, b) X_T, remains twinned during de-twinning, and c) $1 - \kappa$, free of twinning/de-twinning. These areas can be schematically depicted in Figure 30.

4.6 Calibration Procedure

The new model includes six different modules to calibrate. The basic calibration sequences and procedures are described as follows.

1. Calibrate the CPB06ex2 anisotropic yield criterion $f(\sigma_{ij})$ using the data set of both plastic flow and strength, under different monotonic loading conditions and loading orientations. As for the strength part, the material strength difference is influenced by both orientation and loading condition. Commonly, these two factors are coupled together in the anisotropic yield criterion. In the current framework, the latter is decoupled by involving the function $f_{ext}(\eta, \bar{\theta})$ to further consider the loading condition effects. Therefore, the dependency on loading orientation is exclusively governed by the yield criterion. Experimental material strengths can then be normalized by their individual 0° (rolling direction) case under each loading condition.

2. Calibrate the first hardening item, $\bar{\sigma}_{NewSachs}$ for isotropic hardening using the experimental stress-strain curves under different monotonic loading conditions and along referential orientation (0°). If the expected twinning ratio in a grain under compression (X_{TC}) and under tension (X_{TT}) are not readily available from micro-structural investigation, a single unknown value of $X_T \in [0,1]$ rather than the entire function of Equation (19) can be substituted into Equation (35), where h is temporarily set to zero. X_T controls the convexity/concavity of the entire hardening curve. $X_T = 0$ indicates completed convex. The curve gradually grows into a

concave shape as X_T increases. The effects of X_T on different material coefficients in Equation (35) and (36) can be summarized as follows.

a) A_1 and ε_0 control the initial yield stress. A_1 dominates when X_T is closer to one, while ε_0 dominates when X_T is closer to zero.

b) A_2 controls the magnitude of the ultimate plateau when X_T is closer to one. It can also adjust the slope when X_T is closer to zero.

c) A_3 and n control the magnitude and curvature for the entire curve. A_3 exhibits less effect when X_T is closer to one.

d) a and ε_1 control the sigmoidal shape when X_T is closer to one.

If multiple experimental stress-strain curves (with different stress triaxialities) are available to be fitted, different values of isolated X_T can be firstly applied in order to obtain the rest of material coefficients. Secondly, the coefficients, X_{TT}, X_{TC}, C, and η_C in Equation (19) can be obtained by comparing different X_T values to the corresponding stress triaxiality η values. It is noted that only the curvatures should be correlated well in this step, because the magnitude of material strength under different loading conditions can be further adjusted by the function of $f_{ext}(\eta, \bar{\theta})$.

3. Calibrate the stress triaxiality and Lode angle dependency function $f_{ext}(\eta, \bar{\theta})$. Now the stress-strain curves can be generated by incorporating both the anisotropic yield criterion $f(\sigma_{ij})$ and $\bar{\sigma}_{NewSachs}$ under different loading conditions and orientations. Extract initial yield stresses or a set of stress points at any other single strain value from both analytical and experimental curves. Apply their stress triaxialities and Lode angle parameters in the function $f_{ext}(\eta, \bar{\theta})$ and multiply the extracted analytical stresses by the function. Adjust the material coefficients c_η, η_0, c_θ^s, c_θ^t, c_θ^c, and m to correlate them with the extracted experimental stress data. The calibration for

monotonic loading cases is completed through these three steps.

4. Calibrate the kinematic hardening item $\bar{\sigma}_K$ with related state variables. A set of stress-stra in curves from uniaxial compression-tension reversal loading are required, with different compre ssive pre-strains. Firstly, apply all related state variables, κ, μ, α_{ij}, ε_C and X_K, into the governing equation to generate a uniaxial compression-tension scenario. Secondly, adjust the material coeff icients to simultaneously fit the experimental curves under different pre-strains, however, with in dividual de-twinning rate Ω. The effects of different material coefficients in Equation(29), (30), a nd (34), are listed as follows.

a) A_{K1} controls the magnitude of the initial plateau in the sequential tensile part only.

b) A_{K2} controls the magnitude of both the initial and ultimate plateaus simultaneously.

c) Ω controls the evolution rate from the initial to the ultimate plateau in the sequential tensile part.

d) C_0 and ρ in the "dummy" back stress α_{ij} control the smoothness in the transition area.

e) ω and κ_0, even though don't explicitly influence the stress-strain curve, control the twinning rate in both the compressive and tensile loadings. It is noted that the current twinned ratio κ at the transition may possibly be smaller than X_{TT} (the expected twinning ratio in a grain) if the twinning rate is slow enough or the compressive pre-strain is very small. In this case, the de-twinning effect will not happen and the sigmoidal shape will not appear in the sequential tensile step. If this phenomenon is captured in the experimental results, it is important to adjust ω and κ_0 to correlate with the boundary pre-strain, between the occurrence and non-occurrence of the de-twinning effect in the sequential tensile part.

Thirdly, the coefficients Ω_1, Ω_2 and Ω_3 can be obtained by comparing different Ω values to the corresponding ε_C values in Equation (31). The last step is to determine the residual coefficient h in Equation (35) using an experimental stress-strain curve under uniaxial tension-compression reversal.

5. Calibrate the additional cross hardening item $\bar{\sigma}_C$. Cross loading experimental results are required to determine the last material coefficient λ. This type of test could be a two-step uniaxial tension, with different loading orientations. The detail of this test will be discussed in the experimental method section. The exponential coefficient λ is obtained by correlating the transition area in model-generated stress-strain curve to the experimental one.

6. Calibrate the eMMC anisotropic fracture model. The material coefficients are non-associated with the plasticity model. The details of this part will be discussed in the next chapter.

It can be seen that the calibration procedure has non-aftereffect property: the calibration for each step will not affect the calibration result(s) from the previous step(s). Therefore, the entire calibration could be performed straightforwardly within individually modules. A tool in the Excel spreadsheet with Microsoft Visual Basic codes was built to generate the analytical stress-strain curves and compare with the experimental ones, which helps to adjust model parameters to obtain the best curve fitting results for all loading conditions. The calibrated material coefficients for the new derived constitutive model are partially listed in Table 3, while the rest is already listed in Table 2. The calibrated model was then implemented into the FE simulation to reproduce all experimental results.

Table 3 New constitutive model coefficients for magnesium AZ31B-H24 sheets

ω	κ_0	Ω_1	Ω_2	Ω_3	$C_0\,(MPa)$	ρ	$A_{K1}\,(MPa)$	$A_{K2}\,(MPa)$	h	λ

71.00	0.015	550.7	47.40	70.37	9.500	975.6	240.0	260.0	1.000	4.500

4.7 Calibration Result

The predicted equivalent stress-strain curves for 0° under the following loading conditions, uniaxial tension/compression, pure shear, plane strain and through-thickness compression, were compared to the experimental curves in Figure 31. One can see that the asymmetrical characteristic between tension and compression was well modeled, and the unusual concave curves in both uniaxial and plane strain compression were well predicted.

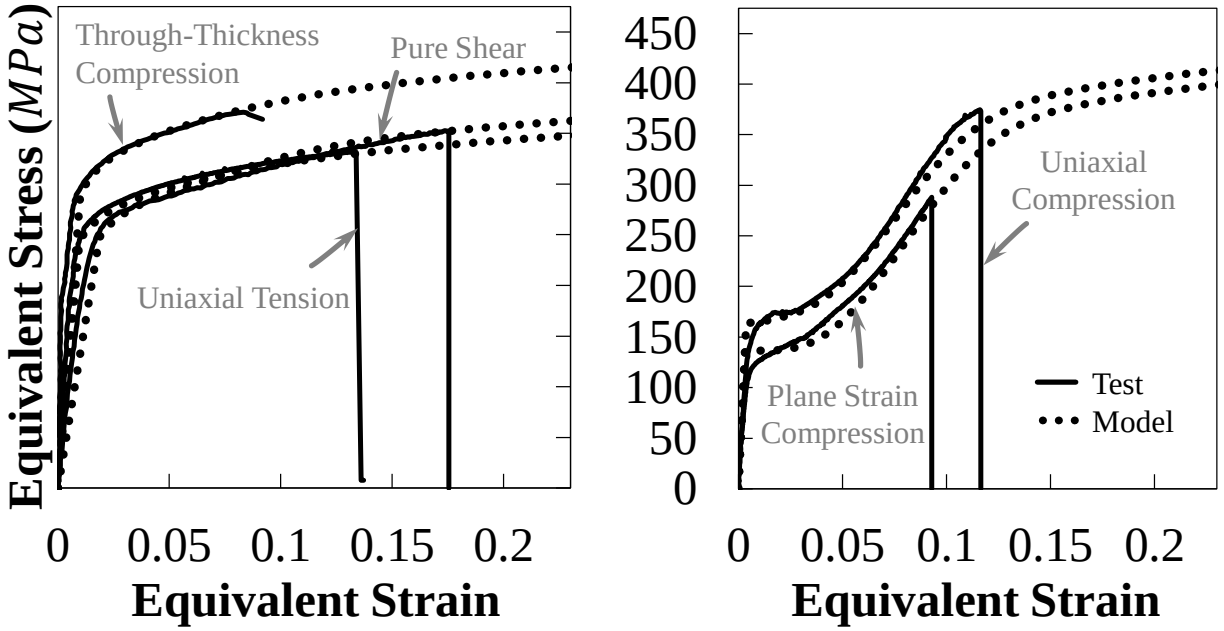

Figure 31 Comparison between predicted and experimental hardening curves among different loading conditions. The orientations are all 0°.

Figure 32 exhibits the anisotropic hardening behavior under those loading conditions along different orientations. An excellent correlation between tested and theoretical stress-strain curves can be observed for all the orientations. Figure 33 illustrates the calibration of plastic flow,

represented as the Φ angle under different loading conditions. Note that the hardening curves under notch tension cannot be obtained directly from the tests, however, the information of plastic flow can be measured by DIC and well calibrated. There are some errors in the plastic flow prediction for shear loading condition, whose Φ angles deviated with test measurements.

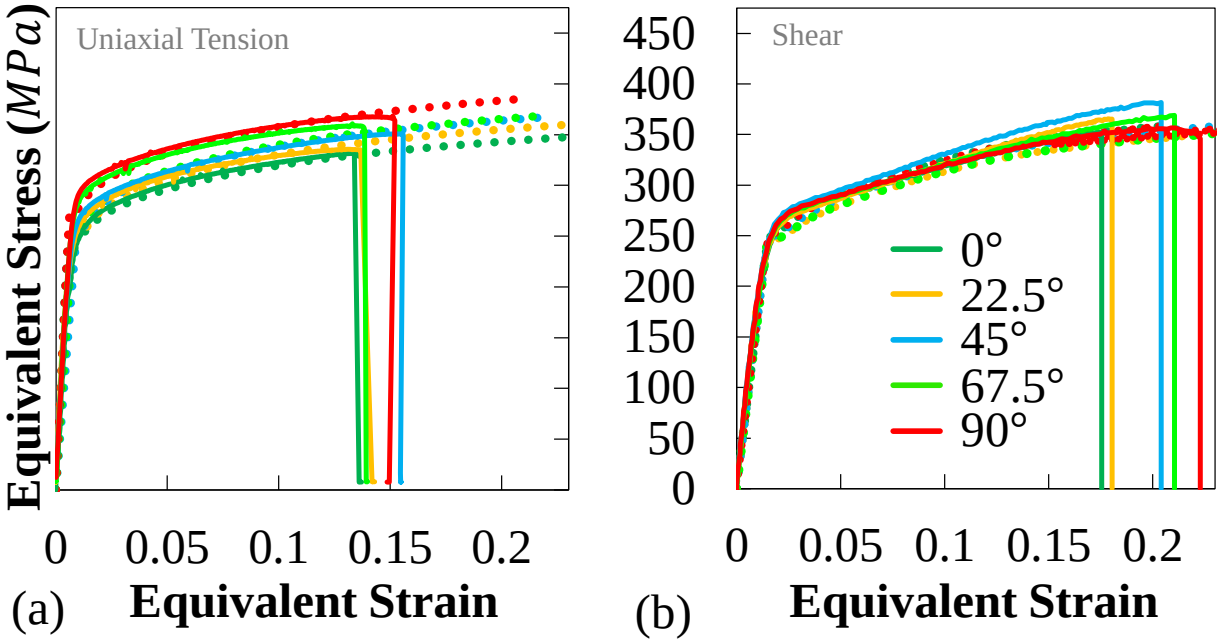

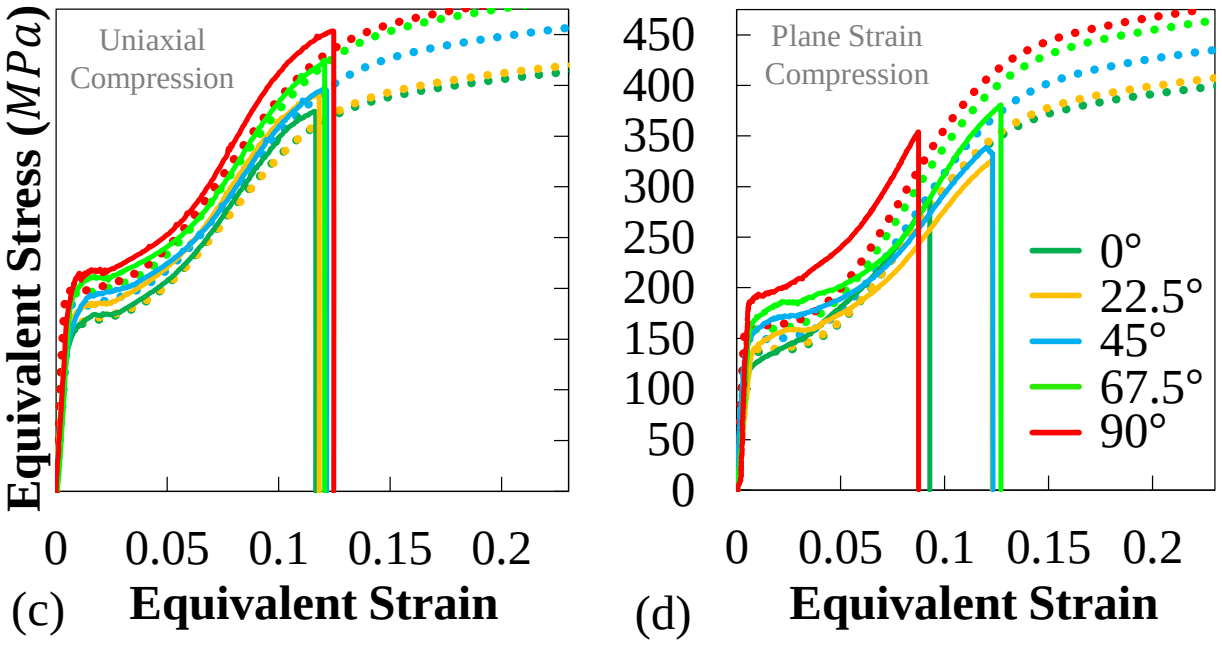

Figure 32 Comparison between predicted and experimental stress-strain curves, (a) uniaxial tension, (b) shear, (c) uniaxial compression, and (d) plane strain compression.

There are two possible reasons for this difference in shear, a) the actual specimen orientation could be rotated during the experiment which was not considered in theoretical solutions, and b) the real stress triaxiality in shear specimen could be slight different from the analytical solution, where $\eta = 0$ was applied. The predicted Φ angles could be much closer in the FE simulations where material orientation change and stress triaxiality are accurately calculated, which will be described in next chapter. The calibrated parameters of CPB06ex2 yield criterion and Sachs hardening rule were listed in Table 1, Table 2, and Table 3, respectively. The part of non-proportional loading cases is given together with the FE simulation results in the next chapter.

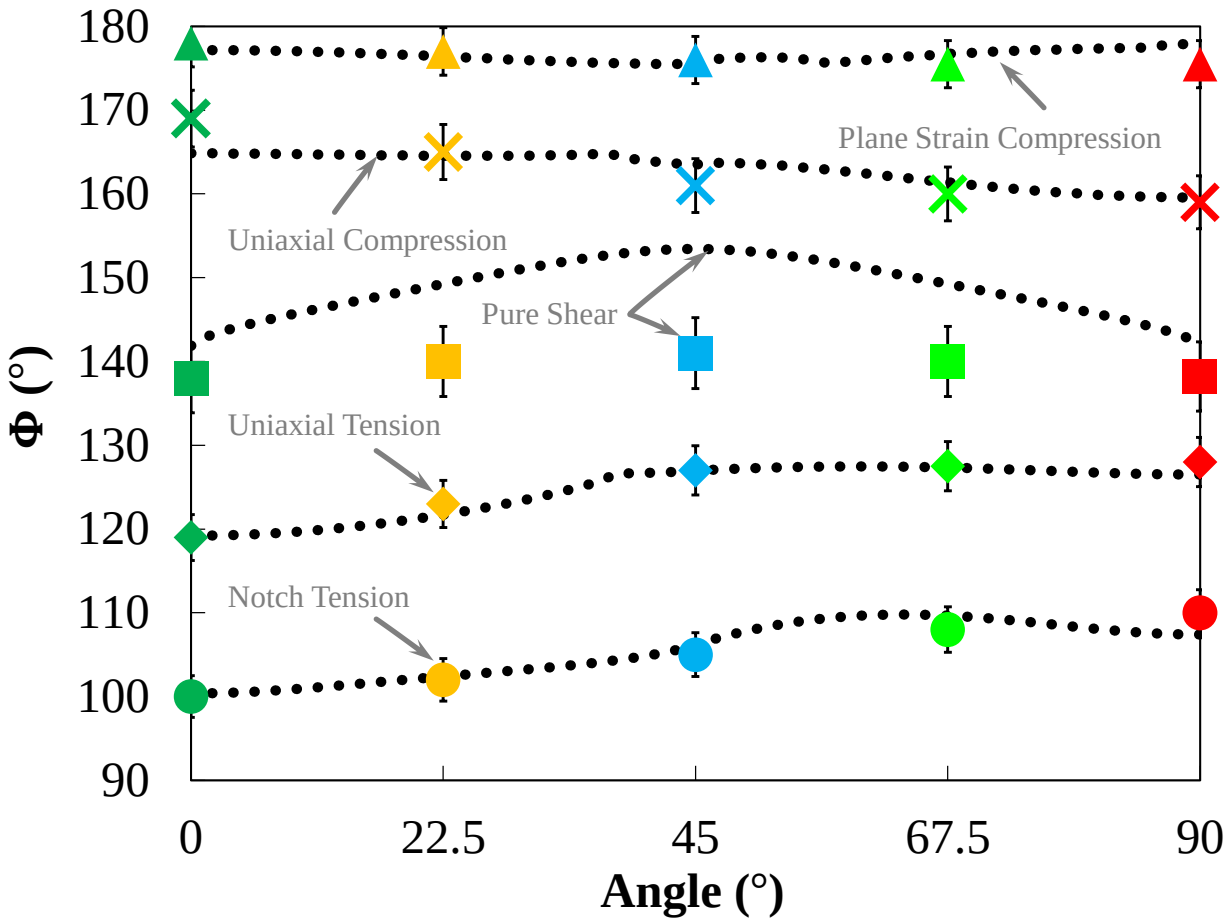

Figure 33 The calibration results for the plastic flow, represented in Φ angle, including uniaxial tension/compression, shear, plane strain compression, and notch tension.

CHAPTER 5 ALL STRAIN BASED ANISOTROPIC DUCTILE FRACTURE MODELING

5.1 Model Framework

The fracture locus of the original MMC fracture criterion based on the work of Bai and Wierzbicki (2010) reads

$$\overline{\varepsilon}_f(\eta,\overline{\theta}) = \left\{\frac{A}{C_2}\left[\tilde{C}_\theta^s + \frac{\sqrt{3}\left(C_\theta^{ax} - \tilde{C}_\theta^s\right)}{2-\sqrt{3}}\left(\sec\frac{\overline{\theta}\pi}{6} - 1\right)\right]\left[\sqrt{\frac{1+C_1^2}{3}}\cos\frac{\overline{\theta}\pi}{6} + C_1\left(\eta + \frac{1}{3}\sin\frac{\overline{\theta}\pi}{6}\right)\right]\right\}^{-\frac{1}{n}}, \quad (42)$$

where

$$C_\theta^{ax} = \begin{cases} 1 & \overline{\theta} \geq 0 \\ \tilde{C}_\theta^c & \overline{\theta} < 0 \end{cases}.$$

Here, η is the stress triaxiality; $\overline{\theta}$ is Lode angle parameter; A, n, C_1, C_2, $\tilde{C}_\theta^s$ and $\tilde{C}_\theta^c$ are the model parameters. The calibration is confined to the tensile loading condition because of the availability of the fracture strains. Due to the difficulty of direct measurement of stress triaxiality evolution (without FE simulations with an adequate plasticity model), the model was transformed into an all-strain based space by involving the stress ratio and the ratio of in-plane principal strain increments (Jia et al., 2013). The strain incremental ratio (α) and stress ratio (β) are defined as

$$\alpha = \frac{d\varepsilon_2}{d\varepsilon_1}, \quad \beta = \frac{\sigma_2}{\sigma_1}. \quad (43)$$

Assuming the Mises-Levy flow rule, it can be derived that

$$\alpha = \frac{d\varepsilon_2}{d\varepsilon_1} = \frac{\frac{\partial f}{\partial \sigma_2}}{\frac{\partial f}{\partial \sigma_1}} = \frac{2\sigma_2 - \sigma_1}{2\sigma_1 - \sigma_2} = \frac{2\beta - 1}{2 - \beta}, \quad (44)$$

where f is the von-Mises plastic potential function. It can be rewritten into

$$\beta = \frac{2\alpha + 1}{2 + \alpha}. \tag{45}$$

From the side of stress state, the three invariants of a stress tensor under plane stress condition are defined, respectively

$$p = -\sigma_m = -\frac{\sigma_1 + \sigma_2}{3}, \tag{46}$$

$$q = \bar{\sigma} = \sqrt{\sigma_1^2 + \sigma_2^2 - \sigma_1\sigma_2}, \tag{47}$$

$$r = \left(\frac{27}{2}\det \boldsymbol{S}\right)^{\frac{1}{3}} = \left[\frac{27}{2}(\sigma_1 - \sigma_m)(\sigma_2 - \sigma_m)(-\sigma_m)\right]^{\frac{1}{3}}$$

$$= \left(\sigma_1^3 - \frac{3}{2}\sigma_1^2\sigma_2 - \frac{3}{2}\sigma_2^2\sigma_1 + \sigma_2^3\right)^{\frac{1}{3}}, \tag{48}$$

where σ_m is the mean stress, $\bar{\sigma}$ is the equivalent stress, $\boldsymbol{S} = \boldsymbol{\sigma} - p\boldsymbol{I}$ is the deviatoric stress tensor, σ_1 and σ_2 denote the in-plane principal stresses. Using the definition of the stress triaxiality under plane stress condition, from Equation (2),

$$\eta = \frac{\sigma_m}{\bar{\sigma}} = \frac{\sigma_1 + \sigma_2}{3\sqrt{\sigma_1^2 + \sigma_2^2 - \sigma_1\sigma_2}}$$

Note the relationship between η and β is, using the definition of stress ratio β,

$$\eta = \frac{\sigma_1 + \sigma_2}{3\sqrt{\sigma_1^2 + \sigma_2^2 - \sigma_1\sigma_2}} = \frac{\beta + 1}{3\sqrt{\beta^2 - \beta + 1}}. \tag{49}$$

Another important stress state related variable, the Lode angle parameter $\overline{\theta}$ is originally defined as

$$\overline{\theta} = 1 - \frac{2}{\pi}\arccos\left(\frac{r}{q}\right)^3. \tag{50}$$

It can be rewritten as, under plane stress condition, recalling Equation (22)

$$\begin{aligned}\overline{\theta} &= 1 - \frac{2}{\pi} arccos\left[-\frac{27}{2}\eta\left(\eta^2 - \frac{1}{3}\right)\right] \\ &= 1 - \frac{2}{\pi}\arccos\left[\frac{\sigma_1^3 - \frac{3}{2}\sigma_1^2\sigma_2 - \frac{3}{2}\sigma_2^2\sigma_1 + \sigma_2^3}{(\sigma_1^2 + \sigma_2^2 - \sigma_1\sigma_2)^{\frac{3}{2}}}\right] \\ &= 1 - \frac{2}{\pi}\arccos\left[\frac{\beta^3 - \frac{3}{2}\beta^2 - \frac{3}{2}\beta + 1}{(\beta^2 - \beta + 1)^{\frac{3}{2}}}\right].\end{aligned} \tag{51}$$

Therefore, both the stress triaxiality and the Lode angle parameter, which are two independent variables in the original 3D MMC fracture model, can be expressed as a function of the stress ratio only, under the plane stress condition. Using the relationship between strain ratio and stress ratio from Equation (45), the fracture strain $\overline{\varepsilon}_f$ is hence expressed as a function of strain ratio (α) only, which can be directly measured by a DIC system. However, the strain ratio (α) could not distinguish different loading conditions between tensile dominated and compression dominated loadings. For example, it gives the same values for both equi-biaxial tension and equi-biaxial compression. In this manner, the parameter Φ can also be used here, based on Equation (4),

$$\Phi = \frac{180°}{\pi} atan2\left(-\dot{\varepsilon}_2^p, \dot{\varepsilon}_1^p\right) + 90°$$

where $atan2$ is the two arguments arctangent function with sign information included. The analogical equation in stress field can be used to calculate the Lode angle (Bai & Atkins, 2012). Φ denotes the angle to the positive minor strain direction in the forming fracture limit diagram (FFLD) under proportional loading, illustrated in Figure 4. The effect of strain/stress state on

ductility is thus measured quantitatively by the angle offset to the specified loadings under the assumption of isotropic J2 plasticity, which are 45° for equi-biaxial tension, 90° for plain strain tension, 116° for uniaxial tension, 135° for pure shear and 153° for uniaxial compression etc.

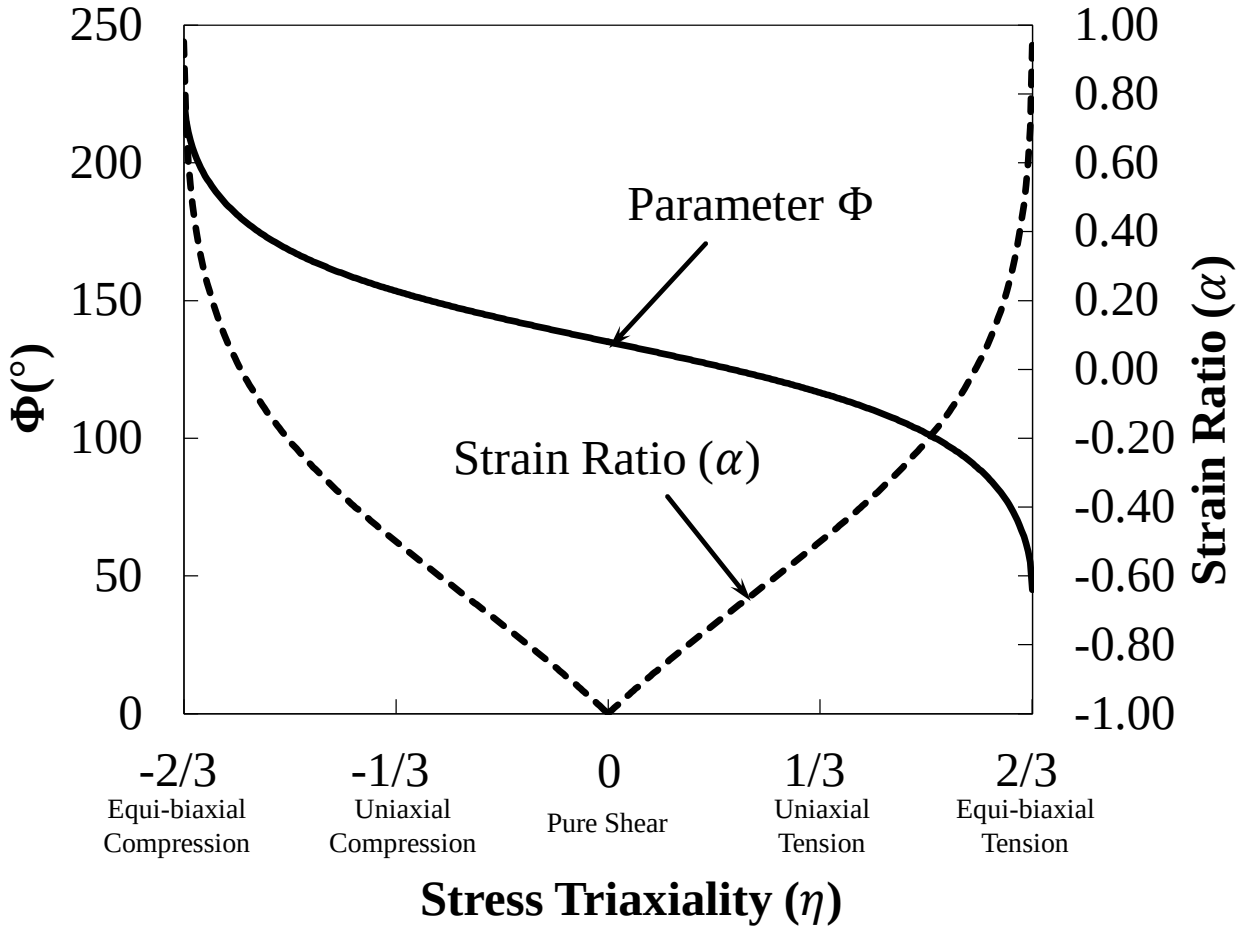

Figure 34 The relationship among stress triaxiality (η), strain ratio (α), and the new parameter Φ. An one-to-one mapping is illustrated from the stress triaxiality to Φ.

One big advantage of the all-strain based fracture model is that it can be used to study fracture while bypassing plasticity. The definition of Φ under tensile loading condition is shown as follow,

$$\Phi = \frac{180^\circ}{\pi} atan2(-\dot{\varepsilon}_2^p, \dot{\varepsilon}_1^p) + 90^\circ = \frac{360^\circ}{\pi} arctan \frac{-\dot{\varepsilon}_2^p}{\sqrt{(\dot{\varepsilon}_2^p)^2 + (\dot{\varepsilon}_1^p)^2} + \dot{\varepsilon}_1^p} + 90^\circ$$

$$= \frac{360^\circ}{\pi} arctan \frac{-\alpha}{\sqrt{1+\alpha^2} + 1} + 90^\circ. \quad (52)$$

Using Equation (52), an one-to-one mapping can be then obtained from the stress triaxiality to the space of Φ. The relationship among η, α and Φ is sketched in Figure 34, under both tensile ($\eta > 0$) and compressive ($\eta < 0$) parts. One can see that it could confuse the loading condition between tension and compression using the strain ratio (α), where there are two values of stress triaxiality (η) corresponding to one α. However, for any given loading condition (expressed by stress triaxiality), there is only a single value of Φ to represent. The fracture strain ($\overline{\varepsilon}_f$) is therefore expressed as a function of Φ only, by Equations (42) to (52), which becomes an all-strain based fracture locus. Furthermore, in order to describe the anisotropic fracture accurately, a non-conjugated anisotropic equivalent plastic strain function was introduced by applying a linear transformation to the strain tensor (Luo, Dunand, & Mohr, 2012). In the present work, the anisotropic equivalent plastic strain is defined as

$$\tilde{\varepsilon}_p = \sqrt{\frac{2}{3}(\boldsymbol{\beta}\boldsymbol{\varepsilon}^p : \boldsymbol{\beta}\boldsymbol{\varepsilon}^p)}, \quad (53)$$

where $\boldsymbol{\varepsilon}^p$ indicates the plastic strain vector under plane stress condition $\boldsymbol{\varepsilon}^p = \{\varepsilon_{11}^p, \varepsilon_{22}^p, \varepsilon_{33}^p, \varepsilon_{12}^p\}$. $\boldsymbol{\beta}$ is a positive semi-definite matrix which characterizes the linear transformation of the strain vector, reads

$$\boldsymbol{\beta} = \begin{bmatrix} \beta_{11} & 0 & 0 & 0 \\ 0 & \beta_{22} & 0 & 0 \\ 0 & 0 & \beta_{33} & 0 \\ 0 & 0 & 0 & \beta_{44} \end{bmatrix}, \tag{54}$$

where β_{11}, β_{22}, β_{33}, and β_{44} are four anisotropic fracture coefficients. Now the new fracture model reads

$$\tilde{\varepsilon}_p \leq \overline{\varepsilon}_f\left(\eta, \overline{\theta}\right) = \hat{\varepsilon}_f(\alpha) = \tilde{\varepsilon}_f(\Phi). \tag{55}$$

Experimental data should be rotated back into the sheet rolling orientation for comparison. Then, coefficients of both fracture locus and the anisotropic equivalent strain can be calibrated.

5.2 Non-Association with Plasticity

Typically the material fracture model is expressed by the stress state variables, including pressure, stress triaxiality, Lode angle parameter, and critical failure stress, etc.. For example, the original Mohr-Coulumb model can be described as, in space of stress triaxiality and Lode angle parameter by Bai and Wierzbicki (2010)

$$\bar{\sigma}_f\left(\eta, \overline{\theta}\right) = C_2\left[\sqrt{\frac{1+C_1^2}{3}}cos\frac{\overline{\theta}\pi}{6} + C_1\left(\eta + \frac{1}{3}sin\frac{\overline{\theta}\pi}{6}\right)\right]^{-1}, \tag{56}$$

where C_1, C_2 are material coefficients, same with the ones in MMC model, and $\bar{\sigma}_f$ is the fracture stress. In fact, one can see that the expression is identical with part of the MMC model in Equation (42). This is because the MMC model was derived by applying a "dummy" hardening law in Equation (56) to transform the critical failure stress into fracture strain. The transformation is necessary in the metal forming application, due to easier measurement of equivalent strain than stress. This "dummy" hardening law also assisted to generalize the

capacity of fracture model under different loading conditions, based on its dependency of both stress triaxiality and Lode angle parameter (Bai & Wierzbicki, 2008b). It reads

$$\bar{\sigma} = A\bar{\varepsilon}^n \left[\tilde{C}_\theta^s + \frac{\sqrt{3}(C_\theta^{ax} - \tilde{C}_\theta^s)}{2-\sqrt{3}}\left(sec\frac{\overline{\theta}\pi}{6} - 1\right)\right], \tag{57}$$

where A, n, $\tilde{C}_\theta^s$, and C_θ^{ax} are material coefficients. Substituting Equation (57) into (56) with solving out the equivalent strain, the MMC model from Equation (42) can be obtained to govern the material fracture behavior. The material plasticity could be coupled with the current fracture model by applying the actual hardening model. However, this will either a) reduce the capacity and flexibility in fracture prediction by using a simpler hardening model (for example, Swift model for TRIP780, with no dependency on different loading conditions), or b) increase the model complexity and instability, especially when the anisotropic plasticity involved (for example, modified Sachs model for magnesium alloy could involve nine more material coefficients, and it would be unobtainable for an explicit expression of equivalent strain like Equation (42) due to its form). The further investigation of their relationship could lead into another topic. Therefore, the actual plasticity model applied in the FE analysis is not required to be the same with Equation (57). Also the material coefficients do not have to be the same even though the same model was applied. Both the stress triaxiality and Lode angle parameter in the original MMC model were transferred into a function of strain angle Φ. Due to the same reason, a J2 plasticity was applied in Equation (44) rather than applying the actual yield criterion (for example CPB06ex2 for AZ31B-H24). This made the stress triaxiality η and Lode angle parameter $\bar{\theta}$ become "dummy" in the equations after applying Equation (44), including the final derived eMMC model. In this way, η and $\bar{\theta}$ are still stress state variables but not representing the actual stress triaxiality and Lode angle parameter in eMMC model if the yield criterion was not

J2. They can be considered as intermediated variables connecting the strain angle Φ to the stress states. Therefore, the fracture model is completely de-coupled with the plasticity or stress states. The eMMC fracture model could be single-handedly calibrated by using a series of ultimate fracture points or strain histories. It should be emphasized that the stress triaxiality and Lode angle parameter are "dummy" only when Equation (44) was applied.

5.3 Calibration Results for Magnesium AZ31B

Figure 35 illustrates the modeled fracture locus by eMMC, with an applied linear transformation. Concerning the asymmetrical characteristic between tension and compression dominated regions in fracture, two separate groups of fracture parameters were calibrated, one for tension dominated and one for compression dominated regions, respectively. A joint point between both fracture loci was extracted as a critical Φ angle to identify the domination of tension or compression, which was located at $\Phi_C = 129°$ approximately for this material. Note that some of the calibration for the compressive half was based on the safe points, which are actually located below the real fracture limits. This was because the latter cannot be directly obtained from tests in the current study. The set of calibrated fracture parameters is listed in Table 4.

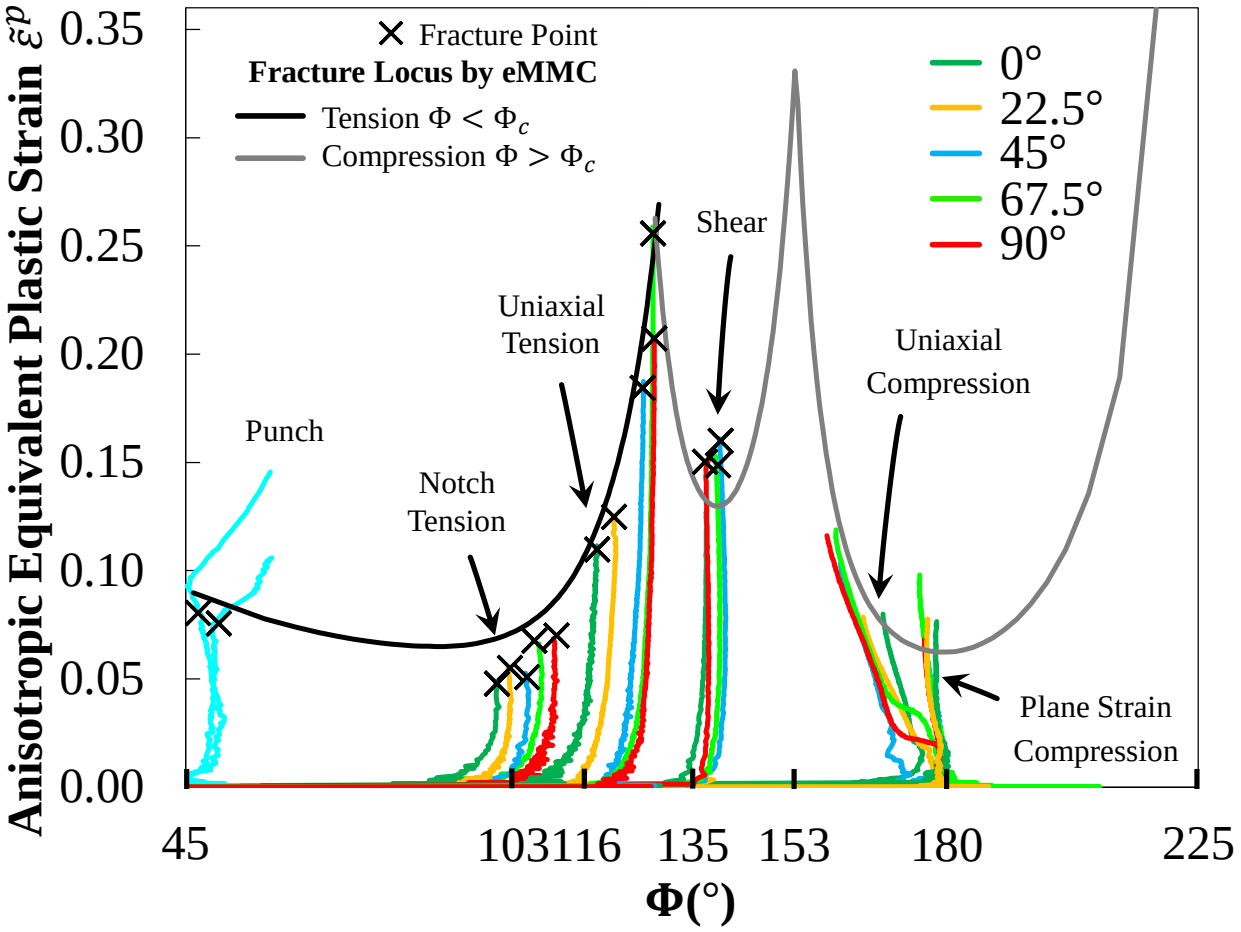

Figure 35 The fracture locus based on eMMC fracture model, with anisotropic equivalent strain.

Specifically for this material, an additional assumption is made to incorporate the twinning/de-twinning effect, which improves the accuracy of fracture prediction under reversal loading, as follows. The damage accumulation is temporarily deactivated, between the initialization and 90% completion of de-twinning. Therefore, the damage accumulation rule is expressed by

$$dD = \begin{cases} 0 & \mu \in (0.1,1) \\ \dfrac{d\tilde{\varepsilon}_p}{\tilde{\varepsilon}_f(\Phi)} & \mu \in [0,0.1], \mu = 1 \end{cases} \tag{58}$$

Here, $\tilde{\varepsilon}_f(\Phi)$ is the anisotropic fracture limit calculated for eMMC model and $\tilde{\varepsilon}_p$ is the anisotropic equivalent plastic strain.

Table 4 Anisotropic all-strain based MMC coefficients for magnesium AZ31B-H24 sheet

	Φ Angle	
	$\leq \Phi_C$	$> \Phi_C$
A	$409.7MPa$	
n	0.1560	
C_1	0.4150	-0.1410
C_2	$217.6MPa$	
$\tilde{C}_\theta^s$	0.9408	1.2321
$\tilde{C}_\theta^c$	1.0300	1.0940
β_{11}	1.0320	
β_{22}	0.5050	
β_{33}	0.5870	
β_{44}	1.0540	

CHAPTER 6 NUMERICAL SIMULATION

The eMMC with plasticity models have been implemented into Abaqus/Explicit as a user subroutine (VUMAT), to perform FE analysis and reproduce both the material strength and plastic strain history. All elements applied were four-node shell elements with reduced integration points (S4R). Five Simpson integration points through the thickness of all shell elements were used to obtain reliable results, especially for simulating punch test with large out-plane bending deformation. The fracture initiation and crack propagation were simulated by deleting elements when the damage accumulation D reached a given critical value D_C.

6.1 FE Model Description

6.1.1 Monotonic Cases

Six types of monotonic loading conditions, including uniaxial tension, notch tension, uniaxial compression, plane strain compression, shear and punch test, were performed in FE simulation for magnesium AZ31B-H24 alloy sheet. All thicknesses were set as $2mm$. Five different orientations, $0°$, $22.5°$, $45°$, $67.5°$, and $90°$ were assigned for all models except for punch test, where a single orientation was assigned. The configurations were the same as the tested specimens. The modeled specimens are shown in Figure 36, with different gauge lengths marked. The total reaction forces were outputted and converted to true stress if needed. Either displacement or true strain between two gauge points was extracted from simulations for a direct comparison with test results. The fracture initiation area was picked to extract the entire strain histories up to failure, for all six types of tests.

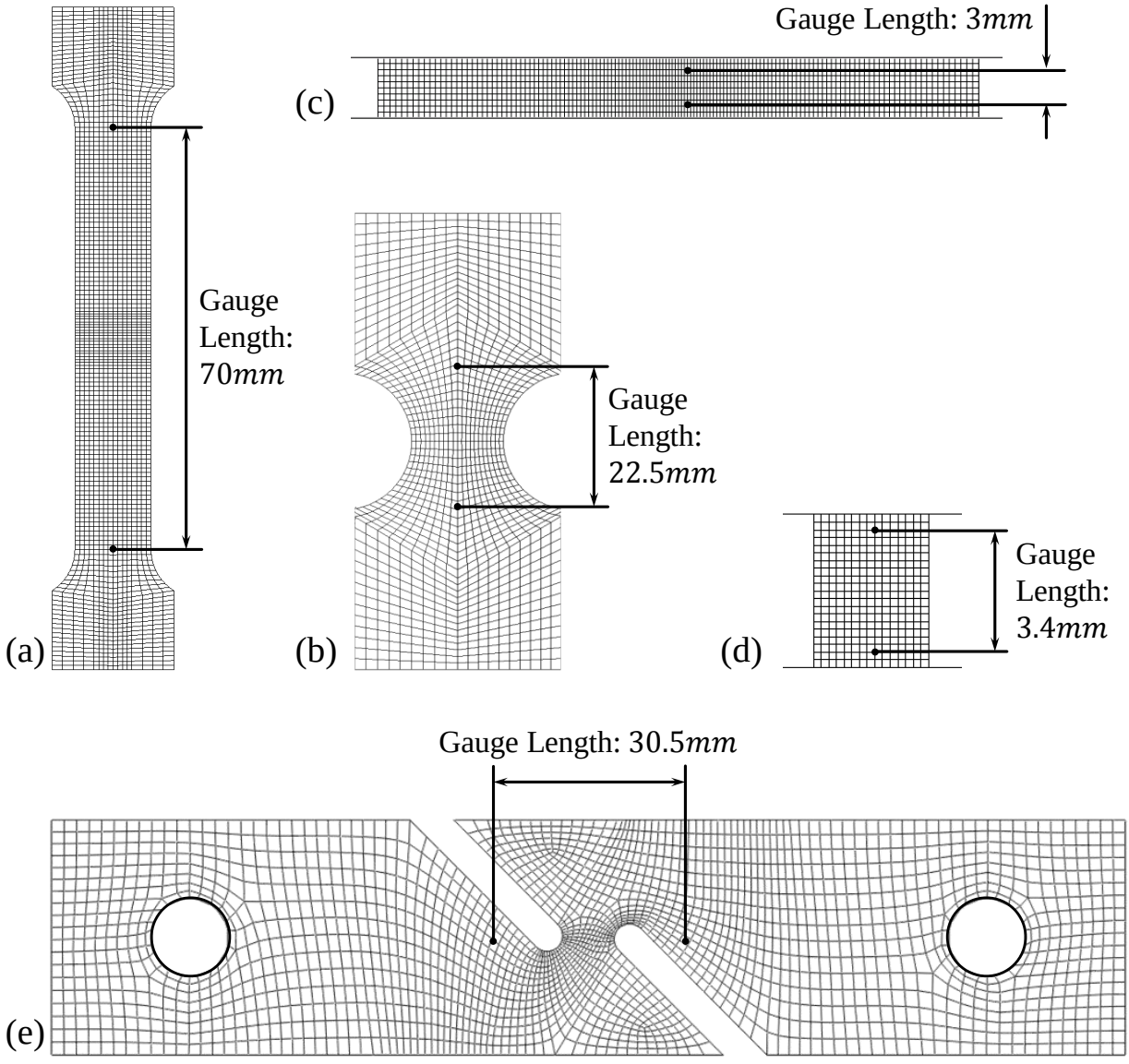

Figure 36 FE meshes for AZ31B-H24 under (a) uniaxial tension, (b) notch tension, (c) plane strain compression, (d) uniaxial compression, and (e) shear.

The experimental measurements were all from DIC. To be identical with experimental scenarios, rigid bodies were added in some of models, together with necessary penalty contact properties and friction coefficients. The details are described as follows:

1. In the models of both uniaxial compression and plane strain compression, two rigid plates

were added at both ends of the specimen, which carried the compressive load. A friction coefficient of 0.1 was set between the specimen and the rigid plate at both ends. This was because a) fracture initiated at the edge in the experiment, which indicated certain friction effect, and b) no apparent barrel effect was observed in the test, which indicated the friction effect was not very large.

2. In the model of shear test, there were two $12.7mm$ pins modeled as discrete rigid bodies at both ends to carry the load. A friction coefficient of 0.05 was set between the pin and the specimen, to be consistent with the punch test configuration.

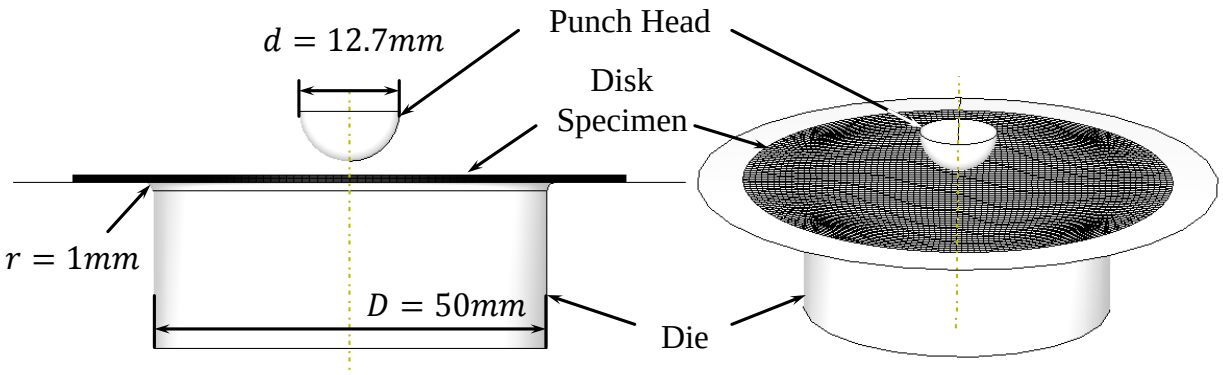

Figure 37 Side (left) and isometric (right) views of the FE punch model for AZ31B-H24.

3. The punch and die were modeled as analytical rigid bodies. The punch had a half-sphere head with a diameter of $d = 12.7mm$ while the die had a radius of $r = 1mm$ with its cavity having a diameter of $D = 50mm$. The external edge of the punch disk was fixed because the disk was fasten by several bolts in the real test. It was also recognized that the friction coefficient had no apparent effect on the final results ranged from 0 to 0.2, therefore a friction coefficient of 0.05 was set for the contact property. The penalty contact with the friction coefficient was defined between a) top surface of the disk specimen and the punch head, and b) bottom surface of the disk specimen and the die. The punch test model for

magnesium alloy sheet is shown in Figure 37.

The following calibrated constitutive models were applied in FE analysis, including CPB06ex2 anisotropic yield criterion, modified Sachs hardening model, and eMMC fracture model, as mentioned in previous sections.

Usually a cutoff region is associated with fracture model, when the analytically calculated fracture strain becomes infinity under a specific strain/stress status. It could be expressed as a limit of stress triaxiality, which means that the fracture behavior is suppressed when the stress triaxiality exceeds the limit. This limit is determined by experience or a function of Lode angle parameter (Bai & Wierzbicki, 2015).

Special cutoff stress triaxiality was applied to the eMMC model in the case of AZ31B-H24, which was not typically a single limit but a range. The fracture behavior was suppressed when the stress triaxiality $\eta \in (-0.577, -0.45)$. The first end of limit range, $\eta = -0.45$, was set for restricting the damage accumulation in uniaxial compression simulation. It was observed that a loading condition closed to plane strain compression ($\eta \leq -0.45$) occurred in the center of both ends of the specimen due to friction effect. The fracture strain is gradually smaller when the loading condition approaches plane strain compression, based on the tested strain histories. It would then cause an early fracture initiation in that center area, failing to capture the tested termination point in the true stress-strain curve. Therefore, this limit was added to assure the damage accumulate critically at the corners, leading the edge crack type failure with well-correlated stress-strain response. On the other hand, the fracture behavior under plane strain compression would be affected if the other end of limit was not set. The deformation for this wide specimen is actually concentrated on the middle, where the stress triaxiality is even smaller

than -0.577. The damage accumulation around the edge is weaker than the one under uniaxial compression due to its large width. Hence the entire specimen could endure more deformation until the edge crack initiated, resulting in a much larger fracture displacement than tested one. Therefore, the cutoff region should be deactivated when stress triaxiality smaller than -0.577, in order to initiate the fracture in the middle area. This would help correlate with the experimental fracture displacement.

It should be noted that shell element (S4R) was applied for both uniaxial compression and plane strain compression, which assumed a plane stress condition. This was because of the consistency of the application of plane stress based anisotropic yield criterion and eMMC model. In fact, this condition might not be the best way to simulate both of the compression tests because the size of thickness was similar with the other two dimensions. For uniaxial compression, the width was $3mm$ and the length along compressive direction is only $4mm$. For plane strain compression the length along compressive direction was $4mm$ as well. Since the thickness was $2mm$, the friction effect could be similarly intensive for both thickness and width direction. An out-of-plane stress could then possibly be exerted along the thickness direction, which made the real stress triaxiality even smaller. More importantly, a slant fracture surface was observed for both of the compression tests, which was generated along the thickness direction. This is not able to be reproduced by using shell element in FE simulation because of unavailable through-thickness geometry. Due to the same reason, the plastic flow under uniaxial compression, where Φ was changing all the time, could not be simulated neither. These features could be incorporated by applying 3D element (C3D8R) with related constitutive models in the future research. Currently the eMMC model is still focusing on plane stress condition due to its wide application in sheet

material. And the force-displacement and fracture point could correlate well with experimental results under these compressive loading conditions.

6.1.2 Non-proportional Cases

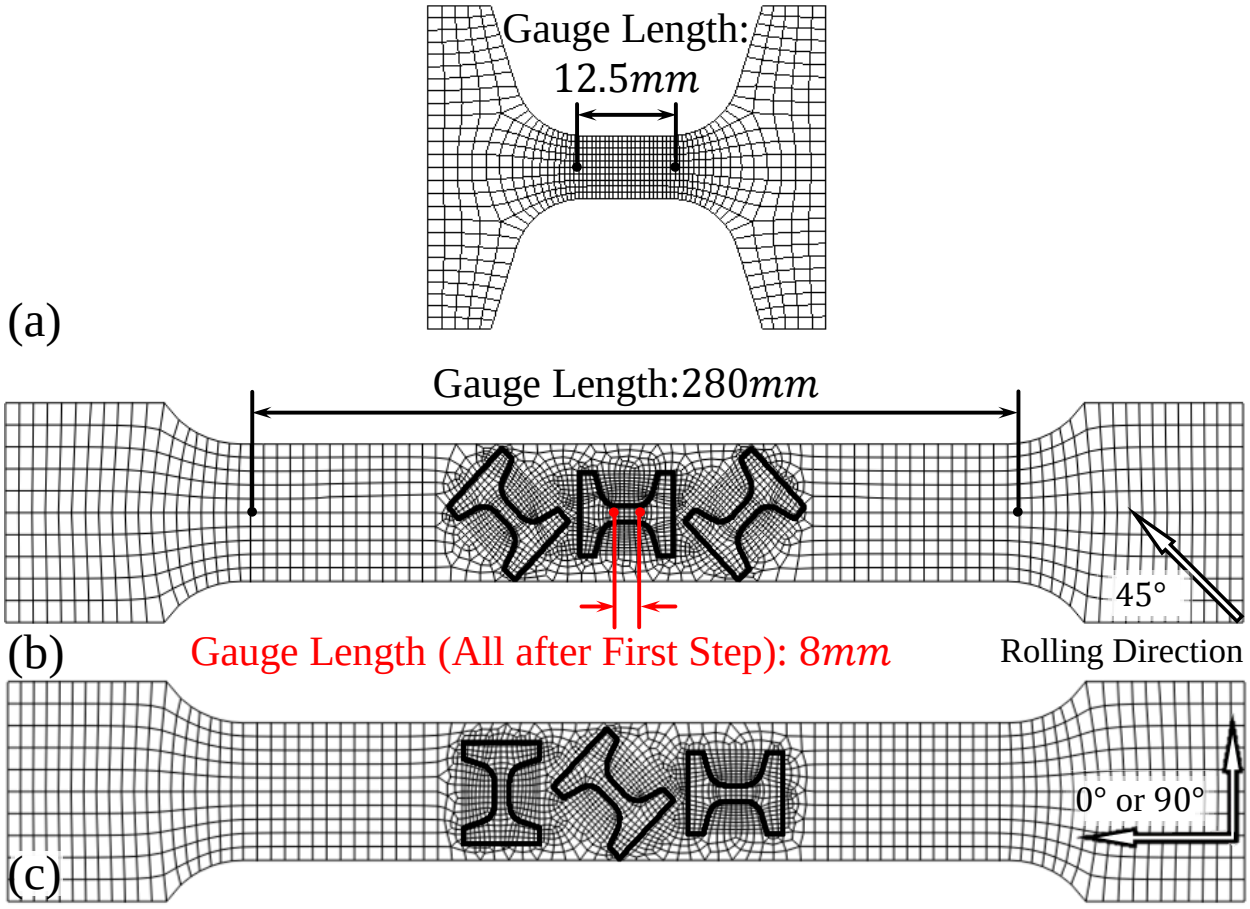

Figure 38 FE meshed different dogbone specimens, under (a) compression-tension reversal loading, (b), and (c) two-step uniaxial tension along 45° and 0°/90° orientation, respectively. Three small scaled dogbone specimens are re-orientated and adjusted to 0°, 45° and 90° respectively for the second step load.

Two types of non-proportional loading conditions, including uniaxial reversal compression-tension and two-step uniaxial tension test were simulated in Abaqus/Explicit. The thickness for reversal loading test specimen was set as $2mm$ while the one for two-step tension was set as

$1mm$. Three different orientations, 0°, 45°, and 90° were assigned for both models. The mesh configurations were the same as the tested specimens.

The meshed specimens are shown in Figure 38, with gauge lengths marked. Multiple solver steps were applied for the two-step uniaxial tension tests, including first-step loading, first-step unloading, and second-step loading up to fracture. A special technique was used to simulate the second step tension: all elements in the large dogbone specimen were configured to be deleted at the end of the unloading step, except the ones for the three small-scaled dogbone. The small-scaled dogbone specimens were then loaded up to fracture in the second step along their new orientations, with all state variables and equivalent plastic strains reserved from the first step uniaxial tension. The geometric boundaries for three small-scaled dogbone specimens were specified in the large-scaled dogbone specimen to be meshed with finer elements, as shown in Figure 38. It is noted that the geometries for small-scaled dogbone specimens should be anti-deformed to compensate the deformation during the first step uniaxial tension. Let ε_{1t}^{p} and ε_{2t}^{p} be the major and minor in-plane plastic pre-strain in the first step, where ε_{1t}^{p} is known by the experimental configuration. Using an associated plastic flow rule under proportional loading, a strain ratio can be obtained by

$$\alpha = \frac{\varepsilon_{2t}^{p}}{\varepsilon_{1t}^{p}} = \frac{d\varepsilon_{2t}^{p}}{d\varepsilon_{1t}^{p}} = \frac{\dfrac{\partial f}{\partial \sigma_2}}{\dfrac{\partial f}{\partial \sigma_1}}, \tag{59}$$

where f is the calibrated CPB06ex2 anisotropic yield criterion. The strain ratio is dependent on orientation due to anisotropy. Therefore, a deformation gradient can be expressed in the in-plane 2D space, as follows

$$\boldsymbol{F} = \begin{bmatrix} 1+\varepsilon_{1t} & \\ & 1+\varepsilon_{2t} \end{bmatrix} = \begin{bmatrix} 1+\varepsilon_{1t} & \\ & 1+\alpha\varepsilon_{1t} \end{bmatrix}. \quad (60)$$

Let $d\boldsymbol{x}$ be a vector indicating the geometry of the small-scaled dogbone specimen after first-step deformation, and $d\boldsymbol{X}$ be the vector indicating the original geometry. Now if the normal geometry is supposed to be obtained after deformation, the anti-deformed geometry can then be yielded by

$$d\boldsymbol{X} = \boldsymbol{F}^{-1} d\boldsymbol{x}, \quad (61)$$

The difference between the normal and the original anti-deformed geometries is depicted in Figure 39.

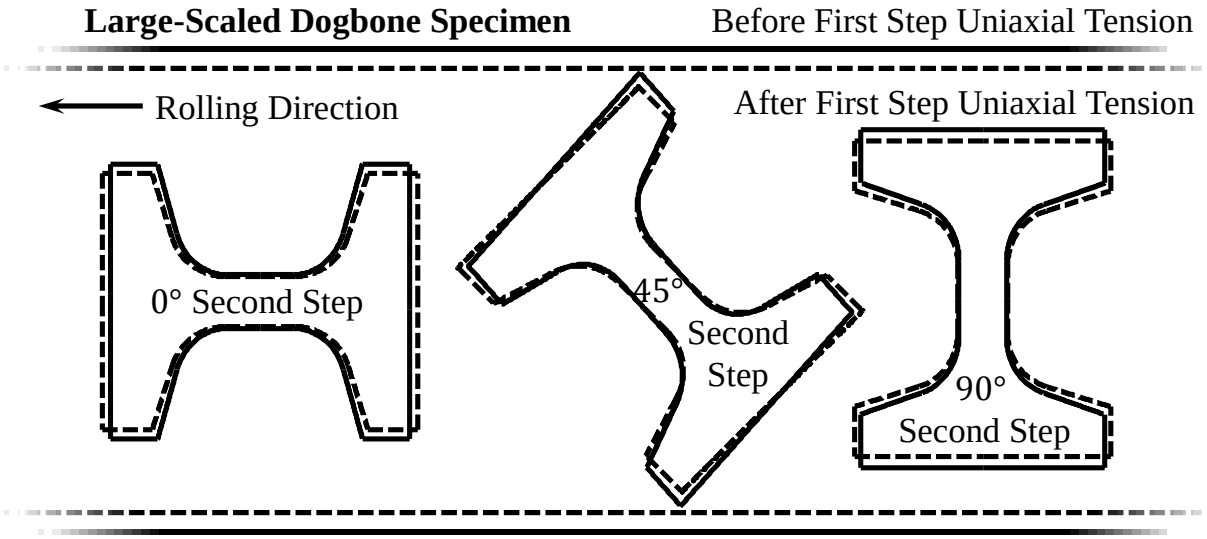

Figure 39 Pre-deformed geometries for small-scaled dogbone specimens along 0°, 45° and 90° orientation, respectively. Solid curves are before tension, and dash curves are after the first step tension.

The experimental scenarios under two-step uniaxial tension tests can be well correlated. The true stress and true strain were obtained from the total reaction force and displacement extracted between the gauge length, respectively. The simulated results were then compared to the experimental ones, which were all from DIC.

6.2 Simulation Results

6.2.1 Monotonic Cases

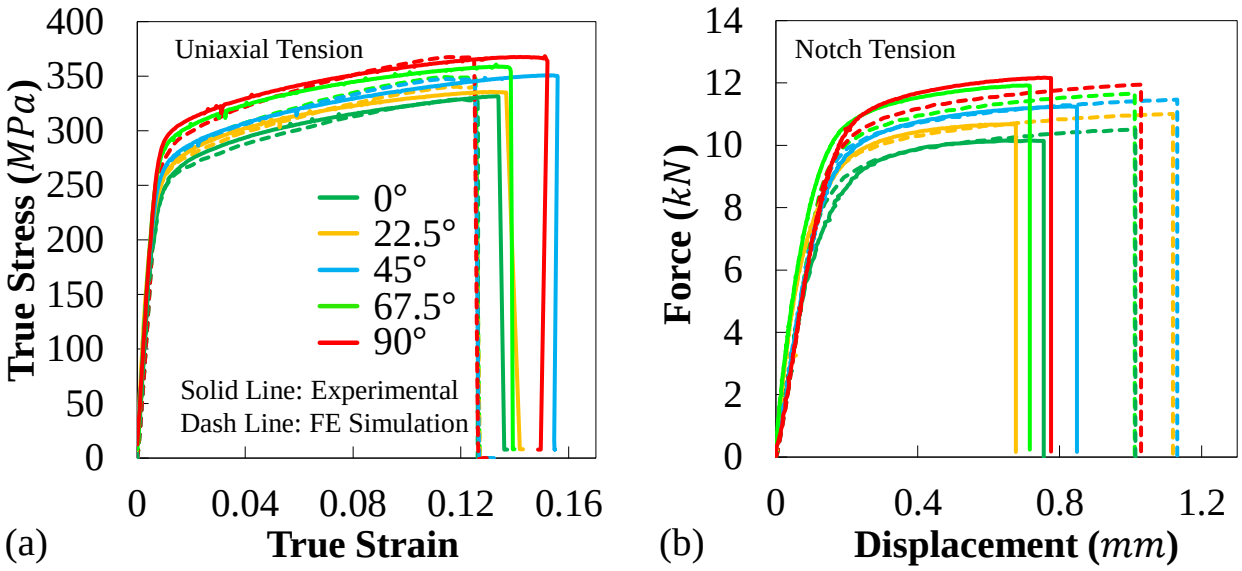

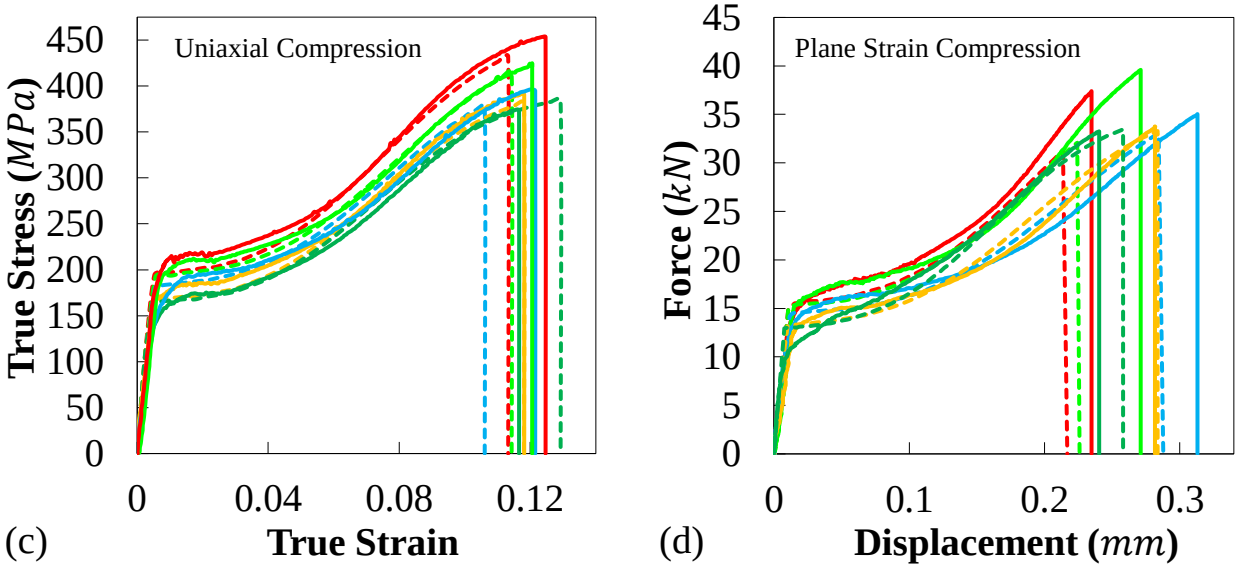

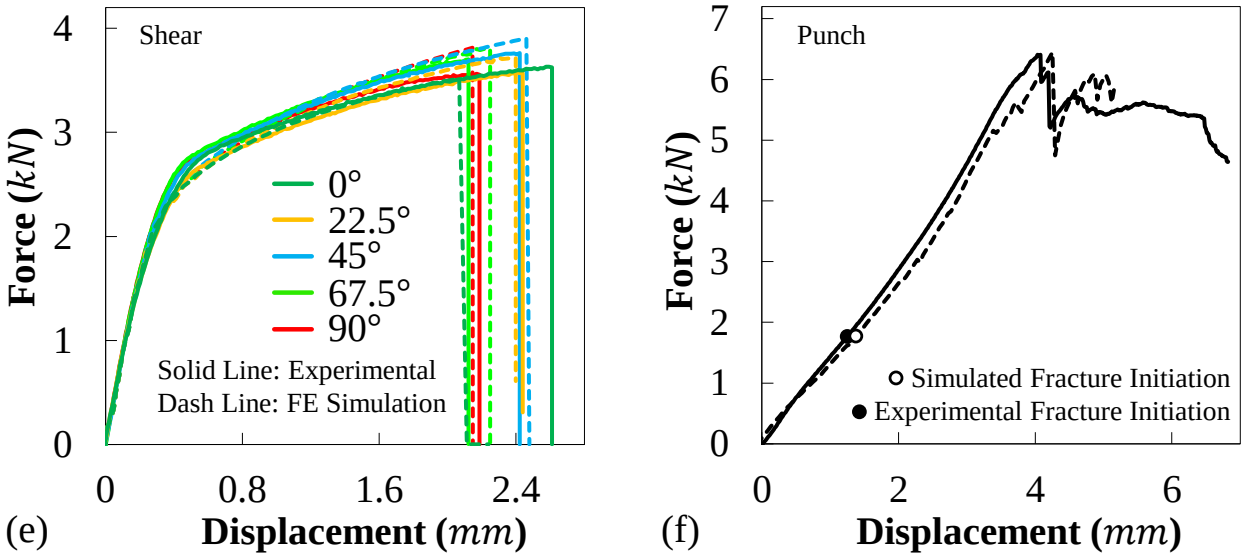

Figure 40 Comparison between tested and simulated results of AZ31B-H24, in (a) true stress-strain under uniaxial tension, (b) force-displacement under notch tension, (c) true stress-strain under uniaxial compression, (d) force-displacement under plane strain compression, (e) force-displacement under shear, and (f) force-displacement under punch.

The experimental data with well-correlated simulation results, under different loading conditions are illustrated in Figure 40a to Figure 40f, respectively. The ones with uniaxial tension and uniaxial compression are presented in the space of true stress-strain due to the uniformity of tested specimen, while the rest loading conditions are presented in the space of force-displacement. All tested and simulated strain histories up to fracture initiation are shown in Figure 41. Tested curves are in solid lines and the FE results are in dash lines. The simulated strain histories for uniaxial compression were omitted, due to the limitation of shell elements applied for cuboid specimen. Usage of 3D solid element (C3D8R) will be more suitable to consider contact boundary conditions.

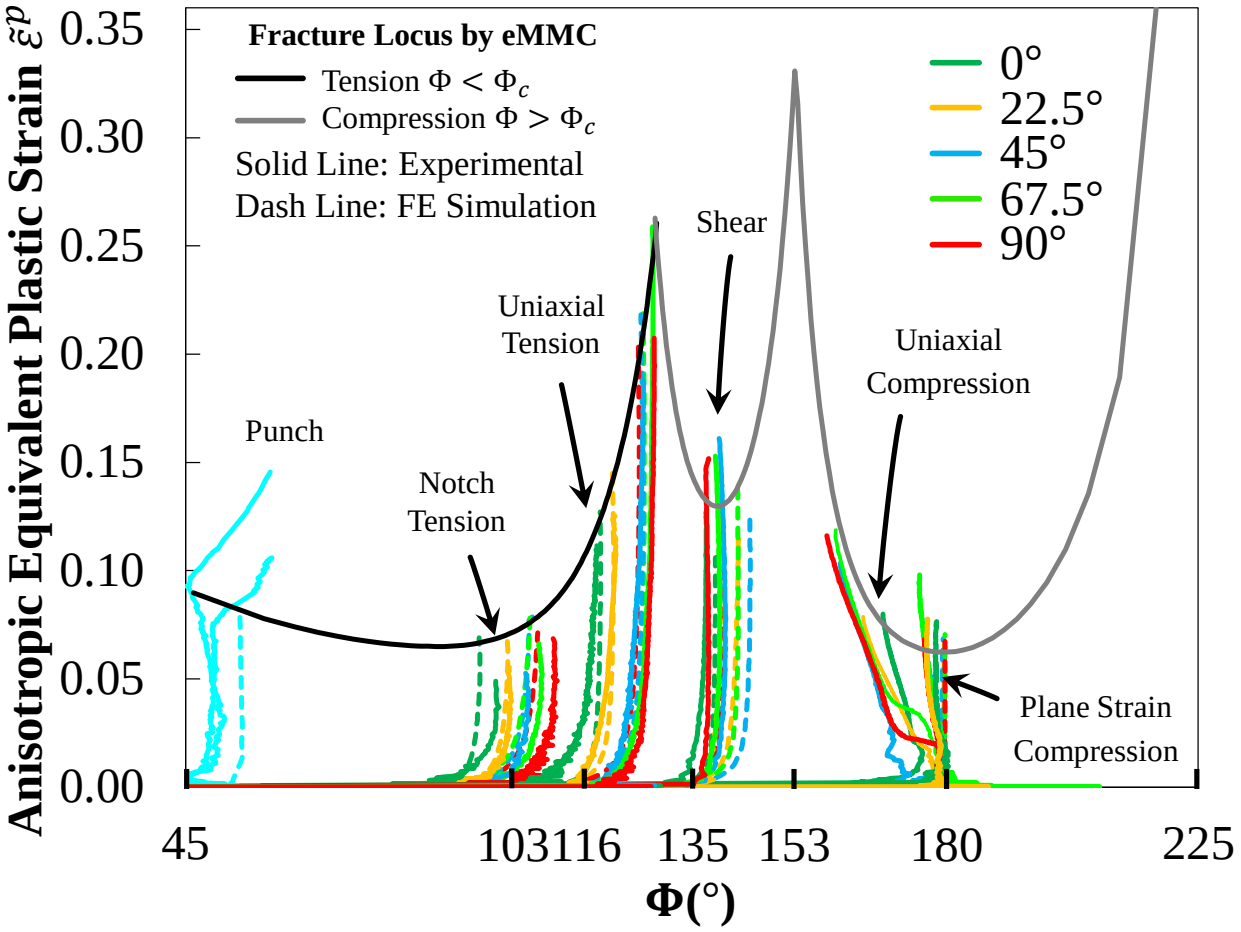

Figure 41 Comparison between tested and simulated strain histories for AZ31B-H24, in the space of equivalent plastic strain versus strain angle Φ.

It can be seen that the anisotropic effect is very strong in both plasticity and fracture, due to apparently different strain paths, strengths, and fracture strains among five orientations. The eMMC model could predict this fracture behavior very well with proper plasticity and hardening models incorporated. The comparison of fracture modes between experiment and simulation is depicted in Figure 42, under the loading conditions.

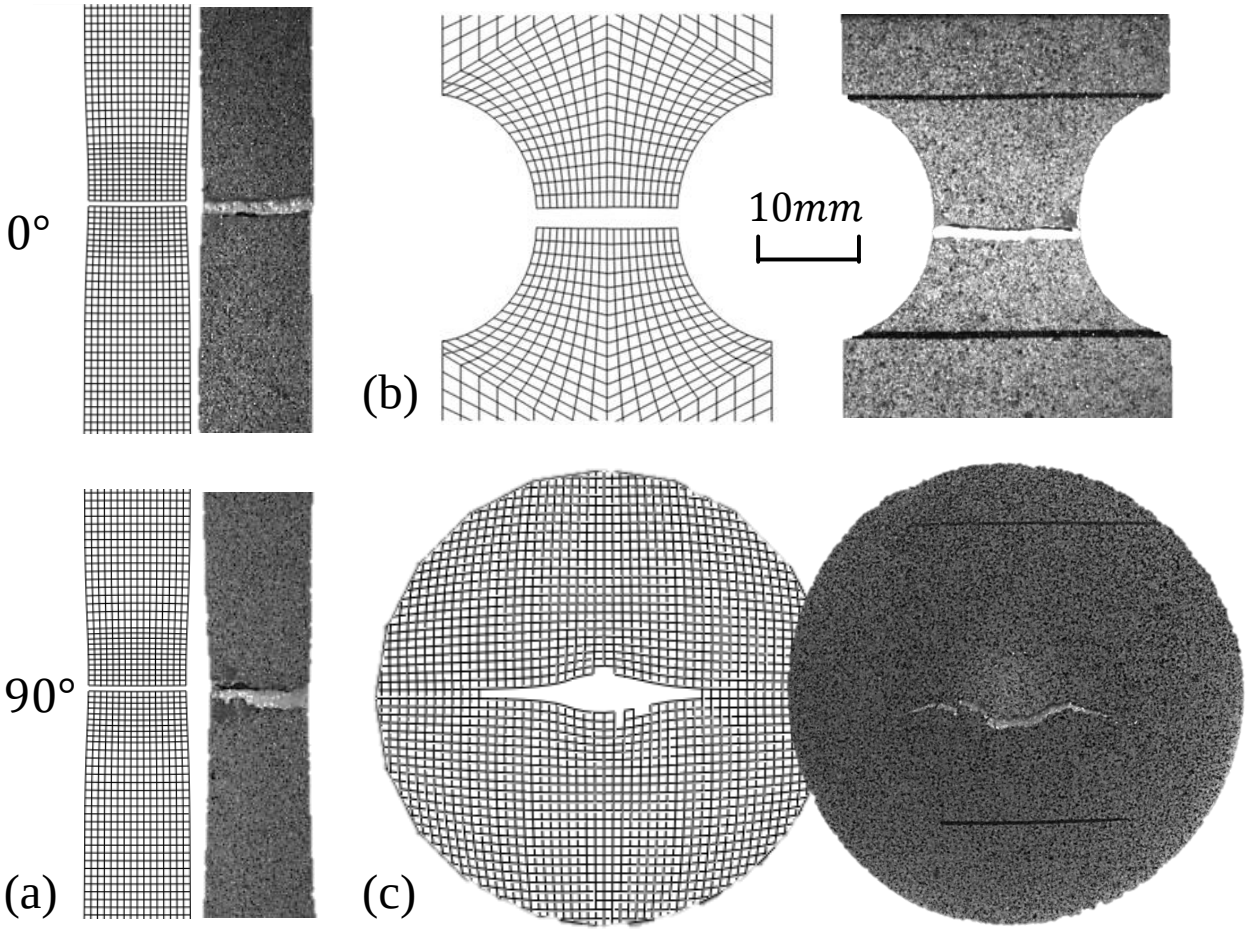

Figure 42 Comparison of fracture modes between experiment and simulation for AZ31B-H24, under (a) uniaxial tension, (b) notch tension, and (c) punch. The scatters on tested specimens are painted dots for DIC measurement. All pictures share the same scale.

The difference of ductility can be seen between 0° and 90° specimens under uniaxial tension: the 90° specimen has a notably necking phenomenon while the 0° one has not. This difference was also well simulated in FE analysis. Specifically, the shear specimen had two competing fracture initiation modes due to the anisotropic effect with this specific geometry, including a) an edge crack at notch area and b) a center crack in the shear zone. The loading conditions are different for different locations of the shear specimen: shear was applied in the center area while uniaxial or biaxial tension was generated at the notch edge. The 90° uniaxial tension had a fracture strain

approximately two times larger than 0° due to its strong anisotropic effect, while the shear fracture strains were similar among all five tested orientations. The shear failure limits are located at somewhere between 0° and 90° uniaxial tensions. This is shown by their strain histories and the fitted eMMC fracture locus in Figure 41.

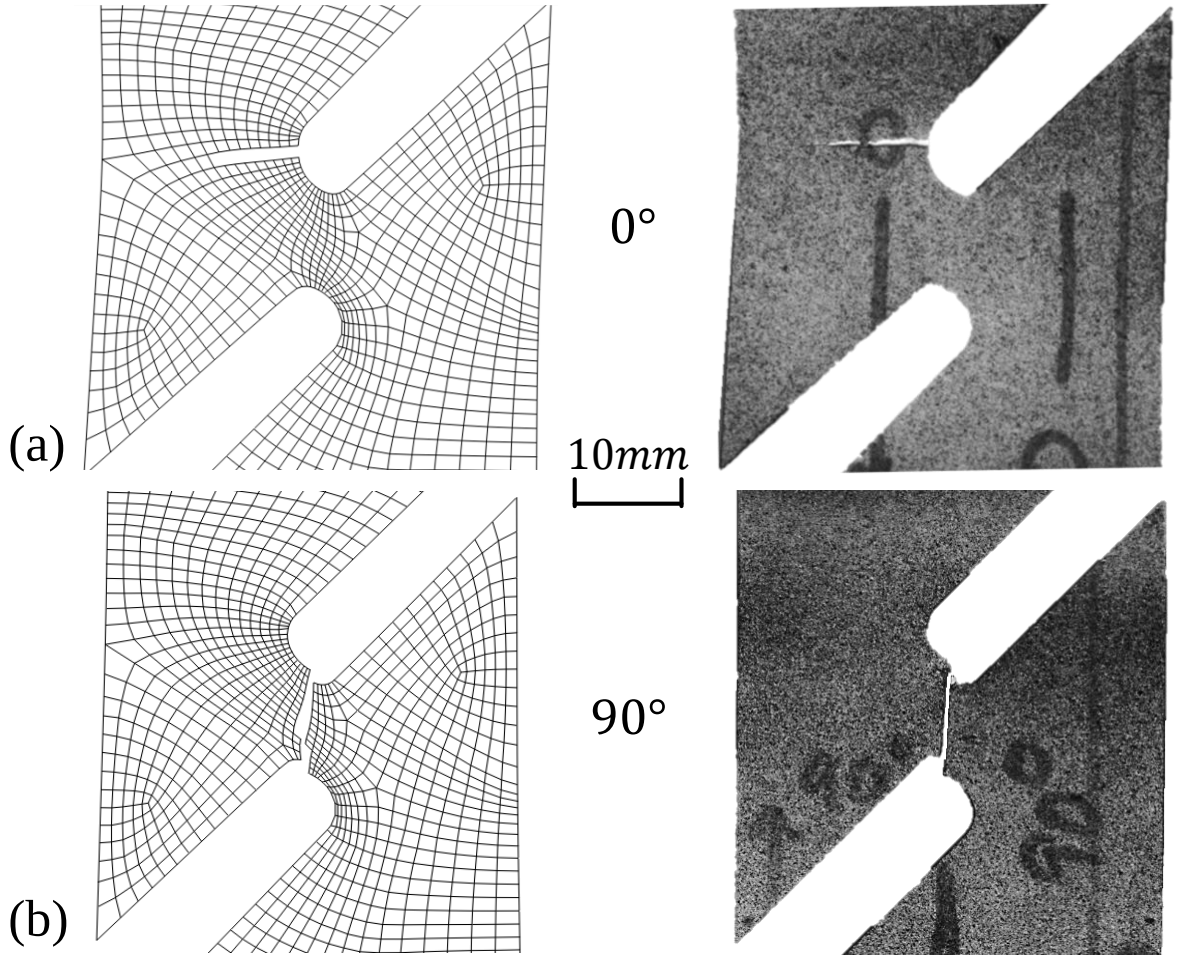

Figure 43 Comparison of the shear fracture modes between experiment and simulation for AZ31B-H24, along (a) 0°, and (b) 90° orientations. The scatters on tested specimens are painted dots for DIC measurement. All pictures share the same scale.

The occurrence of two fracture initiation modes can be explained, as follows. a) The damage accumulation at the notch edge was faster than that in the center area (shear zone) when the

specimen orientation was along 0°, therefore the edge crack was prior to the shear failure. b) Damage accumulation was slower at the notch edge than in the center area when the orientation was along 90°, therefore the center crack due to shear happened firstly. This phenomenon is captured in FE simulation by using the anisotropic eMMC model, illustrated in Figure 43.

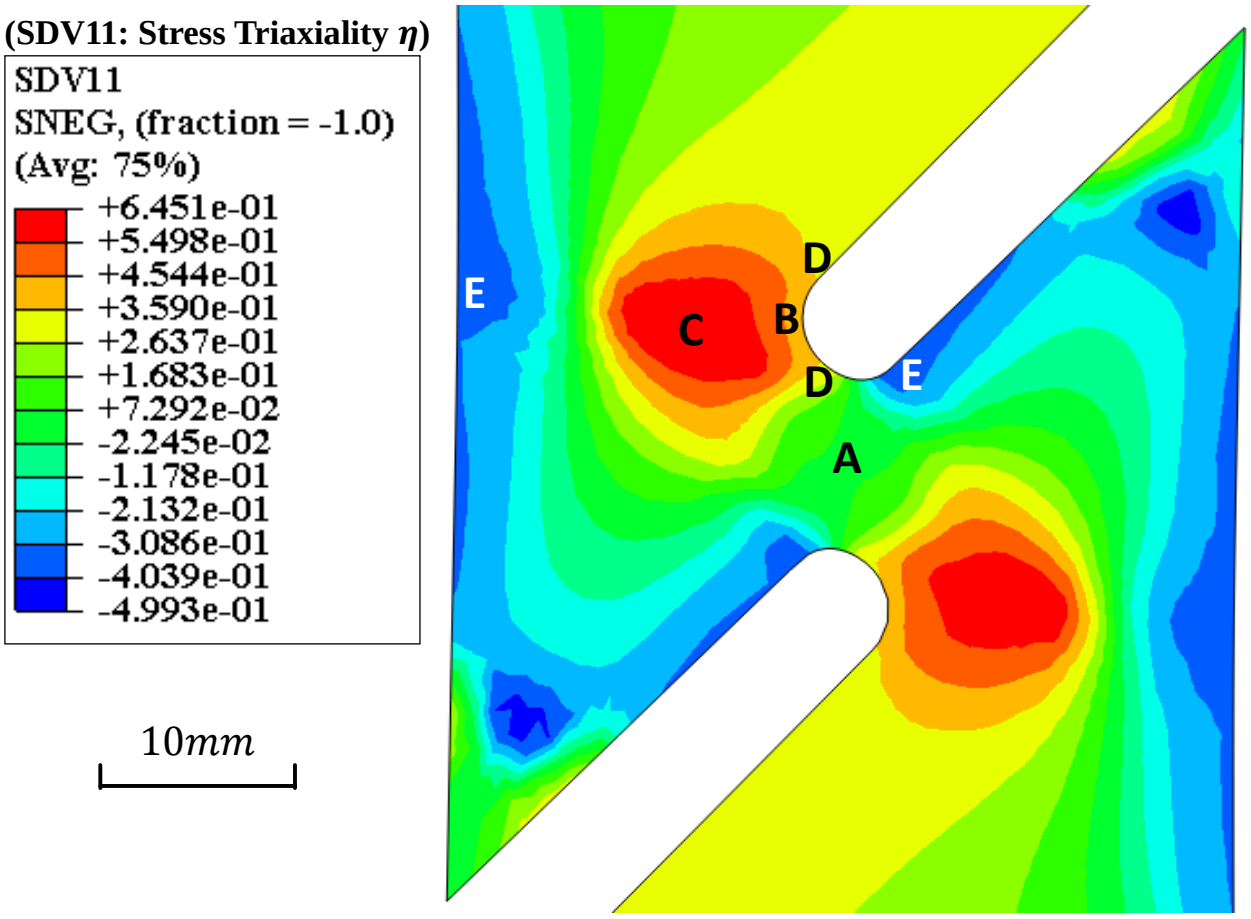

Figure 44 Stress triaxiality contour for the shear specimen in FE simulation.

It is also noted that the calibrated fracture locus has been adjusted a little bit from direct DIC calibration for the shear test prediction. This was mainly because there was not an even distribution of loading condition or stress triaxiality for the current shear specimen. The stress triaxiality contour from FE simulation is illustrated in Figure 44, at the moment of half the

displacement to fracture was applied. Different types of loading conditions appeared in a single test are described as below:

1. Region A (shear zone), the stress triaxiality is about 0.06, a little bit different from pure shear (whose stress triaxiality is zero). This is the primarily region transferring the shear force.
2. Region B (center area at the notch edge), the stress triaxiality is about 0.4. This indicates a loading condition of biaxial tension, somewhere between uniaxial tension ($\eta = 1/3$) and the used notch tension ($\eta = 0.4486$ analytically).
3. Region C (inner notch area), the stress triaxiality is increased from 0.4 close to the edge gradually to 0.65, which indicates an almost equi-biaxial tension loading.
4. Region D, the stress triaxiality is about 0.34, which is uniaxial tension.
5. Region E, the stress triaxiality is about -0.34. This area is dominated by uniaxial compression loading.

The material yields only in these regions for carrying large amount of deformation. It was also observed that this stress triaxiality contour approximated remained during loading. Note that a) the strain angle Φ corresponding to a given loading condition would also vary among different orientations due to its anisotropic effect, and b) the intensity of damage accumulation are certain uneven as well, because the eMMC fracture locus is dependent on Φ. The fracture will initiate in the critical region that has the largest damage accumulation. It can be seen from the simulations that the critical region is also dependent on the specimen orientation:

1. For $0°$ and $22.5°$, region B, dominated by notch tension,
2. For $45°$, both region B and A, dominated by either notch tension or shear,
3. For $67.5°$ and $90°$, region A, dominated by shear.

This is also consistent with the difference in fracture modes observed in experiments, shown in Figure 43. The 45° case was the only one that was not correlated well: the simulation had a fracture initiation at the notch while the experiment had one in the shear zone. Note that the damage accumulations for 45° specimen were competitively increasing between region A and B, resulting in a slight larger damage in region B where notch crack was initiated. This dependency is caused by a combination of very low fracture limit under notch tension and its special geometry. The fracture limit under notch tension is specifically low for AZ31B-H24 along some orientations, based on the tested notch tension strain histories. And the geometry includes a pair of notches that could exert the some biaxial loading condition at the edges. Therefore, the eMMC fracture locus had to be slightly elevated in the area of notch tension while it was used in FE simulation. Good correlation was achieved between experimental and simulated shear test in a) force-displacement curves (shown in Figure 40e), b) strain histories (shown in Figure 41), and c) fracture modes (shown in Figure 43). It is also this special phenomenon for shear test, per se, that makes the correlation able to verify both anisotropic plasticity and fracture models, and their performance under/along different loading conditions/orientations. On the other hand, the simulated fracture displacements under notch tension are consequently somehow larger than the tested ones, as a trade-off.

6.2.2 Non-proportional Cases

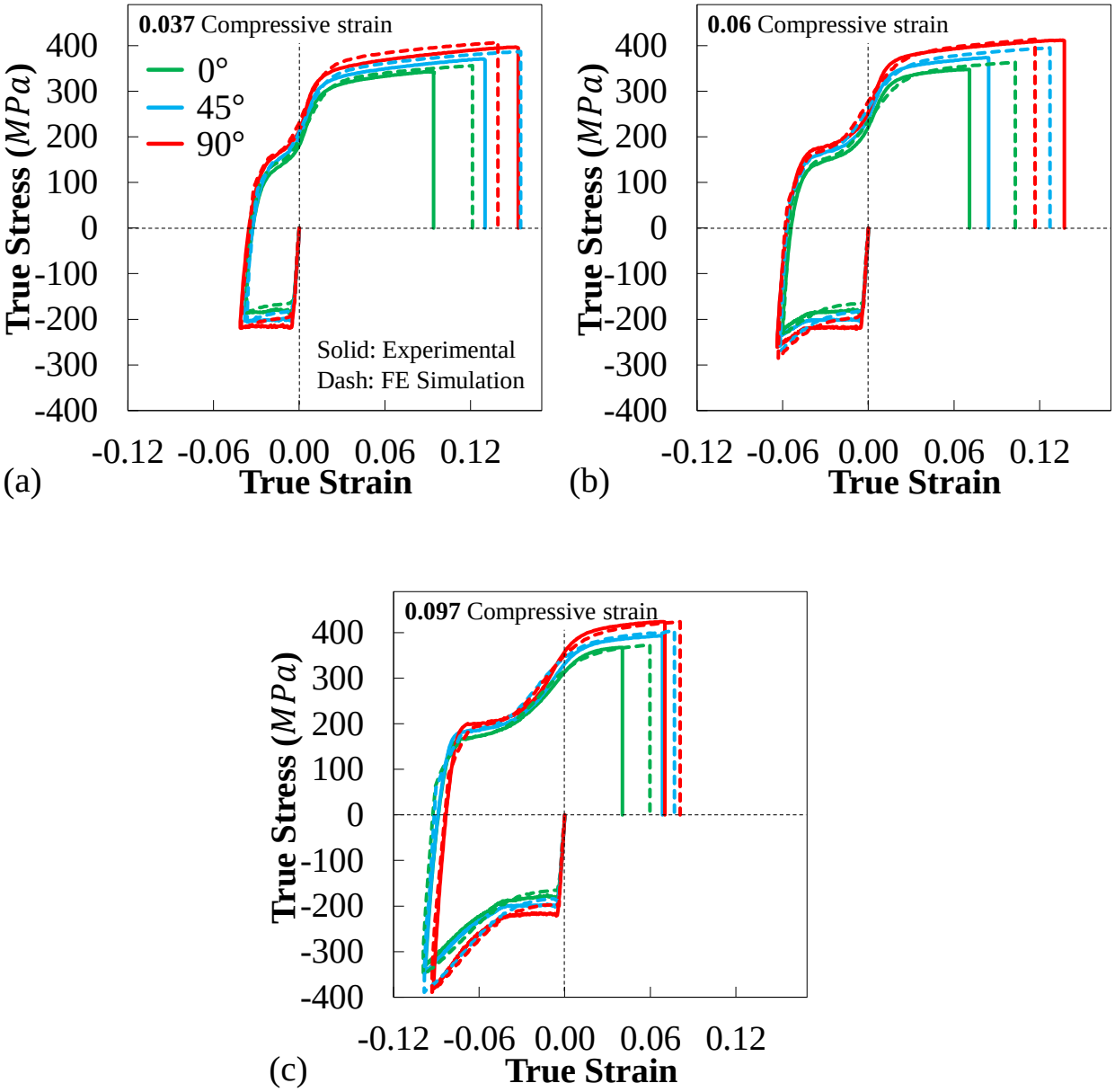

Figure 45 Comparison between tested and simulated true stress-strain curves of 2mm thickness AZ31B-H24 sheets up to fracture along 0°, 45° and 90° orientations, under compression-tension reversal loading with a pre-compressive strain of (a) 0.037, (b) 0.06, and (c) 0.097.

The 2mm thickness experimental data with well-correlated simulation results, under reversal loading conditions with different pre-strains, are illustrated in Figure 40. Tested curves are in

solid lines and the FE results are in dash lines. One can see that the new hardening model is capable to predict the compression-tension kinematic hardening behavior with pre-strain effect. The eMMC model with associated de-twinning effect could predict the fracture strains very well under 10% nominal pre-strain, while exhibit good tendencies under the rest types of pre-strain.

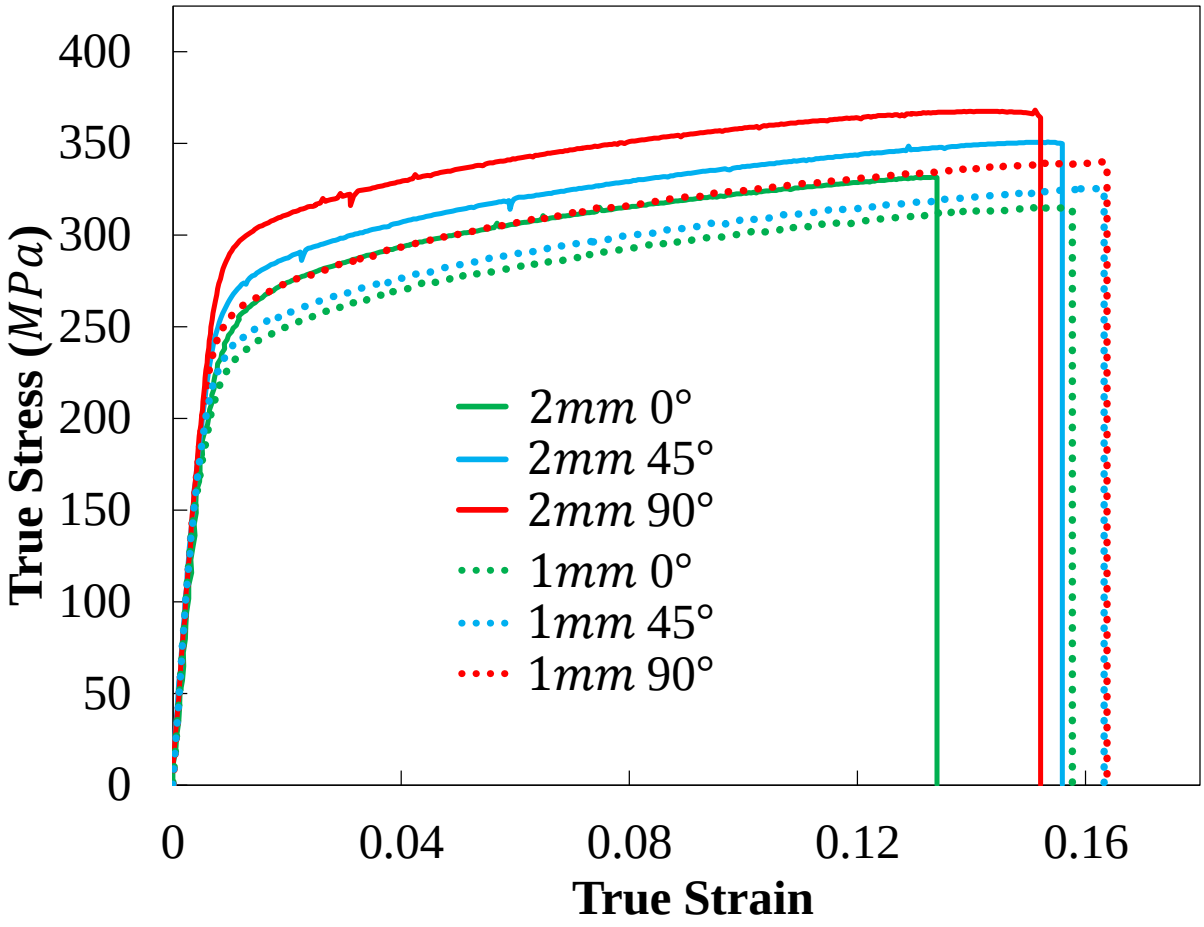

Figure 46 Comparison between tested 1mm (dot lines) and 2mm (solid lines) thickness true stress-strain curves of AZ31B-H24, along 0°, 45° and 90° orientations. Tests are monotonic uniaxial tension.

Figure 46 compares the experimental true stress-strain curves between $1mm$ thickness and $2mm$ thickness under monotonic uniaxial tension with different orientations. The similarity in shape and fracture strain between two types of thickness can be observed in the curves, while slight

difference is observed in material strength. Therefore, the same set of constitutive models can be applied to the 1mm thickness sheet with a scale factor of 0.92 in material strength.

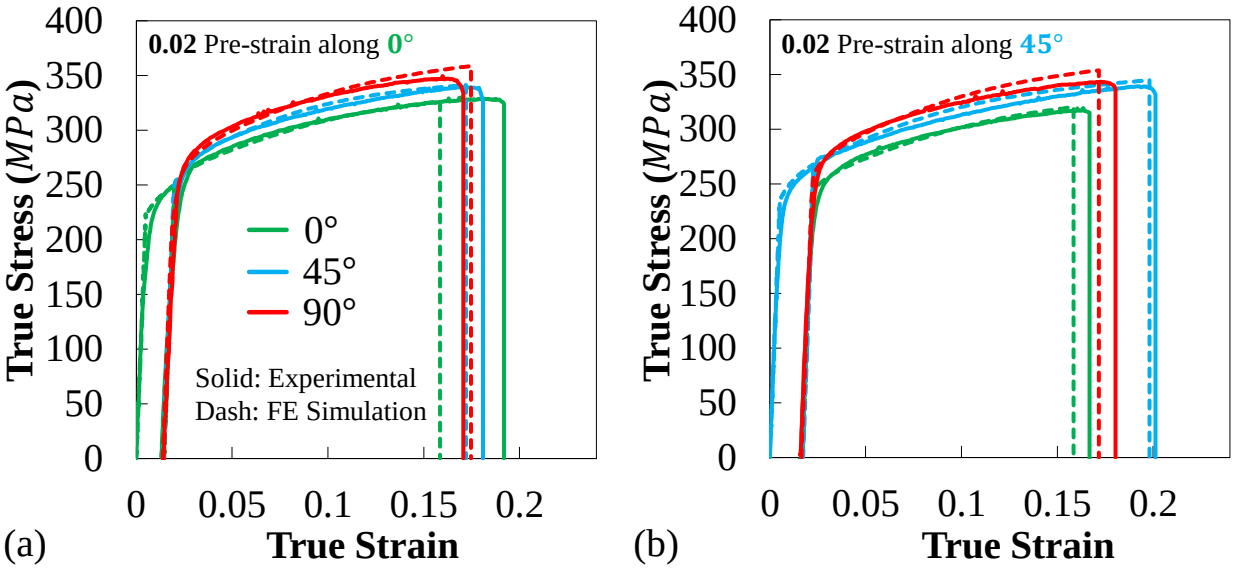

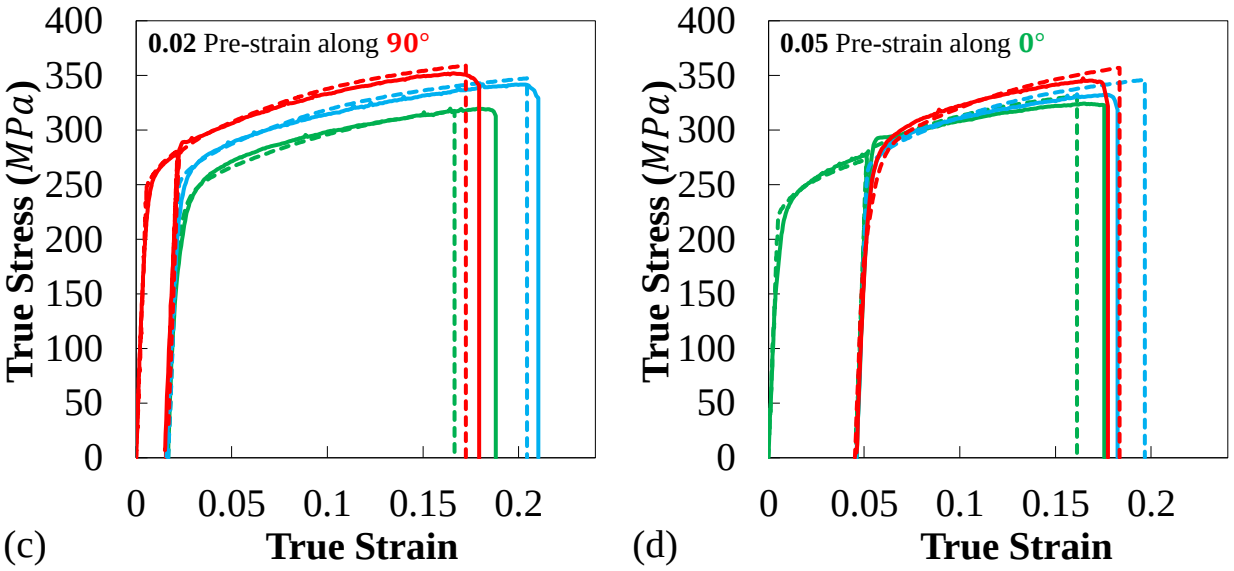

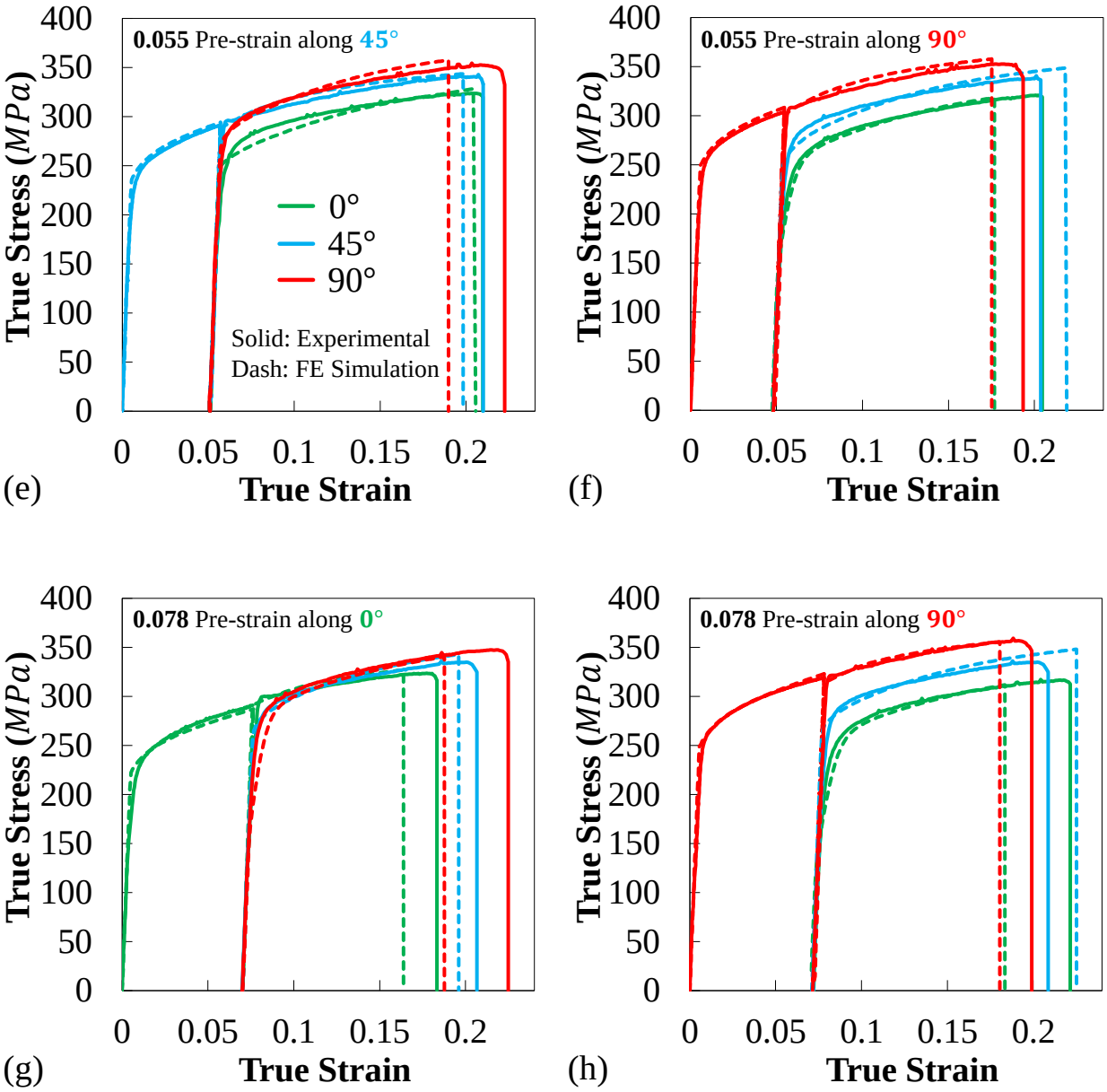

Figure 47 Comparison between tested and simulated true stress-strain curves of 1mm thickness AZ31B-H24 sheets up to fracture, under two-step uniaxial tension with a pre-strain of (a), (b), (c) 0.02, (d) 0.05, (e), (f) 0.055, and (g), (h) 0.078, along a orientation of (a), (d), (g) 0°, (b), (e) 45°, and (c), (f), (h) 90°. The second step loading is along 0°, 45°, and 90° respectively for each type of pre-strain.

The comparison of true stress-strain between experimental and simulated two-step uniaxial tension is illustrated in Figure 47, with pre-strains under different amounts and orientations. One

can see that the second step true stress-strain curves with the same orientation are similar under different pre-strains. No additional hardening is apparently observed at the beginning of the second step uniaxial tension, when the loading orientation changes. Fair consistency can be observed between the monotonic and second step stress-strain curves with the loading orientation remaining and different pre-strains, due to typical strain hardening. In conclusion, no clear cross-hardening effect is observed for magnesium AZ31B-H24 alloy sheet in the current experimental result. The ultimate fracture strains in that step are generally larger than the monotonic ones in Figure 46. Their fracture behaviors are well predicted by the combination of new kinematic hardening model and eMMC fracture model under lower pre-strain. The hardening curves under all scenarios are well correlated with experimental results.

CHAPTER 7 MODEL PERFORMANCE FOR STEEL SHEETS

The new framework presented in the current thesis can be also applied for steel sheets with limited adjustments in different modules, for example using simplified hardening models. Two different cases are specifically evaluated, TRIP780 steel sheets under multi-axial monotonic loading, and three types of steel sheets (BH240, DP600, and EDDQ) under two-step uniaxial tension tests.

7.1 TRIP780 Steel Sheet

Three sets of experiments with strain histories available were performed for TRIP780 steel sheets: uniaxial tension, notch tension (biaxial tension), and plane strain tension. Three orientations (0°, 45°, and 90° with respect to the rolling direction) were tested for each of the loading condition. All specimens had a thickness of $1.58mm$.

7.1.1 Plasticity

An anisotropic yield criterion, Yld2000-2D by Barlat, Brem, et al. (2003), was calibrated using both the stabilized experimental Φ value and material strength under different loading conditions and orientations. This was necessary because the plastic strain histories should be precisely predicted to correlate with the experimental scenario, in order to hit the specified points on the fracture locus. The Yld2000-2D anisotropic yield criterion offers a symmetric yield surface, with two linear transformations onto the stress tensor, as follows

$$|X_1' - X_2'|^M + |2X_1'' + X_2''|^M + |2X_2'' + X_1''|^M = 2\overline{\sigma}^M, \tag{62}$$

where $\bar{\sigma}$ is the equivalent stress, M is the exponential coefficient. $X_1', X_2', X_1'', \text{and } X_2''$ are principal values of two second order tensor $\boldsymbol{X}'$ and $\boldsymbol{X}''$, respectively. $\boldsymbol{X}'$ and $\boldsymbol{X}''$ are obtained by operating two different linear transformation matrix onto the Cauchy stress tensor $\boldsymbol{\sigma}$.

$$\begin{bmatrix} X_{11}' \\ X_{22}' \\ X_{12}' \end{bmatrix} = \begin{bmatrix} L_{11}' & L_{12}' & 0 \\ L_{21}' & L_{22}' & 0 \\ 0 & 0 & L_{66}' \end{bmatrix} \begin{bmatrix} \sigma_{11} \\ \sigma_{22} \\ \sigma_{12} \end{bmatrix}, \tag{63}$$

$$\begin{bmatrix} X_{11}'' \\ X_{22}'' \\ X_{12}'' \end{bmatrix} = \begin{bmatrix} L_{11}'' & L_{12}'' & 0 \\ L_{21}'' & L_{22}'' & 0 \\ 0 & 0 & L_{66}'' \end{bmatrix} \begin{bmatrix} \sigma_{11} \\ \sigma_{22} \\ \sigma_{12} \end{bmatrix}. \tag{64}$$

The number of parameters can be reduced by using

$$\begin{bmatrix} L_{11}' \\ L_{12}' \\ L_{21}' \\ L_{22}' \\ L_{66}' \end{bmatrix} = \begin{bmatrix} 2/3 & 0 & 0 \\ -1/3 & 0 & 0 \\ 0 & -1/3 & 0 \\ 0 & 2/3 & 0 \\ 0 & 0 & 1 \end{bmatrix} \begin{bmatrix} \alpha_1 \\ \alpha_2 \\ \alpha_7 \end{bmatrix}, \tag{65}$$

$$\begin{bmatrix} L_{11}'' \\ L_{12}'' \\ L_{21}'' \\ L_{22}'' \\ L_{66}'' \end{bmatrix} = \frac{1}{9} \begin{bmatrix} -2 & 2 & 8 & -2 & 0 \\ 1 & -4 & -4 & 4 & 0 \\ 4 & -4 & -4 & 1 & 0 \\ -2 & 8 & 2 & -2 & 0 \\ 0 & 0 & 0 & 0 & 9 \end{bmatrix} \begin{bmatrix} \alpha_3 \\ \alpha_4 \\ \alpha_5 \\ \alpha_6 \\ \alpha_8 \end{bmatrix}, \tag{66}$$

where α_1 to α_8 with the exponential coefficient M are nine material coefficients to be determined by experimental data. The calibrated set of parameters is listed in Table 5.

Table 5 Yld2000-2D material coefficients for TRIP780

α_1	α_2	α_3	α_4	α_5	α_6	α_7	α_8	M
0.524	1.049	0.953	0.793	0.828	0.640	0.811	0.841	4.669

A Swift power hardening law, $\bar{\sigma} = K(\bar{\varepsilon}^p + \varepsilon_0)^n$, was applied, where $K = 1220.0MPa$, $n = 0.2500$, and $\varepsilon_0 = 0.0240$. This was calibrated by the true stress-strain curve under uniaxial tension along rolling direction.

7.1.2 eMMC Calibration

The calibrated results based on eMMC model are shown in Figure 48. The set of used fracture parameters is listed in Table 6. Since this material has weak fracture anisotropy, these fracture parameters are the same as those of MMC model published by Bai and Wierzbicki (2010), and anisotropic parameters (β_{ii}) are set as unity. It is interesting to find that the eMMC takes some anisotropy of uniaxial tension into account even though $\boldsymbol{\beta} = \boldsymbol{I}$ through the different strain state angles (Φ). Some other experimental results including pure shear, equi-biaxial tension and plane strain tension (Bai & Wierzbicki, 2010) were also plotted for comparison, where the strain history and orientation information were not available. It is noted that there were two series of plane strain tension data. One with strain history was obtained by uniform plane strain specimen with the thickness machined down entirely. The other one was obtained by butterfly shape specimens (D. Mohr & Henn, 2007). Since the plane strain specimen's flatness and surface quality were inadequate, the fracture strains from the uniform specimens could be underestimated. As for the butterfly specimens, the fracture strain could exceed the one under actual plane strain tension due to the non-uniformity. Therefore an average value between both of them was taken for the eMMC model calibration. For the equi-biaxial tension (from punch test), the fracture initiation strain is also presented in Figure 48.

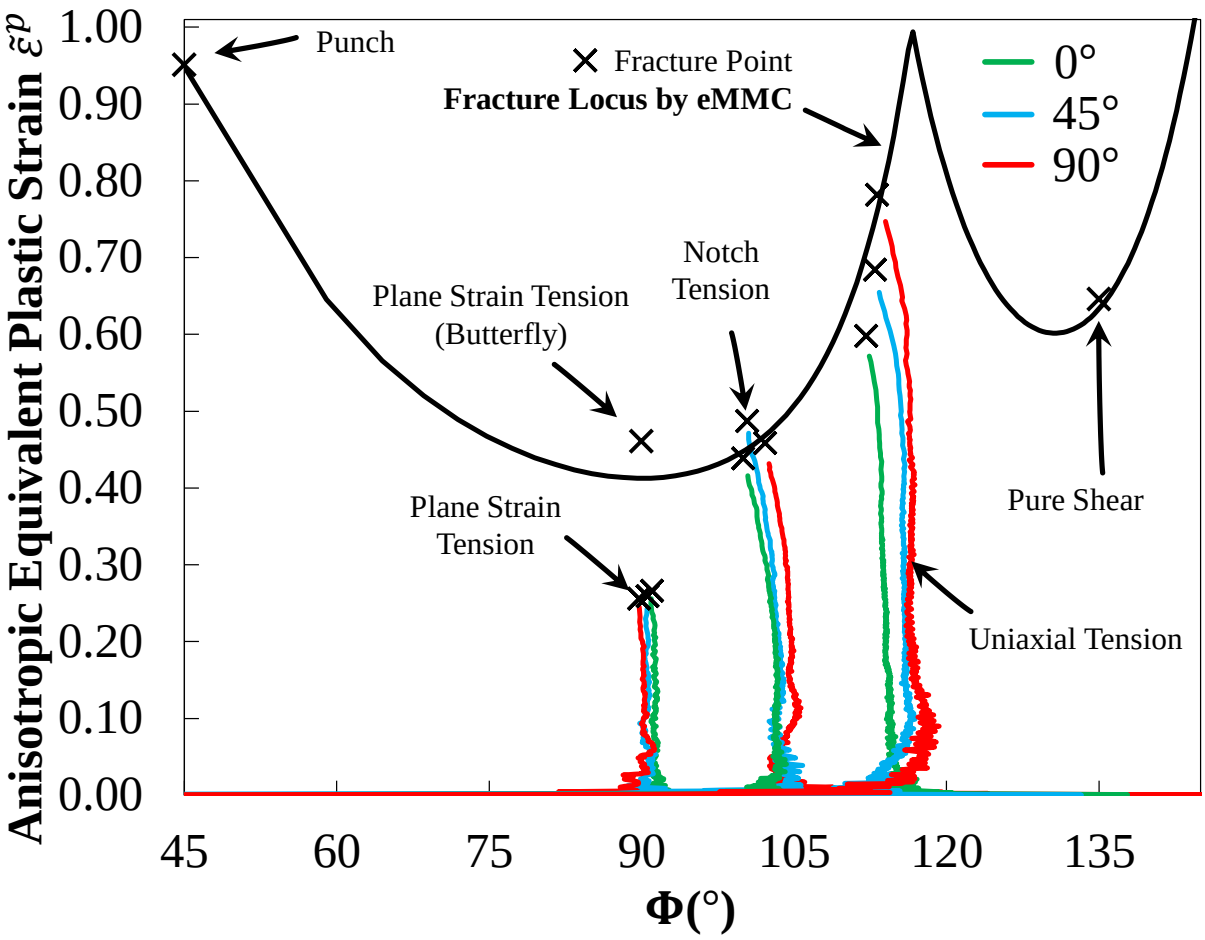

Figure 48 The fracture locus based on eMMC fracture model for TRIP780, calibrated by the linear transformed anisotropic equivalent plastic strain. The isolated fracture initiation points without the entire strain history are taken from Bai and Wierzbicki (2010).

Table 6 Anisotropic eMMC parameters for TRIP780

$A\ (MPa)$	n	C_1	$C_2\ (MPa)$	$\tilde{C}_\theta^s$	$\tilde{C}_\theta^c$	β_{11}	β_{22}	β_{33}	β_{44}
1275.9	0.266	0.121	720.2	1.096	1.001	1.000	1.000	1.000	1.000

7.1.3 FE Model Description

Finite element models were set up for three types of tests, include uniaxial tension, notch tension, and punch test of TRIP780 steel sheet. Three orientations, 0°, 45°, and 90° were assigned for both of uniaxial and notch tension models. The geometry configurations were identical to the tested specimens. The specimens for uniaxial and notch tension are shown in Figure 49.

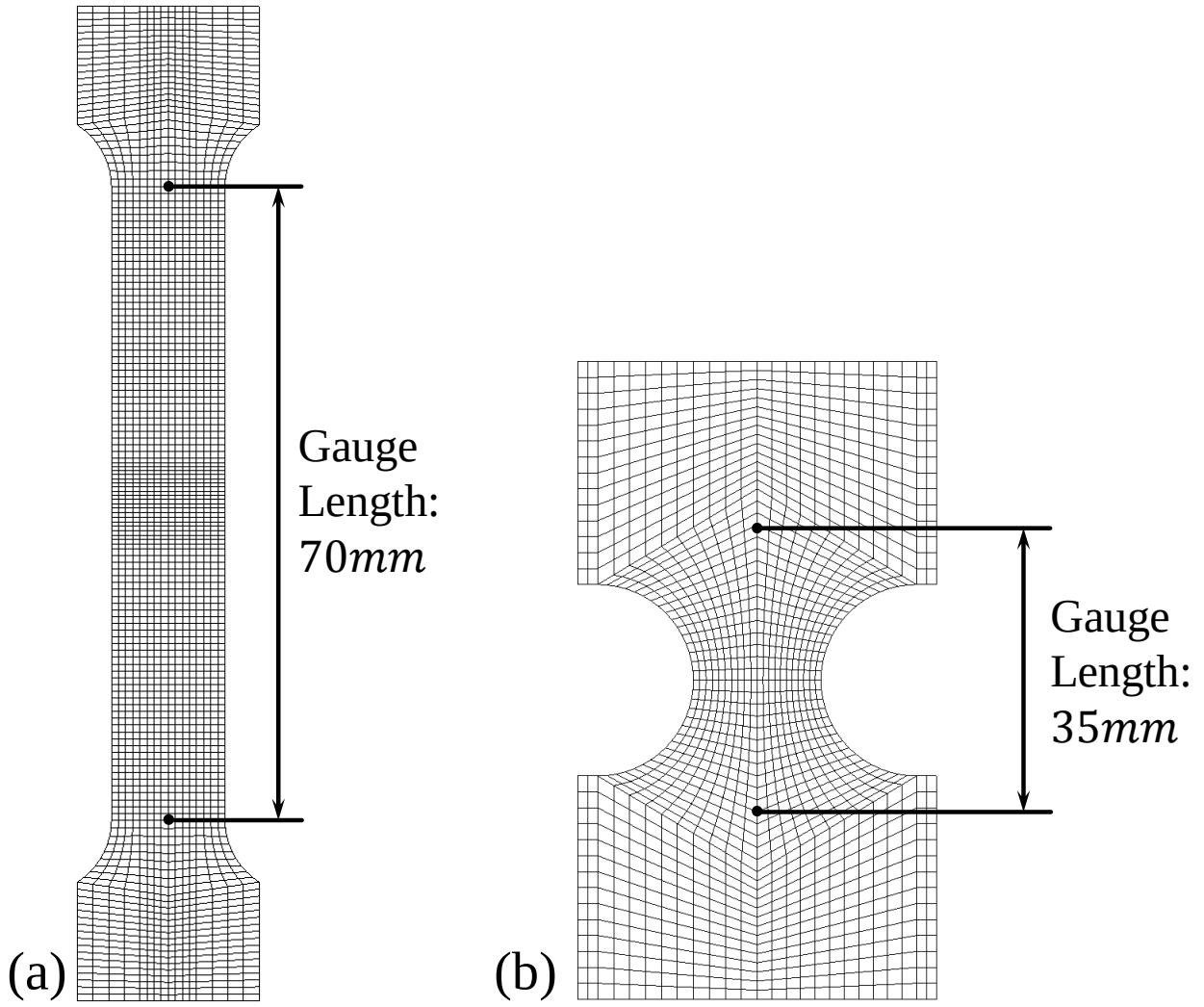

Figure 49 Model specimens for TRIP780 under (a) uniaxial tension, and (b) notch tension.

The same measurements were made for both FE simulation and experimental results for correlation, which are listed as follows.

1. A gauge of 70mm was taken for uniaxial tension tests along the vertical center line of the dogbone specimen, to calculate true strain.
2. A gauge of 35mm was made for notch tension tests along the same position, to extract vertical displacement.
3. Total forces for uniaxial tension are outputted to calculate true stress.

4. Total forces for notch tension and punch tests are outputted for comparison.
5. The fracture initiation area was picked to extract the entire strain history for all three tests.

The positions of the strain gauges are also shown in Figure 49. The experimental measurements were all based on DIC.

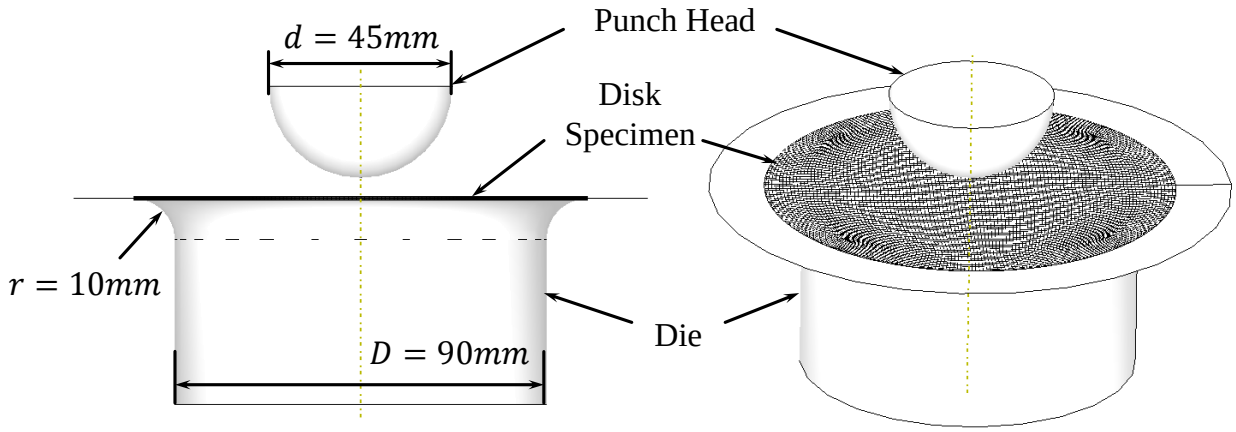

Figure 50 Side (left) and isometric (right) views of the FE punch model for TRIP780.

Additionally, the following specifications are set up for the punch test:

1. The entire model is shown in Figure 50 with key geometries. The punch and die were modeled as analytical rigid bodies. The punch had a half-sphere head with a diameter of $d = 45mm$ while the die had a radius of $r = 10mm$ with its cavity diameter $D = 90mm$.
2. The external edge of the punch disk was fixed because the disk was fastened by bolts in test.
3. It was also recognized that the friction coefficient had no apparent effect on the final results ranged from 0 to 0.2, therefore a friction coefficient of 0.05 was set for the contact property. The penalty contact with the friction coefficient was defined between a) top surface of the disk specimen and the punch head, and b) bottom surface of the disk specimen and the die.

The calibrated constitutive models were applied in FE analysis, including Yld2000-2D anisotropic yield criterion, Swift hardening, and eMMC fracture model.

7.1.4 Simulation Results

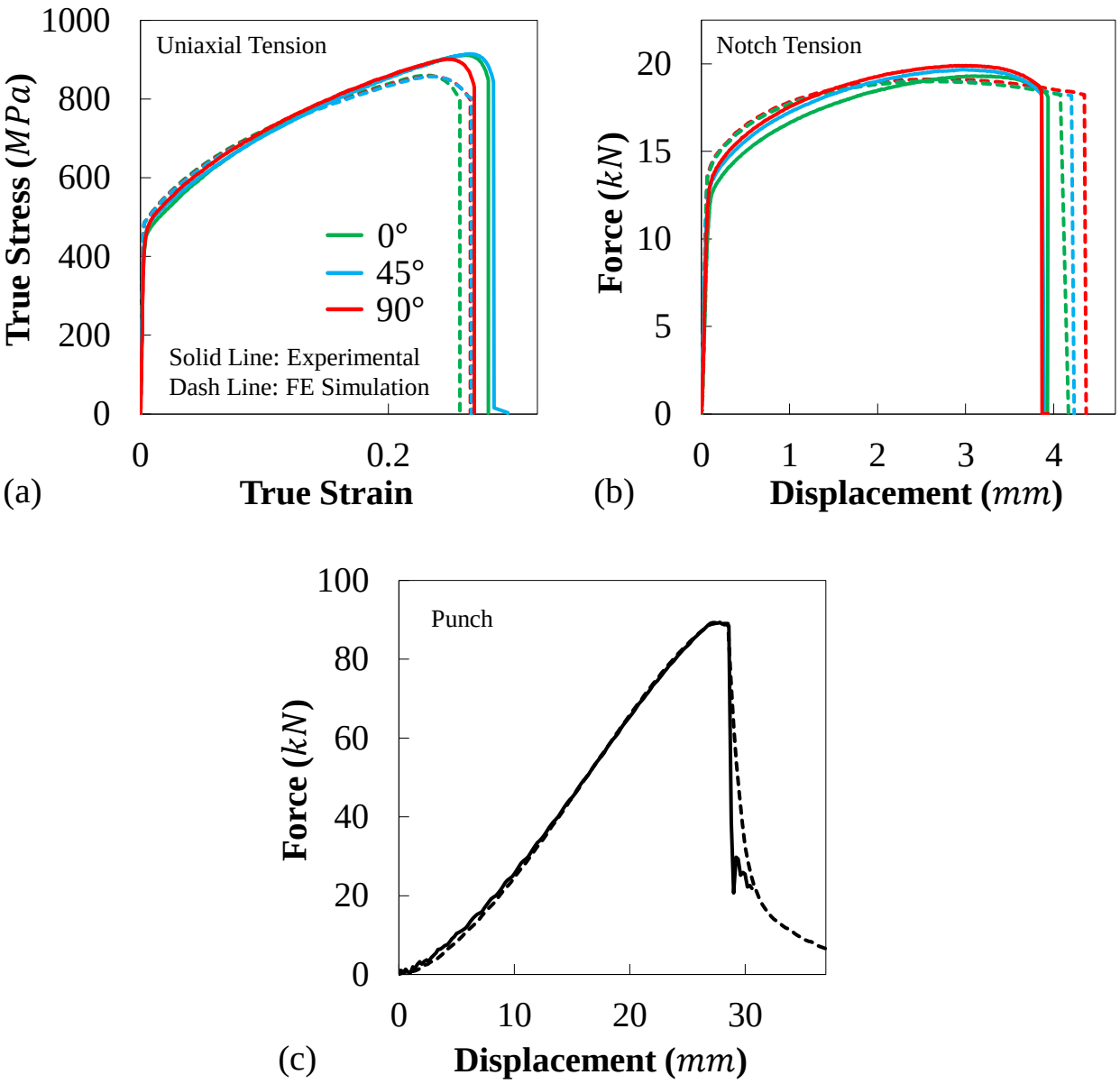

Figure 51 Comparison between tested and simulated results for TRIP780, in (a) true stress-strain under uniaxial tension, (b) force-displacement curves under notch tension, and (c) force-displacement under punch test.

The experimental true stress-strain curves from uniaxial tension tests and force-displacement curves from notch tension and punch test are respectively illustrated in Figure 51a, Figure 51b, and Figure 51c, together with the well-correlated simulation results. Their strain histories are shown in Figure 52, terminated by fracture initiation. All tested curves are in solid lines and all FE results are in dash lines.

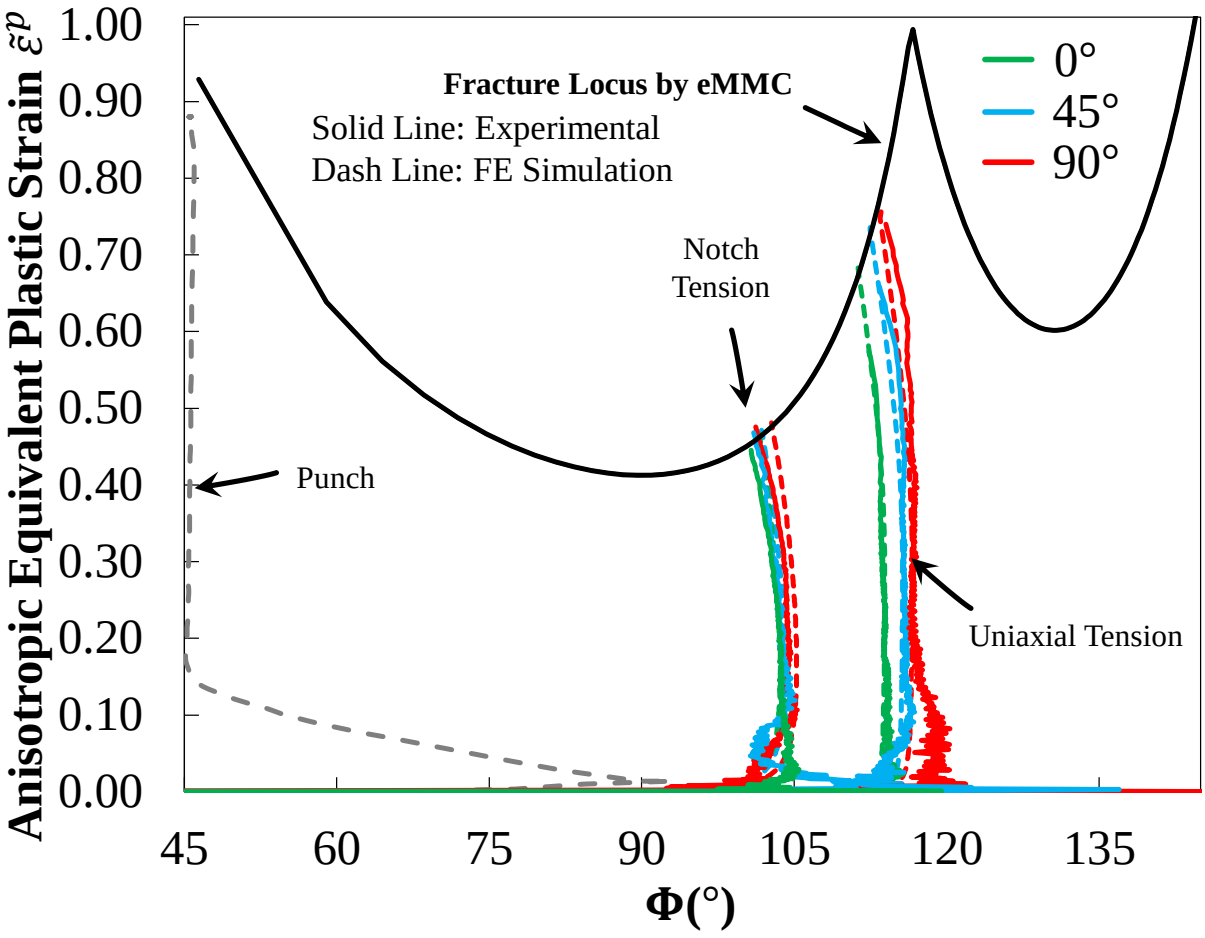

Figure 52 Comparison between tested and simulated strain histories for TRIP780, in the space of equivalent plastic strain versus strain angle Φ.

One can see that the anisotropic effect for this material is not apparent in views of a) plasticity: both the tested strength and strain histories under different orientations are very close, for both uniaxial and notch tensions, and b) fracture: all tested fracture points have slight difference

among three orientations for these loading conditions. It is also important that the plastic flow can be precisely captured by the anisotropic yield criterion, presented by the perfectly-fitted strain histories between FE and tested results. This is a key point for eMMC model to give great performance in fracture prediction. It can be seen that all simulated fracture points are well correlated with the experimental ones, in both aspects of strength and strain history. The fracture modes are also similar to the experimental ones under three different loading conditions, as shown in Figure 53.

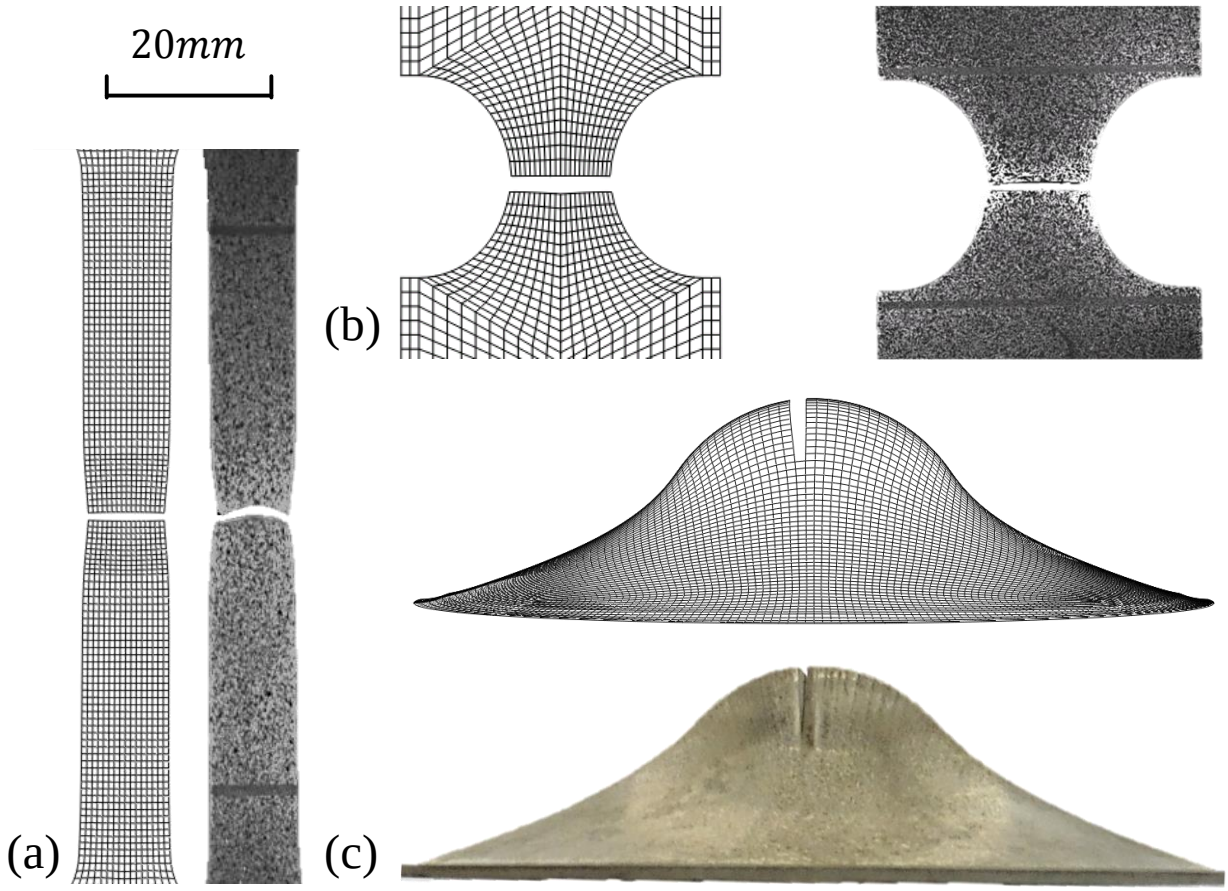

Figure 53 Comparison of the fracture modes between experiment and simulation for TRIP780, under (a) uniaxial tension, (b) notch tension, and (c) punch. The scatters on tested specimens are painted dots for DIC measurement. All pictures share the same scale. The fracture modes were similar among different orientations.

7.2 BH240, DP600, and EDDQ Steel Sheet

The two-step tests were also accomplished for the following materials by Auto Steel Partnership (ASP), BH240, DP600, and EDDQ. The pre-load conditions were uniaxial tension and equi-biaxial tension (bulge test). For uniaxial tension, a large-scaled dogbone specimen was used.

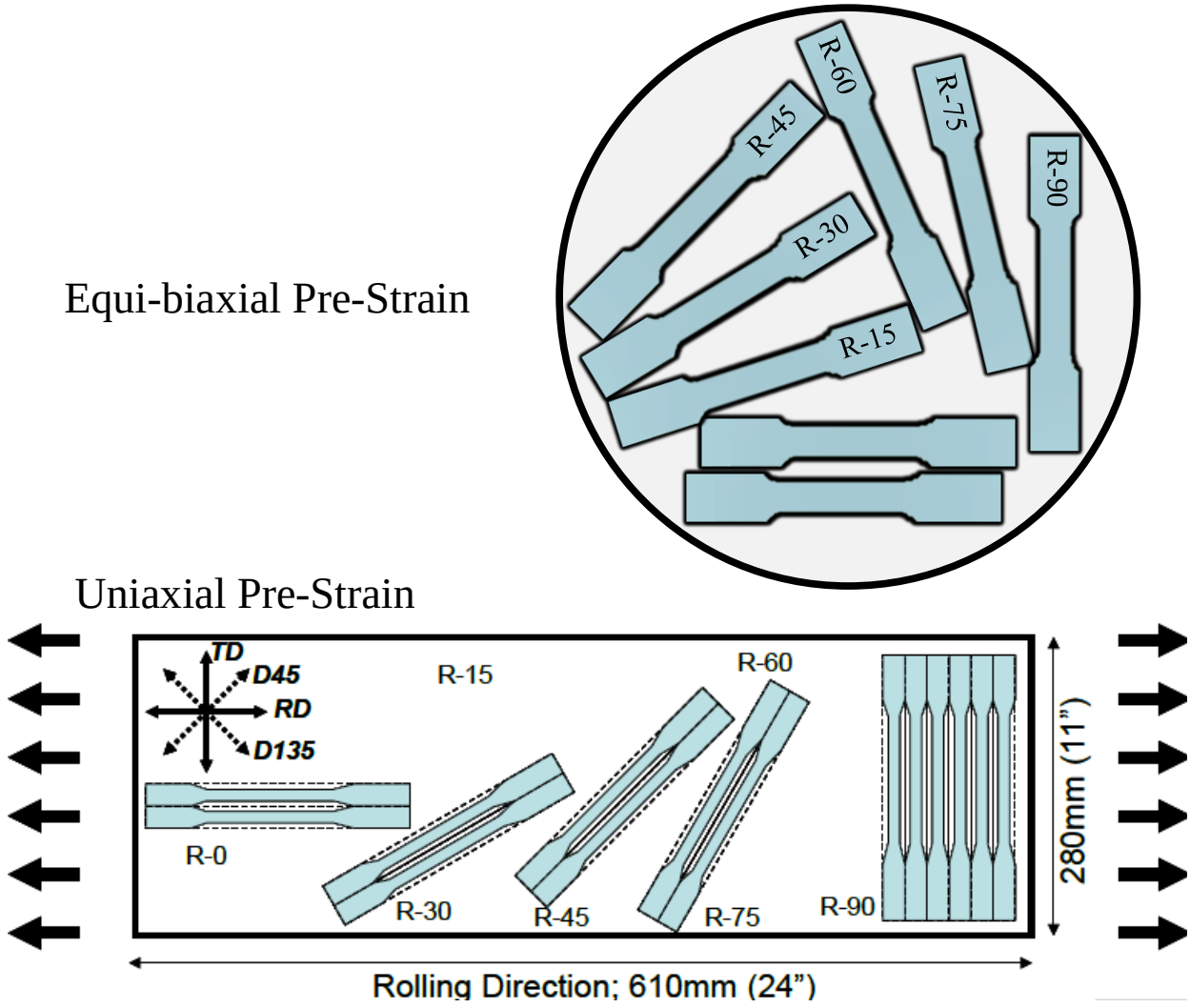

Figure 54 Schematic graph for the two-step uniaxial tension specimen cutting pattern. The big circle and rectangular indicate big specimens undergone bulge test and uniaxial tension, respectively, from which the second step uniaxial tension specimens were cut.

The pre-strain were configured along three different orientations: 0 ° (rolling), 45 ° (diagonal), and 90 ° (transversal), with the nominate amount of 5%, 10%, and 15% for each orientation. For equi-biaxial tension the amount of equivalent strain was configured as 6% and 10%. The actual plastic strain for pre-loading was corrected by fitting with the monotonic strain-stress curves. After the first step, the pre-strained specimens were cut into small-sized dogbone specimens with the orientations of 0 °, 15 °, 30 °, 45 °, 60 °, 75 °, and 90 ° for uniaxial tensions until fracture. All the orientations mentioned were according to the rolling direction of the original metal sheets. The cutting pattern for two-step uniaxial tension specimens can be shown in Figure 54.

7.2.1 Plasticity

A Yld2000-2D yield criterion with hardening models (Swift for isotropic and Armstrong-Frederick for kinematic) were calibrated by using the monotonic data with the Lankford ratio from BH240, DP600, and EDDQ. The strain-stress curves for the second step uniaxial tension were used for the verification. The calibrated set of parameters is listed in Table 7, Table 8, and Table 9.

Table 7 Yld2000-2D material coefficients for BH240

α_1	α_2	α_3	α_4	α_5	α_6	α_7	α_8	M
0.858	1.63	0.726	1.144	1.068	0.054	1.234	1.734	8

Table 8 Yld2000-2D material coefficients for DP600

α_1	α_2	α_3	α_4	α_5	α_6	α_7	α_8	M
0.772	0.896	0.846	0.84	0.828	0.708	0.84	0.978	5

Table 9 Yld2000-2D material coefficients for EDDQ

α_1	α_2	α_3	α_4	α_5	α_6	α_7	α_8	M
1.148	1.014	0.657	0.912	0.862	0.872	1.048	1.15	3

A Swift power hardening law, $\bar{\sigma} = K(\bar{\varepsilon}^p)^n + Y$, was applied, together with an Armstrong-Fredrick kinematic hardening model. This was calibrated by the true stress-strain curve under uniaxial tension along rolling direction, individually for each material. Different from magnesium AZ31B alloy sheets, the cross hardening effect can be commonly observed in BH240 and DP600 steel sheets, as reported by Barlat et al. (2013); Jia and Bai (2015a). The true stress-strain curve at the beginning of the re-oriented secondary uniaxial tension could exhibit an excess from the one under monotonic uniaxial tension. Slight stagnation is also observed before the curve becoming consistent with the monotonic one. The magnitude of excess and the length of stagnation depend on the both the amount of pre-strain and the orientation change between two steps. In this case, the additional cross-hardening item $\bar{\sigma}_C$ is capable to predict this behavior, with a modified expression based on Jia and Bai (2015a),

$$\bar{\sigma}_C = A_0[1 - \exp(-C_1\bar{\varepsilon}^p)]X_C^{\lambda}, \tag{67}$$

where A_0 and C_1 are material coefficients controlling the magnitude of cross-hardening with pre-strain effect, and λ remains as the exponential coefficient adjusting the decaying process. The evolution of this item along the growth of equivalent plastic strain is depicted in Figure 55.

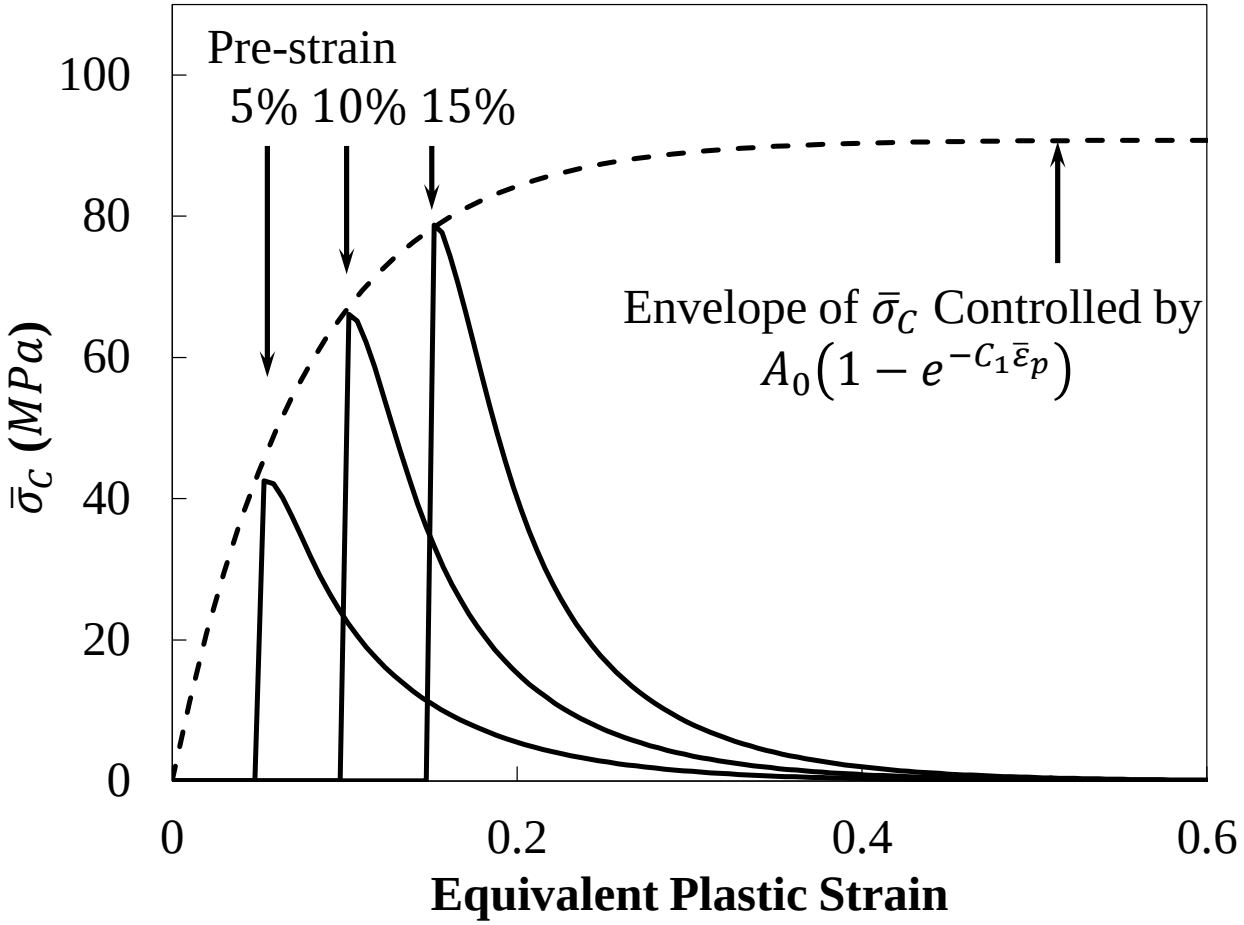

Figure 55 Schematic graph for the adjusted cross-hardening item $\bar{\sigma}_C$ based on (67). Three different pre-strains, 5%, 10%, and 15% are plotted, with the envelope dash curve of their peak magnitudes.

Therefore, the plastic potential function from Equation (24) becomes

$$f\left(\sigma_{ij}-\alpha_{ij}\right)-\bar{\sigma}\left(\bar{\varepsilon}_p\right)-\bar{\sigma}_C=0, \tag{68}$$

where the back stress α_{ij} is incorporated into the yield criterion f, following the incremental definition of Equation (23),

$$\dot{\alpha_{ij}}=C_0\left(\rho\frac{\sigma_{ij}-\alpha_{ij}}{\bar{\sigma}}-\alpha_{ij}\right)\dot{\bar{\varepsilon}}^p \text{And } \bar{\sigma}\left(\bar{\varepsilon}_p\right) \text{ is the Swift hardening}$$

Table 10 Hardening model coefficients for BH240

$K\ (MPa)$	n	$Y\ (MPa)$	C_0	$\rho\ (MPa)$	$A_0\ (MPa)$	C_1	λ
351.6	0.82	266.0	84.00	0.226	105.6	13.15	0.350

Table 11 Hardening model coefficients for DP600

$K\ (MPa)$	n	$Y\ (MPa)$	C_0	$\rho\ (MPa)$	$A_0\ (MPa)$	C_1	λ
492.2	0.78	360.5	218.4	0.098	155.0	100.0	0.370

Table 12 Hardening model coefficients for EDDQ

$K\ (MPa)$	n	$Y\ (MPa)$	C_0	$\rho\ (MPa)$	$A_0\ (MPa)$	C_1	λ
323.6	0.96	151.8	135.6	0.133	172.0	14.40	0.400

7.2.2 Analytical Results

With the previous models implemented, a set of analytical stress-strain curves can be generated. The results are illustrated in Figure 56 for BH240, where the comparison to a without cross-hardening case is depicted in a magnified local figure. It can be seen that the analytical stress-strain curves correlate well with the experimental ones, especially around the loading transition area. All orientations in Figure 56 are described inclined to rolling direction. The longitudinal, diagonal, and transversal pre-strain indicate an orientation along 0°, 45°, and 90°, respectively. The experimental test result marked as "AR" indicates a monotonic uniaxial tension along a specific orientation. It is noted that the original experimental stress-strain data is not available under equi-biaxial tension as the first step loading. The rest of the results are shown in Appendix.

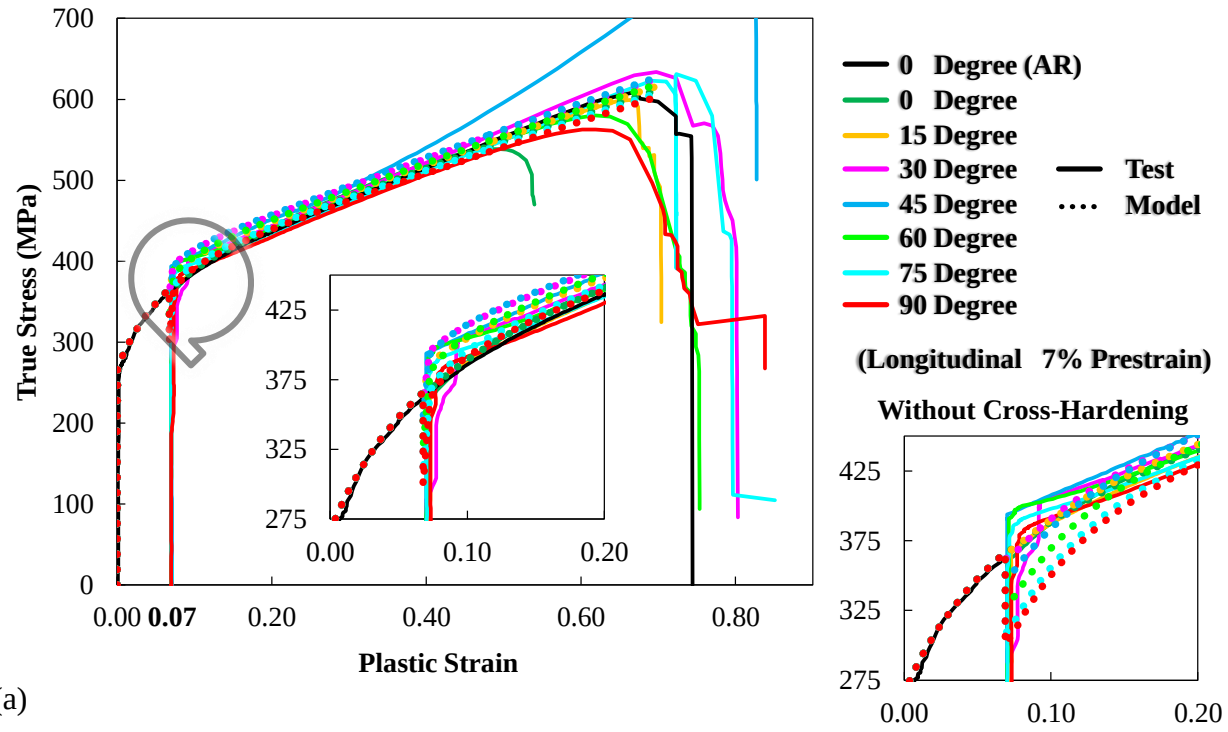
True Stress (MPa)
Plastic Strain
0.07
0 Degree (AR)
0 Degree
15 Degree
30 Degree
45 Degree
60 Degree
75 Degree
90 Degree
Test
Model
(Longitudinal 7% Prestrain)
Without Cross-Hardening

(a)

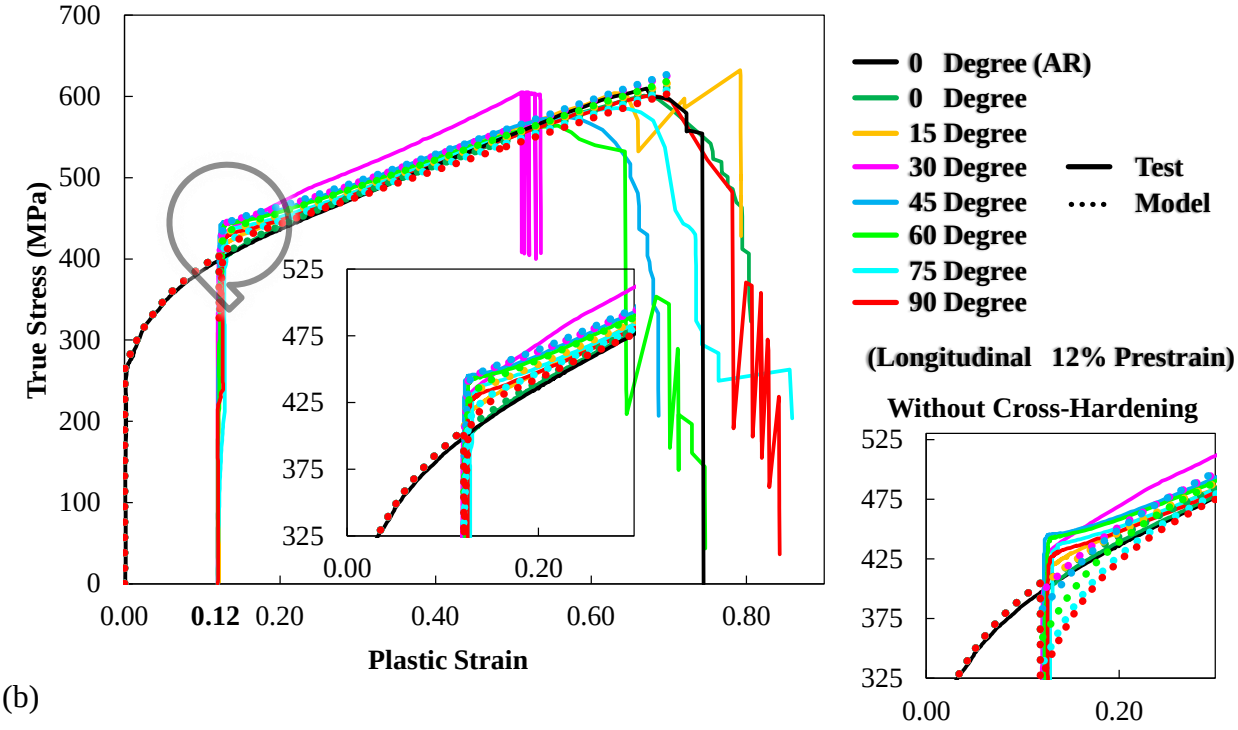
True Stress (MPa)
Plastic Strain
0.12
0 Degree (AR)
0 Degree
15 Degree
30 Degree
45 Degree
60 Degree
75 Degree
90 Degree
Test
Model
(Longitudinal 12% Prestrain)
Without Cross-Hardening

(b)

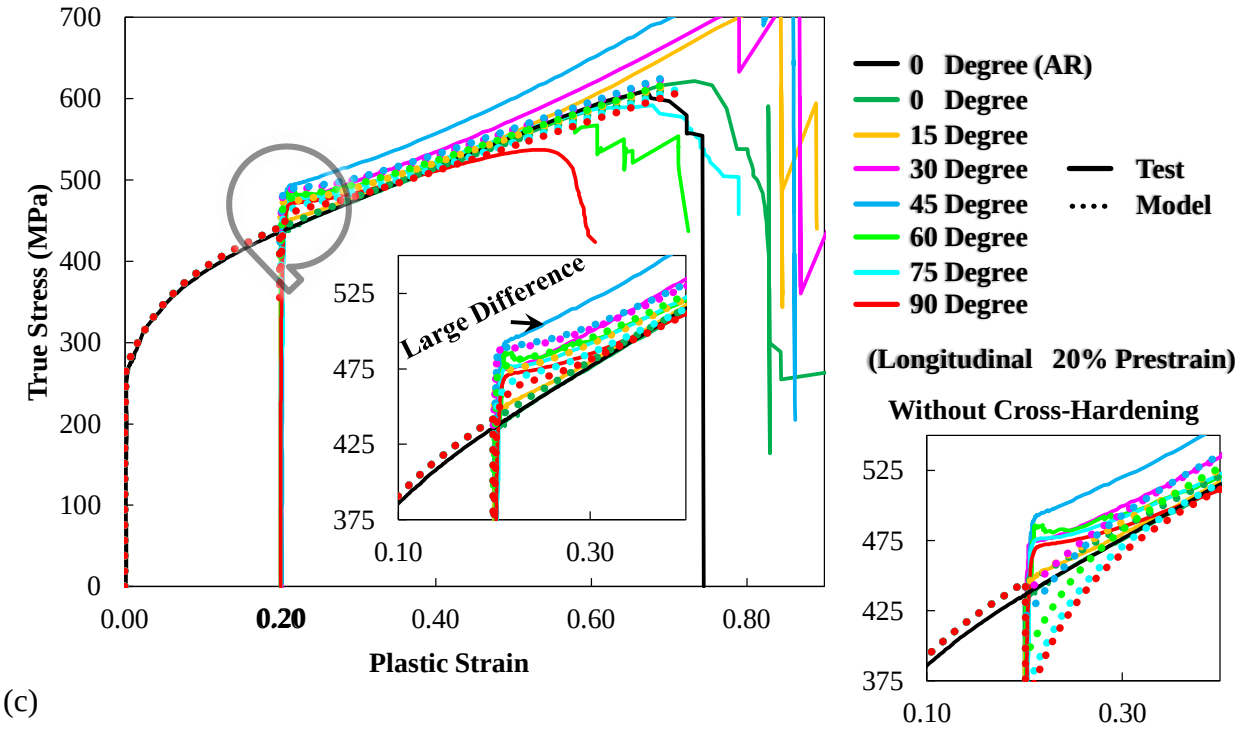
True Stress (MPa)
Plastic Strain
Large Difference
0 Degree (AR)
0 Degree
15 Degree
30 Degree
45 Degree
60 Degree
75 Degree
90 Degree
Test
Model
(Longitudinal 20% Prestrain)
Without Cross-Hardening

(c)

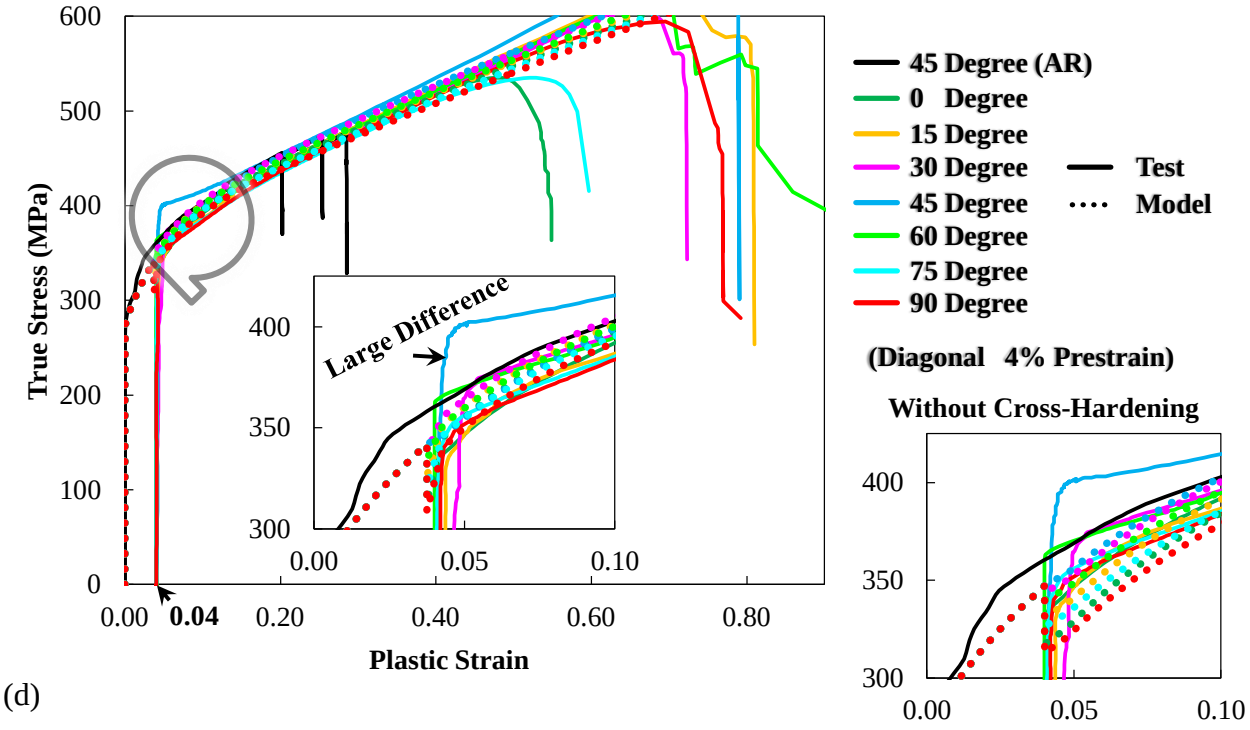
True Stress (MPa)
Plastic Strain
Large Difference
45 Degree (AR)
0 Degree
15 Degree
30 Degree
45 Degree
60 Degree
75 Degree
90 Degree
Test
Model
(Diagonal 4% Prestrain)
Without Cross-Hardening

(d)

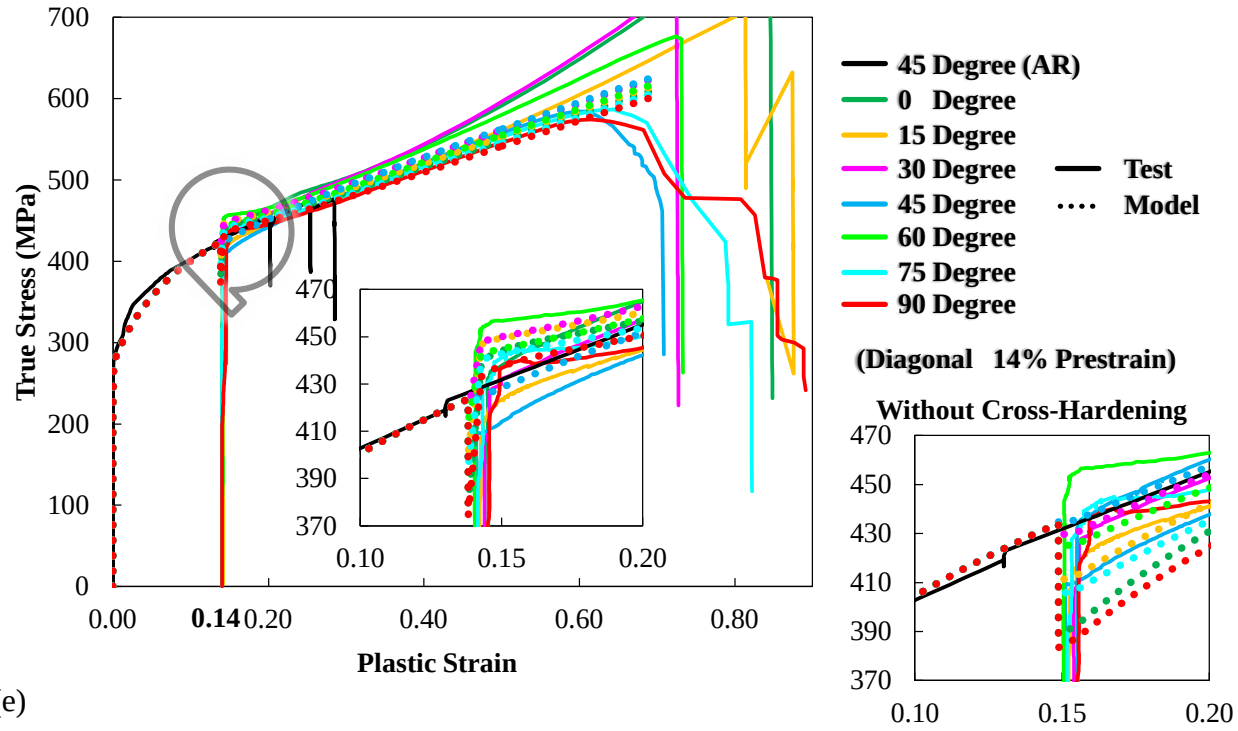
True Stress (MPa)
Plastic Strain
45 Degree (AR)
0 Degree
15 Degree
30 Degree
45 Degree
60 Degree
75 Degree
90 Degree
Test
Model
(Diagonal 14% Prestrain)
Without Cross-Hardening

(e)

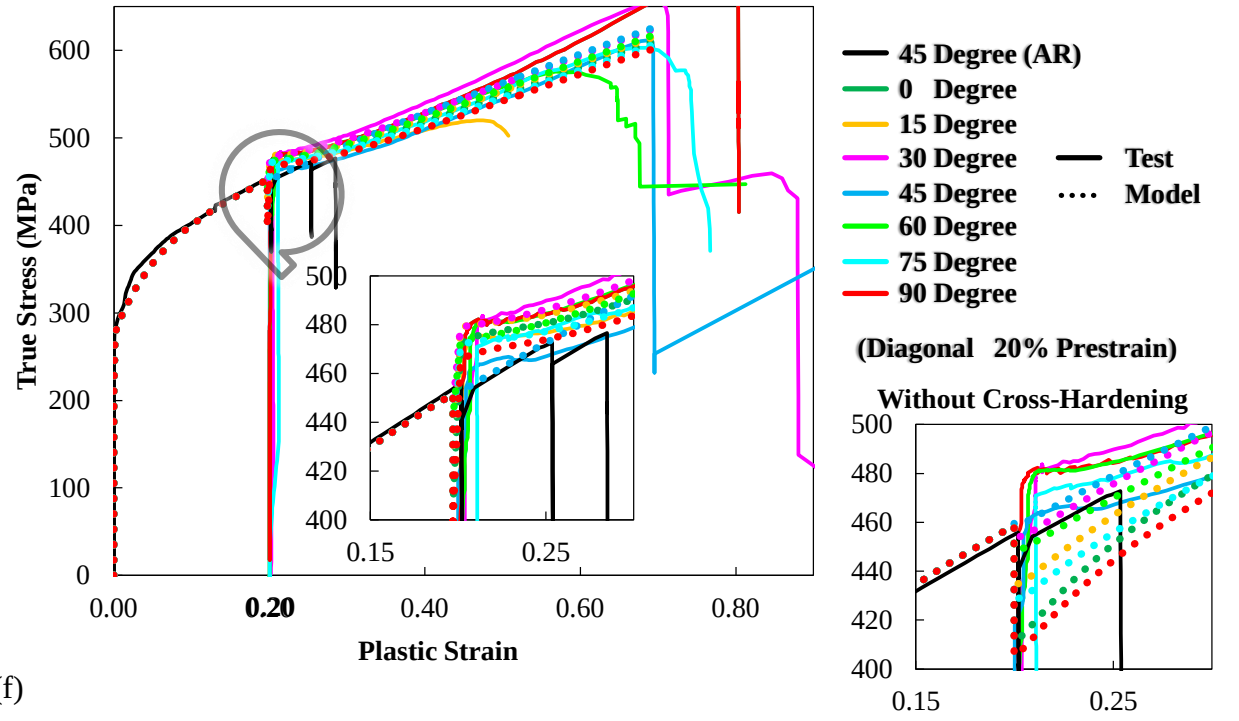
True Stress (MPa)
Plastic Strain
45 Degree (AR)
0 Degree
15 Degree
30 Degree
45 Degree
60 Degree
75 Degree
90 Degree
Test
Model
(Diagonal 20% Prestrain)
Without Cross-Hardening

(f)

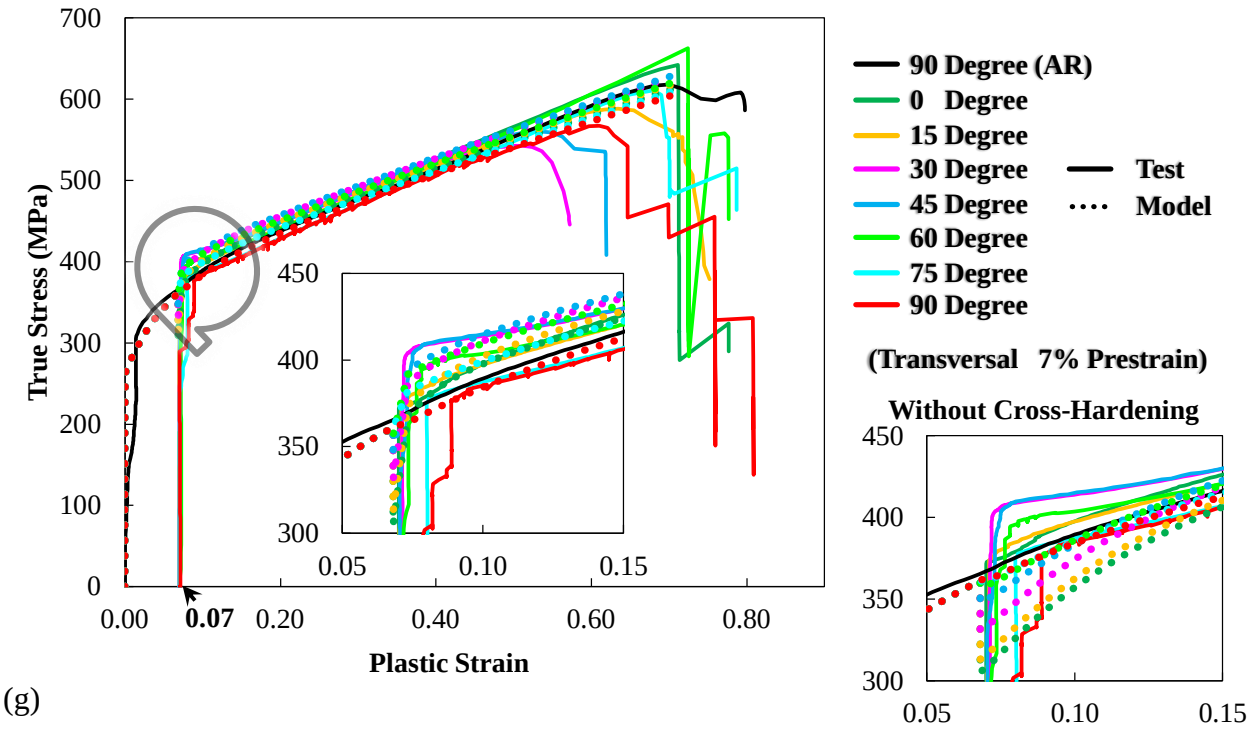
True Stress (MPa)
Plastic Strain
0.07
90 Degree (AR)
0 Degree
15 Degree
30 Degree
45 Degree
60 Degree
75 Degree
90 Degree
Test
Model
(Transversal 7% Prestrain)
Without Cross-Hardening

(g)

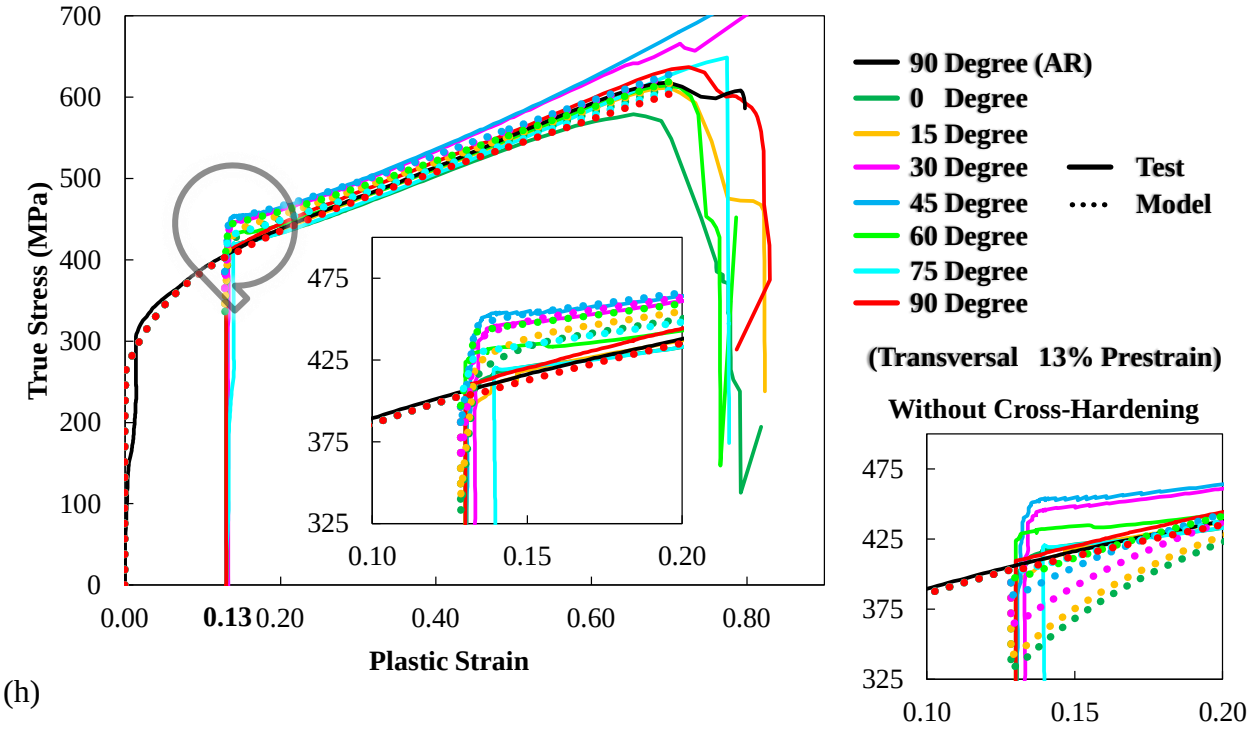
True Stress (MPa)
Plastic Strain
0.13
90 Degree (AR)
0 Degree
15 Degree
30 Degree
45 Degree
60 Degree
75 Degree
90 Degree
Test
Model
(Transversal 13% Prestrain)
Without Cross-Hardening

(h)

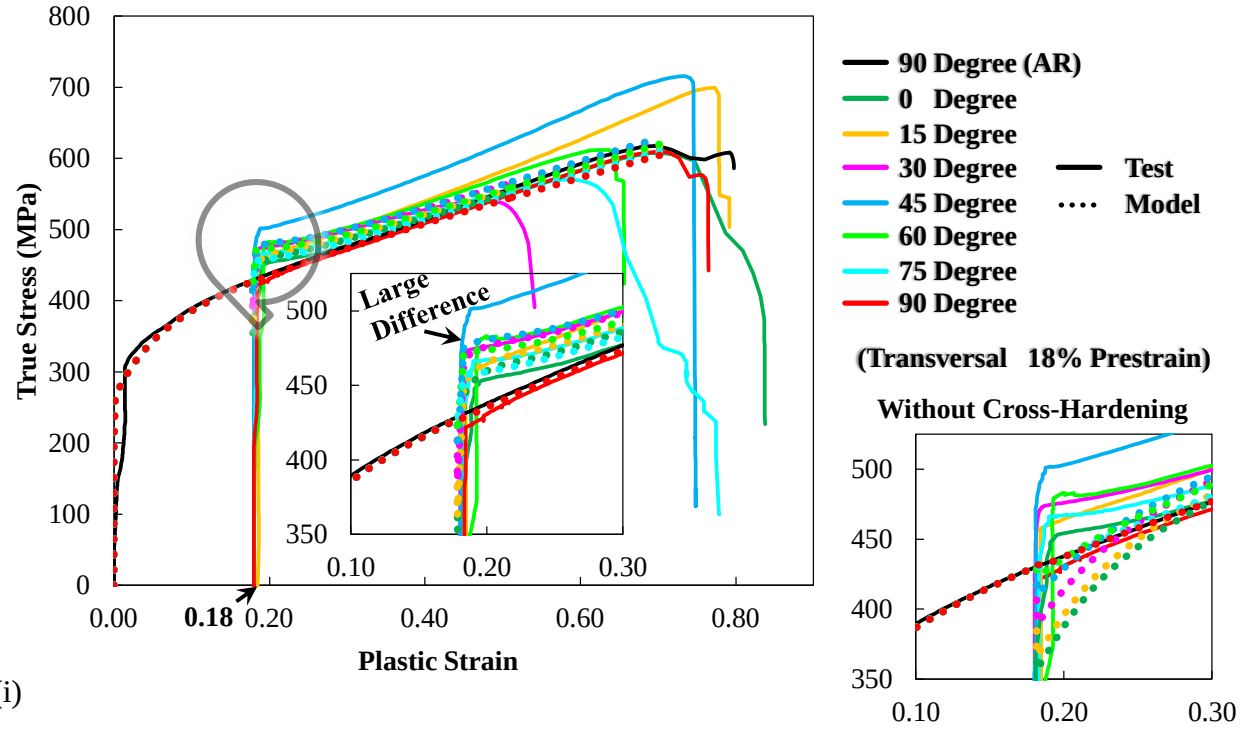
True Stress (MPa)
Plastic Strain
0.18
Large Difference
90 Degree (AR)
0 Degree
15 Degree
30 Degree
45 Degree
60 Degree
75 Degree
90 Degree
Test
Model
(Transversal 18% Prestrain)
Without Cross-Hardening

(i)

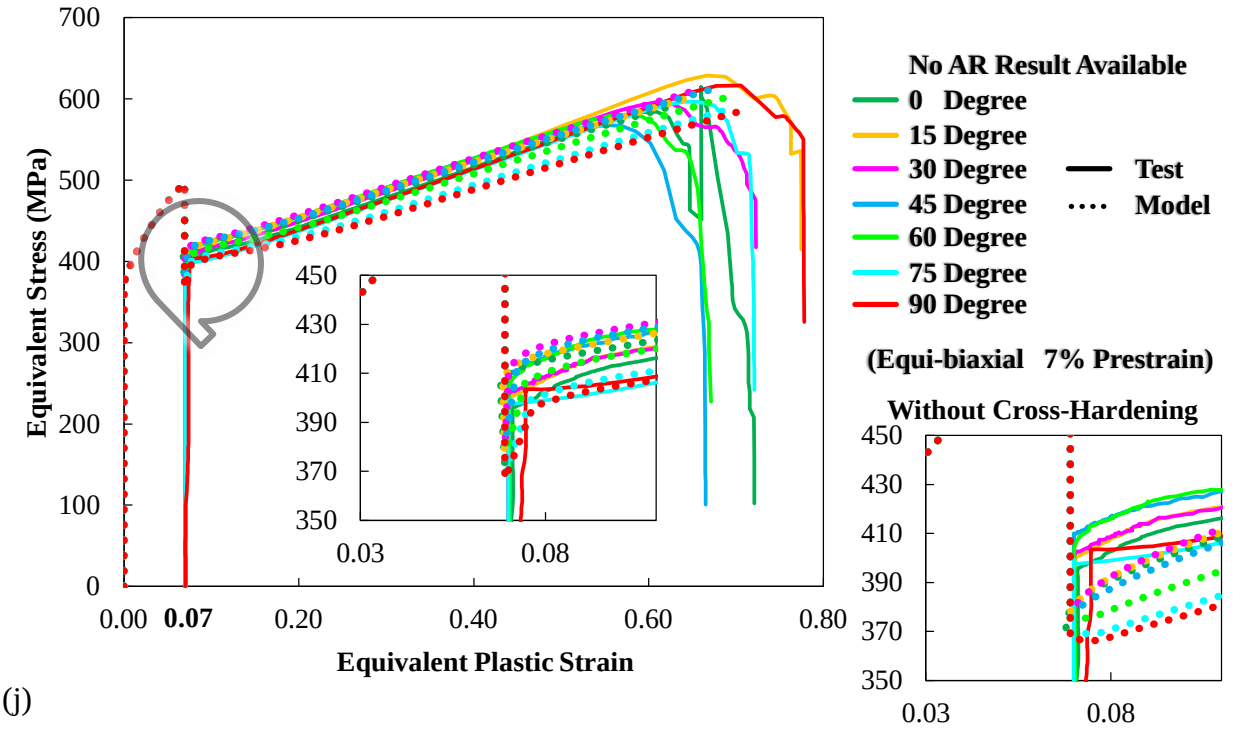
Equivalent Stress (MPa)
Equivalent Plastic Strain
0.07
No AR Result Available
0 Degree
15 Degree
30 Degree
45 Degree
60 Degree
75 Degree
90 Degree
Test
Model
(Equi-biaxial 7% Prestrain)
Without Cross-Hardening

(j)

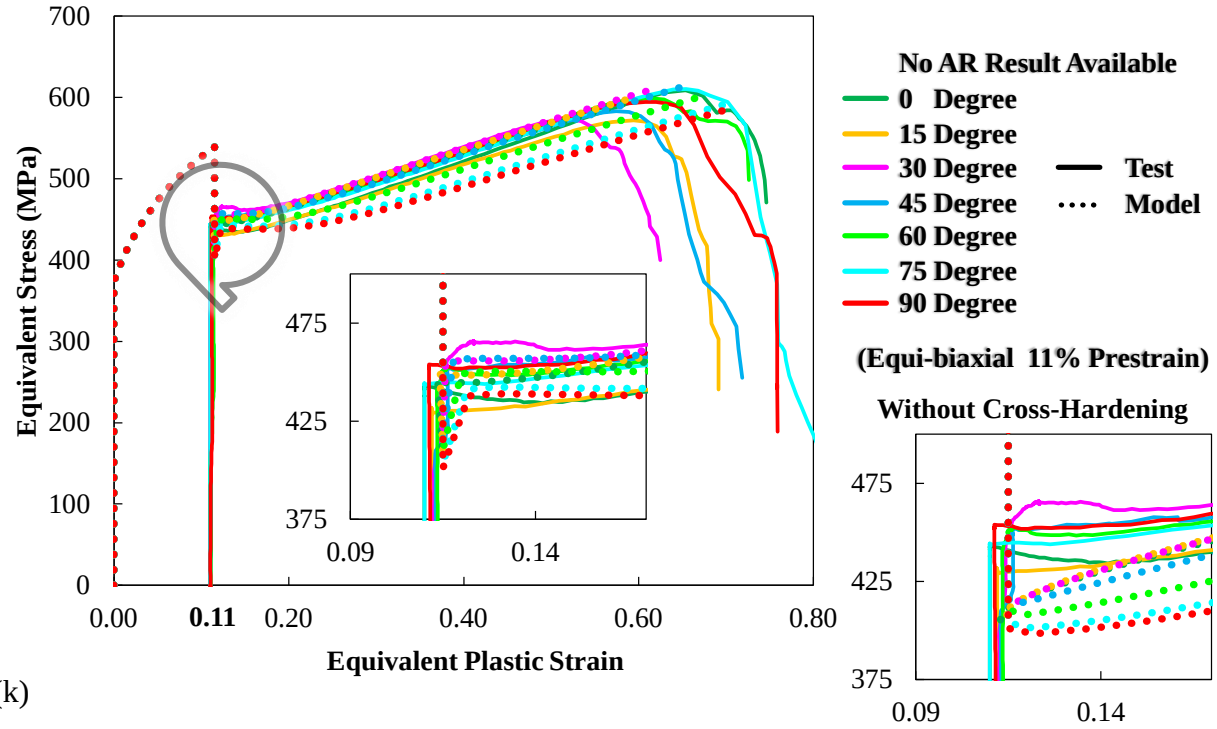

(k)

Figure 56 Calibration results for the cross-hardening for the materials of BH240, under the conditions of (a) 5% pre-strain, (b) 10% pre-strain, (c) 15% pre-strain along 0°, (d) 5% pre-strain, (e) 10% pre-strain, (f) 15% pre-strain along 45°, (g) 5% pre-strain, (h) 10% pre-strain, (i) 15% pre-strain along 90° uniaxial tension test, (j) 6% pre-strain, (j) 10% pre-strain of equi-biaxial tension (bulge) test.

CHAPTER 8 CONCLUSIONS AND FUTURE STUDIES

8.1 Summary of contribution

- A comprehensive set of mechanical experiments was conducted for magnesium AZ31B sheets under different monotonic loading conditions, including uniaxial tension, notch tension (equivalent to biaxial tension), uniaxial compression, biaxial compression, plane strain compression, through-thickness compression (equivalent to equi-biaxial tension with a hydrostatic pressure), pure shear, and punch test.
- Two different types of non-proportional loading tests were conducted along different orientations, a) uniaxial compression-tension reversal loading with different pre-compressive strains, and b) two-step uniaxial tension, known as cross-loading conditions, with different pre-strains. No apparent cross-hardening effect was observed in the two-step uniaxial tension experimental results.
- A new plastic flow parameter, Φ angle, was proposed to characterize the loading condition with the anisotropic effect as a uniform approach, comparing to the Lankford ratio or in-plane strain ratio. Both the plastic strain histories (exhibited by using equivalent plastic strain versus Φ angle) and strength behaviors were obtained for the loading conditions above, revealing a big picture of the mechanical responses of this material.
- A new Sachs-based constitutive model was developed for magnesium AZ31B-H24 alloy sheet, with a fully decoupled framework to combine isotropic, kinematic, and cross hardening behaviors. Three sets of state variables were defined to describe the following effects, a) loading history, including α_{ij} (known as the "dummy" back stress), X_K and X_C, b) twinning and de-twinning, including κ and μ, and c) pre-strain, including ε_C and ε_B. The

state variables were applied to incorporate the twinning/de-twinning effect under reversal loading and the cross-hardening behavior. The new model, with a CPB06ex2 anisotropic yield criterion, was sequentially calibrated by the experimental results from a set of different monotonic loading conditions, and a), b) above, with non-aftereffect.

- The mixed strain/stress invariants based MMC fracture model was transferred into an all-strain based MMC model under the plane stress condition, predicting the fracture strain in the space of Φ angle, instead of stress triaxiality and Lode angle parameter. The Φ angle could be directly measured by DIC, while stress triaxiality and Lode angle parameter required FE analysis to be determined. This method makes it possible to study fracture of materials while bypassing plasticity for materials with complex plastic properties.
- The calibrated new constitutive model, an anisotropic yield criterion CPB06ex2, and an eMMC anisotropic fracture model have been implemented into FE analysis to reproduce the non-proportional experiments through a user material subroutine (VUMAT) in Abaqus/Explicit. Good correlation was observed between experimental and simulation results, in both material strength and fracture behavior.
- The new developed framework was applied for TRIP780 with simplification under different monotonic loading conditions. The simulated results correlated well with experimental results.
- Two-step loading experiment results for the materials of BH240, DP600 and EDDQ were used to validate the cross-hardening model. Good correlation between experimental data and modeled strain-stress curves was observed.

8.2 Recommended Future Studies

In the present thesis, a comprehensive set of experiments and models has been conducted and developed for predicting material plasticity, hardening, and fracture behaviors. However, there are several more topics suggested for the future research.

1. **Generalization**. The magnesium AZ31B alloy sheet has a very special twinning/de-twinning effect during reversal loading, which can be incorporated by the current framework. However, this constitutive model is also expected to work for other materials, for example aluminum alloy sheets, steel sheets, under reversal loading. The model can be simplified or adjusted into a more generalized form, applying for a wider range of materials.

2. **Compressive failure simulation**. The current framework is implemented into FE simulation with using shell elements. However, a shape of slant fracture was observed in the compressive experiments, which cannot be completely simulated by shell elements. Ground on this, a FE model with 3D elements should be implemented to correlate with this phenomenon.

3. **Fracture propagation**. The post-fracture behavior, for example the growth of cracks after the initial fracture of punch test, is difficult to be simulated using the current fracture model with element deletion. The accuracy can be improved by using element split technique in the future**.**

4. **Simplification of anisotropic yield criterion**. This material, magnesium AZ31B alloy sheet has a complicated anisotropic yielding behavior, which requires the involvement of many material coefficients. This is not very user-friendly in the future application. An alternative way can be applied by using an associated plastic flow rule with the stress triaxiality and Lode angle dependency item, to reduce the number of material coefficients.

5. **Mechanical properties under high strain rates and elevated temperatures**. In the real applications of magnesium sheets, materials may be subjected to high strain rate (i.e. impact or stamping loading) and elevated temperatures (i.e. warm or hot forming). Therefore, it is important to extend the current theoretical framework to consider these two effects in the future.

APPENDIX: ANALYTICAL RESULTS FOR DP600 AND EDDQ

The analytical results for DP600 and EDDQ steel sheets are provided in Figure 57 and Figure 58, comparing to the experimental results under two-step uniaxial tension. The comparison to a without cross-hardening case is depicted in a magnified local figure. It can be seen that the analytical stress-strain curves correlate well with the experimental ones, especially around the loading transition area. All orientations in Figure 57 and Figure 58 are described inclined to rolling direction. The longitudinal, diagonal, and transversal pre-strain indicate an orientation along 0°, 45°, and 90°, respectively. The experimental test result marked as "AR" indicates a monotonic uniaxial tension along a specific orientation. It is noted that the original experimental stress-strain data is not available under equi-biaxial tension as the first step loading.

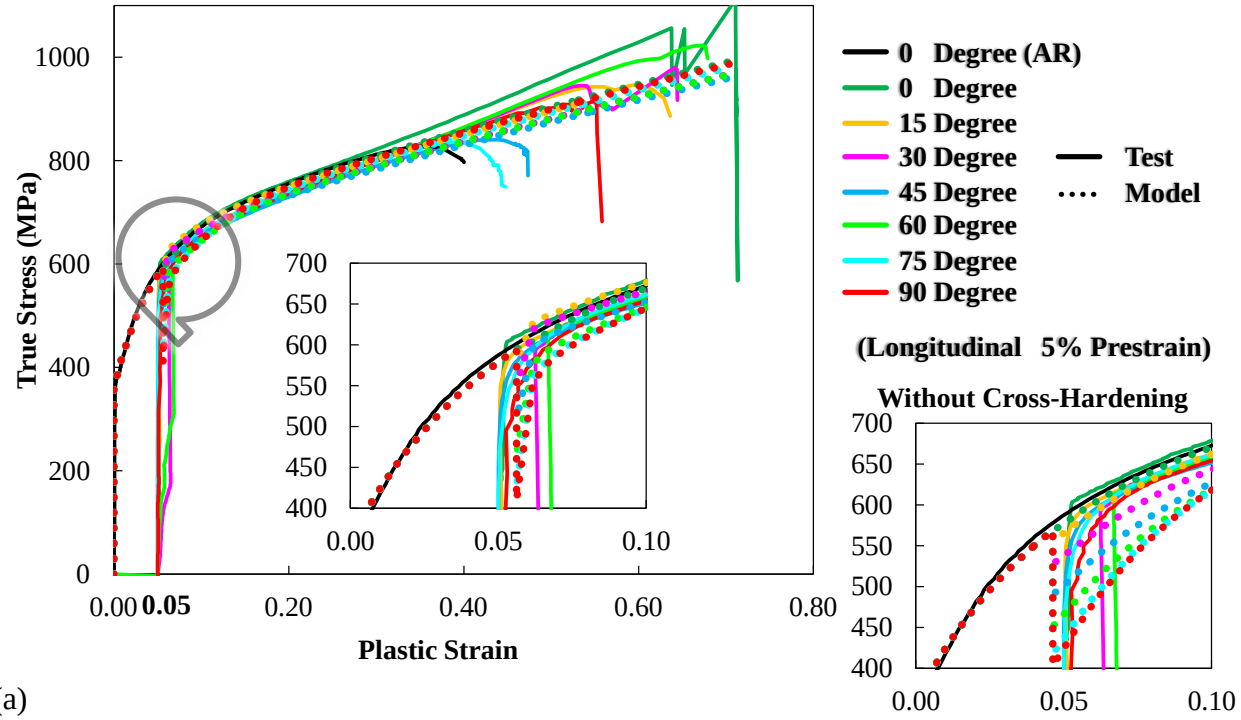
True Stress (MPa)
Plastic Strain
0 Degree (AR)
0 Degree
15 Degree
30 Degree
45 Degree
60 Degree
75 Degree
90 Degree
Test
Model
(Longitudinal 5% Prestrain)
Without Cross-Hardening

(a)

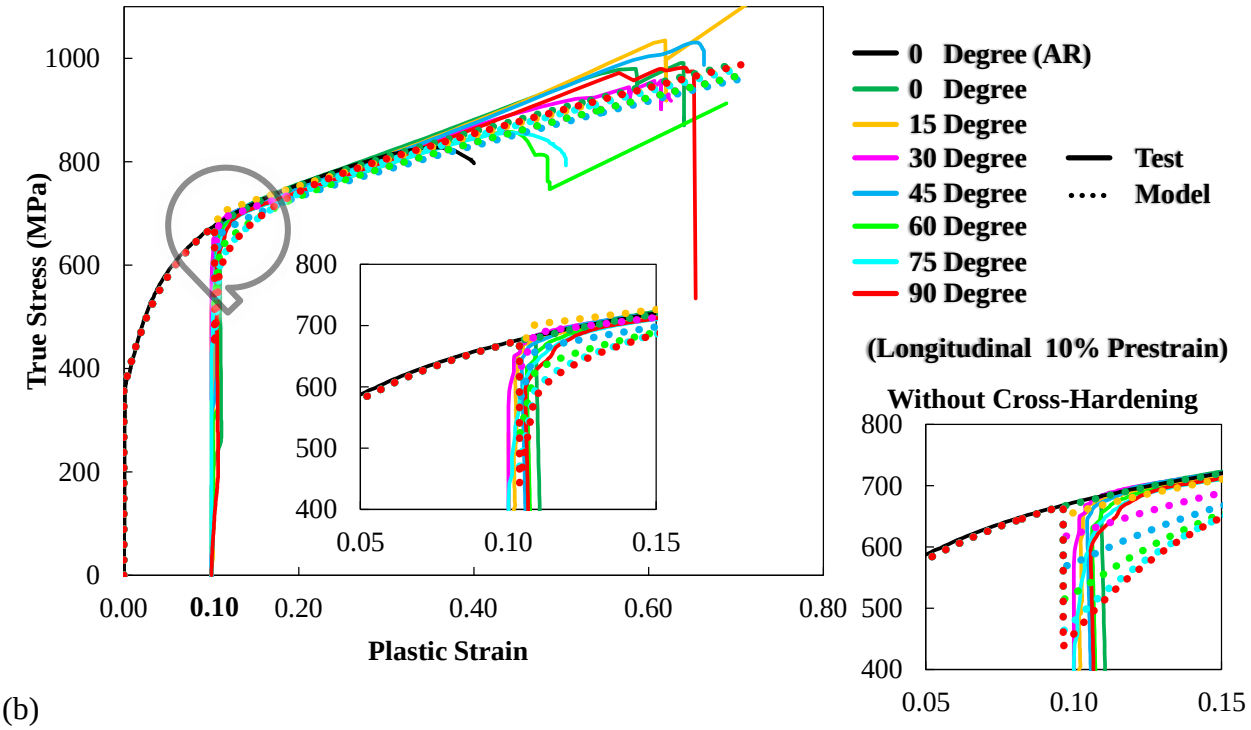
True Stress (MPa)
Plastic Strain
0 Degree (AR)
0 Degree
15 Degree
30 Degree
45 Degree
60 Degree
75 Degree
90 Degree
Test
Model
(Longitudinal 10% Prestrain)
Without Cross-Hardening

(b)

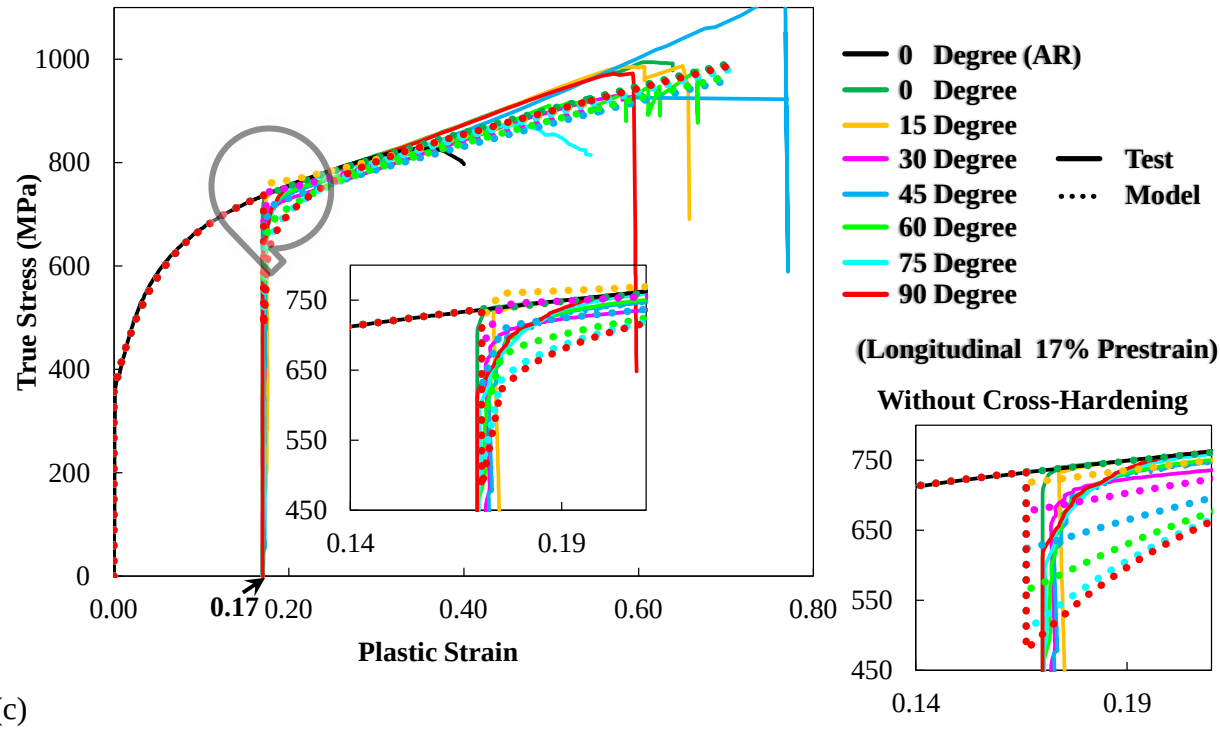
True Stress (MPa)
Plastic Strain
0.17
0 Degree (AR)
0 Degree
15 Degree
30 Degree
45 Degree
60 Degree
75 Degree
90 Degree
Test
Model
(Longitudinal 17% Prestrain)
Without Cross-Hardening

(c)

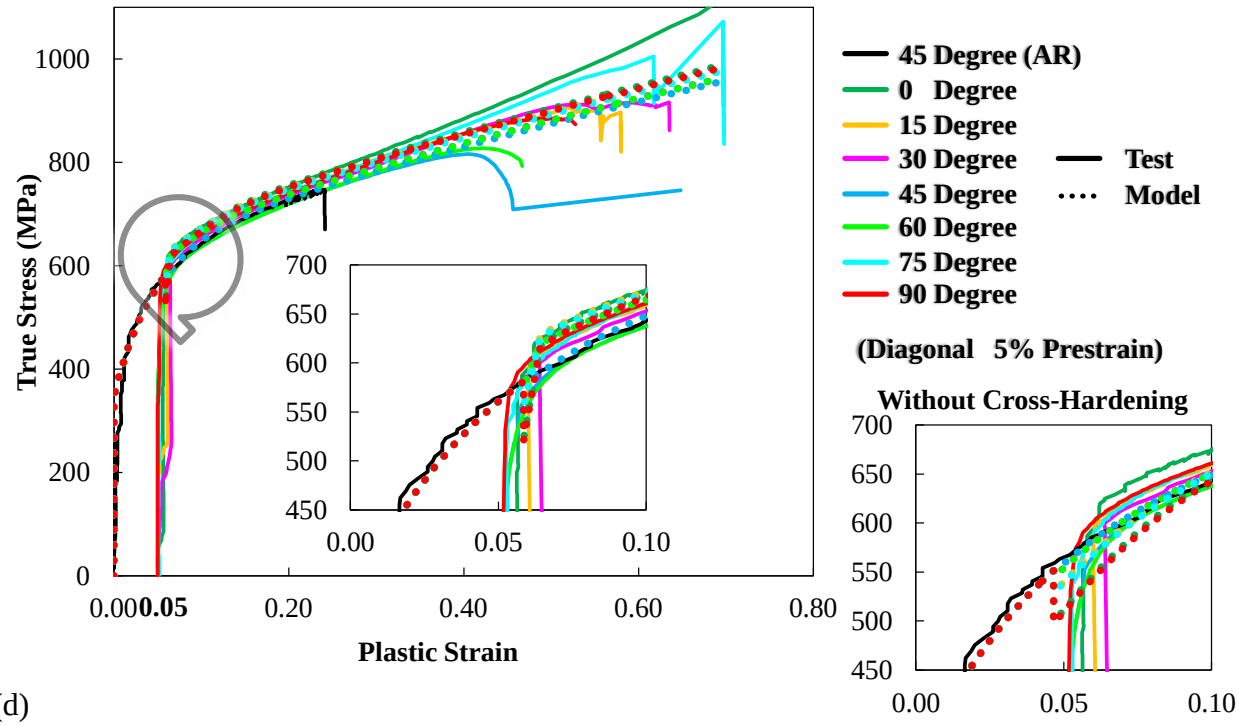
True Stress (MPa)
Plastic Strain
0.05
45 Degree (AR)
0 Degree
15 Degree
30 Degree
45 Degree
60 Degree
75 Degree
90 Degree
Test
Model
(Diagonal 5% Prestrain)
Without Cross-Hardening

(d)

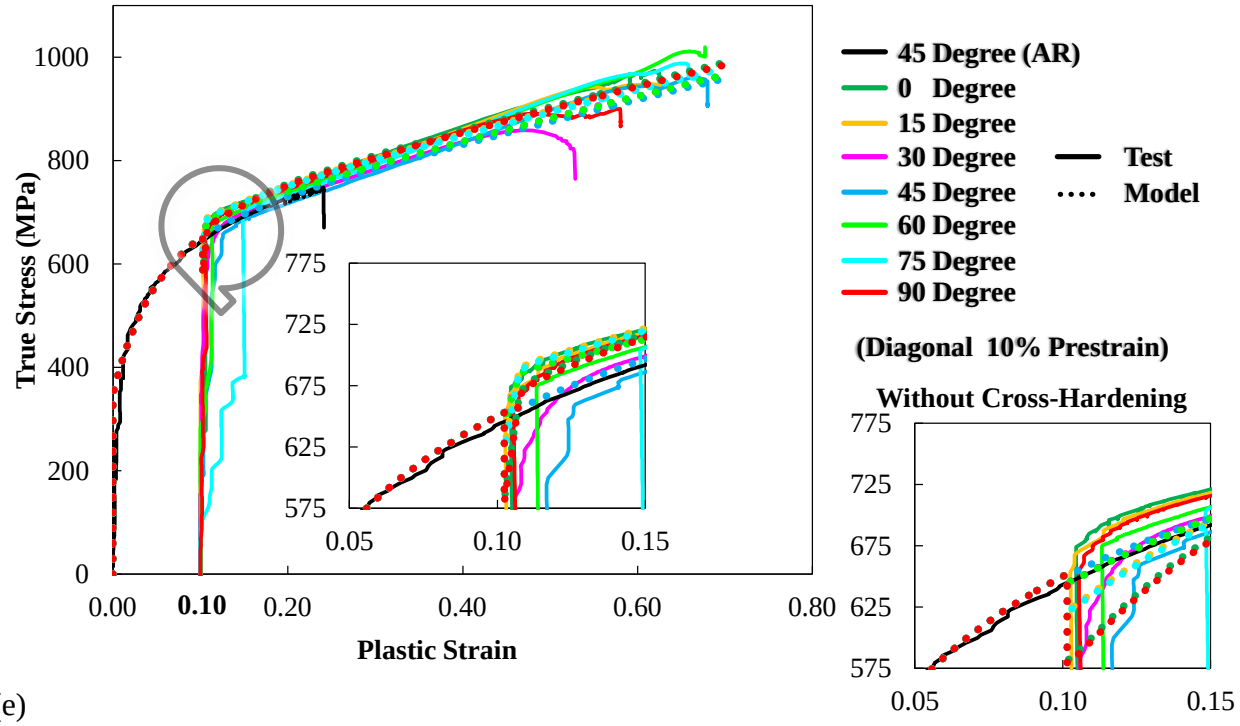
True Stress (MPa)
Plastic Strain
0.10
45 Degree (AR)
0 Degree
15 Degree
30 Degree
45 Degree
60 Degree
75 Degree
90 Degree
Test
Model
(Diagonal 10% Prestrain)
Without Cross-Hardening

(e)

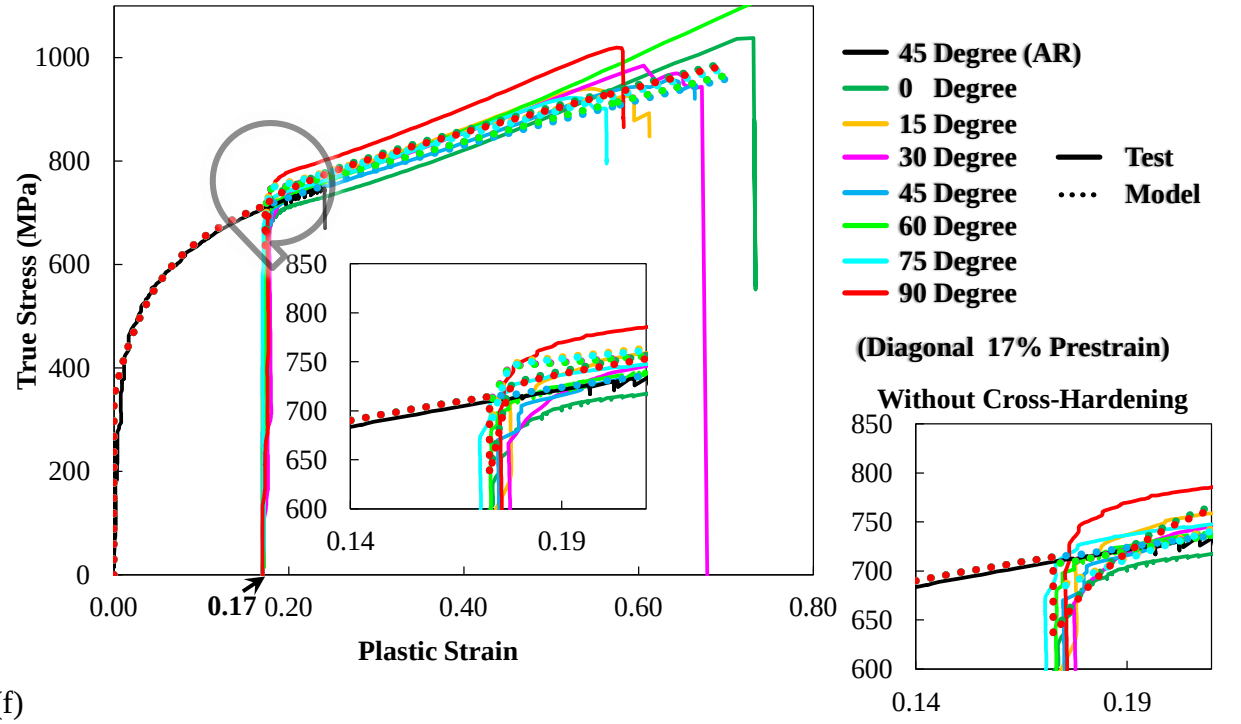
True Stress (MPa)
Plastic Strain
0.17
45 Degree (AR)
0 Degree
15 Degree
30 Degree
45 Degree
60 Degree
75 Degree
90 Degree
Test
Model
(Diagonal 17% Prestrain)
Without Cross-Hardening

(f)

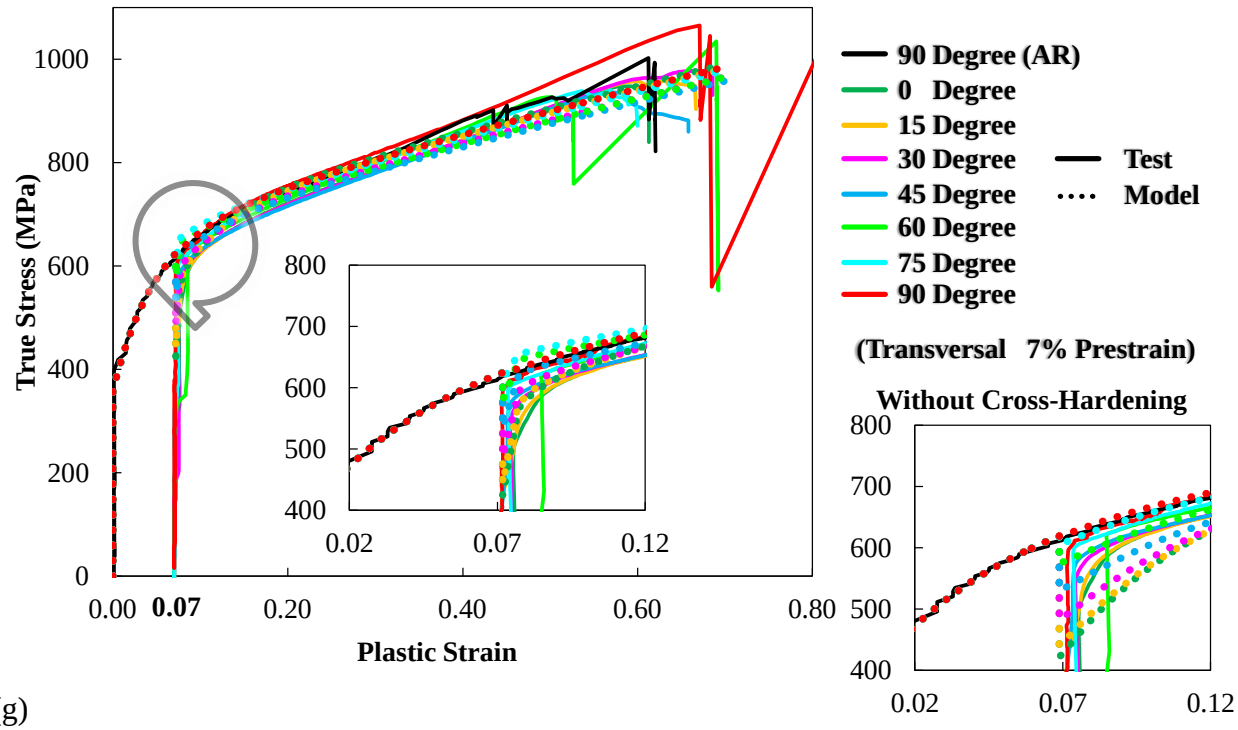
True Stress (MPa)
Plastic Strain
0.07
90 Degree (AR)
0 Degree
15 Degree
30 Degree
45 Degree
60 Degree
75 Degree
90 Degree
Test
Model
(Transversal 7% Prestrain)
Without Cross-Hardening

(g)

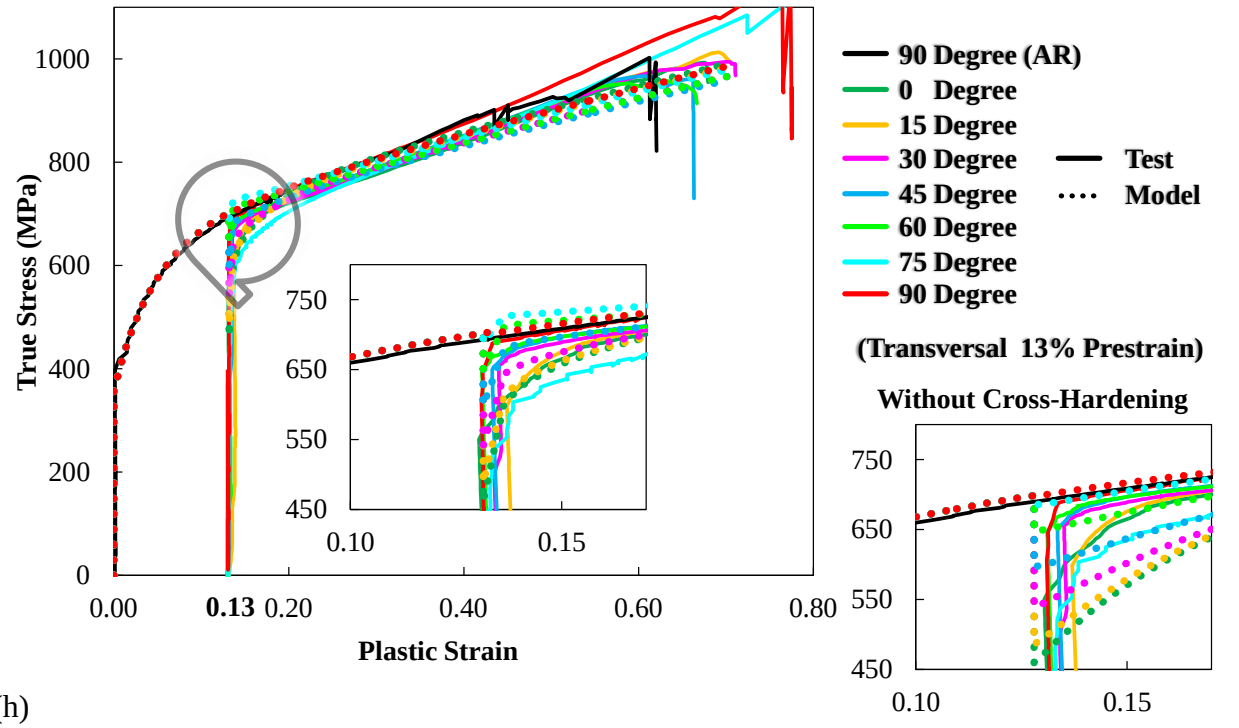
True Stress (MPa)
Plastic Strain
0.13
90 Degree (AR)
0 Degree
15 Degree
30 Degree
45 Degree
60 Degree
75 Degree
90 Degree
Test
Model
(Transversal 13% Prestrain)
Without Cross-Hardening

(h)

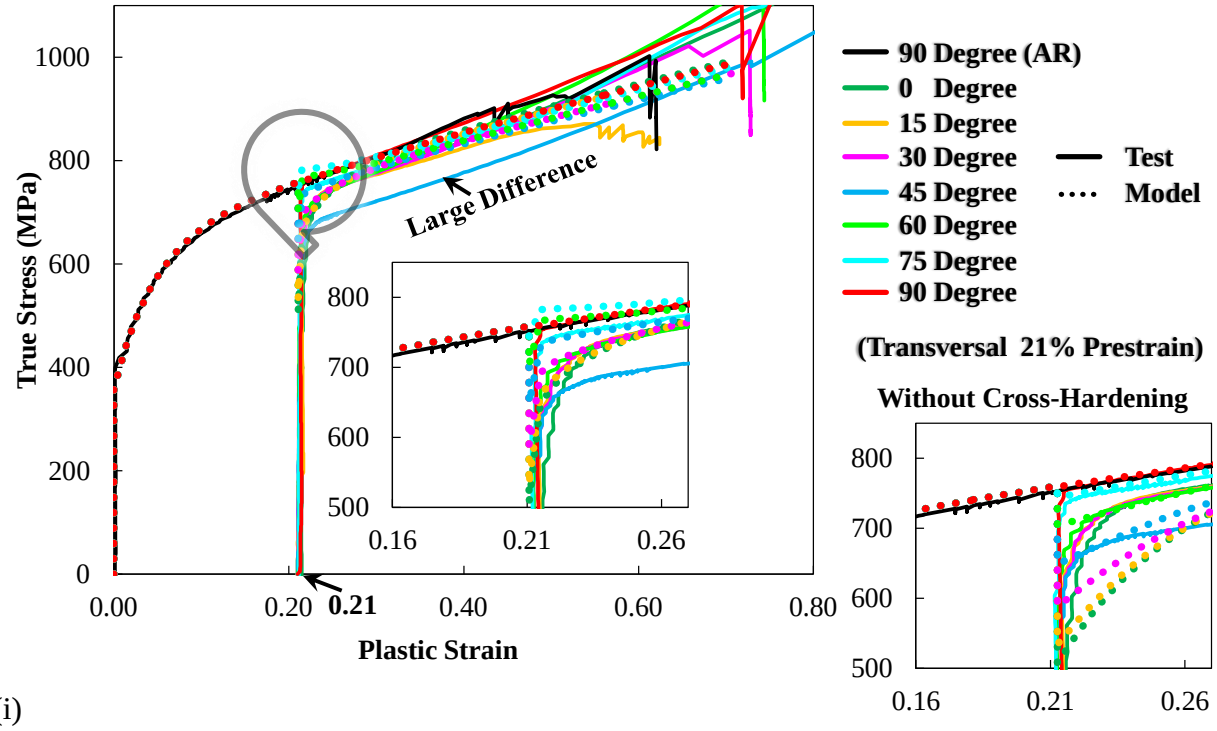
True Stress (MPa)
Plastic Strain
Large Difference
0.21
90 Degree (AR)
0 Degree
15 Degree
30 Degree
45 Degree
60 Degree
75 Degree
90 Degree
Test
Model
(Transversal 21% Prestrain)
Without Cross-Hardening

(i)

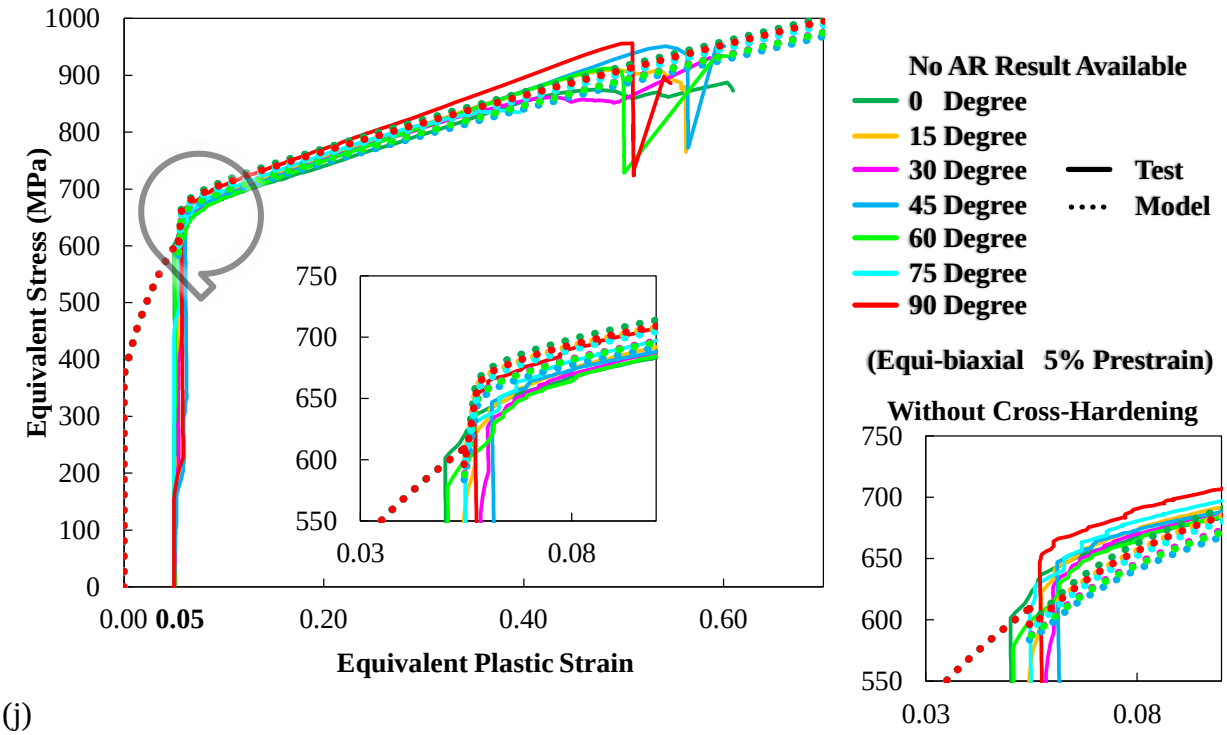
Equivalent Stress (MPa)
Equivalent Plastic Strain
0.05
No AR Result Available
0 Degree
15 Degree
30 Degree
45 Degree
60 Degree
75 Degree
90 Degree
Test
Model
(Equi-biaxial 5% Prestrain)
Without Cross-Hardening

(j)

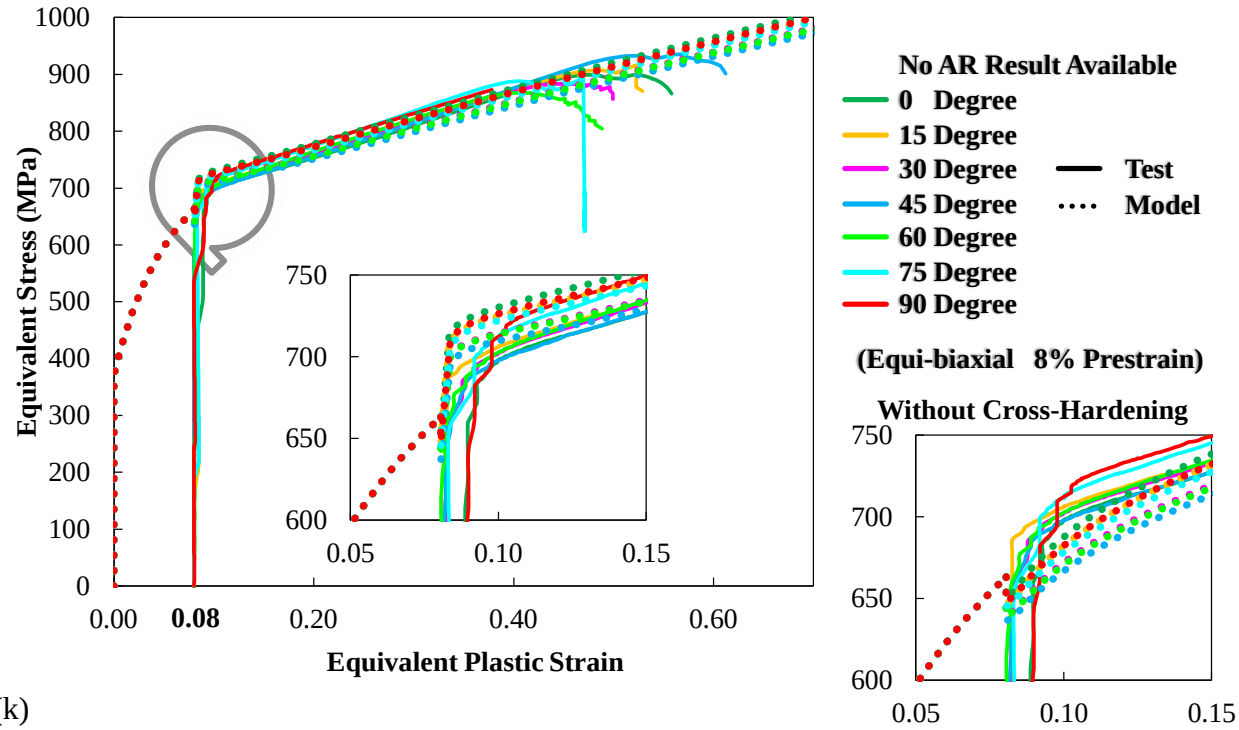

(k)

Figure 57 Calibration results for the cross-hardening for the materials of DP600, under the conditions of (a) 5% pre-strain, (b) 10% pre-strain, (c) 15% pre-strain along 0°, (d) 5% pre-strain, (e) 10% pre-strain, (f) 15% pre-strain along 45°, (g) 5% pre-strain, (h) 10% pre-strain, (i) 15% pre-strain along 90° uniaxial tension test, (j) 6% pre-strain, (j) 10% pre-strain of equi-biaxial tension (bulge) test.

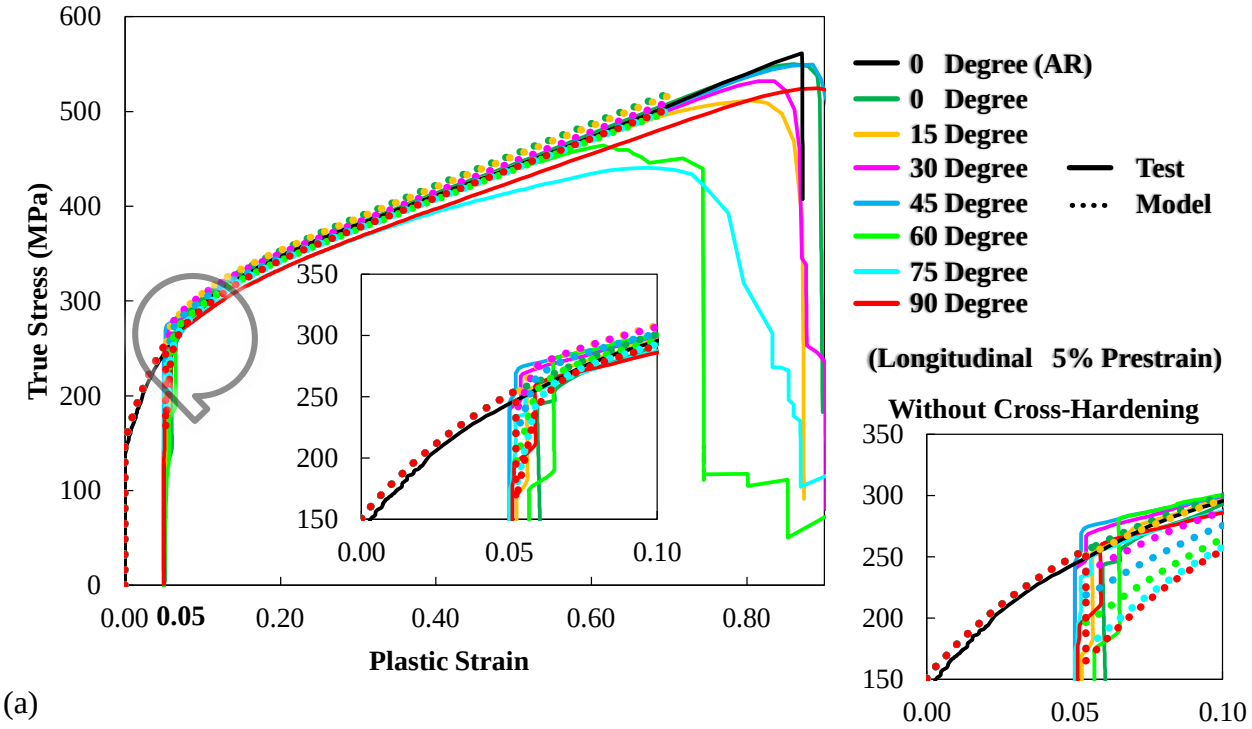
True Stress (MPa)
Plastic Strain
0.05
0 Degree (AR)
0 Degree
15 Degree
30 Degree
45 Degree
60 Degree
75 Degree
90 Degree
Test
Model
(Longitudinal 5% Prestrain)
Without Cross-Hardening

(a)

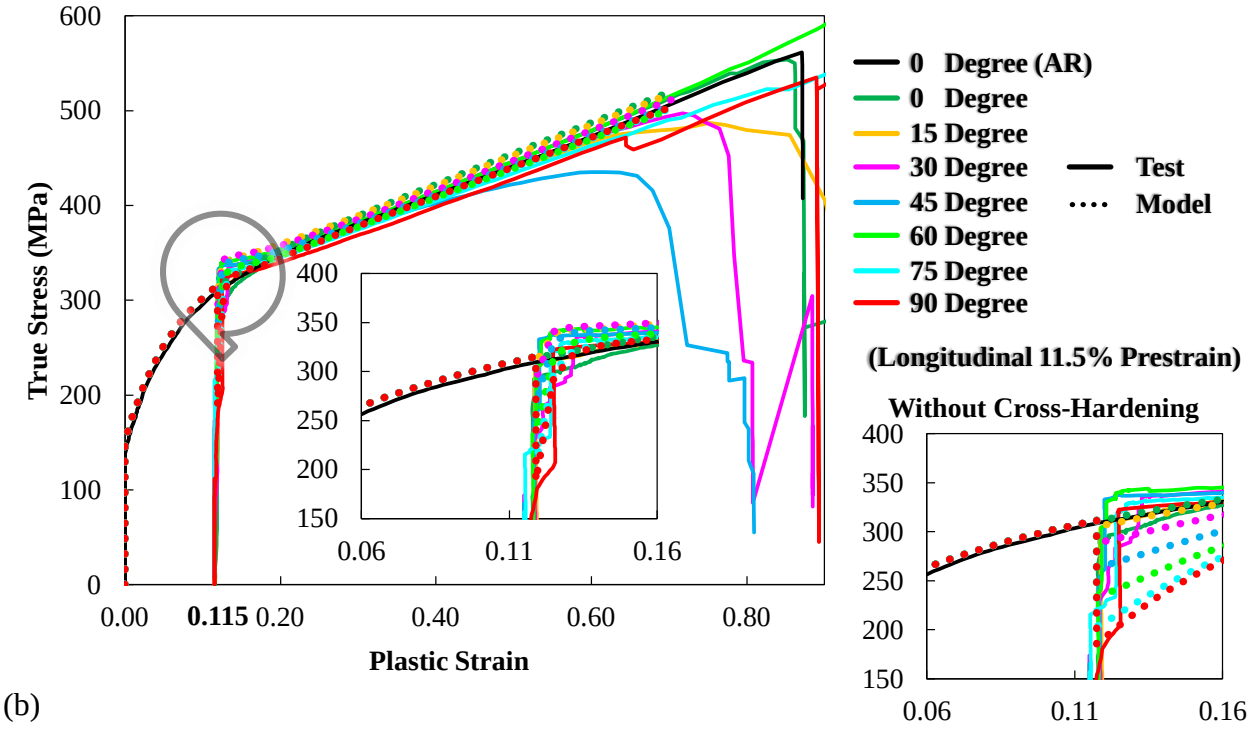
True Stress (MPa)
Plastic Strain
0.115
0 Degree (AR)
0 Degree
15 Degree
30 Degree
45 Degree
60 Degree
75 Degree
90 Degree
Test
Model
(Longitudinal 11.5% Prestrain)
Without Cross-Hardening

(b)

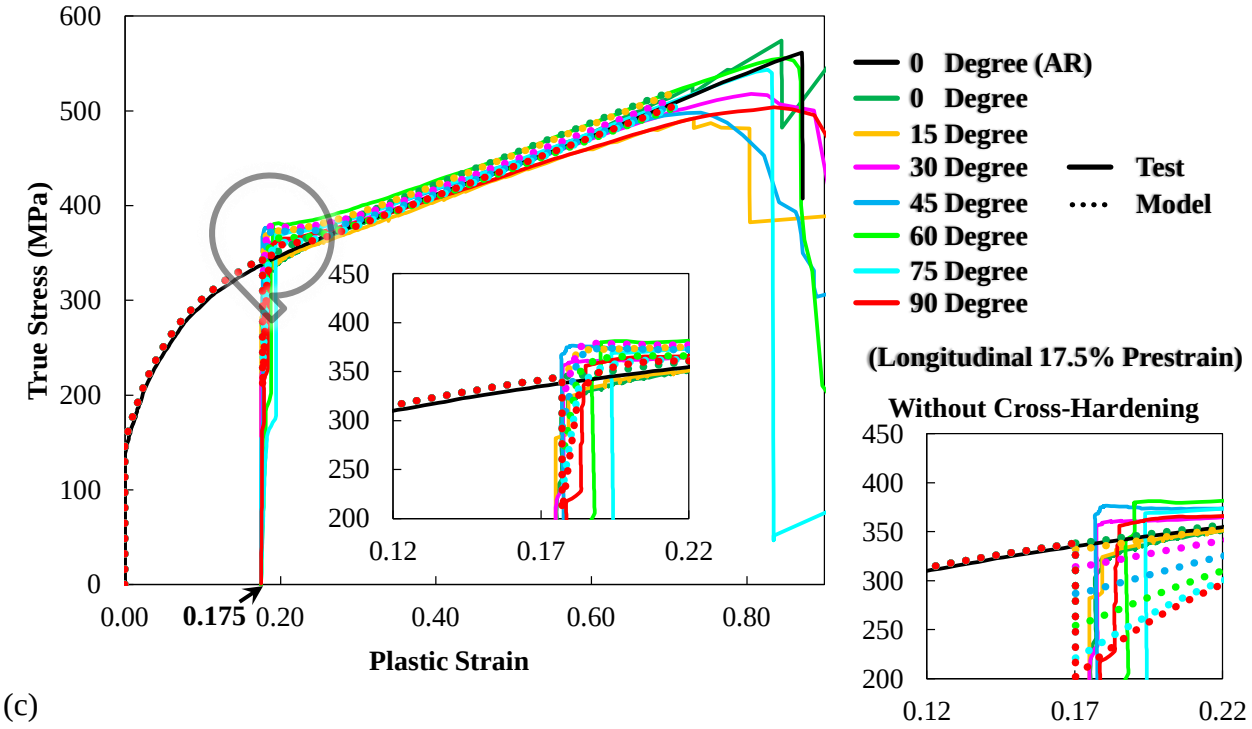
True Stress (MPa)
Plastic Strain
0.175
0 Degree (AR)
0 Degree
15 Degree
30 Degree
45 Degree
60 Degree
75 Degree
90 Degree
Test
Model
(Longitudinal 17.5% Prestrain)
Without Cross-Hardening

(c)

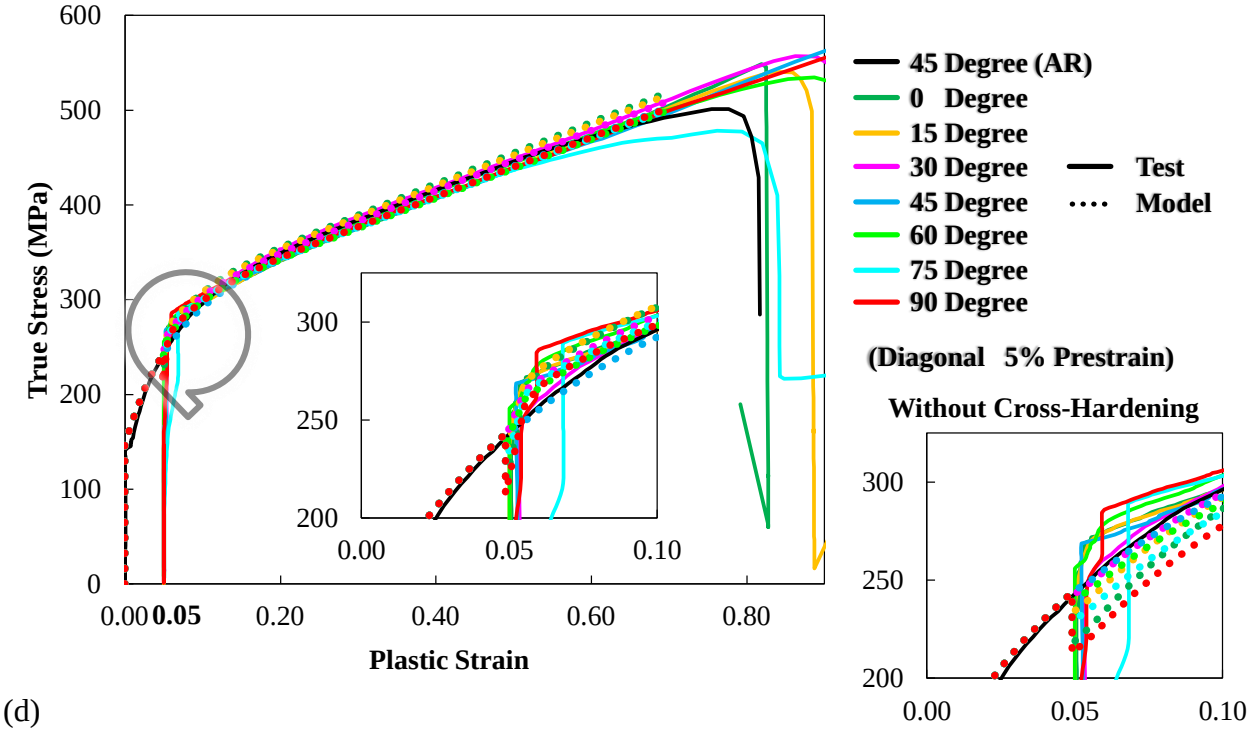
True Stress (MPa)
Plastic Strain
0.05
45 Degree (AR)
0 Degree
15 Degree
30 Degree
45 Degree
60 Degree
75 Degree
90 Degree
Test
Model
(Diagonal 5% Prestrain)
Without Cross-Hardening

(d)

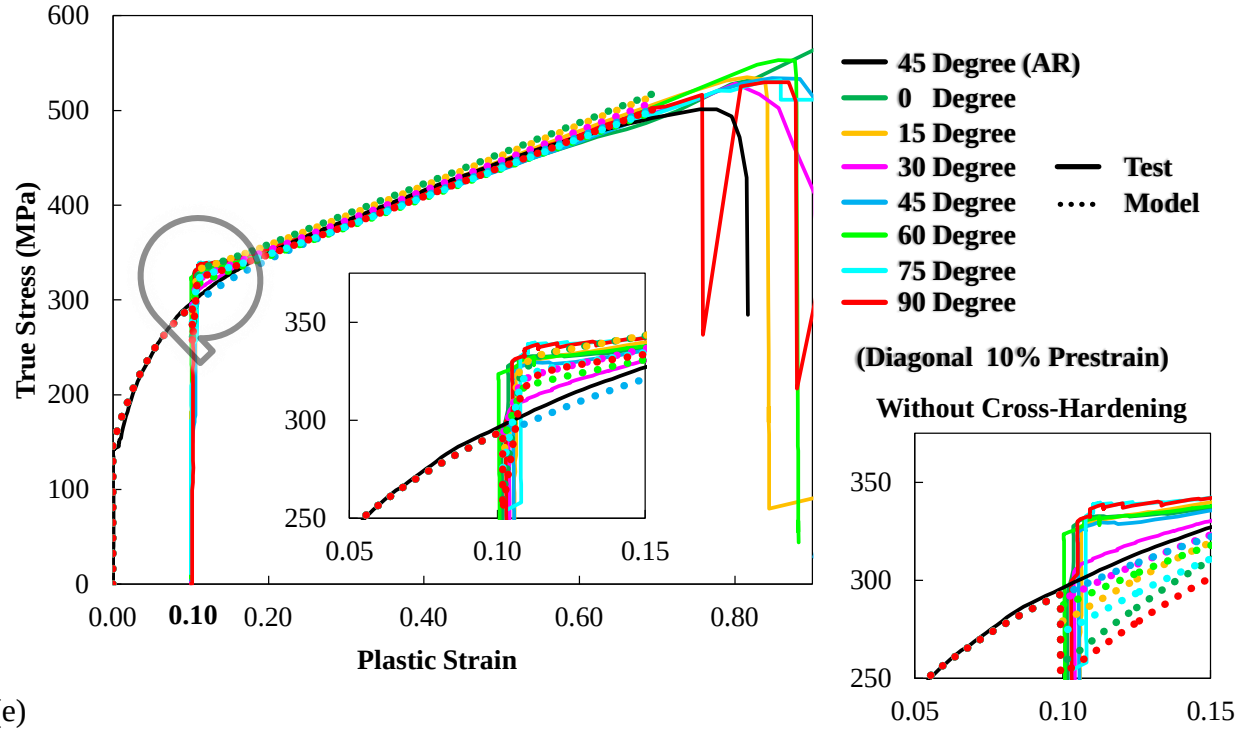
True Stress (MPa)
Plastic Strain
0.10
45 Degree (AR)
0 Degree
15 Degree
30 Degree
45 Degree
60 Degree
75 Degree
90 Degree
Test
Model
(Diagonal 10% Prestrain)
Without Cross-Hardening

(e)

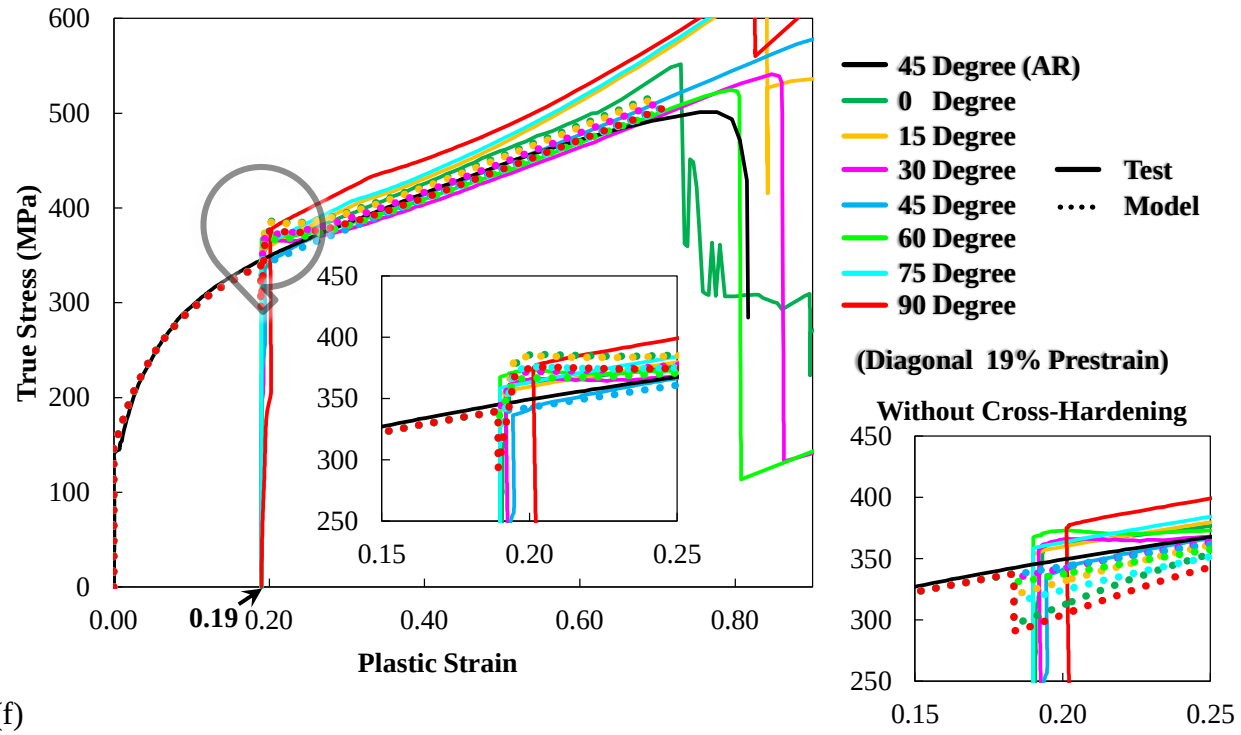
True Stress (MPa)
Plastic Strain
0.19
45 Degree (AR)
0 Degree
15 Degree
30 Degree
45 Degree
60 Degree
75 Degree
90 Degree
Test
Model
(Diagonal 19% Prestrain)
Without Cross-Hardening

(f)

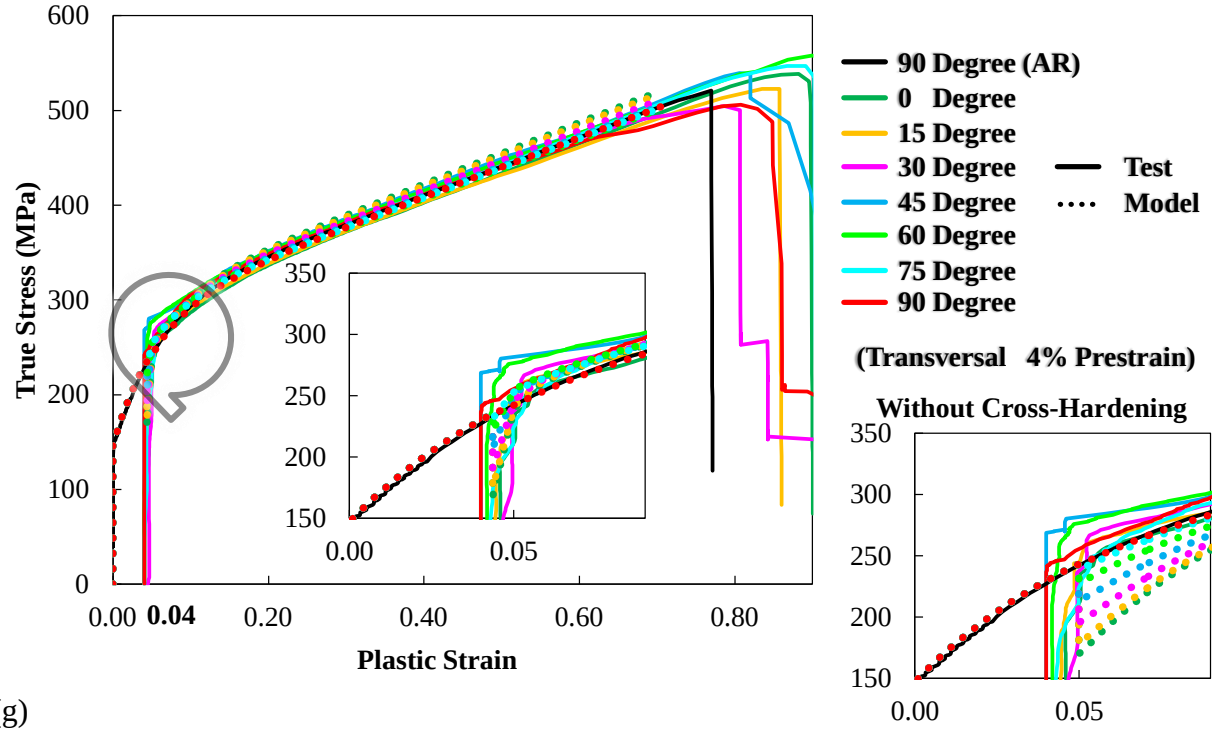
True Stress (MPa)
Plastic Strain
0.04
90 Degree (AR)
0 Degree
15 Degree
30 Degree
45 Degree
60 Degree
75 Degree
90 Degree
Test
Model
(Transversal 4% Prestrain)
Without Cross-Hardening

(g)

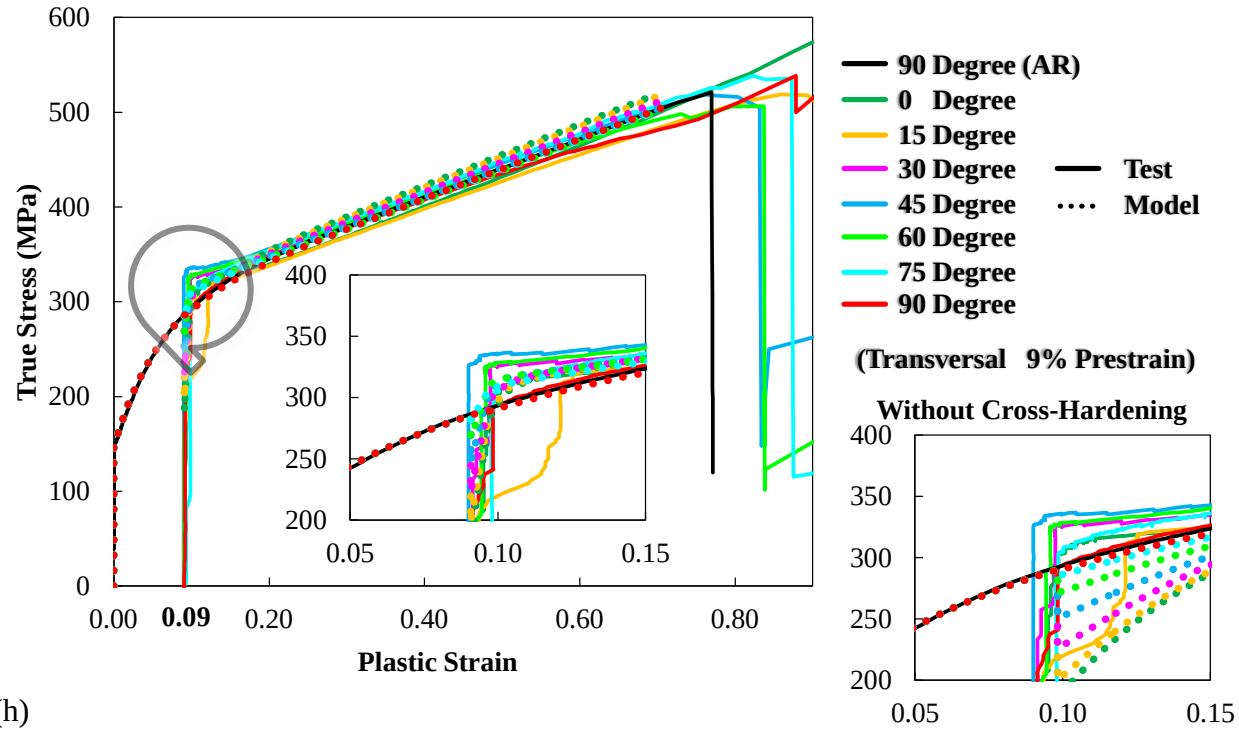
True Stress (MPa)
Plastic Strain
0.09
90 Degree (AR)
0 Degree
15 Degree
30 Degree
45 Degree
60 Degree
75 Degree
90 Degree
Test
Model
(Transversal 9% Prestrain)
Without Cross-Hardening

(h)

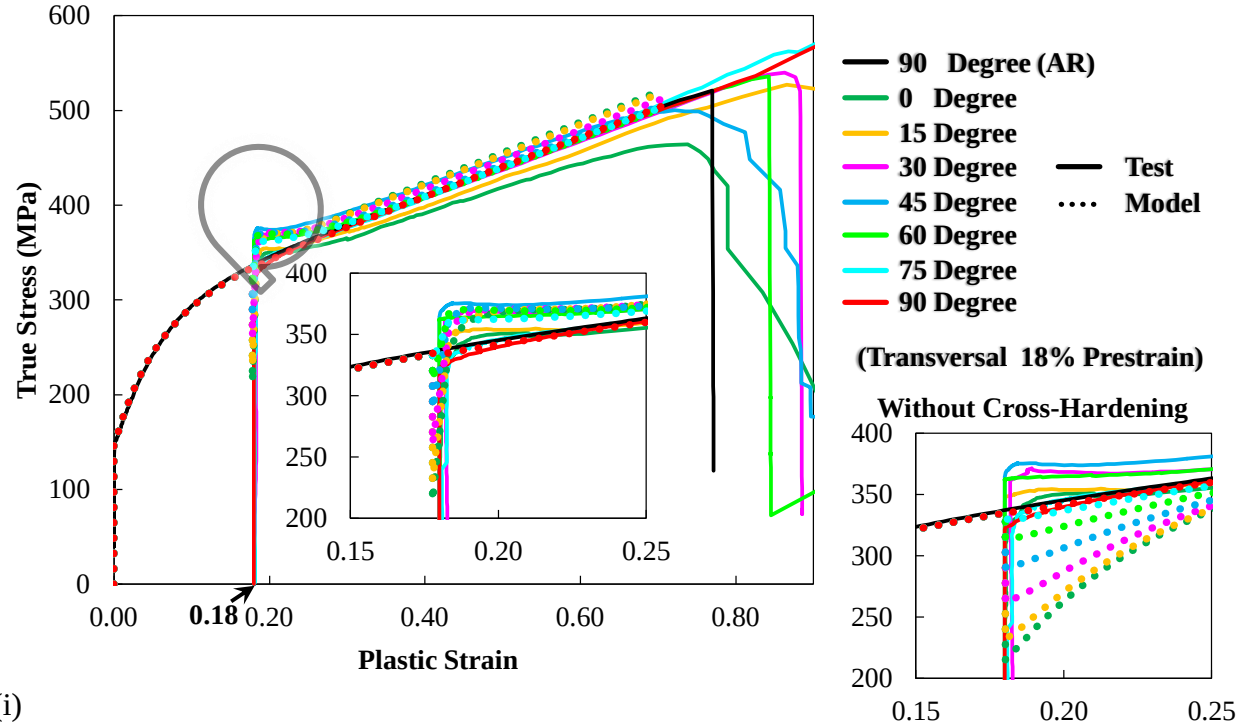
True Stress (MPa)
Plastic Strain
0.18
90 Degree (AR)
0 Degree
15 Degree
30 Degree
45 Degree
60 Degree
75 Degree
90 Degree
Test
Model
(Transversal 18% Prestrain)
Without Cross-Hardening

(i)

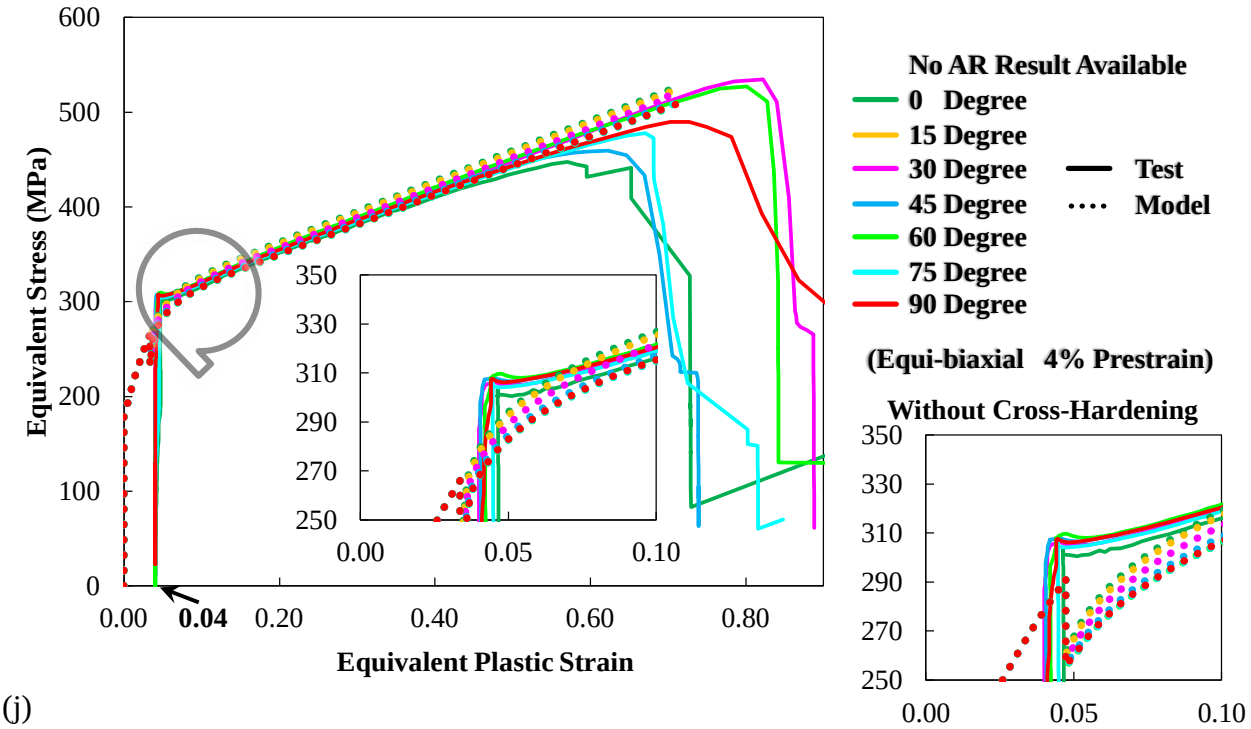
Equivalent Stress (MPa)
Equivalent Plastic Strain
0.04
No AR Result Available
0 Degree
15 Degree
30 Degree
45 Degree
60 Degree
75 Degree
90 Degree
Test
Model
(Equi-biaxial 4% Prestrain)
Without Cross-Hardening

(j)

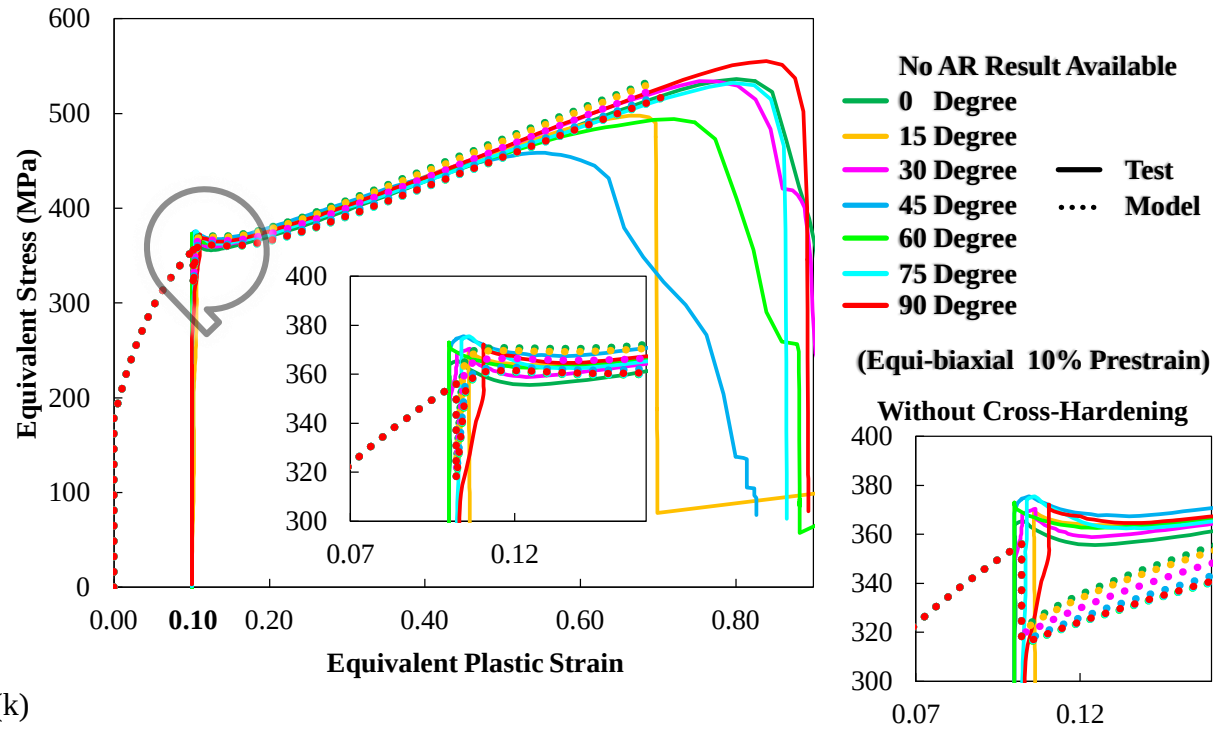

(k)

Figure 58 Calibration results for the cross-hardening for the materials of EDDQ, under the conditions of (a) 5% pre-strain, (b) 10% pre-strain, (c) 15% pre-strain along 0°, (d) 5% pre-strain, (e) 10% pre-strain, (f) 15% pre-strain along 45°, (g) 5% pre-strain, (h) 10% pre-strain, (i) 15% pre-strain along 90° uniaxial tension test, (j) 6% pre-strain, (j) 10% pre-strain of equi-biaxial tension (bulge) test.

REFERENCES

Abu-Farha, F., Hector, L. G., Jr., & Khraisheh, M. (2009). Cruciform-shaped specimens for elevated temperature biaxial testing of lightweight materials. *JOM, 61*(8), 48-56. doi: 10.1007/s11837-009-0121-8

Agnew, S. R., Tomé, C. N., Brown, D. W., Holden, T. M., & Vogel, S. C. (2003). Study of slip mechanisms in a magnesium alloy by neutron diffraction and modeling. *Scripta Materialia, 48*(8), 1003-1008. doi: http://dx.doi.org/10.1016/S1359-6462(02)00591-2

Agnew, S.R. (2002). *Plastic anisotropy of magnesium alloy AZ31B sheet*. Paper presented at the Magnesium Technology 2002, Seattle, WA; United States.

Algarni, Mohammed, Bai, Yuanli, & Choi, Youngsik. (2015). A study of Inconel 718 dependency on stress triaxiality and Lode angle in plastic deformation and ductile fracture. *Engineering Fracture Mechanics, 147*, 140-157. doi: http://dx.doi.org/10.1016/j.engfracmech.2015.08.007

Ambrogio, G., Bruni, C., Bruschi, S., Filice, L., Ghiotti, A., & Simoncini, M. (2008). Characterisation of AZ31B magnesium alloy formability in warm forming conditions. *International Journal of Material Forming, 1*(1), 205-208. doi: 10.1007/s12289-008-0027-y

Andar, Mohammad Omar, Kuwabara, Toshihiko, & Steglich, Dirk. (2012). Material modeling of AZ31 Mg sheet considering variation of r-values and asymmetry of the yield locus. *Materials Science and Engineering: A, 549*(0), 82-92. doi: http://dx.doi.org/10.1016/j.msea.2012.04.009

Armero, Francisco, & Oller, Sergio. (2000). A general framework for continuum damage models. II. Integration algorithms, with applications to the numerical simulation of porous metals. *International Journal of Solids and Structures, 37*(48–50), 7437-7464. doi: http://dx.doi.org/10.1016/S0020-7683(00)00206-7

Armstrong, P.L., & Frederick, C.O. (1966). A mathematical representation of the multiaxial Bauschinger effect, G.E.G.B. Report RD/B/N 731.

ASTM-E8-00. (2000). Standard test methods for tension testing of metallic materials. ASTM, West Conshohocken, PA, USA.

Bai, Yuanli. (2008). *Effect of Loading History on Necking and Fracture.* Massachusetts Institute of Technology.

Bai, Yuanli, & Atkins, Tony. (2011). Tension and Shear Cracking during Indentation of Ductile Materials by Opposed Wedges. *Submitted for publication*.

Bai, Yuanli, & Atkins, Tony. (2012). Tension and shear cracking during indentation of ductile materials by opposed wedges. *Engineering Fracture Mechanics, 96*(0), 49-60. doi: http://dx.doi.org/10.1016/j.engfracmech.2012.06.014

Bai, Yuanli, Teng, Xiaoqing, & Wierzbicki, Tomasz. (2009). On the Application of Stress Triaxiality Formula for Plane Strain Fracture Testing. *Journal of Engineering Materials and Technology, 131*(2), 021002.

Bai, Yuanli, & Wierzbicki, Tomasz. (2007). Application of Mohr-Coulomb Criterion to Ductile Fracture. *Submitted for publication*.

Bai, Yuanli, & Wierzbicki, Tomasz. (2008a). Forming Severity Concept for Predicting Sheet Necking under Complex Loading Histories. *International Journal of Mechanical Sciences, 50*, 1012-1022.

Bai, Yuanli, & Wierzbicki, Tomasz. (2008b). A new model of metal plasticity and fracture with pressure and Lode dependence. *International Journal of Plasticity, 24*, 1071-1096.

Bai, Yuanli, & Wierzbicki, Tomasz. (2010). Application of extended Mohr-Coulomb criterion to ductile fracture. *International Journal of Fracture, 161*, 1-20.

Bai, Yuanli, & Wierzbicki, Tomasz. (2015). A comparative study of three groups of ductile fracture loci in the 3D space. *Engineering Fracture Mechanics, 135*, 147-167. doi: http://dx.doi.org/10.1016/j.engfracmech.2014.12.023

Ball, EA, & Prangnell, PB. (1994). Tensile-compressive yield asymmetries in high strength wrought magnesium alloys. *Scripta Metallurgica et Materialia;(United States), 31*(2).

Bao, Yingbin. (2003). *Prediction of ductile crack formation in uncracked bodies.* Massachusetts Institute of Technology.

Bao, Yingbin, & Wierzbicki, Tomasz. (2004). On fracture locus in the equivalent strain and stress triaxiality space. *International Journal of Mechanical Sciences, 46*(1), 81-98.

Barlat, F., Brem, J. C., Yoon, J. W., Chung, K., Dick, R. E., Lege, D. J., . . . Chu, E. (2003). Plane stress yield function for aluminum alloy sheets--part 1: theory. *International Journal of Plasticity, 19*(9), 1297-1319.

Barlat, F., Ferreira Duarte, J. M., Gracio, J. J., Lopes, A. B., & Rauch, E. F. (2003). Plastic flow for non-monotonic loading conditions of an aluminum alloy sheet sample. *International Journal of Plasticity, 19*(8), 1215-1244. doi: http://dx.doi.org/10.1016/S0749-6419(02)00020-7

Barlat, Frédéric, Gracio, José J., Lee, Myoung-Gyu, Rauch, Edgar F., & Vincze, Gabriela. (2011). An alternative to kinematic hardening in classical plasticity. *International*

Journal of Plasticity, 27(9), 1309-1327. doi: http://dx.doi.org/10.1016/j.ijplas.2011.03.003

Barlat, Frédéric, Ha, Jinjin, Grácio, José J., Lee, Myoung-Gyu, Rauch, Edgar F., & Vincze, Gabriela. (2013). Extension of homogeneous anisotropic hardening model to cross-loading with latent effects. *International Journal of Plasticity, 46*(0), 130-142. doi: http://dx.doi.org/10.1016/j.ijplas.2012.07.002

Barnett, M. R. (2007). Twinning and the ductility of magnesium alloys: Part I: "Tension" twins. *Materials Science and Engineering: A, 464*(1–2), 1-7. doi: http://dx.doi.org/10.1016/j.msea.2006.12.037

Barnett, M. R., Keshavarz, Z., Beer, A. G., & Atwell, D. (2004). Influence of grain size on the compressive deformation of wrought Mg–3Al–1Zn. *Acta Materialia*, *52*(17), 5093-5103. doi: http://dx.doi.org/10.1016/j.actamat.2004.07.015

Barnett, M. R., Keshavarz, Z., & Ma, X. (2006). A semianalytical sachs model for the flow stress of a magnesium alloy. *Metallurgical and Materials Transactions A, 37*(7), 2283-2293. doi: 10.1007/BF02586147

Barsoum, Imad, & Faleskog, Jonas. (2007). Rupture mechanisms in combined tension and shear-Experiments. *International Journal of Solids and Structures, 44*(6), 1768-1786.

Beese, Allison M. (2011). *Experimental investigation and constitutive modeling of the large deformation behavior of anisotropic steel sheets undergoing strain-induced phase transformation.* Massachusetts Institute of Technology.

Boba, Mariusz. (2014). *Warm Forming Behaviour of ZEK100 and AZ31B Magnesium Alloy Sheet.* University of Waterloo.

Boger, R. K., Wagoner, R. H., Barlat, F., Lee, M. G., & Chung, K. (2005). Continuous, large strain, tension/compression testing of sheet material. *International Journal of Plasticity, 21*(12), 2319-2343. doi: http://dx.doi.org/10.1016/j.ijplas.2004.12.002

Brown, D. W., Agnew, S. R., Bourke, M. A. M., Holden, T. M., Vogel, S. C., & Tomé, C. N. (2005). Internal strain and texture evolution during deformation twinning in magnesium. *Materials Science and Engineering: A, 399*(1–2), 1-12. doi: http://dx.doi.org/10.1016/j.msea.2005.02.016

Cazacu, Oana, & Barlat, Frederic. (2004). A criterion for description of anisotropy and yield differential effects in pressure-insensitive metals. *International Journal of Plasticity, 20*(11), 2027-2045.

Cazacu, Oana, Plunkett, Brian, & Barlat, Frederic. (2006). Orthotropic yield criterion for hexagonal closed packed metals. *International Journal of Plasticity, 22*(7), 1171-1194.

Chaboche, J.L. (1977). Viscoplastic constitutive equations for the description of cyclic and anisotropic behavior of metals. *Bulletin de l'Academie Poloanise des Sciences. Serie des Sciences Techniques, 25*, 33.

Chandola, Nitin, Lebensohn, Ricardo A., Cazacu, Oana, Revil-Baudard, Benoit, Mishra, Raja K., & Barlat, Frédéric. (2015). Combined effects of anisotropy and tension–compression asymmetry on the torsional response of AZ31 Mg. *International Journal of Solids and Structures, 58*(Complete), 190-200. doi: 10.1016/j.ijsolstr.2015.01.001

Elektron, Magnesium. (2014): 1001 College Street, P.O. Box 258, Madison, IL 62060, USA.

Feigenbaum, H., & Dafalias, Y. (2008). Simple Model for Directional Distortional Hardening in Metal Plasticity within Thermodynamics. *Journal of Engineering Mechanics, 134*(9), 730-738. doi: 10.1061/(ASCE)0733-9399(2008)134:9(730)

Feigenbaum, Heidi P., & Dafalias, Yannis F. (2007). Directional distortional hardening in metal plasticity within thermodynamics. *International Journal of Solids and Structures, 44*(22–23), 7526-7542. doi: http://dx.doi.org/10.1016/j.ijsolstr.2007.04.025

Feng, Fei, Huang, Shangyu, Meng, Zhenghua, Hu, Jianhua, Lei, Yu, Zhou, Mengcheng, & Yang, Zhenzhen. (2014). A constitutive and fracture model for AZ31B magnesium alloy in the tensile state. *Materials Science and Engineering: A, 594*(0), 334-343. doi: http://dx.doi.org/10.1016/j.msea.2013.11.008

Fischer, F. D., Kolednik, O., Shan, G. X., & Rammerstorfer, F. G. (1995). A note on calibration of ductile failure damage indicators. *International Journal of Fracture, 73*(4), 345-357. doi: 10.1007/BF00027274

Gatea, Shakir, Lu, Bin, Ou, Hengan, & McCartney, Graham. (2015). Numerical simulation and experimental investigation of ductile fracture in SPIF using modified GTN model. *MATEC Web of Conferences, 21*, 04013.

Ghaffari Tari, D., Worswick, M. J., Ali, U., & Gharghouri, M. A. (2014). Mechanical response of AZ31B magnesium alloy: Experimental characterization and material modeling considering proportional loading at room temperature. *International Journal of Plasticity, 55*(0), 247-267. doi: http://dx.doi.org/10.1016/j.ijplas.2013.10.006

Guo, X., Chang, K., Chen, L. Q., & Zhou, M. (2012). Determination of fracture toughness of AZ31 Mg alloy using the cohesive finite element method. *Engineering Fracture Mechanics, 96*(0), 401-415. doi: http://dx.doi.org/10.1016/j.engfracmech.2012.08.014

Gurson, A.L. (1977). Continuum theory of ductile rupture by void nucleation and growth, Part I — Yield criteria and flow rules for porous ductile media. *Journal of Engineering Materials and Technology, 99*, 2-15.

Ha, Jinjin, Lee, Myoung-Gyu, & Barlat, Frédéric. (2013). Strain hardening response and modeling of EDDQ and DP780 steel sheet under non-linear strain path. *Mechanics of Materials, 64*(0), 11-26. doi: http://dx.doi.org/10.1016/j.mechmat.2013.04.004

Hama, Takayuki, & Takuda, Hirohiko. (2011). Crystal-plasticity finite-element analysis of inelastic behavior during unloading in a magnesium alloy sheet. *International Journal of Plasticity, 27*(7), 1072-1092. doi: http://dx.doi.org/10.1016/j.ijplas.2010.11.004

Hammer, Jeremiah Thomas. (2012). *Plastic Deformation and Ductile Fracture of Ti-6Al-4V under Various Loading Conditions.* Ohio State University.

Hammi, Y., Bammann, D. J., & Horstemeyer, M. F. (2004). Modeling of Anisotropic Damage for Ductile Materials in Metal Forming Processes. *International Journal of Damage Mechanics, 13*(2), 123-146. doi: 10.1177/1056789504039255

Hancock, J. W., & Brown, D. K. (1983). On the role of strain and stress state in ductile failure. *Journal of the Mechanics and Physics of Solids, 31*(1), 1-24.

Hasek, V. (1978). Research and theoretical description concerning the influences on the FLDs. *Blech Rohre Profile, 25*, 213-220.

Jain, A., & Agnew, S. R. (2007). Modeling the temperature dependent effect of twinning on the behavior of magnesium alloy AZ31B sheet. *Materials Science and Engineering: A, 462*(1–2), 29-36. doi: http://dx.doi.org/10.1016/j.msea.2006.03.160

Jia, Yueqian, & Bai, Yuanli. (2015a). *A Combined Isotropic, Kinematic and Cross Hardening Model for BH240 and DP600 Steel Sheets*. Paper presented at the International Deep-Drawing Research Group (IDDRG), Shanghai, China.

Jia, Yueqian, & Bai, Yuanli. (2015b). Ductile fracture prediction for metal sheets using all-strain-based modified Mohr-Coulomb model. *Submitted for publication*.

Jia, Yueqian, & Bai, Yuanli. (2015c). Experimental Study on the Mechanical Properties of AZ31B-H24 Magnesium Alloy Sheets under Various Loading Conditions. *International Journal of Fracture*, 1-24.

Jia, Yueqian, Long, Xiang, & Bai, Yuanli. (2012). Experimental Study on Mechanical Properties of AZ31B-H24 Magnesium Alloy Sheets uder Multi-Axial Loading Conditions. *Journal Of Automotive Safety And Energy, 3*(4), 390-400. doi: 10.3969/j.issn.1674-8484.2012.04.011

Jia, Yueqian, Long, Xiang, Wang, Kai, & Bai, Yuanli. (2013, January 3-8). *Calibration of Plasticity and Fracture of Magnesium Alloy Sheets Under Biaxial Loading Conditions.* Paper presented at the International Symposium on Plasticity and Its Current Applications, Bahamas.

John Neil, C., & Agnew, Sean R. (2009). Crystal plasticity-based forming limit prediction for non-cubic metals: Application to Mg alloy AZ31B. *International Journal of Plasticity, 25*(3), 379-398. doi: http://dx.doi.org/10.1016/j.ijplas.2008.05.003

Johnson, Gordon R., & Cook, William H. (1985). Fracture characteristics of three metals subjected to various strains, strain rates, temperatures and pressures. *Engineering Fracture Mechanics, 21*(1), 31-48.

Kaya, S., Altan, T., Groche, P., & Klöpsch, C. (2008). Determination of the flow stress of magnesium AZ31-O sheet at elevated temperatures using the hydraulic bulge test. *International Journal of Machine Tools and Manufacture, 48*(5), 550-557. doi: http://dx.doi.org/10.1016/j.ijmachtools.2007.06.011

Kelley, E.W., & Hosford, W.F. (1968). The deformation characteristics of textured magnesium. *Trans. TMS-AIME, 242*, 654–661.

Khan, Akhtar S., & Liu, Haowen. (2012a). A new approach for ductile fracture prediction on Al 2024-T351 alloy. *International Journal of Plasticity, 35*, 1-12. doi: http://dx.doi.org/10.1016/j.ijplas.2012.01.003

Khan, Akhtar S., & Liu, Haowen. (2012b). Strain rate and temperature dependent fracture criteria for isotropic and anisotropic metals. *International Journal of Plasticity, 37*, 1-15. doi: http://dx.doi.org/10.1016/j.ijplas.2012.01.012

Khan, Akhtar S., Pandey, Amit, Gnäupel-Herold, Thomas, & Mishra, Raja K. (2011). Mechanical response and texture evolution of AZ31 alloy at large strains for different strain rates and temperatures. *International Journal of Plasticity, 27*(5), 688-706. doi: http://dx.doi.org/10.1016/j.ijplas.2010.08.009

Kim, Dae-Guen, Son, Hyeon-Taek, Kim, Dae-Won, Kim, Yong-Ho, & Lee, Kye-Man. (2011). Effect of Cross-Roll Angle on Microstructures and Mechanical Properties during Cross-Roll Rolling in AZ31 Alloys. *Materials Transactions, 52*(12), 2274-2277.

Kim, Hyung Jong, Choi, Sun Chul, Lee, Kyoung Taek, & Kim, Heon Young. (2008). Experimental determination of forming limit diagram and springback characteristics of AZ31B Mg alloy sheets at elevated temperatures. *Materials transactions, 49*(5), 1112-1119.

Kim, Ji Hoon, Lee, Myoung-Gyu, Ryou, Hansun, Chung, Kwansoo, Youn, Jae Ryoun, & Kang, Tae Jin. (2008). Development of nonlinear constitutive laws for anisotropic and asymmetric fiber reinforced composites. *Polymer Composites, 29*(2), 216-228. doi: 10.1002/pc.20413

Kim, Junehyung, Ryou, Hansun, Kim, Dongun, Kim, Daeyong, Lee, Wonoh, Hong, Seung-Hyun, & Chung, Kwansoo. (2008). Constitutive law for AZ31B Mg alloy sheets and finite

element simulation for three-point bending. *International Journal of Mechanical Sciences, 50*(10–11), 1510-1518. doi: http://dx.doi.org/10.1016/j.ijmecsci.2008.08.004

Kiran, R., & Khandelwal, K. (2014). Experimental Studies and Models for Ductile Fracture in ASTM A992 Steels at High Triaxiality. *Journal of Structural Engineering, 140*(2), 04013044. doi: 10.1061/(ASCE)ST.1943-541X.0000828

Kiran, Ravi, & Khandelwal, Kapil. (2013). A micromechanical model for ductile fracture prediction in ASTM A992 steels. *Engineering Fracture Mechanics, 102*, 101-117. doi: http://dx.doi.org/10.1016/j.engfracmech.2013.02.021

Kurukuri, S., Worswick, M. J., Ghaffari Tari, D., Mishra, R. K., & Carter, J. T. (2014). Rate sensitivity and tension-compression asymmetry in AZ31B magnesium alloy sheet. *Philos Trans A Math Phys Eng Sci, 372*(2015), 20130216. doi: 10.1098/rsta.2013.0216

Lee, M. G., Kim, S. J., Wagoner, R. H., Chung, K., & Kim, H. Y. (2009). Constitutive modeling for anisotropic/asymmetric hardening behavior of magnesium alloy sheets: Application to sheet springback. *International Journal of Plasticity, 25*(1), 70-104. doi: http://dx.doi.org/10.1016/j.ijplas.2007.12.003

Lee, Myoung-Gyu, Wagoner, R. H., Lee, J. K., Chung, K., & Kim, H. Y. (2008). Constitutive modeling for anisotropic/asymmetric hardening behavior of magnesium alloy sheets. *International Journal of Plasticity, 24*(4), 545-582. doi: http://dx.doi.org/10.1016/j.ijplas.2007.05.004

Lemaitre, Jean. (1996). *A course on damage mechanics*: Springer, Berlin, Germany.

Levkovitch, Vladislav, & Svendsen, Bob. (2007). Accurate hardening modeling as basis for the realistic simulation of sheet forming processes with complex strain ‐ path changes. *AIP Conference Proceedings, 907*(1), 358-363. doi: doi:http://dx.doi.org/10.1063/1.2729539

Li, H., Fu, M. W., Lu, J., & Yang, H. (2011). Ductile fracture: Experiments and computations. *International Journal of Plasticity, 27*(2), 147-180. doi: http://dx.doi.org/10.1016/j.ijplas.2010.04.001

Li, M., Lou, X.Y., Kim, J.H., & Wagoner, R.H. (2010). An efficient constitutive model for room-temperature, low-rate plasticity of annealed Mg AZ31B sheet. *International Journal of Plasticity, 26*(6), 820-858.

Li, Saiyi, Hoferlin, Eric, Bael, Albert Van, Houtte, Paul Van, & Teodosiu, Cristian. (2003). Finite element modeling of plastic anisotropy induced by texture and strain-path change. *International Journal of Plasticity, 19*(5), 647-674. doi: http://dx.doi.org/10.1016/S0749-6419(01)00079-1

Li, Yaning, Luo, Meng, Gerlach, Jörg, & Wierzbicki, Tomasz. (2010). Prediction of shear-induced fracture in sheet metal forming. *Journal of Materials Processing Technology, 210*(14), 1858-1869.

Lian, J, Wu, J, & Münstermann, S. (2015). Evaluation of the cold formability of high-strength low-alloy steel plates with the modified Bai–Wierzbicki damage model. *International Journal of Damage Mechanics, 24*(3), 383-417. doi: 10.1177/1056789514537587

Lou, X.Y., Li, M., Boger, R.K., Agnew, S.R., & Wagoner, R.H. (2007). Hardening evolution of AZ31B Mg sheet. *International Journal of Plasticity, 23*(1), 44-86.

Lou, Yanshan, & Huh, Hoon. (2013). Prediction of ductile fracture for advanced high strength steel with a new criterion: Experiments and simulation. *Journal of Materials Processing Technology, 213*(8), 1284-1302. doi: http://dx.doi.org/10.1016/j.jmatprotec.2013.03.001

Luo, Meng, Dunand, Matthieu, & Mohr, Dirk. (2012). Experiments and modeling of anisotropic aluminum extrusions under multi-axial loading â€“ Part II: Ductile fracture. *International Journal of Plasticity, 32-33*(0), 36-58.

Luo, Meng, & Wierzbicki, Tomasz. (2010). Numerical failure analysis of a stretch-bending test on dual-phase steel sheets using a phenomenological fracture model. *International Journal of Solids and Structures, 47*(22-23), 3084 - 3102.

Mackenzie, A. C., Hancock, J. W., & Brown, D. K. (1977). On the influence of state of stress on ductile failure initiation in high strength steels. *Engineering Fracture Mechanics, 9*(1), 167-168.

Maksoud, Ismael Abdel, Ahmed, H., & Rödel, Johannes. (2009). Investigation of the effect of strain rate and temperature on the deformability and microstructure evolution of AZ31 magnesium alloy. *Materials Science and Engineering: A, 504*(1–2), 40-48. doi: http://dx.doi.org/10.1016/j.msea.2008.10.033

Malcher, L., Andrade Pires, F. M., & César de Sá, J. M. A. (2014). An extended GTN model for ductile fracture under high and low stress triaxiality. *International Journal of Plasticity, 54*, 193-228. doi: http://dx.doi.org/10.1016/j.ijplas.2013.08.015

McClintock, F A. (1968). A criterion of ductile fracture by the growth of holes. *Journal of Applied Mechanics, 35*, 363-371.

Mekonen, M. Nebebe, Steglich, D., Bohlen, J., Letzig, D., & Mosler, J. (2012). Mechanical characterization and constitutive modeling of Mg alloy sheets. *Materials Science and Engineering: A, 540*(0), 174-186. doi: http://dx.doi.org/10.1016/j.msea.2012.01.122

Min, Dong-Kyun, Jeon, Byung-Hee, Kim, Hyung-Jong, & Kim, Naksoo. (1995). A study on process improvements of multi-stage deep-drawing by the finite-element method. *Journal*

of Materials Processing Technology, 54(1–4), 230-238. doi: http://dx.doi.org/10.1016/0924-0136(94)01775-1

Mohr, D., & Henn, S. (2007). Calibration of Stress-triaxiality Dependent Crack Formation Criteria: A New Hybrid Experimental-Numerical Method. *Experimental Mechanics, in press*.

Mohr, D., & Oswald, S. (2007). A new experimental technique for the multi-axial testing of advanced high strength steel sheets. *Experimental Mechanics, In press*.

Mohr, Dirk, Chevin, Marc-Antoine, & Greve, Lars. (2013). Deformation Behavior of Magnesium Extrusions With Strong Basal Texture: Experiments and Modeling. *Journal of Applied Mechanics, 80*(6), 061002-061002. doi: 10.1115/1.4023958

Nahshon, K., & Hutchinson, J. W. (2008). Modification of the Gurson Model for shear failure. *European Journal of Mechanics - A/Solids, 27*(1), 1-17. doi: http://dx.doi.org/10.1016/j.euromechsol.2007.08.002

Nguyen, Ngoc-Trung, Lee, Myoung-Gyu, Kim, Ji Hoon, & Kim, Heon Young. (2013). A practical constitutive model for AZ31B Mg alloy sheets with unusual stress–strain response. *Finite Elements in Analysis and Design, 76*(0), 39-49. doi: http://dx.doi.org/10.1016/j.finel.2013.08.008

Nixon, Michael E., Cazacu, Oana, & Lebensohn, Ricardo A. (2010). Anisotropic response of high-purity α-titanium: Experimental characterization and constitutive modeling. *International Journal of Plasticity, 26*(4), 516-532. doi: http://dx.doi.org/10.1016/j.ijplas.2009.08.007

Park, Jingee, Lee, Jongshin, You, Bongsun, Choi, Seogou, & Kim, Youngsuk. (2007). Plastic Deformation Characteristics Of AZ31 Magnesium Alloy Sheets At Elevated Temperature.

AIP Conference Proceedings, 908(1), 1269-1274. doi: doi:http://dx.doi.org/10.1063/1.2740984

Park, N., Huh, H., Nam, J. B., & Jung, C. G. (2015). Anisotropy effect on the fracture model of DP980 sheets considering the loading path. *International Journal of Automotive Technology, 16*(1), 73-81. doi: 10.1007/s12239-015-0008-3

Piao, Kun, Chung, Kwansoo, Lee, Myoung-Gyu, & Wagoner, RobertH. (2012). Twinning-Slip Transitions in Mg AZ31B. *Metallurgical and Materials Transactions A, 43*(9), 3300-3313. doi: 10.1007/s11661-012-1154-0

Plunkett, B., Cazacu, O., & Barlat, F. (2008). Orthotropic yield criteria for description of the anisotropy in tension and compression of sheet metals. *International Journal of Plasticity, 24*(5), 847-866. doi: http://dx.doi.org/10.1016/j.ijplas.2007.07.013

Rauch, E. F., Gracio, J. J., & Barlat, F. (2007). Work-hardening model for polycrystalline metals under strain reversal at large strains. *Acta Materialia, 55*(9), 2939-2948. doi: http://dx.doi.org/10.1016/j.actamat.2007.01.003

Revil-Baudard, Benoit, Chandola, Nitin, Cazacu, Oana, & Barlat, Frédéric. (2014). Correlation between swift effects and tension–compression asymmetry in various polycrystalline materials. *Journal of the Mechanics and Physics of Solids, 70*(0), 104-115. doi: http://dx.doi.org/10.1016/j.jmps.2014.05.012

Rice, J R., & Tracey, D M. (1969). On the ductile enlargement of voids in triaxial stress fields. *Journal of the Mechanics and Physics of Solids, 17*, 201-217.

Roberts, C.S. (1960). *Magnesium and its alloys*: Wiley.

Rousselier, G., Barlat, F., & Yoon, J. W. (2009). A novel approach for anisotropic hardening modeling. Part I: Theory and its application to finite element analysis of deep drawing.

International Journal of Plasticity, 25(12), 2383-2409. doi: http://dx.doi.org/10.1016/j.ijplas.2009.04.002

Schmitt, J. H., Fernandes, J. V., Gracio, J. J., Vieira, M. F., & Vieira, M. F. (1991). Plastic behaviour of copper sheets during sequential tension tests. *Materials Science and Engineering: A, 147*(2), 143-154. doi: http://dx.doi.org/10.1016/0921-5093(91)90840-J

Schmitt, J. H., Shen, E. L., & Raphanel, J. L. (1994). A parameter for measuring the magnitude of a change of strain path: Validation and comparison with experiments on low carbon steel. *International Journal of Plasticity, 10*(5), 535-551. doi: http://dx.doi.org/10.1016/0749-6419(94)90013-2

Shi, Baodong, & Mosler, Jörn. (2013). On the macroscopic description of yield surface evolution by means of distortional hardening models: Application to magnesium. *International Journal of Plasticity, 44*, 1-22. doi: http://dx.doi.org/10.1016/j.ijplas.2012.11.007

Shojaei, Amir, Dahi Taleghani, Arash, & Li, Guoqiang. (2014). A continuum damage failure model for hydraulic fracturing of porous rocks. *International Journal of Plasticity, 59*, 199-212. doi: http://dx.doi.org/10.1016/j.ijplas.2014.03.003

Staroselsky, A., & Anand, L. (2003). A constitutive model for hcp materials deforming by slip and twinning: application to magnesium alloy AZ31B. *International Journal of Plasticity, 19*(10), 1843-1864. doi: http://dx.doi.org/10.1016/S0749-6419(03)00039-1

Steglich, D., Jeong, Y., Andar, M. O., & Kuwabara, T. (2012). Biaxial deformation behaviour of AZ31 magnesium alloy: Crystal-plasticity-based prediction and experimental validation. *International Journal of Solids and Structures, 49*(25), 3551-3561. doi: http://dx.doi.org/10.1016/j.ijsolstr.2012.06.017

Steglich, D., Tian, X., Bohlen, J., & Kuwabara, T. (2014). Mechanical Testing of Thin Sheet Magnesium Alloys in Biaxial Tension and Uniaxial Compression. *Experimental Mechanics, 54*(7), 1247-1258. doi: 10.1007/s11340-014-9892-0

Steglich, Dirk, Brocks, Wolfgang, Bohlen, Jan, & Barlat, Frederic. (2011). Modelling direction-dependent hardening in magnesium sheet forming simulations. *International Journal of Material Forming, 4*(2), 243-253. doi: 10.1007/s12289-011-1034-y

Teodosiu, C, & Hu, Z. (1995). *Evolution of the intragranular microstructure at moderate and large strains: modelling and computational significance.* Paper presented at the Proc. Numiform.

Teodosiu, C, & Hu, Z. (1998). *Microstructure in the continuum modelling of plastic anisotropy.* Paper presented at the Nineteenth Riso International Symposium on Materials Science 1998.

Thuillier, S., Manach, P. Y., Menezes, L. F., & Oliveira, M. C. (2002). Experimental and numerical study of reverse re-drawing of anisotropic sheet metals. *Journal of Materials Processing Technology, 125–126*(0), 764-771. doi: http://dx.doi.org/10.1016/S0924-0136(02)00387-4

Tvergaard, V., & Needleman, A. (1984). Analysis of the cup-cone fracture in a round tensile bar. *Acta Materialia, 32*, 157-169.

Vial, Christian, Hosford, William F., & Caddell, Robert M. (1983). Yield loci of anisotropic sheet metals. *International Journal of Mechanical Sciences, 25*(12), 899-915. doi: http://dx.doi.org/10.1016/0020-7403(83)90020-6

Walters, Carey. (2009). *Development of a Punching Technique for Ductile Fracture Testing Over a Wide Range of Stress States and Strain Rates.* Massachusetts Institute of Technology.

Wang, H., Wu, P. D., Wang, J., & Tomé, C. N. (2013). A crystal plasticity model for hexagonal close packed (HCP) crystals including twinning and de-twinning mechanisms. *International Journal of Plasticity, 49*(0), 36-52. doi: http://dx.doi.org/10.1016/j.ijplas.2013.02.016

Wang, Kai, Luo, Meng, & Wierzbicki, Tomasz. (2014). Experiments and modeling of edge fracture for an AHSS sheet. *International Journal of Fracture, 187*(2), 245-268. doi: 10.1007/s10704-014-9937-5

Wang, Kai, & Wierzbicki, Tomasz. (2015). Experimental and numerical study on the plane-strain blanking process on an AHSS sheet. *International Journal of Fracture, 194*(1), 19-36. doi: 10.1007/s10704-015-0034-1

Wierzbicki, Tomasz, Bao, Yingbin, & Bai, Yuanli. (2005). A new experimental technique for constructing a fracture envelope of metals under multi-axial loading. *Proceedings of the 2005 SEM Annual Conference and Exposition on Experimental and Applied Mechanics,* 1295 - 1303.

Wierzbicki, Tomasz, & Xue, Liang. (2005). On the effect of the third invariant of the stress deviator on ductile fracture: Impact and Crashworthiness Laboratory, Massachusetts Institute of Technology, Cambridge, MA.

Wilkins, M L., Streit, R D., & Reaugh, J E. (1980). Cumulative -strain-damage model of ductile fracture: simulation and prediction of engineering fracture tests, UCRL-53058: Lawrence Livermore Laboratory, Livermore, California.

Xue, Liang. (2008). Constitutive modeling of void shearing effect in ductile fracture of porous materials. *Engineering Fracture Mechanics, 75*(11), 3343-3366. doi: http://dx.doi.org/10.1016/j.engfracmech.2007.07.022

Yan, Yun Qi, Zhang, H, Chen, Q, Zhong, H, & Weng, WP. (2007). *Microstructures, Tensile Properties and Forming Process of AZ31 Alloy Sheets.* Paper presented at the Materials science forum.

Yoshida, Fusahito, Uemori, Takeshi, & Fujiwara, Kenji. (2002). Elastic–plastic behavior of steel sheets under in-plane cyclic tension–compression at large strain. *International Journal of Plasticity, 18*(5–6), 633-659. doi: http://dx.doi.org/10.1016/S0749-6419(01)00049-3